Technische Universität München
TUM School of Natural Sciences

Development of Scattering Photon-Correlation Fourier Spectroscopy for In-Solution Sensing

Korneel Ridderbeek

Vollständiger Abdruck der von der TUM School of Natural Sciences der Technischen Universität München zur Erlangung der akademischen Grades eines

Doktors der Naturwissenschaften
(Dr. rer. nat.)

genehmigten Dissertation.

Vorsitz: Prof. Dr. Martin Zacharias

Prüfer*inner der Dissertation:

1. TUM Junior Fellow Dr. Jian Cui
2. Prof. Dr. Michael Sattler
3. Prof. Dr. Don C. Lamb

Die Dissertation wurde am 23.03.2023 bei der Technischen Universität München eingereicht und durch die TUM School of Natural Sciences am 11.07.2023 angenommen.

HELMHOLTZ MUNICH

Development of Scattering Photon-Correlation Fourier Spectroscopy for In-Solution Sensing

Korneel Ridderbeek

Supervisor Dr. Jian Cui (TUM Junior Fellow)

Mentor Dr. Thomas Bischof

March 20, 2023

Dedicated to

my fiancée and my parents

Abstract

Cells consist of thousands of proteins that interact constantly, which underlay almost all of the cellular functions, such as nutrient transport, signal perception, cellular action and cell anchoring. Recently, more than half of these interactions have been found to bind weakly and transiently, making them prime targets to study. However, transient biomolecular interactions are difficult to measure, because they occur near the diffusion limit. In this dissertation, a novel optical method is introduced to unveil kinetic information of transient biomolecular systems. For this, we utilize the local dielectric sensitivity of freely diffusing metallic nanoparticles in solution and an optical setup with high temporal and spectral resolution. Silver decahedra nanoparticles with a thin layer of Gold and surface ligand modification are used as biocompatible optical nanosensors that change their scattering resonances upon sensing of biomolecular interactions in their proximity. A custom-built optical setup measures the scattered light of these nanoparticles freely diffusing in solution with single photon detectors and an interferometer to obtain ns and $\mu\mathrm{eV}$ resolution, respectively. We observe biomolecular dynamics computationally and experimentally in the range of $0.1\,\mu\mathrm{s}$ to $100\,\mu\mathrm{s}$, being well in the transient regime. This work opens up a new path towards label-free measurements of fast and transient biomolecular interactions in solution.

Zusammenfassung

Zellen bestehen aus tausenden von Proteinen, die ständig miteinander interagieren und so ihre biologische Funktion bestimmen. Kürzlich wurde festgestellt, dass mehr als die Hälfte dieser Interaktionen schwach und transient sind, was sie zu erstklassigen Zielen für Untersuch macht. Allerdings sind transiente biomolekulare Interaktionen schwer zu messen, da sie nahe an der Diffusionsgrenze stattfinden. In dieser Dissertation wird eine neuartige optische Methode vorgestellt, mit der kinetische Informationen über transiente biomolekulare Systeme enthüllt werden kann. Hierzu werden die lokalen dielektrischen Sensitivitäten von metallischen Nanopartikeln sowie ein optischer Aufbau mit hoher zeitlicher und spektraler Au-

flösung genutzt. Unter Verwendung von Silber Decahedra-Nanopartikel, welche mit einer dünnen Goldschicht beschichtet wurden, und einer zur Biokompatibilität adaptierten Oberflächenligandenmodifikation, dienen diese als optische Nanosensoren. Sie änderen ihre Streuresonanzen, wenn biomolekulare Interaktionen in ihrer räumlichen Nähe auftreten. Ein *home-built* optischer Aufbau misst das gestreute Licht der Nanopartikeln, die sich frei in der Lösung bewegen, mithilfe von Einzelphotonendetektoren und einem Interferometer. Die Auflösung befindet sich im Bereich von ns bzw. $\mu\mathrm{eV}$. In dieser Arbeit analysieren wir biomolekulare Dynamiken, jeweils durch Simulation und Experiment, die im Bereich von $0.1\,\mu\mathrm{s}$ to $100\,\mu\mathrm{s}$ und somit durchaus als transient bezeichnet werden können. Sie eröffnet daher einen Weg zur Messung schneller und vorübergehender biomolekularer Wechselwirkungen in Lösung ohne die Verwendung von Markern.

Samenvatting

Cellen bestaan uit duizenden proteïnen die voortdurend op elkaar inwerken om de biologische functie van de cel te bepalen. Onlangs is gebleken dat meer dan de helft van deze interacties zwak en transiënt bindt, waardoor ze zeer geliefd zijn om te bestuderen. Echter zijn transiënte biomoleculaire interacties moeilijk te meten, omdat ze dicht bij de diffusielimiet optreden. In dit proefschrift wordt een nieuwe optische methode geïntroduceerd om kinetische informatie van transiënte biomoleculaire systemen bloot te leggen, gebruikmakend van de lokale diëlektrische sensitiviteit van metalen nanodeeltjes en een optische opstelling met hoge temporele en spectrale resolutie. Wij gebruiken Zilveren decahedra nanodeeltjes met een dun laagje Goud en oppervlakte-ligandmodificatie als biocompatibele optische nanosensoren die hun scattering resonanties veranderen bij detectie van biomoleculaire interacties in hun nabijheid. Een *home-built* optische opstelling meet het gescatterde licht van nanodeeltjes die vrij in de oplossing diffunderen met *single photon* detectoren en een interferometer om respectievelijk een resolutie van ns en $\mu\mathrm{eV}$ te behalen. We observeren biomoleculaire kinetiek computationeel en experimenteel in het bereik van $0.1\,\mu\mathrm{s}$ to $100\,\mu\mathrm{s}$, dus ruim in het transiënte regiem. Hierdoor opent dit werk een nieuwe weg naar het meten van snelle en transiënte biomoleculaire interacties zonder labeling in oplossing.

Acknowledgement

First and foremost, I would like to thank my supervisor Dr. Jian Cui for attracting me to come to Munich to work on this exciting project. I am happy that he took me on as his first PhD-student, because he offered a great working environment which really is knowledge and technology driven. I am grateful for your guidance and all the scientific and non-scientific think you have taught me.

Secondly, a word of gratitude goes out to my mentor Dr. Thomas Bischof. Your insights during technical discussions definitely have helped to shape this project. However, I not only want to thank you for your professional advice, but also on a personal note. All our brewing, hiking, disc golfing, and climbing have contributed to a pleasant time in Munich.

Next, I would want to thank a few people that I also have grown close relationships with, namely the members of the nanoPROBE lab. You guys are pleasant to work and discuss with. Also, I enjoyed all the fun things we did as group, such as the alpaca hike, disc golf outing, and the many dinners. Specifically, I would like to thank Dr. Fangyuan Song and Dr. Jieying Zhou for the close collaboration on the nanosenors syntheses. Your chemistry knowledge has helped me to understand colloidal chemistry much better. I would also like to thank all the technician trainees that we have had; Nicole Dürndorfer, Wendy Gonzalez, Marius Maibach, Henri Hoppe, Felix Dorn, and Alex Hellmann. You guys were a tremendous help in the lab, but also have taught me important project management skills. The same is also true for Lara Jakob, who was a pleasure to work with in the lab. My office mates; Sapthagiri Sukumaran, Serkan Aslan, and Dr. Zhizi Jing have been great. Thank you guys for all the explanations of biological concepts. Those definitely helped me understand this research field much better. I also appreciated all the fruitful discussions and input from Dr. Luciano Santino and Dr. Nicolai Hoinka about experiments and simulations. The last group member I would like to thank is Ruyu Ma. It was a pleasure sharing a lab with you and the great communication we had. Also the distractions of throwing frisbee discs or playing badminton have helped to keep my mind clear.

My gratitude also goes out to Jakob Lingg with whom I could always chat about life as a physicist in biology land. Our conversations have helped to relativise all things.

I would also like to acknowledge the HPC admin team for all their support; Dr. Thomas Schwarz-Romond, Dr. Manuela Hartmann, Dr. Andreas Schröder, Stephanie Montag, Dr. Barbara Schröder, and Almut Barden. The entire pioneer campus has been a nice environment for discussions, especially at the HPC PhD/PostDoc-seminar. Here, my fellow committee members have to be thanked to help organize these amazing events.

Lastly, I would like to thank my friends and family for their support, especially my parents and my fiancée. I am very grateful for my parents to take me in their home during the covid lockdown period and their overall support during all of my studies. To my fiancée I would like to say: "Thank you for letting me take this career opportunity and for your support throughout. It forced us into a long-distance relationship, but I am proud at you and how we managed."

Contents

1 Introduction

During my doctoral studies, the world went through a pandemic of SARS-CoV-2 coronavirus.[1] Due to this fast spreading virus, the entire world came in contact with bio-sensors. At first, nose and throat swabs were analyzed with Polymerase Chain Reaction (PCR) tests. Later, lateral flow antigen tests were introduced to identify whether a person was infected with SARS-CoV-2. These two examples of bio-sensors detect the presence or absence of a particular biomolecule. In the case of a PCR this is the virus' RNA and for the antigen test the spike-protein (S-protein) of the virus' membrane is tested. In general, biosensors are tools that give insight into a biological system and many physicochemical methods have been explored for a variety of systems.[2] All these methods have their own benefits and drawbacks, therefore they have been used for different niches of biomolecular sensing, however we found one niche being underserved; the niche of obtaining kinetic information of fast and transient interacting biomolecules.[2] In this dissertation, we therefore present a novel label-free optical biosensing method with the potential of obtaining binding kinetics of fast interacting biomolecules.

This chapter starts by discussing what a biomolecular interaction is and what function it has on a cellular level. Then several biosensing techniques are discussed that are commonly used to obtain information about biomolecular interactions. Here, two groups can be formed, where the first group consists of methods that can study many interactions quickly at a relative low cost, making them perfects for biomolecular interaction screening. Thereafter, the second group of techniques with more specificity is discussed. These techniques usually trade in cost or experimental time for lower false-negative detection rates. These techniques are therefore in the biomolecular interaction field known as verification techniques. From comparison of these techniques, we realize that a subsection of biomolecular interactions has limited experimental measurement methods available, and due to recent discussion in literature we believe that there is great interest in these fast and transient biomolecular interactions. This finding is the main driver of the research presented in this dissertation. Lastly, we finalize the chapter by introducing physical laws, mathematical definitions, and field specific language that are used throughout this work.

1.1 Biomolecular Interactions

In modern medicine, a biosensor that can tell the presence or absence of a specific biomolecule is useful, for instance the presence of the Alpha-fetoprotein in blood is used as a marker for cancer, since it is not present in healthy humans.[3] However, some biomolecules are always present, and it is the way they interact with each other that causes changes to a cell. Namely, cells are integrated systems with over thousands of proteins and other biomolecules, where interactions happen constantly and these interactions underlie all biological functions and processes in the cell.[4] Understanding how these biomolecules interact, and ultimately being able to control certain interactions, is crucial for basic biology but also drug development.[5] Namely, medical drugs exert their effect by interacting with a biomolecule to either inhibit or initiate one or multiple cascades of biomolecular interactions in the cell, causing the cell to react.

A biomolecular interaction is thus when two biomolecules come together to form a complex through multiple specific molecular contacts.[6] The complex then offers different biological functions than the two individual biomolecules. The intra-molecular contacts can be made through Van der Waals forces, hydrogen bonds, electrostatic, covalent and other non-covalent interactions. To simplify a model describing the interaction between two biomolecules, all the contacts are combined into one. This way, the simplest model describes a probe molecule (P) that binds to a target molecule (T) to form a complex (C) as $P + T \rightarrow C$. This equation describes the formation of the complex, but it is not necessarily a one way process. The contacts between the biomolecules could loosen due to thermal effects, such that a better description is given as an equilibrium equation:

$$P + T \underset{k_\mathrm{d}}{\overset{k_\mathrm{a}}{\rightleftharpoons}} C \tag{1.1}$$

where ka is the association rate constant and kd is the dissociation rate constant. A general measure for where the equilibrium of this equation is shifted towards is the dissociation constant $K_\mathrm{D} = \frac{k_\mathrm{d}}{k_\mathrm{a}}$ and is sometimes also called the binding constant with the units of molar. Namely, K_D describes the concentration needed of the probe molecule to obtain half unbound and half bound. In Figure 1.1 an overview is given of the terminology and the K_D values of different biomolecular interactions.[7] Here, we see that strong/permanent binding proteins only need little concentration to have half of them bound, whereas weak binding biomolecules need orders of magnitude higher concentrations. Binding affinity is thus inversely define to K_D.

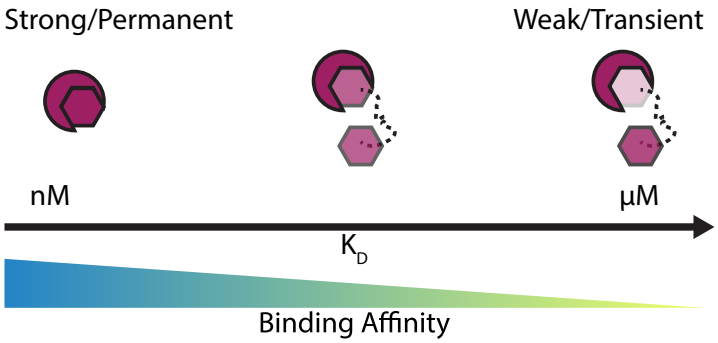

Fig. 1.1.: An illustration of different types of biomolecular interactions ranging from strong/permanent interactions to weak/transient interactions. Adapted from Perkins et al.[7]

Since the range of biomolecular interactions is so broad and because of the many different types of biomolecules, there exist many different methods to measure biomolecular interactions. All of these methods are specialized towards certain types of biomolecules or certain binding affinities. Typically, to identify whole networks of interactions and interaction pathways, screening techniques are used that can measure many different biomolecules at once. Thereafter, specific interaction pairs are validated with other methods that have higher specificities. In the following parts, both screening and verification methods are discussed and compared.

1.2 Screening of Biomolecular Interactions

This section summarizes the four common screening methods of biomolecular interactions: affinity-tagged proteins, two-hybrid systems, quantitative mass spectrometry, and *in-silico*.[8] All the methods presented in this section have benefits and downsides and therefore are tailored to different niches. However, to get a global view of how these methods compare to each other, the throughput, accuracy, cost-effectiveness, and measurement time are put into Table 1.1.

Affinity-Tag

Affinity tagging of biomolecules takes advantage of selective binding to a bait protein through genetically fusing it with a tag. Typically, cells are transfected with a plasmid to express the bait-tag molecule in the cell. After the appropriate expression period

the cells are lysed and the bait-tags, together with bound proteins, are purified.[8] The purification can be performed through various methods, e.g. magnetic beads, protein columns, and gel-electrophoresis. There also exists varieties of possible tags, each with their own pros and cons. But generally, affinity-tags are biased towards high abundance proteins, high affinity, and slow kinetics. Because of this reason, affinity tagging is commonly used to purify overexpressed proteins from cell lysates.[9] Efforts to tag protein pairs with low affinity and fast kinetic usually results in higher false positive rates on the order of $25\,\%$.[10]

Two-Hybrid System

The most well-known two-hybrid system is the Yeast-2-Hybrid (Y2H) system, where the survival of a yeast culture is monitored based on a specific protein-protein interaction. A genetically engineered yeast strain that cannot produce its own nutrients for survival is transfected with two plasmids: one expressing a bait protein that is fused to the first half of a transcription factor (DNA binding), and the other a target protein fused to the second half of the transcription factor (gene activating). Only when the two halves of the transcription factor are close to each other, the gene is transcribed. In the Y2H system, the reporter gene generates the nutrients needed for survival.[11] The advantages of the Y2H system include ease of use, low cost, *in-cellulo* detectability, and sensitive towards low affinity interactions.[8] The downside to Y2H is that only binary protein interactions can be measured at a time, and it generates a large number of false positives. The false positive rate has been estimated to be on the order of $50\,\%$.[10] Efforts are made to reduce the high false negative rate, but this is still the major limiting factor of Y2H systems.[12, 13, 14]

Quantitative Mass-Spectrometry

Quantitative Mass-Spectrometry (MS) is a combined method of affinity purification with MS. MS ionizes molecules to propel and deflect them with electric and magnetic fields. This way, the mass-to-charge ratio of small cellular elucidates can be measured. Alternatively, the molecules can be broken up into fragments to determine the amino acid sequence of the whole molecule. Therefore, MS is a very sensitive technique, but in order to be quantitative in biomolecular interaction screening one has to introduce stable isotopes or chemical labels into the cell culture. The cultures are then crossbred with unlabeled ones to find whether the labeled proteins are taking

part in an interaction cluster.[15] The pros and cons are very similar to the affinity-tag method, with the exception that MS can detect low abundance proteins more easily.[16]

In-Silico Methods

Computational methods have significantly increased in use for drug discovery over the last decades. Quantitative Systems Pharmacology (QSP) uses accumulated data on approved and failed drugs to screen for new biomolecular interaction partners. Reusing existing drugs that got stuck in a far stage of the drug development process for other deceases reduces the development time of a drug for that new decease significantly. Likewise, Quantitative Systems Toxicology (QST) utilizes existing datasets to generate information about potential side effects or other effector pathways.[17] Due to these novel approaches in the computational field, the chemical parameter space for the experimentalists could be reduced effectively. Even screening for drug-like molecules without experimental data has been employed to reduce the chemical parameter space.[18]

	Thoughput	**Accuracy**	**Cost Effectiveness**	**Measurement Time**
Affinity-tag				
Two-Hybrid				
QMS*				
In Silico				

Tab. 1.1.: Table of various biomolecular-interaction screening techniques and their throughput, accuracy, cost-effectiveness and measurement times. *QMS is Quantitative Mass-Spectrometry.

In Table 1.1 the throughput, accuracy, cost-effectiveness, and measurement time of four different common screening methods for biomolecular interaction detection are shown. All four of these screening methods have a high throughput, are cost-effective, and have relative short measurement times. Unfortunately, these techniques have high false-negative rates, reducing their accuracy, therefore verification techniques are used with higher specificity to check specific interaction pairs from the screening methods. These methods are discussed in the next section.

1.3 Verification Methods of Biomolecular Interactions

The screening methods discussed in the previous section are designed to generate large datasets at low costs. However, this goal of high throughput most of the time comes at the cost of having higher false-negative rates or other methodological artifacts. However, this allows for relatively cheap and fast data acquisition of biomolecular interaction maps. To verify the most promising binding pairs, methods with more specificity have been engineered. They can verify hits from biomolecular screenings in exchange for higher research costs or experimental time, and thus are employed less often. This section summarizes them, categorizing them into: colocalization, co-immunoprecipitation, surface plasmon resonance (SPR), and Nuclear Magnetic Resonance (NMR).[10] Again, the throughput, accuracy, cost effectiveness, and measurement time are compared and can be found in Table 1.2.

Co-Localization

The physical presence and proximity of biomolecules can be visualized through microscopy. If two target biomolecules are in physical proximity of each other, this is known as colocalization. It is to be expected that if biomolecules interact, they will colocalize as well. To visualize the interacting biomolecular pair, they are typically stained or labeled with two different dyes or fluorophores. Then confocal microscopy, a microscopic technique that gives near-diffraction limit resolution ($\sim 250\,\mathrm{nm}$), can be used to measure the overlap of the two fluorescent signals. The resolution is improved when using super microscopy techniques that are able to detect down to $\sim 40\,\mathrm{nm}$.[19] Lastly, Förster Resonance Energy Transfer (FRET) microscopy, a method utilizing non-radiative energy transfer between two fluorophores, can be used to detect co-localization below $10\,\mathrm{nm}$.[20] With higher resolution these optical systems become more complex, costly, and it takes longer to acquire a frame.[21, 22, 23]

Proximity Ligation Assay (PLA) is an alternative technique to traditional staining which utilizes two antibodies, that both have a short DNA strand attached to them. The two antibodies target two different biomolecules, which co-localize when they interact. In that case, the DNA strands of the antibodies can take part in a DNA synthesis process, which produces long coils of fluorescent DNA.[24] These can be visualized with microscopic techniques like confocal microscopy, since subdiffraction limited resolution is not per se necessary anymore. The generation of the fluorescent DNA already indicates co-localization. The advantage of PLA over traditional

staining is that low abundance proteins can be visualized much easier due to the amplification.[25]

Co-Immunoprecipitation

In co-immunoprecipitation (co-IP), a polymer bead coated with an antibody is mixed with cell lysate targeting a specific bait biomolecule. When the bead is eluted from the lysate, the antibody captures the bait biomolecule and all the biomolecules interacting with it. The resulting biomolecular complex can be identified through mass-spectrometry. Even though co-IP can capture very complex clusters of interacting biomolecules, it is biased towards high-affinity proteins, similar to affinity tag methods. Additionally, the need for a highly specific antibody for the bait molecules makes this method rather costly.[26] Unspecific antibodies namely bind with other proteins leading to noise in the measurement.[27]

Surface Plasmon Resonance

Surface Plasmon Resonance (SPR) is a biosensing technique that is based on the interaction of light with a thin metal sheet. Incoming light results in a reflected beam and a surface-bound mode. The surface-bound mode is sensitive to dielectric changes at the opposite side of the surface and influences at what angle the outgoing beam is reflected. Typically, the surface is coated with antibodies for a biomolecule, after which that particular biomolecule is flushed over the surface that binds to the antibody. Lastly, the second biomolecule is flushed over the construct and any change in signal would indicate interaction or binding events between the two biomolecules. Since the device is flushing in specific concentrations for a specific period of time, the signal can be tracked as a function of concentration and time.[28] This flushing in and out allows SPR to obtain kinetic data ($k_{\mathrm{a}}, k_{\mathrm{d}}, and k_{\mathrm{D}}$), since effectively the fraction of bound and unbound proteins changes over time. Most of the other techniques presented in this introduction only indicate whether binding is present or at most can output KD. Other advantages of SPR are that it only needs small quantities of the biomolecules at study, and it is label-free. Unfortunately, the presence of an extended flat surface can affect the binding kinetics by inhibiting the motion of the biomolecules.[29] Additionally, it is difficult to distinguish specific from unspecific binding of biomolecules with this method.

Nuclear Magnetic Resonance

There exist many different spectroscopic methods that can verify biomolecular interactions. Nuclear Magnetic Resonance (NMR) is a popular spectroscopic method, because of its high specificity and atomic resolution. NMR is a technique that utilizes the magnetic nuclear spin of atoms, which can be aligned to a constant magnetic field. Then a radio frequency pulse is used to perturb the alignment, causing the nuclear spins to precess. This response to the perturbation has characteristic frequencies dependent on the applied magnetic field, the nuclei, and the surrounding nuclei. This way, it is possible to deduce molecular identity and the structure of the biomolecule with high resolution. When binding pairs are studied with NMR the folding structure can be resolved giving insight into binding pockets and which amino acids are taking part in the binding. Due to its high accuracy, NMR has been employed in biomolecular interaction studies with very low false-positive rates. Despite these advantages, NMR is usually limited to biomolecular systems with small molecular mass, data collection is slow, and the infrastructure needed for NMR is expensive.[30]

	Thoughput	**Accuracy**	**Cost Effectiveness**	**Measurement Time**
co-loc				
co-IP				
SPR				
NMR				

Tab. 1.2.: Table of various verification techniques for biomolecular interactions and their throughput, accuracy, cost effectiveness and measurement times. *co-loc = colocalization, co-IP =Co-immunoprecipitation, SPR = Surface Plasmon Resonance, and NMR = Nuclear Magnetic Resonance

In Table 1.2, four common verification techniques for biomolecular interaction sensing are compared. Here we find, in contrary to the screening methods from Table 1.1, that all of these techniques have moderate to low throughput. Instead, the overall accuracy of the methods is much greater than we have seen before, indicative of the low false-negative rates of these techniques. This is why these methods most of the time of used in combination.

1.4 Kinetic Biomolecular Interactions are Underserved in Screening and Verification Methods

From reviewing common screening and verification techniques for biomolecular interactions, we have found that there exist limited methods optimized for obtaining kinetic data or even are able to detect low-affinity proteins. Hein et al. mention that protein networks actually are dominated by weakly interacting biomolecules.[31] In addition, Luck et al. conclude the same from many observations of single hits in repeated experiments. In their view, it is difficult to quantify these transient proteins interactions with the current methods available.[32] Similarly, Ghadie et al. hypothesize that $80\,\%$ of the fast interacting proteins in Humans actually might have important cellular functionality.[33]

From the screening and verification methods discussed previously only three are tailored towards low-affinity, kinetic biomolecular interactions: Y2H, SPR, and FRET microscopy. Unfortunately, Y2H systems can only indicate the presence of the interaction and cannot grant information about the time dynamics. SPR can output kinetic information, but is not tailored towards fast-kinetics, because of its microfluidics system ($< 1\,\mathrm{s}$). Lastly, FRET microscopy has been employed for biomolecular interaction measurements, but blinking (switching on and off) and photobleaching, make the detection of fast interactions ($< 1\,\mathrm{ms}$) difficult too.[34] Additionally, for FRET studies the biomolecules have to be engineered with fluorescent labels, which modifies the structure and thus likely the kinetics.

1.5 Dissertation Aim

The aim of this work is to develop a novel optical method with the potential of kinetic bio-sensing. This method is optimized for fast and transient biomolecular interaction sensing, since these are underserved interactions that researchers want to study. We propose an optical method consisting of two parts: freely diffusing nanosensors and an optical setup with high temporal and spectral resolution. First optimal nanosensors are developed that can be used to measure interacting biomolecules in solutions, mitigating unwanted substrate effects. These nanosensors should change their optical output, based on interaction events in their proximity. For this, we propose the use of metallic nanoparticles, see Figure 1.2. Freely diffusing metallic

nanosensors offer the advantage to study the biomolecules in their native environment and thermal equilibrium, therefore not having to rely on slow microfluidics as in SPR.

Second, the optical setup is developed that can analyze the changes in the optical output of the nanosensors with high timing and spectral resolution, while the particles freely diffuse in solution. For this, we propose a combination of a Fluorescence Correlation Spectroscopy setup and an interferometer. Here, fitting models for the obtained data that describe the interactions in the proximity of the nanosensors must be developed to extract information from the system, such as the rate constants.

Third, the data obtained with the novel optical method should be compared to literature or other optical techniques to ensure its working and show that the measurement range exceeds what is accessible with other techniques. Here, the earlier obtained models can be used to extract kinetic data from biomolecular study material.

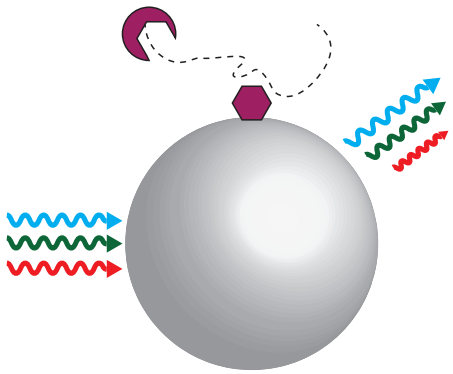

Fig. 1.2.: An illustration of a nanosensor changing its optical output (indicated by changes in the arrow size) due to a biomolecular interaction event that occurs in its proximity, where the dashed line is the path of one of the interaction partners diffusing through solution.

1.6 Dissertation Structure

In this dissertation, an optical bio-sensing method is introduced with the potential of measuring kinetic interactions of biomolecules freely diffusing in solution. The optical device consists of two main parts: metallic nanosensors and optical setup

itself. Chapter 2 starts with theoretically describing the interaction between light and metallic nanosensors. Various parameters, such as size, material, shape and surrounding dielectric medium are found to influence the optical output of the nanosensor. Through computational exploration, these parameters are examined to find an optimal nanosensor, and predictions are made on what signals to expect from kinetic biomolecular binding events. As the second part of Chapter 2, an experimental exploration is performed on the synthesis and the stability in different biological buffers. A few strategies such as surface capping and coating are employed to improve the stability, obtaining a highly sensitive and stable nanosensor.

In Chapter 3, the second part of in-solution biosensing is discussed: the optical setup. Theoretical descriptions of how light interacts with the individual optical components of the setup are formulated. Eventually they are combined to descriptive formulae for the different operation modes of the entire optical device. Fourier Transform Spectroscopy (FTS) and Photon-Correlation Fourier Spectroscopy (PCFS) are introduced as the main methods in this dissertation. The analytical theory is then converted into computational models to explore the experimental parameter space faster. Predictions are made for expected outputs from kinetic biomolecular binding events. Thereafter, experimental verification of the setup is performed to prove that the computational outputs are consistent with experiments.

In the last chapter, Chapter 4, the nanosensors from Chapter 2 are combined with the optical setup from Chapter 3. In simulation and experiments, the spectral differences between the average single nanosensor and an ensemble of nanoparticles are revealed. It is proposed that this information can be used for chemical synthesis optimization. For this, luminescent and scattered light, coming from the nanosensors, are explored to discuss the advantages and disadvantages of both illumination strategies. In the second part of Chapter 4, in-solution sensing experiments are performed. Both FTS and PCFS are employed to obtain different signals from nanosensors and analyte to prove the potential of this overall method of this work can be utilized for in-solution sensing of kinetic biomolecular interactions.

Before we can dive into the science, a few mathematical definitions have to be introduced. Additionally, a few words should be mentioned about the writing style that follows in this dissertation. I am aware that scientific writing commonly is done in a passive voice. However, I am of the opinion that readability and intent are better captured actively. Therefore, I try to describe existing literature and theory with passive sentences, but switch to active sentences to describe our experiments, train of thought, and decisions.

1.7 Mathematical Basis

Here, general mathematical definitions and notations are described, such that the reader understands the mathematical steps taken later on in this dissertation. Consequently, I do not have to introduce the same topic multiple times. The reader should find that the topics connect and sometimes repeat. A core concept throughout this work is the mathematical description of how light interacts with matter. Therefore, let us first discuss Maxwell's equation.

1.7.1 Maxwell's Equations

Maxwell's equations are a set of coupled partial differential equations that are the foundation of electromagnetism. Since light can be described classically as electromagnetic waves, this set of equations also becomes important to describe light-matter interactions. The differential Maxwell's equations can be written as:

$$\nabla \cdot \vec{E} = \frac{\rho}{\epsilon_0} \tag{1.2}$$

$$\nabla \cdot \vec{B} = 0 \tag{1.3}$$

$$\nabla \times \vec{E} = -\frac{\partial \vec{B}}{\partial t} \tag{1.4}$$

$$\nabla \times \vec{B} = \mu_0 \left(\vec{J} + \epsilon \frac{\partial \vec{E}}{\partial t} \right) \tag{1.5}$$

Here, the electric-field, $\vec{E}$, and magnetic-field, $\vec{B}$, are the quantities usually sought after. The arrow on top, $\vec{\ }$, indicates that these are vector quantities, meaning we speak of vector fields. ρ is the total electric charge density and $\vec{J}$ is the total electric current density flowing in a specific direction. Therefore, the electric current is represented as a vector as well. ϵ_0 and μ_0 are universal constants for the free space permittivity and permeability, respectively. Together, they describe the wavelength of light in a vacuum as $c = \frac{1}{\sqrt{\epsilon_0 \mu_0}}$. Lastly, we find mathematical operators in front of the electric- and magnetic-field vectors. ∇ indicates a three-dimensional gradient operation, with $\nabla\cdot$ as the divergence operator and $\nabla\times$ as the curl operator.

1.7.2 Mathematical Definitions

This section is intended to help the reader understand the notations used in this thesis. The following mathematical definitions are used throughout. First, the physical notation for electromagnetic waves are presented:

- λ is the wavelength of a wave
- T is the period of a wave, related to the wavelength as $T = \lambda/c$, with c being the speed of light
- f is the frequency of a wave with $f = 1/T$
- ω is the angular frequency with $\omega = 2\pi f$
- $\widetilde{\nu}$ is the wavenumber, related to previous units as $\widetilde{\nu} = f \cdot c = \frac{1}{\lambda}$
- k is the angular wavenumber, related to previous units as $k = 2\pi\widetilde{\nu} = \frac{2\pi}{\lambda}$

Second, the refractive indices and dielectric constants:

- i is the imaginary number $i = \sqrt{-1}$ to denote complex numbers
- $\widetilde{\dots}$ denotes that the parameter can be complex
- $\overline{\dots}$ denotes the complex conjugate
- $\mathfrak{Re}\{\dots\}$ denotes taking the real part of the complex number
- $\mathfrak{Im}\{\dots\}$ denotes taking the imaginary part of the complex number
- the refractive index of a material $n = \sqrt{\epsilon'\mu_\mathrm{r}}$ can be described by its relative permittivity (ϵ') and relative permeability (μ_r)
- ϵ' and ϵ'', the dielectric constants (or permittivity's real and imaginary parts) are related to the complex refractive index as $\epsilon' + i\epsilon'' = n^2$, since $\mu_r \approx 1$ for non-magnetic materials.

Then, general operations:

- $\langle\dots\rangle$ is the time average as $\langle\dots\rangle = \frac{1}{T}\int\dots dt$
- $\mathcal{F}[f(g)]$ is the Fourier transform, going from g-space to δ-space, $\mathcal{F}[f(g)](\delta) = \int_{-\infty}^{\infty} f(g)\, e^{-2\pi i\delta g} dg$
- $f \star g(\tau) = \int_{-\infty}^{\infty} \overline{f(t)} g(t+\tau)\, dt$ is the cross-correlation equivalent to $f \star g(\tau) = \int_{-\infty}^{\infty} \overline{f(t-\tau)} g(t)\, dt$

- $f * g\,(\tau) = \int_{-\infty}^{\infty} f\,(t)\,g\,(\tau - t)\,dt$ is the convolution equivalent to $f * g\,(\tau) = \int_{-\infty}^{\infty} \overline{f\,(\tau - t)} g\,(t)\,dt$

1.7.3 Dissertation Jargon

Throughout this dissertation, various words are used to describe observations or explain physical phenomena, therefore an overview of those words is given in this paragraph.

- Nanosensor, nanoparticle, plasmonic particle, and metallic nanoparticle are terms used to describe particles with a size smaller than $100\,\mathrm{nm}$ used in this work as optical sensors due to their dielectric sensitivity.
- "Full-width at half maximum" describes the width of a peaked function measured between the points where the function is half the value of the maximum.
- "Focal volume" is the volume in which excitation or driving light is focussed into, becoming the effective detection space of the optical setup.
- "Sensing volume" is the volume of concentrated electromagnetic fields created by the nanosensor, where it is most sensitive to dielectric changes.
- "Hotspot of a Nanoparticle" is a synonym of the sensing volume, where the electromagnetic fields are concentrated by the nanosensor.
- "FTS interferogram" is the modulated output intensity of an interferometer as a function of the path-length difference of the two optical paths.
- "PCFS interferogram" is the Photon-Correlation Fourier Spectroscopy obtained interferogram, representing the envelope squared of the FTS interferogram.
- "Fringes" are the oscillating bands in a FTS interferogram, typically at spectral center frequency.
- "White fringe" is the most center fringe in the FTS interferogram with the highest amplitude.
- "Coherence Length" is the distance over which the amplitude of the fringes significantly drops. This distance is also known as the full-width at half maximum of the FTS intereferogram.
- "Dither" a small periodic motion around a particular path-length difference, used in PCFS measurements.

- "Sensitivity" describes the amount of spectral shift per refractive index unit change.
- "Figure of merit" describes a unitless number that is the sensitivity over the full-width at half maximum of the spectrum of the optical sensor, describing how well optical shifts can be observed.
- k_{on}, on-rate, is the rate constant of association, related to molecular rate constant of association $k_{\mathrm{a}} = k_{\mathrm{on}} / [P]$
- k_{off}, off-rate, is the rate constant of dissociation, related to molecular rate constant of dissociation $k_{\mathrm{d}} = k_{\mathrm{off}}$
- K_{d} is the dissociation constant, related to the rate constant as $K_{\mathrm{d}} = k_{\mathrm{d}} / k_{\mathrm{a}} = [P]\, k_{\mathrm{off}} / k_{\mathrm{on}}$
- "Smoluchowski limit" is the interaction limit of molecules because of diffusion. For proteins this is typically $10^{10} \mathrm{M\,s}$

2 Nanosensors

To develop a novel optical device for kinetic interaction-sensing of biomolecules in solution, two main parts have been identified: metallic nanosensors and an optical setup. This chapter discusses the first component, namely the nanosensors. Metallic particles shrunk to the nanoscale, exhibit different properties than their bulk counterpart. For small metallic nano-sized particles, the optical response becomes sensitive to changes in their direct dielectric environment. Therefore first, some theoretical background on the physical working principle of these nanosensors is given. From the theory, it is found that material and shape besides dielectric environment of the nanosensor are important parameters for the optical response. We computationally explore, the expected output of biomolecular binding events in the proximity of spherical nanosensors. To examine different sensor geometries, another computational method, discrete dipole approximation (DDA), is employed. From the computational findings, one particular design is chosen to establish its chemical synthesis, because of it high sensitivity and great figure of merit (FOM). Thereafter, several optimizations of the synthetic protocol are discussed, before the sensitivity and FOM of our nanosensors with literature. Here, we find that our sensors have high sensitivity and excellent FOM. Subsequently, the biocompatibility and stability of the nanosensors are examined. To improve both biocompatibility and stability, we discuss strategies of nanosensor coating and surface chemistry to obtain a sensor that can be used in solution bio-sensing.

2.1 Theoretical Background of Plasmonics Nanoparticles

The downscale from bulk to the nano-size brings unique physical properties to materials. These properties include electronic, thermal, mechanical or optical properties. Plasmonic particles are a subset of nanomaterials with unique optical properties, due to the way their electron density couples with light at wavelengths much greater than their size. Plasmonic nanoparticles are typically made of metals, because of their loosely bound electrons in the outer shell of the atoms. These

electrons are essentially "free" to move around the positive metal ions. Whenever electromagnetic waves hit the particle, the free electrons start to move in the direction of the electric field. But since the electromagnetic radiation is not stationary but oscillating, the electron sea in the particle oscillate as well. This oscillation can either be damped or resonant, based on the frequency of the light and the characteristics of the plasmonic particle. Whenever both are matched to resonate, we speak of a Localized Surface Plasmon Resonance (LSPR), and this sections describes the mathematics of the physical principles. Here, Maxwell's equations are solved for plane-wave excitation to obtain the parameters that influence the LSPR. First, theoretical expressions are derived for spherical nanoparticles. Later, small shells are added to them, which allows us to predict shifts in the LSPR for binding events at the plasmonic particle's surface. Lastly, LSPRs of generically shaped particles are explored through a computational method, Discrete Dipole Approximation, to find an optimal nanosensor shape with sensitivity.

2.1.1 Quasistatic Wave Approximation

In this section, the simplest way to describe the interaction of a sub-wavelength metallic particle with electromagnetic radiation, namely the quasistatic approximation (QSA), is discussed. In this approach, solutions to Maxwell's equations are calculated by assuming that the diameter of the metallic particle is smaller than the wavelength of the electromagnetic wave, $d \ll \lambda$. When this assumption is met, the phase of the oscillating electromagnetic wave can be treated to be constant over the volume of the particle. This simplifies the calculation, since now only the spatial field distribution of a particle in a static electric field has to be calculated. Hence, its name; quasistatic approximation. The time dependence is introduced back after the spatial fields are known to find the final solution to the problem. The entire derivation can be found in Maier.[35] In this dissertation, the focus lies on explaining the steps to obtain the solution and the implications of the outcome. Even though this solution is an approximation, it has proven to describe the interaction of nanoparticles decently for diameters less than $100\,\mathrm{nm}$ in the visible spectrum.[36]

Let an isotropic, homogeneous sphere with radius a and diameter $d = 2 \cdot a$ be positioned at the origin inside a uniform static electric field $\overrightarrow{E} = E_0\hat{y}$, with parallel field lines far from the particle. The medium surrounding the sphere is non-absorbing and isotropic, and its dielectric properties are described with ϵ_m. The dielectric properties of the sphere, are captured with $\epsilon\,(\lambda)$, which means that they are dependent on the wavelength of the incoming radiation, λ. All this is illustrated in Figure 2.1.

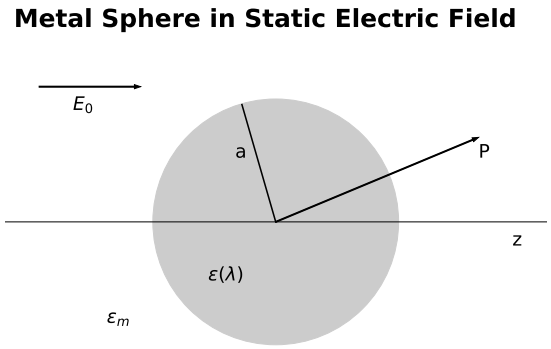

Fig. 2.1.: Illustration of an isotropic, homogeneous sphere positioned in a static electric field.

For electrostatics, the Maxwell's equation can be reduced to the Laplace equation, $\nabla^2\Phi = 0$. From this equation the potential, Φ, is obtained. Then from the potential, the electric field, $\overrightarrow{E} = -\nabla\Phi$, can be calculated. Due to the spherical symmetry of the problem, one can find solutions in the form of a series of Legendre Polynomials.[37] Assuring the solution remains finite at the origin and implementing boundary conditions at the sphere's surface and far from the sphere, the solution becomes:

$$\Phi = \begin{cases} -\frac{3\epsilon_{\mathrm{m}}}{\epsilon(\lambda)+2\epsilon_{\mathrm{m}}} E_0 r\cos\theta & \text{for} \quad r \le a \\ -E_0 r\cos\theta + \frac{\epsilon(\lambda)-\epsilon_{\mathrm{m}}}{\epsilon(\lambda)+2\epsilon_{\mathrm{m}}} E_0 a^3 \frac{\cos\theta}{r^2} & \text{for} \quad r \ge a, \end{cases} \tag{2.1}$$

where θ is the angle with y-axis, and r is the radial distance for spherical coordinates. Now, the electric field can be calculated as $\overrightarrow{E} = -\nabla\Phi$:

$$\overrightarrow{E} = \begin{cases} -\frac{3\epsilon_m}{\epsilon(\lambda)+2\epsilon_m}\overrightarrow{E_0} & \text{for} \quad r < a \\ \overrightarrow{E_0} + \frac{3\hat{n}\left(\hat{n}\cdot\overrightarrow{p}\right)-\overrightarrow{p}}{4\pi\epsilon_0\epsilon_m}\frac{1}{r^3} & \text{for} \quad r \ge a. \end{cases} \tag{2.2}$$

A key observation is that the solution for $r \ge a$ describes the superposition of the applied electric field and that of an electric dipole located at the origin of the nanoparticle with $\hat{n}$ as the unit vector in the direction of the point of interest and the dipole moment $\overrightarrow{p} = \epsilon_0\epsilon_{\mathrm{m}}\alpha\overrightarrow{E_0}$. Then, α is introduced as the polarizability $\alpha = 4\pi a^3\frac{\epsilon(\lambda)-\epsilon_{\mathrm{m}}}{\epsilon(\lambda)+2\epsilon_{\mathrm{m}}}$, which physically described the tendency of the nanoparticle to acquire a dipole moment.

Dipoles typically are described by 2 point charges very close to each other: one negative and one positive. In our nanoparticle, the applied electric field moves

the electron sea towards one side, generating an excess of negative charge at that boundary. Whereas the positive metal ions on the other side of the particle stayed behind without any electrons, generating an excess of positive charge at that boundary. In Figure 2.2, the field distribution of a Silver sphere in an electric field according to Equation 2.2 (Figure 2.2a) and that of two point charges with opposing charge, both slightly displaced from the origin (Figure 2.2b) are shown. The fields of the quasi-static approximation indeed quantitatively match with those of 2 point charges forming a dipole. Obviously, the absolute strength and the distribution of the fields are slightly different because of charge density and geometry.

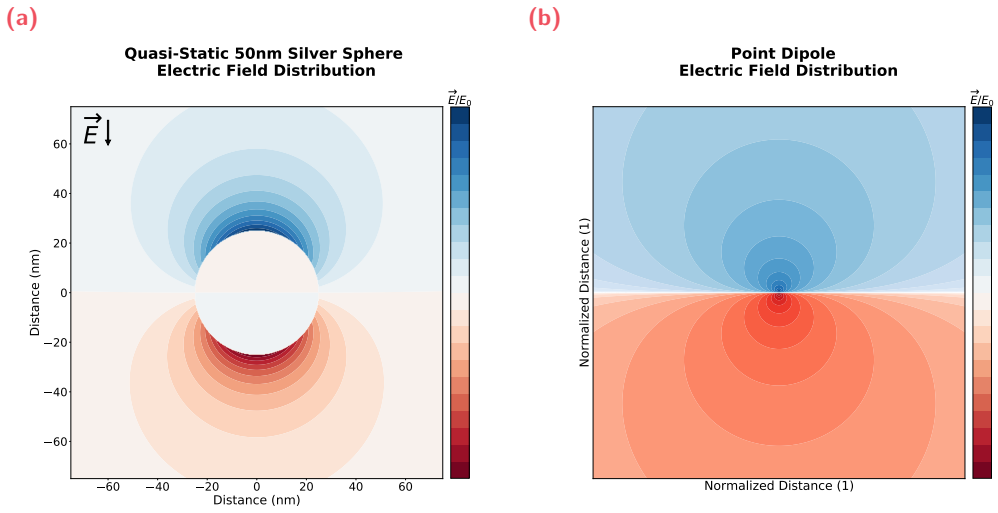

Fig. 2.2.: Quasi-Static Approximation field distributions of *(a)* a 50nm Silver nanosphere and *(b)* a dipole consisting of 2 point charges.

So far, a solution has been found for the electro-static problem. Now, a time-varying plane-wave excitation $\overrightarrow{E}\left(\overrightarrow{r},t\right)=\overrightarrow{E_0}e^{-i\omega t}$ is introduced, which induces an oscillating dipole moment $\overrightarrow{p}\left(t\right)=\epsilon_0\epsilon_{\mathrm{m}}\alpha\overrightarrow{E_0}e^{-i\omega t}$. The total fields for the near, intermediate and far-field are described in Jackson.[37] For the near-field the exact same outcome as in the electro-static case, Equation 2.2, is retrieved. The magnetic fields are found to be much smaller than the electric fields, such that the oscillation of the dipole can be considered to be electric in nature only. Both fields are shown in Equation 2.3.

$$\begin{cases}\overrightarrow{E}=\sqrt{\frac{\mu_0}{\epsilon_0\epsilon_{\mathrm{m}}}}\left(\overrightarrow{H}\times\hat{n}\right)\\ \overrightarrow{H}=\frac{ck^2}{4\pi}\left(\hat{n}\times\overrightarrow{p}\right)\frac{e^{ikr}}{r},\end{cases}\tag{2.3}$$

with k being the angular wavenumber, defined by $k = \frac{2\pi}{\lambda}$. For further derivation I will focus on the far-field only, since from those fields that will be detected by our optical setup. Therefore, we continue with calculating optical cross-sections, such as absorption, scattering and extinction. They namely give us inside into the optical spectrum of the resonance, assuming $E_0(\lambda) = E_0$. The scattering and absorption cross-sections can be calculated from the Poynting-vector, $\overrightarrow{S} = \overrightarrow{E} \times \overrightarrow{H}$, as Bohren and Huffman show:[38]

$$C_{sca} = \frac{8\pi}{3} k^4 a^6 \frac{\epsilon(\lambda) - \epsilon_{\mathrm{m}}}{\epsilon(\lambda) + 2\epsilon_{\mathrm{m}}} \tag{2.4a}$$

$$C_{abs} = 4\pi k a^3 \mathfrak{Im}\left\{\frac{\epsilon(\lambda) - \epsilon_{\mathrm{m}}}{\epsilon(\lambda) + 2\epsilon_{\mathrm{m}}}\right\}. \tag{2.4b}$$

In Equations 2.4 it can be observed that the cross-sections are wavelength dependent (through the angular wavenumber k and through the sphere's dielectric constant $\epsilon(\lambda)$). Therefore, when plotted as a function of wavelength, see Figure 2.3, spectral information of the dipolar resonance can be obtained. The values for the dielectric constants are obtained from Johnson and Christy.[39] In these graphs, a maximum arises at a specific wavelength, where the frequency of the electromagnetic wave is resonant with the oscillation of the sea of electrons in the particle. This effect is known as the Localized Surface Plasmon Resonance (LSPR), and from Equation 2.4, we can see that the LSPR arises when the denominator, $\epsilon(\lambda) + 2\epsilon_{\mathrm{m}}$, is at its minimum. This expression can be re-written when the imaginary part of $\epsilon(\lambda)$ is assumed to be only slowly-varying at the LSPR, such that the Fröhlich condition is obtained:

$$\mathfrak{Re}\{\epsilon(\lambda)\} = -2\epsilon_{\mathrm{m}}. \tag{2.5}$$

Of particular interest are materials that possess negative relative permittivities, and interestingly, metals are such materials. The relative permittivity, ϵ, is namely a measure for how materials respond to electric fields. Due to the sea of free electrons, metals can respond readily to electric fields and also cancel them completely. Therefore, most metals have optical permittivities with real parts below zero. Another interesting observation from the Fröhlich condition is that the LSPR is tightly dependent on the dielectric of the media surrounding the nanoparticle, more particular the surrounding media in the localized electric field regions. This is the reason why metal nanoparticles are a promising platform for optical sensing, because small

dielectric changes in the nanoparticle's vicinity result in changes in its optical output. This is the main use case of metallic nanoparticles in this dissertation.

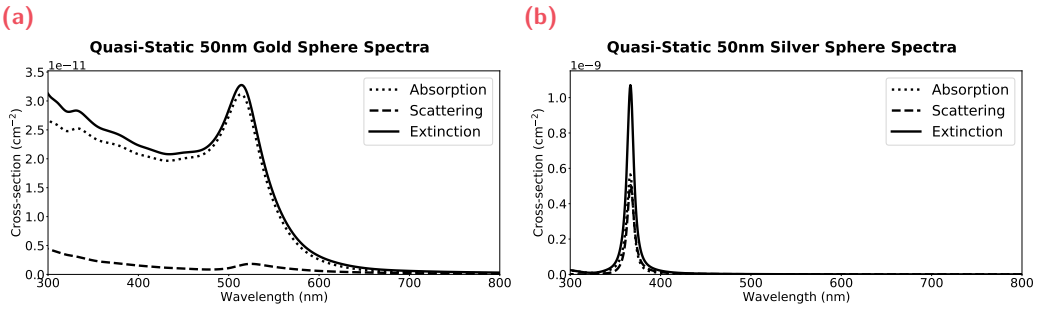

Fig. 2.3.: Quasi-Static Approximation cross-section spectra of *(a)* a $50\,\mathrm{nm}$ Gold nanosphere and *(b)* a $50\,\mathrm{nm}$ Silver nanosphere in water ($\mathrm{n} = 1.33$). Note that the cross-section for a Silver nanosphere is a factor 100 larger than for Gold.

2.1.2 Mie Theory

In the previous section, a mathematical description of a small metallic particle that gets hit by a plane-wave excitation is derived. To find a solution to Maxwell's equations, it is assumed that the diameter of the sphere is much smaller than the wavelength of the light $d \ll \lambda$, such that the phase of the field can be considered constant. For particles with larger diameters, this assumption breaks down. Additionally, with increased size the charges inside the particle are separated more, such that more time is needed move from one side to the other side. These additional physical effects need to be considered to obtain an exact solution to Maxwell's equations. In the early 1900s, Lorenz, Mie and Debye developed a theory that is an exact solution to Maxwell's equation for a sphere interacting with a plane wave excitation.[40] The full derivation is a bit cumbersome and is beyond the scope of this dissertation. If the reader is interested, numerous of good books, presentations and lecture slides that describe this derivation in its full are available.[41, 38, 40] Therefore, I will give a textual description of the steps taken to derive the solution and focus more on the physical interpretation of the results, and why Mie theory has found more use years after the theory was described.

The solution to this problem starts by combining Maxwell's equations with the elimination of the time dependence by writing $\overrightarrow{E}(x,y,z,t) = \overrightarrow{E}(x,y,z)\,e^{-i\omega t}$ and $\overrightarrow{H}(x,y,z,t) = \overrightarrow{H}(x,y,z)\,e^{-i\omega t}$ and by acknowledging that the sphere and the environment are homogeneous and uniform. We then arrive at the vector Helmholtz equations:

$$\begin{aligned}\left(\Delta + k^2\right)\overrightarrow{E} &= 0\\ \left(\Delta + k^2\right)\overrightarrow{H} &= 0,\end{aligned} \tag{2.6}$$

where $k^2 = \epsilon\mu\omega^2$, with ϵ the dielectric constant, μ the magnetic permittivity, ω the angular frequency and Δ the second-order differential Laplace operator $\Delta = \nabla \cdot \nabla$. Additionally, both the electric and magnetic field must be divergence free $\nabla \cdot \overrightarrow{E} = \nabla \cdot \overrightarrow{H} = 0$. The vector Helmholtz equations are solved for by constructing vector functions $(\overrightarrow{M}, \overrightarrow{N})$ that rely on a scalar function (ψ) and radius vector $\overrightarrow{r}$, as $\overrightarrow{M} = \nabla \times (\overrightarrow{r}\psi)$, and $\overrightarrow{N} = \frac{\nabla \times \overrightarrow{M}}{k}$. Thanks to these definitions of vector functions, one only has to solve the scalar Helmholtz equations and find a solution for ψ.

Next, the symmetry of the system is acknowledged and the solution for ψ is sought for in spherical coordinates. Specifically, $\psi(r, \theta, \phi)$ is considered a product of functions that only operate in a single spherical coordinate as $\psi(r, \theta, \phi) = R(r)\,\Theta(\theta)\,\Phi(\phi)$. This simplifies the math and individual solutions for $R(r)$, $\Theta(\theta)$, and $\Phi(\phi)$ can be found. For $R(r)$, after the introduction of a dimensionless variable $\rho = \mathrm{k}a$, spherical Bessel functions are found as solutions. For $\Theta(\theta)$, Legendre polynomials with $\cos\theta$ as argument are retrieved and for $\Phi(\phi)$, sinusoidal functions are found as solutions. Thus, the solution for the scalar Helmholtz equations takes the form:

$$\begin{aligned}\psi(r, \theta, \phi)_{\mathrm{even,m,n}} &= \cos(m\phi)\, P_{\mathrm{n}}^{\mathrm{m}}(\cos\theta)\, z_{\mathrm{n}}(\mathrm{k}r)\\ \psi(r, \theta, \phi)_{\mathrm{odd,m,n}} &= \cos(m\phi)\, P_{\mathrm{n}}^{\mathrm{m}}(\cos\theta)\, z_{\mathrm{n}}(\mathrm{k}r)\,.\end{aligned} \tag{2.7}$$

The solutions to the scalar Helmholtz equations can be plugged into the vector functions $\overrightarrow{M}$ and $\overrightarrow{N}$ to find solutions to the vector Helmholtz equations. Moreover, because of completeness, any solution of the scalar Helmholtz equations can be expanded into an infinite series and still be a solution to the Helmholtz vector equations. This expansion in spherical coordinates is called vector harmonics. Next, this is also applied to expand the incident plane wave. Even though this seems overkill, the input wave is being matched to the general solutions for electromagnetic waves interacting with a sphere in spherical coordinates that have just been obtained. This math is really lengthy, therefore, I simply provide the findings. A proper work through the entire expansion can be found in Bohren et al.[38] Eventually, the incident electric field and magnetic field are described by:

$$\begin{aligned}
\overrightarrow{E_{\mathrm{inc}}} &= E_0 e^{ikr\cos(\theta)}\tilde{e_{\mathrm{x}}} = E_0 \sum_{n=1}^{\infty} i^n \frac{2n+1}{n\left(n+1\right)} \left(\overrightarrow{M^{(1)}_{\mathrm{odd,m,n}}}\left(k, \overrightarrow{r}\right) - i\overrightarrow{N^{(1)}_{\mathrm{even,m,n}}}\left(k, \overrightarrow{r}\right) \right) \\
\overrightarrow{H_{\mathrm{inc}}} &= \frac{-k}{\omega\mu} E_0 \sum_{n=1}^{\infty} i^n \frac{2n+1}{n\left(n+1\right)} \left(\overrightarrow{M^{(1)}_{\mathrm{even,m,n}}}\left(k, \overrightarrow{r}\right) + i\overrightarrow{N^{(1)}_{\mathrm{odd,m,n}}}\left(k, \overrightarrow{r}\right) \right).
\end{aligned} \tag{2.8}$$

Here, the superscript (1) means that the radial part of $\psi\left(r,\theta,\phi\right)_{\mathrm{even/odd,m,n}}$ consists of spherical Bessel functions of the first kind. The subscript m is lost, because of the orthogonality of the vector spherical harmonics, where the coefficients of the plane-wave expansion can be calculated via an integral that vanishes over the angle ϕ, except for $m = 1$.

Next, the scattered fields of the sphere can be solved for. First, the internal fields are a series of spherical Bessel functions, due to the fact that they need to be finite at the origin. To calculate the external fields, they are matched at the boundary with the internal fields, and solutions are found in a series of Hankel functions of the first and second order. The Hankel functions have asymptotic behavior, such that the first order represents an outgoing spherical wave and the second order represents an incoming spherical wave. Since it is expected that the scattered field only consist of outgoing waves, the second order solution is simply dropped. A final expression for the scattered fields is obtained as:

$$\begin{aligned}
\overrightarrow{E_{\mathrm{s}}} &= \sum_{n=1}^{\infty} i^n \frac{E_0\left(2n+1\right)}{n\left(n+1\right)} \left(ia_{\mathrm{n}} \overrightarrow{N^{(3)}_{\mathrm{even,m,n}}}\left(k, \overrightarrow{r}\right) + b_{\mathrm{n}} \overrightarrow{M^{(3)}_{\mathrm{odd,m,n}}}\left(k, \overrightarrow{r}\right) \right) \\
\overrightarrow{H_{\mathrm{s}}} &= \frac{k}{\omega\mu} \sum_{n=1}^{\infty} i^n \frac{E_0\left(2n+1\right)}{n\left(n+1\right)} \left(a_{\mathrm{n}} \overrightarrow{M^{(3)}_{\mathrm{even,m,n}}}\left(k, \overrightarrow{r}\right) + ib_{\mathrm{n}} \overrightarrow{N^{(3)}_{\mathrm{odd,m,n}}}\left(k, \overrightarrow{r}\right) \right).
\end{aligned} \tag{2.9}$$

Here superscript (3) means that the radial part of $\psi\left(r,\theta,\phi\right)_{\mathrm{even/odd,m,n}}$ are spherical Hankel function of the first kind. All that is left to obtain a complete solution for the problem is to calculate the expansion coefficients a_{n} and b_{n}. A description of these coefficients, also known as Mie coefficients, follows from the boundary conditions at the surface of the sphere and from orthogonality, such that they become:

$$\begin{aligned}
a_{\mathrm{n}} &= \frac{m^2\left[\rho j_{\mathrm{n}}\left(\rho\right)\right]' j_{\mathrm{n}}\left(m\rho\right) - \left[m\rho j_{\mathrm{n}}\left(m\rho\right)\right]' j_{\mathrm{n}}\left(\rho\right)}{m^2\left[\rho h_{\mathrm{n}}\left(\rho\right)\right]' j_{\mathrm{n}}\left(m\rho\right) - \left[m\rho j_{\mathrm{n}}\left(m\rho\right)\right]' h_{\mathrm{n}}\left(\rho\right)} \\
b_{\mathrm{n}} &= \frac{\left[\rho j_{\mathrm{n}}\left(\rho\right)\right]' j_{\mathrm{n}}\left(m\rho\right) - \left[m\rho j_{\mathrm{n}}\left(m\rho\right)\right]' j_{\mathrm{n}}\left(\rho\right)}{\left[\rho h_{\mathrm{n}}\left(\rho\right)\right]' j_{\mathrm{n}}\left(m\rho\right) - \left[m\rho j_{\mathrm{n}}\left(m\rho\right)\right]' h_{\mathrm{n}}\left(\rho\right)}.
\end{aligned} \tag{2.10}$$

There are two more Mie coefficients, however those are used to describe the fields inside the sphere. In this dissertation, we are interested in the far-field, since those are the fields our optical setup will detect. Therefore, I only provide the Mie coefficients for the external fields. In these equations, m is the refractive index ratio between the sphere and the surrounding medium as $m = \frac{\sqrt{\epsilon}}{\sqrt{\epsilon_\mathrm{m}}}$, j_n are spherical Bessel-functions of order n, h_n are spherical Hankel-functions of order n, $\rho = ka$ is the size parameter, with a is the radius of the sphere.

When these Mie coefficients are plugged into Equation 2.10 to obtain the electric field, a similar outcome is obtained as in the Quasistatic Approximation. Namely, that the excitation field gives rise to a dipole moment inside the sphere. However, from the Mie expansion, we obtain higher order terms that affect the outcome. The easiest way to discuss these higher order terms and their physical interpretation is to look at the polarizability, α, similar to the polarizability from the dipole moment in Equation 2.2. Kuwata et al. find the polarizability from the expanding the first Transverse Magnetic (TM) mode to be: [42]

$$\alpha_\mathrm{Mie} = \frac{1 - \left(\frac{1}{10}\right)(\epsilon + \epsilon_\mathrm{m})\,\rho^2 + O\left(\rho^4\right)}{\left(\frac{1}{3} + \frac{\epsilon_\mathrm{m}}{\epsilon - \epsilon_\mathrm{m}}\right) - \frac{1}{30}(\epsilon + 10\epsilon_\mathrm{m})\,\rho^2 - i\frac{4\pi^2\epsilon_\mathrm{m}^{3/2}}{2}\frac{V}{\lambda_0^3} + O\left(\rho^4\right)} V. \tag{2.11}$$

Let us focus on terms as a function of ρ and compare them with the Quasistatic Approximation, even though the prefactors might be different. In the numerator, we find an additional second order (quadratic) term, which includes the retardation effect of the exciting field over the volume of the sphere. This is the exact process, that is neglected in the Quasistatic approximation by assuming the phase of the excitation wave constant in the Quasistatic Approximation. In the denominator, a second order (quadratic) term is found, which comes from the retardation of the depolarization field in the sphere. Physically, this effect comes from the separation of the charges on the surface of the sphere. With increasing particle size, the interaction between the charged interfaces decreases, thus lowering the resonance energy. The third term, without ρ dependence, accounts for radiation damping. This is the effect when an electron oscillation can radiatively decay into photons, increasing the scattering, but also broadening the LSPR. These higher order terms, lead to higher order resonances, and their prefactors depend on the morphology of the nanoparticle.

The beauty of Mie-theory is that it is an exact solution to Maxwell's equations of how a sphere interacts with an incoming plane wave. Unfortunately, calculating all the expansions of Equation 2.9 and all coefficients of Equation 2.10 by hand is

undoable. However, nowadays, computers can perform these calculations much faster. Therefore, this theory has gained popularity in the last half century, even though it was described in the early 1900s. For computer computation, we however need to get rid of the nasty derivative in Equation 2.10 and a upper value, $n_{\max}$, for the computation of the expansion is needed. Namely, calculating infinite sums on a computer also yields no results.

To get rid of the derivative, Aden was the first to introduce the logarithmic derivate, $D_{\mathrm{n}}(\rho) = \frac{d}{d\rho} \ln \psi_{\mathrm{n}}(\rho)$, for computing scattering coefficients.[43] Note that this ψ_{n} is different from the *Ansatz* function $\psi(r, \theta, \phi)$ we used earlier. By implementing the logarithmic derivative, the Mie-coefficients can be re-written as:

$$\begin{aligned} a_{\mathrm{n}} &= \frac{\left[D_{\mathrm{n}}(m\rho)/m + n/\rho\right]\psi_{\mathrm{n}}(\rho) - \psi_{\mathrm{n-1}}(\rho)}{\left[D_{\mathrm{n}}(m\rho)/m + n/\rho\right]\xi_{\mathrm{n}}(\rho) - \xi_{\mathrm{n-1}}(\rho)} \\ b_{\mathrm{n}} &= \frac{\left[mD_{\mathrm{n}}(m\rho) + n/\rho\right]\psi_{\mathrm{n}}(\rho) - \psi_{\mathrm{n-1}}(\rho)}{\left[mD_{\mathrm{n}}(m\rho) + n/\rho\right]\xi_{\mathrm{n}}(\rho) - \xi_{\mathrm{n-1}}(\rho)}, \end{aligned} \tag{2.12}$$

with the recurrence relations:

$$\begin{aligned} \psi'_{\mathrm{n}}(\rho) &= \psi_{\mathrm{n-1}}(\rho) - \frac{n\psi(\rho)}{\rho} \\ \xi'_{\mathrm{n}}(\rho) &= \xi_{\mathrm{n-1}}(\rho) - \frac{n\xi(\rho)}{\rho}, \end{aligned} \tag{2.13}$$

where $\psi_{\mathrm{n}}(\rho) = z j_{\mathrm{n}}(\rho)$ and $\xi_{\mathrm{n}}(\rho) = z h_{\mathrm{n}}^{(1)}(\rho)$ are the Riccati-Bessel functions, and $f_{\mathrm{n+1}}(z)$, is the recurrence formula used to obtain higher order Bessel and Hankel functions:

$$f_{\mathrm{n+1}}(z) = \frac{2n+1}{z} f_{\mathrm{n}}(z) - f_{\mathrm{n-1}}(z). \tag{2.14}$$

With these equations, Mie coefficients can almost be calculated on a computer. Only the maximum n in the expansion should be discovered, such that higher orders of n have negligible effect on the outcome. Bohren and Huffman, hypothesized that n should be on the order of ρ. They then explored a broad parameter space of n and came up with the empirical formula:

$$n_{\max} = \rho + 4\rho^{1/3} + 2. \tag{2.15}$$

Similar, as in the Quasistatic case (Equation 2.4), we are interested in the far-field implications and want to calculate extinction, scattering and absorption efficiencies. Here, we find that they can be expressed as a series of Mie-coefficients:

$$\begin{aligned} Q_{\mathrm{s}} &= \frac{2}{k^2 a^2} \sum_{n=1}^{\infty} (2n+1) \left(|a_{\mathrm{n}}|^2 + |b_{\mathrm{n}}|^2 \right) \\ Q_{\mathrm{e}} &= \frac{2}{k^2 a^2} \sum_{n=1}^{\infty} (2n+1) \, \mathfrak{Re} \left\{ a_{\mathrm{n}} + b_{\mathrm{n}} \right\} \\ Q_{\mathrm{a}} &= Q_{\mathrm{e}} - Q_{\mathrm{s}}. \end{aligned} \tag{2.16}$$

The scattering, extinction and absorption efficiencies, from Equation 2.16, are normalized ratios of the respective cross-sections to the area that a particle occupies. The efficiencies can thus be converted into cross-sections via: $\sigma_{\mathrm{i}} = Q_{\mathrm{i}} \cdot \pi a^2$, where i denotes the subscript for the respective process (absorption, scattering or extinction). The cross-section is a useful parameter to look at since it tells us something about the probability that an event will take place. Physically, it represents the effective size of a particle interacting with light to make a process occur (absorption, scattering or extinction). In Figure 2.4, the absorption, scattering, and extinction cross-sections are plotted for a Gold and Silver nanoparticle of $50\,\mathrm{nm}$ in diameter, respectively. This size is chosen, because it results with a typical LSPR peak position in the visible and absorption and scattering effects are of the same order of magnitude. The dielectric constants have been obtained from Johnson and Christy.[39] At first glance, there is not much difference compared to the cross-sections from figure 2.3, computed with the quasistatic approximation. However, upon closer inspection, we observe that the absolute values are slightly different and that the shoulder of the Gold nanoparticle, figure 2.4a, in the $300\,\mathrm{nm}$ to $450\,\mathrm{nm}$ range is shaped differently. This can be explained from the fact that Mie-theory includes higher-order effects like multipoles that are typically present with lower contributions at higher energies (blue-side) of the dipolar resonance. Specifically in Figure 2.4b, we observe a shifted dipolar resonance to a higher wavelength (lower energy), meaning that the higher-order effects are of greater importance for the cross-sections of Silver particle than for Gold.

Computation of cross-sections with Mie-theory for nanoparticles of various materials can give a first hint into a good choice of material with great optical properties. These findings would help reduce the experimental synthesis space in our search for an optical biosensor. To answer this question, we would like to know what the optical response to a sensing event is. This can be induced artificially by simulating the sensor in different media with corresponding refractive indices. Then, a feature

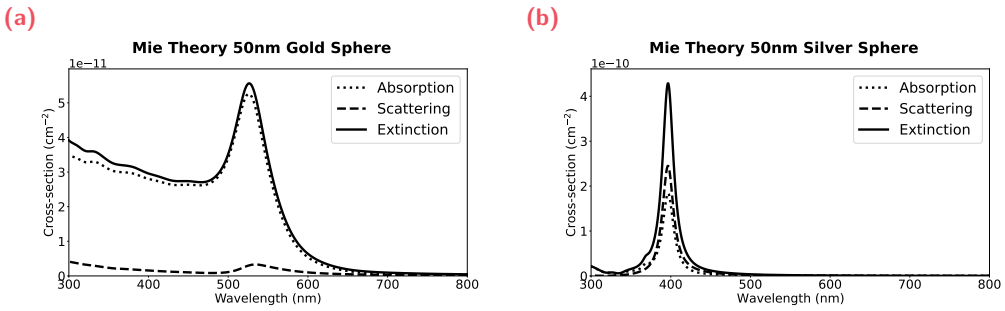

Fig. 2.4.: Mie theory cross-section spectra of *(a)* a $50\,\mathrm{nm}$ Gold nanosphere and *(b)* a $50\,\mathrm{nm}$ Silver nanosphere in water ($\mathrm{n} = 1.33$). Note that the cross-section for a Silver nanosphere is a factor 100 larger than for Gold.

in the spectrum of the sensors (typically the dipolar LSPR resonance) can be tracked as a function of that refractive-index change. The slope of this optical response to refractive index change is known as the sensitivity of the nanosenor. Figure 2.5, shows the overall process of sensitivity determination for a Gold and Silver sphere. In Figure 2.5a and Figure 2.5b, a Gold and Silver nanoparticle have been placed computationally in various media to extract the position of their dipolar resonance (red dots), respectively. These peak positions have then been plotted as a function of refractive index change, Figure 2.5c and Figure 2.5d, where the selection of the refractive index zero point is somewhat arbitrary. Computationally, we can go both directions, but experimentally you typically start in medium A and slowly add medium B to either increase or decrease the refractive index. Additionally, in Figure 2.5c and Figure 2.5d, the dipolar resonance shift induced by refractive index changes has been tracked not only in wavelength, but also in energy. We believe that the latter is a more physical way of representing sensitivity curves. Eventually, the slope of the curve if found from fitting with a linear fit. The slope intuitively indicates; the higher the sensitivity value, the more optical change one can expect for a similar sensing event. Lastly, the Figure-of-Merit (FOM) is calculated by dividing the sensitivity by the Full-Width at Half-Maximum (FWHM) of the spectrum. The FOM is a dimensionless parameter that indicates how easy it is to observe a sensing event. A high FOM indicates that the initial spectrum is **not** overlapping as much with the spectrum from the sensing event.

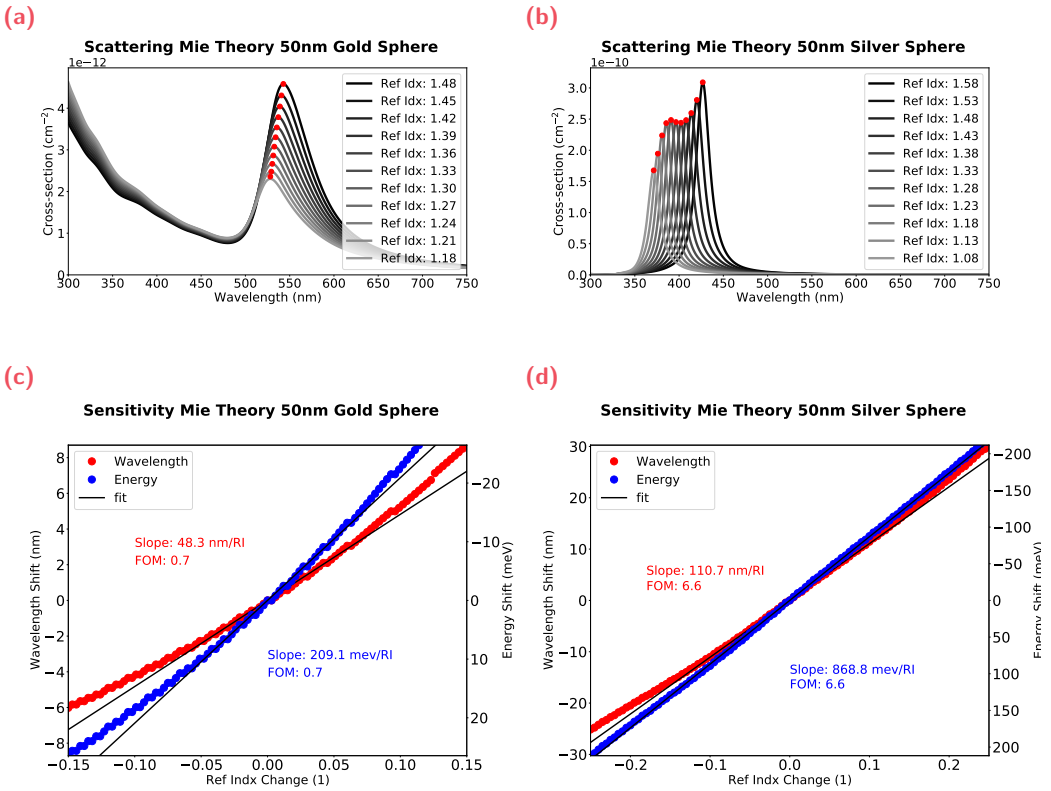

Fig. 2.5.: Mie theory cross-section spectra of *(a)* a $50\,\mathrm{nm}$ Gold nanosphere and *(b)* a $50\,\mathrm{nm}$ Silver nanosphere in various refractive index media. Sensitivity curves extracted from the peaks of *(a)* and *(b)* for the Gold nanosphere in *(c)* and the Silver nanosphere *(d)*, respectively. The slope of the sensitivity curves is known as the sensitivity and the Figure-of-Merit (FOM), is the sensitivity value divided by the FWHM. Both properties indicate how good an optical nano sensor performs.

Material	**LSPR peak position**(nm)	**Sensitivity** (nm RIU^{-1})	**Sensitivity** meV RIU^{-1}	FOM
Gold	540	48	209	0.7
Silver	400	111	880	6.7
Aluminium	250	118	2240	2.1
Copper	580	53	190	1.0
Lithium	450	234	1420	2.8

Tab. 2.1.: A summary of the sensitivity values and figure-of-merit (FOM) for 50 nm spherical nanoparticles of various materials calculated with Mie theory.

In Figure 2.5c and 2.5d, we observe that a 50 nm Gold sphere theoretically has a sensitivity of 209 meV RIU^{-1} with a FOM of 0.7. Impressively, a Silver nanoparticles has a sensitivity that theoretically is a factor 4 higher (869 meV RIU^{-1}) with an FOM, that is a factor 10 higher, of 6.6. We then also explored 50 nm spherical nanoparticles made of Aluminum, Copper, and Lithium. The findings are summarized in Table 2.1. These findings hint that Silver has greater optical properties, and thus should be explored experimentally as material for a nanosensor.

2.1.3 Core-Shell Mie Theory

In this section, an extension to Mie theory is discussed, based on the work of Aden and Kerker.[43] Finding exact solutions to Maxwell's equations for spheres hit by plane-wave excitation can be used to explore material properties to find excellent nanosensors. However, it does not give insight into expected optical output changes from biomolecular sensing events. Core-shell Mie theory describes the solution to Maxwell's equations for concentric spheres and can be used to emulate a protein ring formation on the nanosensor's surface, giving insight into the expected optical output of our nanosensor.

The mathematical solution is constructed similarly to Mie theory through vector spherical Harmonics. The description for the core and the far-field take the same functional form as before. However, the shell is found to be a series of both Bessel functions (j_n and y_n). Working through the boundary conditions at both interfaces, Aden finds solutions for the scattering coefficients similar to Mie's, see Equation 2.17. Only this time a few new parameters are introduced such as: the size parameter of the core $\rho_\mathrm{c} = ka$, the size parameter of shell $\rho_\mathrm{s} = kb$, the refractive index of the core relative to the surrounding medium m_1 and the refractive of the shell relative to the surrounding medium m_2. ψ_n and χ_n, similar to Mie, are the n-th order Riccati-Bessel functions. Core-shell Mie theory only affects the expression of the Mie coefficients, such that Equation 2.16 can still be used to obtain scattering, extinction and absorption cross-sections.

$$
\begin{aligned}
a_\mathrm{n} &= \frac{\psi_\mathrm{n}(\rho_\mathrm{s})\left[\psi_\mathrm{n}'(m_2\rho_\mathrm{s}) - A_\mathrm{n}\chi_\mathrm{n}'(m_2\rho_\mathrm{s})\right] - m_2\psi_\mathrm{n}'(\rho_\mathrm{s})\left[\psi_\mathrm{n}(m_2\rho_\mathrm{s}) - A_\mathrm{n}\chi_\mathrm{n}(m_2\rho_\mathrm{s})\right]}{\xi_\mathrm{n}(\rho_\mathrm{s})\left[\psi_\mathrm{n}'(m_2\rho_\mathrm{s}) - A_\mathrm{n}\chi_\mathrm{n}'(m_2\rho_\mathrm{s})\right] - m_2\xi_\mathrm{n}'(\rho_\mathrm{s})\left[\psi_\mathrm{n}(m_2\rho_\mathrm{s}) - A_\mathrm{n}\chi_\mathrm{n}(m_2\rho_\mathrm{s})\right]} \\
b_\mathrm{n} &= \frac{m_2\psi_\mathrm{n}(\rho_\mathrm{s})\left[\psi_\mathrm{n}'(m_2\rho_\mathrm{s}) - B_\mathrm{n}\chi_\mathrm{n}'(m_2\rho_\mathrm{s})\right] - \psi_\mathrm{n}'(\rho_\mathrm{s})\left[\psi_\mathrm{n}(m_2\rho_\mathrm{s}) - B_\mathrm{n}\chi_\mathrm{n}(m_2\rho_\mathrm{s})\right]}{m_2\xi_\mathrm{n}(\rho_\mathrm{s})\left[\psi_\mathrm{n}'(m_2\rho_\mathrm{s}) - B_\mathrm{n}\chi_\mathrm{n}'(m_2\rho_\mathrm{s})\right] - \xi_\mathrm{n}'(\rho_\mathrm{s})\left[\psi_\mathrm{n}(m_2\rho_\mathrm{s}) - B_\mathrm{n}\chi_\mathrm{n}(m_2\rho_\mathrm{s})\right]} \\
A_\mathrm{n} &= \frac{m_2\psi_\mathrm{n}(m_2\rho_\mathrm{c})\,\psi_\mathrm{n}'(m_1\rho_\mathrm{c}) - m_1\psi_\mathrm{n}'(m_2\rho_\mathrm{c})\,\psi_\mathrm{n}(m_1\rho_\mathrm{c})}{m_2\chi_\mathrm{n}(m_2\rho_\mathrm{c})\,\psi_\mathrm{n}'(m_1\rho_\mathrm{c}) - m_1\chi_\mathrm{n}'(m_2\rho_\mathrm{c})\,\psi_\mathrm{n}(m_1\rho_\mathrm{c})} \\
B_\mathrm{n} &= \frac{m_2\psi_\mathrm{n}(m_1\rho_\mathrm{c})\,\psi_\mathrm{n}'(m_2\rho_\mathrm{c}) - m_1\psi_\mathrm{n}(m_2\rho_\mathrm{c})\,\psi_\mathrm{n}'(m_1\rho_\mathrm{c})}{m_2\psi_\mathrm{n}(m_1\rho_\mathrm{c})\,\chi_\mathrm{n}'(m_2\rho_\mathrm{c}) - m_1\chi_\mathrm{n}(m_2\rho_\mathrm{c})\,\psi_\mathrm{n}'(m_1\rho_\mathrm{c})}.
\end{aligned}
\tag{2.17}
$$

With this added feature in our model, we explore the scattering cross-section spectra of a Silver nanoparticle with protein rings surrounding it. This computation indicates what optical changes could potentially be expected for protein binding events in the vicinity of a nanosensor. Here, we assumed that initially a protein ring would be formed around the nanosensor, consisting of protein A. Next, a second protein ring would form around this construct, consisting of protein B, due to biomolecular

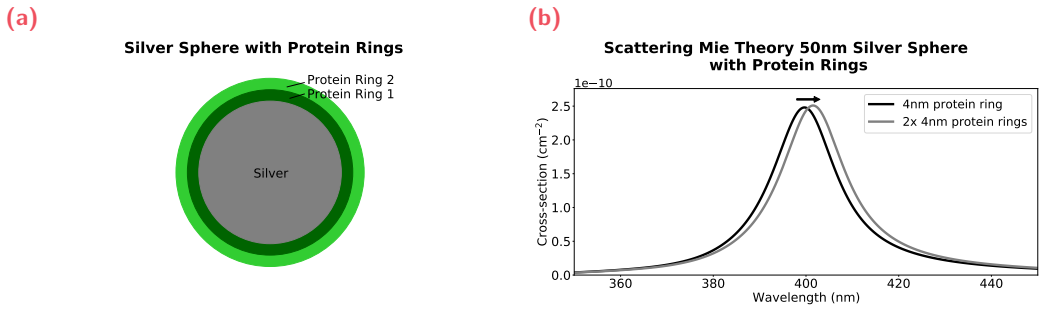

Fig. 2.6.: Mie theory scattering spectra *(b)* of *(a)* a $50\,\mathrm{nm}$ Silver nanosphere with one and two protein ($\mathrm{n} = 1.4$) rings of $4\,\mathrm{nm}$ in water ($\mathrm{n} = 1.33$).

interactions with protein A. We simulate protein ring formation that would increase the radius with $4\,\mathrm{nm}$, and assume that the protein has a density of $1.37\,\mathrm{g\,cm^{-3}}$ and a refractive index of $n_{prot} = 1.4$.[44] A $4\,\mathrm{nm}$ protein size translates to a molecular weight of $30\,\mathrm{kDa}$, which is a reasonable assumption, since most proteins fall in a range of $35\,\mathrm{kDa}$ to $52\,\mathrm{kDa}$.[45] Silver is chosen as material for the nanosensor after the exploration of materials in Section 2.1.2, where it was found that Silver has the highest sensitivity and FOM in the visible for identically shaped and sized nanosensors. The nanosensor and protein rings are simulated in water ($n = 1.33$), which is a valid approximation for most biological buffers, because the refractive index of the buffers differs less than 1% from pure water.[46].

In Figure 2.6, an illustration of the computational model (Figure 2.7b) and the scattering cross-sections (Figure 2.6b) are shown. Here, we only consider the scattering of the nanosensor, since that is the optical output we expect to observe in our experiments later. In this simulation, we find a Silver nanosensor with an initial protein ring (protein A) has maximum of the dipolar LSPR at $399.7\,\mathrm{nm}$ ($3.103\,\mathrm{eV}$). After binding of a second protein ring (protein B), the maximum is observed at $401.6\,\mathrm{nm}$ ($3.089\,\mathrm{eV}$). Biomolecular interaction of proteins of the same size detected by spherical Silver nanosensors is thus expected to result in a $1.9\,\mathrm{nm}$ ($14\,\mathrm{meV}$) with on a FWHM of $17.2\,\mathrm{nm}$ ($134\,\mathrm{meV}$), which is roughly 10% of the nanosensor's linewidth.

Next, we simulated the expected LSPR shifts from biomolecular interactions for various molecular weights of Protein A and Protein B, see Figure 2.7. To convert protein size to molecular weight, spherical proteins are assumed with a density of $1.37\,\mathrm{g\,cm^{-3}}$, following Erickson relationship between size and molecular weight.[44] We used the same computational model as in Figure 2.7b and first plot the LSPR shift for the case where both protein rings are increased the same amount, see Figure

2.7a. We observe that when protein rings have equal sizes, a maximum LSPR shift of approximately $2\,\mathrm{nm}$ occurs around $200\,\mathrm{kDa}$. Next, we simulated non-equal sizes of protein rings, as shown in Figure 2.7b. From this simulation, we find that the shifts increase with increasing molecular weight. Additionally, we observe that when Protein A is small, larger shifts are observed.

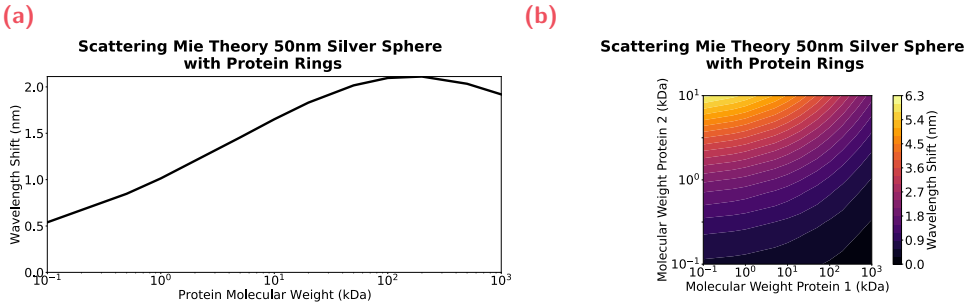

Fig. 2.7.: Localized Surface Plasmon-Resonance maximum differences calculated with Mie theory scattering spectra for a 50nm Silver nanosphere with one and two protein ($\mathrm{n} = 1.4$) rings in water ($\mathrm{n} = 1.33$) with varying protein weight.

In Figure 2.2, we have seen that these fields are mostly concentrated at the nanoparticle's surface and drop inversely proportional with the distance to the surface. Thus, we rationalize that the sensing volume has to be filled with biomolecules to observe a shift. Larger proteins would fill the sensing volume more and cause greater shifts. However, at a given molecular weight the first ring of proteins already occupies the sensing volume, causing the addition of a second ring to have only little effect. Therefore, we find that optimally, the first protein layer should consist of small proteins and the second one of large proteins. It should be noted, though, that all of this reasoning is assuming the same dielectric values for both Protein A and Protein B and that they behave as rigid molecules, which is a reasonable assumption, but is not necessarily always correct.

2.1.4 Discrete Dipole Approximation

This section discusses a computational method that can be used to compute scattering cross-sections of arbitrarily shaped particles. With this method, we explore what nanosensor shape would give the highest optical change when biomolecules interact in its vicinity. So far we have used Mie theory, an analytical solution to Maxwell's equations, to find that Silver has the greatest optical properties. Additionally, we found expected LSPR shifts of $10\,\%$ through core-shell Mie theory with biomolecules of $30\,\mathrm{kDa}$. However, these analytical solutions are limited to spherical particles

only. Efforts to describe ellipsoidal particles have been made for the Quasi-Static Approximation[38] and later with approximations to Mie theory[47, 48].

Unfortunately, analytical solutions for arbitrarily shapes are not possible, hence approximations are needed. The inspiration for the model, discussed in this section, comes from Lorentz's proof, that dielectric properties are related to the polarizabilities of the atoms composing the material.[49] The main idea of the model is, to describe the combined effect of every dipole moment of every atom constituting to the nanoparticle. Thus, the sum of the dipole moments including the interactions between them due to excitation of incoming light is computed. Therefore, this model is known as the Discrete Dipole Approximation (DDA), and sometimes it is named the Coupled Dipole Approximation.

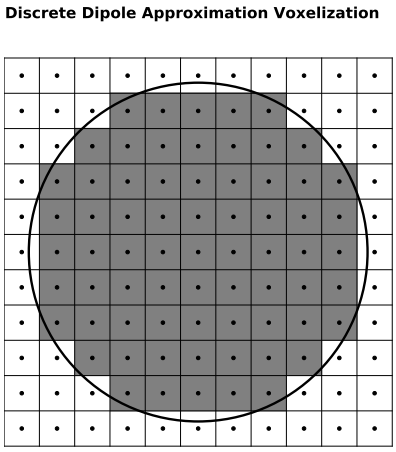

Fig. 2.8.: 2D representation of voxelization of an spherical nanoparticle in DDA computation.

To compute the interactions between arbitrarily placed dipoles is rather difficult, but when the dipoles are placed in a cubical lattice there is an exact relationship, known as the Clausius-Mossotti relation, resulting in a set of linear equations that can be solved. The approximation we thus make, is to describe the nanosenor's shape by dividing it into small cubical subvolumes (dipoles), which actually consist of a few atoms combined, but is rather described by just one dipole moment. This is illustrated in two dimensions in Figure 2.8 with a spherical nanoparticle that is voxelized cubically. Describing a small subvolume as a single dipole is analytically not correct, hence this method is an approximation. However, from Equation 2.2 we have already seen that the solution to Maxwell's equations of a sphere interacting with a plane-wave, mathematically resulted in one single dipole moment at its center. Therefore, we already observed that a sum of atomic dipole moments got combined

into one single dipole moment. In this section, we aim to utilize the DDA to examine variously shaped nanosensors to compute their sensitivities and FOMs. This way we can computationally examine the parameter space of possible shapes to select the most optimal nanosensor, to later synthesize it experimentally. For the computations presented in this work, we used the ADDA package by Yurkin and Hoekstra.[50]

Discrete Dipole Approximation Formalism

This paragraph describes the mathematical formalism on which DDA operates. The most simple implementation is presented here to illustrate what the computational model is doing. However, the ADDA package offers a lot of different options, such as computation of arbitrarily shaped particles close to surfaces or faster computation and many other optimizations. The working principle of those options is still roughly the same, they are however optimized for special use cases. The key task of any DDA package is to determine the unknown dipole polarizations $\overrightarrow{P}_\mathrm{i}$ from the linear system:

$$\overline{\alpha}_\mathrm{i}^{-1}\overrightarrow{P}_\mathrm{i} - \sum_{j\neq i}\overline{G}_\mathrm{ij}\overrightarrow{P}_\mathrm{j} = \overrightarrow{E}_\mathrm{i}^{inc}, \tag{2.18}$$

with $\overrightarrow{E}_\mathrm{i}^{inc}$ the incident field, $\overline{\alpha}_\mathrm{i}$ the polarizability of dipole i, and $\bar{G}_\mathrm{ij}$ the Green's tensor of interaction terms that enumerates over the indices of different voxels i and j. Note that the bar operator in this section indicates tensors and not complex conjugates. The polarizability is determined by the volume of the voxel, V_d, the voxel's dielectric ϵ_i, and the identity tensor $\bar{I}$ as:

$$\overline{\alpha}_i = \bar{I}V_\mathrm{d}\frac{3}{4\pi}\frac{\epsilon_\mathrm{i}-1}{\epsilon_\mathrm{i}+2}. \tag{2.19}$$

The Green's tensor, $\overline{G}_\mathrm{ij}$, captures the interaction between point dipoles with the distance between them determined by $R = |\overrightarrow{r_\mathrm{j}} - \overrightarrow{r_\mathrm{i}}|$, such that a dyadic product tensor can be defined as $\hat{R}\hat{R}$ of the normalized distance vectors:

$$\bar{G_{ij}} = \bar{G}\left(\overrightarrow{r_\mathrm{i}}, \overrightarrow{r_\mathrm{j}}\right) = \frac{e^{ikR}}{R}\left[k^2\left(\bar{I} - \frac{\hat{R}\hat{R}}{R}\right) - \frac{1-ikR}{R^2}\left(\bar{I} - 3\frac{\hat{R}\hat{R}}{R^2}\right)\right]. \tag{2.20}$$

During a calculation ADDA solves the linear system for the polarizations, $\overrightarrow{P}_\mathrm{i}$, using the Green's tensor, $\overline{G}_\mathrm{ij}$, of a previous solution. Note, that the initial Green's tensor is interactionless. After solving the linear system, a convergence value is computed and the process is repeated iteratively with an updated Green's tensor. The convergence value is tracked for every update of the linear equations, and once a convergence

criterion is met (i.e. the polarizations vary less than $1\,\%$ from the previous computation step), the computation is stopped. All scattering, extinction and absorption quantities can directly be computed from those polarizations. In Appendix A.2, a convergence study is performed to find the optimal number of dipoles per nanometer to ensure that the outcome is correct.

Identifying an Optimal Nanosensor Shape

In this section, an evolutionary algorithm is implemented to find an optimal nanosensor shape. The algorithm is inspired by biological evolution and uses reproduction, mutation, and selection to find solutions to an optimization problem. The algorithm works by mutating individual solutions, then calculating their fitness, and lastly killing solutions that have low fitness and duplicating high-fitness solutions. The fitness is defined by the user and can vary in definition. Algorithms like these perform well for optimization problems, because they do not make assumptions about the fitness landscape. However, noteworthy is that the final solution heavily depends on the definition of fitness. Additionally, the obtained solution does **not** have to be a global solution.

In Listing 2.1, psuedocode describing an evolution algorithm is shown. The full code is lengthy and distracting, but can found on Gitlab. First, 3D arrays for individual nanoparticles shape are constructed. The cluster of nanoparticle shapes is called the cohort, and the first generation all start with the same shape. For every generation, a loop going through the individual nanoparticles shapes is implemented. In this loop, a random number of voxels is mutated, meaning we adjust its shape by a set number of voxels. First, some voxels are removed from the shape to thereafter add them elsewhere in or on the nanoparticle. This is all done under conservation of volume. Additionally, it is important that there are no floating voxels, thus we ensure that voxels are adjacent to each other. Next, a DDA calculation can be performed on that mutated shape, where after its fitness is calculated. In our algorithm, the fitness is equal to the sensitivity of the nanoparticle. The same is done for all the individuals in the cohort, where after the cohort is sorted on their fitness. Not just the least fit nanoparticles (shape less conform to our selection criterion) are removed from the cohort, rather the cohort is filtered with and error-function probability distribution to give "unfit" candidates a chance for survival. This generally leads to mutations that can move past local maxima in the fitness landscape, allowing to find better optimal solutions. Lastly, the cohort is replenished by duplicating random survivors, filling the cohort back up to the initial number of nanoparticles per cohort. All of these steps described above are for one single generation. Next the simulation runs

for several generations, until a maximum generation number or until another break criterion is met. In our case, a break criterion could be that the sensitivity is higher than x value.

Evolution Simulator for Nanosensor Shape

```
generate 3D array of nanoparticle spherical shape
generate cohort of cohort_size*nanoparticles

gen_loop = true
while gen_loop:
  for contestant in cohort:
    mutate random voxels from nanoparticle (keep volume the same)

     perform DDA on contestant

    extract fitness #compute sensitivity

  sort cohort on fitness

  for contestant in cohort:
    remove contestant through error-function filtering

  replicate survivors to fill cohort back-up

  generation += 1
  if generation is large enough or selection criterium is met:
    gen_loop = false
```

Listing 2.1: Psuedocode of an evolution simulator for DDA computation to optimize nanosensor shape.

In the pseudocode in Listing 2.1 I have highlighted one particular line that makes this algorithm unfortunately extremely computational costly, namely the DDA computation for every individual nanoparticle shape. Additionally, to compute sensitivities just one DDA computation does not suffice, but rather several are needed at different wavelengths and refractive indices. I realized that the identification of an optimal nanosensor shape would be great to know, but it computationally would be impossible. Additionally, knowing the perfect nanosensor shape does not guide us on how

to synthesize it. Therefore, we decided to scan the literature for existing synthetic protocols of various nanoparticle shapes and reduce the shape parameter space by identifying a candidate among those. Nevertheless, I want to show, that when the computational costly operation is exchanged for something cheaper, this algorithm can give optimized outputs. In Figure 2.9, we start with a generation of spherical nanoparticle shapes and compute the fitness of the nanoparticle by deciding how cube-like it looks. The fitness function then takes the following shape:

```
1 import numpy as np
2
3 fitness = np.sum(nanoparticle*nanoparticle_goal)
```

Listing 2.2: Fitness function for nanosensor shape evolution simulator to become cube.

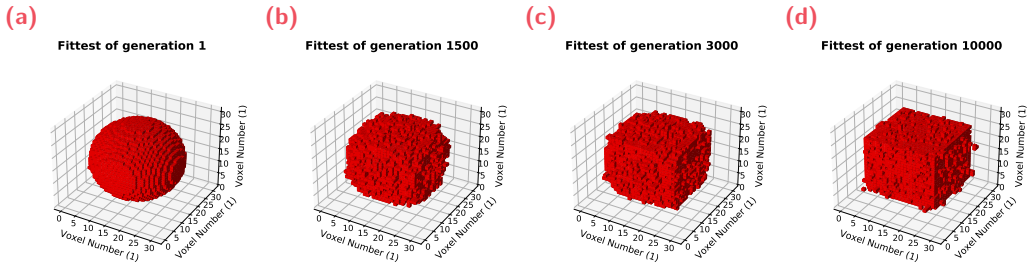

Fig. 2.9.: Evolution simulator of nanoparticle shape starting with a spherical sphere in generation 1 *(a)*, having an intermediate shape in generation 1500 *(b)*, and lastly converging to a cubic shape in generation 3000 *(c)*, and we do not see major improvements in generation 10000 *(d)*.

Identifying an Optimal Nanosensor from existing Synthetic Protocols

Here, DDA simulations are compared for particle shapes with existing synthetic protocols in the literature. By using existing synthetic protocols, we already have a starting position experimentally to produce the desired shape, and the shape parameter space is reduced for the costly DDA computation. A DDA comparison is still desired, because it allows us to compare the same sized particles with the same conditions in an ideal system. Not all the particle shapes in the synthetic protocols have been explored computationally. In the cases they are, they have been reported with different sizes, different dielectric constants for both medium and particle, and with completely different computational models, making direct comparisons difficult. Experimentally, difference in measurements, sample inhomogeneity, and size make direct comparison difficult too.

Therefore, we have simulated four differently shaped nanosensors in Figure 2.10: spherical, cubical, rod-like and decahedral. Note that many more shapes of metallic nanoparticle exist with syntheses in the literature, however we pre-filtered the synthetic protocols on three criteria: being a one-pot synthesis, being incomplex, and obtaining particles with a LSPR peak maximum in the visible. The shapes are simulated with $6.25\,\mathrm{dipoles\,nm^{-1}}$ and all sharp corners are slightly rounded to mitigate singularity effects in the DDA computation.[51] All particles are simulated with a size of $40\,\mathrm{nm}$ along the x-axis and have been voxelized mathematically, except for the decahedral nanoparticle, which has been designed in a CAD software and exported to python for voxelization. The rod-shaped nanoparticle was simulated with an aspect ratio of 3.444 and the dimensions of the decahedron are taken as regular Johnson solid J_{16} as mentioned by Pietrobon et al.[52] All nanoparticles are simulated in water ($n = 1.33$) and the refractive index is stepwise increased with $\delta n = 0.02\,\mathrm{RIU}$ for 5 different refractive indices.

Here, we show the scattering cross-sections of a Silver decahedral nanoparticle in Figure 2.10a and sensitivity in Figure 2.10b as an example. From these curves a sensitivity of $210\,\mathrm{nm\,RIU^{-1}}$ ($1185\,\mathrm{meV\,RIU^{-1}}$) and a FOM of 12.5. The scattering cross-sections and sensitivities curves for the other particles can be found in Appendix A.4, their values however are summarized here in Table 2.2. From these data, we conclude that the Silver decahedral nanoparticle is the most promising nanosensor with an existing synthetic protocol.

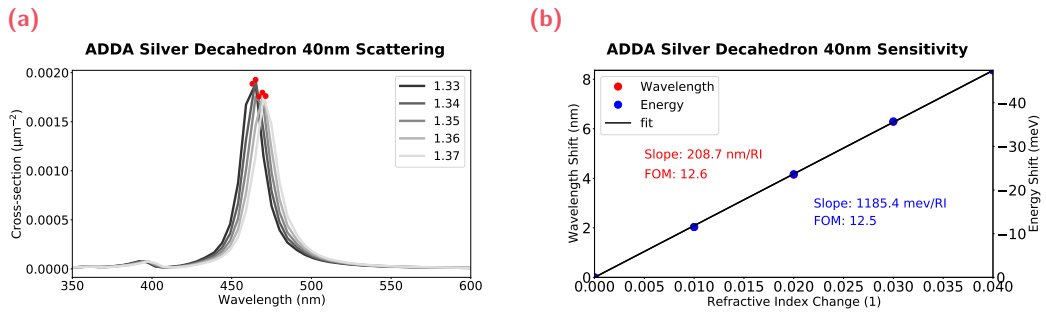

Fig. 2.10.: Discrete Dipole Approximation simulations of Silver decahedral nanoparticles to obtain *(a)* the scattering cross-section at various refractive indices and *(b)* the sensitivity curve with a slope of $210\,\mathrm{nm\,RIU^{-1}}$ ($1185\,\mathrm{meV\,RIU^{-1}}$) and a FOM of 12.5

Shape	**LSPR peak position**(nm)	**Sensitivity** (nm RIU^{-1})	**Sensitivity** meV RIU^{-1}	FOM
Sphere	395	110	880	8.2
Cube	460	190	1125	12.4
Rod	600	300	1025	8.6
Decahedron	465	210	1185	12.5

Tab. 2.2.: Table with sensitivity and Figure-of-Merit values obtained through Discrete Dipole Approximation calculations of Silver nanoparticles with various shapes. All sized $40\,\mathrm{nm}$ along the x-axis.

Biomolecular Sensing with Decahedral Nanoparticle

In this paragraph, we examine the expected LSPR peak shift from a protein detection event of a Silver decahedra nanoparticle (AgDNP). A $40\,\mathrm{nm}$ decahedron is simulated with a $4\,\mathrm{nm}$ protein sphere at its tip along the x-axis. In Figure 2.11 the LSPR peak position from scattering cross-sections as a function of protein distance between the nanosensor and the protein are shown. The voxelized computational model is shown in 2.11a. From an exponential fit, we extract a $1/e$ distance of $0.752\,\mathrm{nm}^{-1}$. Zijlstra et al. found a focal volume for a Gold nanorod of $31\,\mathrm{nm}$ by $9\,\mathrm{nm}$ to be on the same order of magnitude.[53] We expect that sharp tipped nanoparticles have a greater confinement, thus that the nanoparticle's sensing volume would be slightly smaller than in Zijlstra's case.[54]

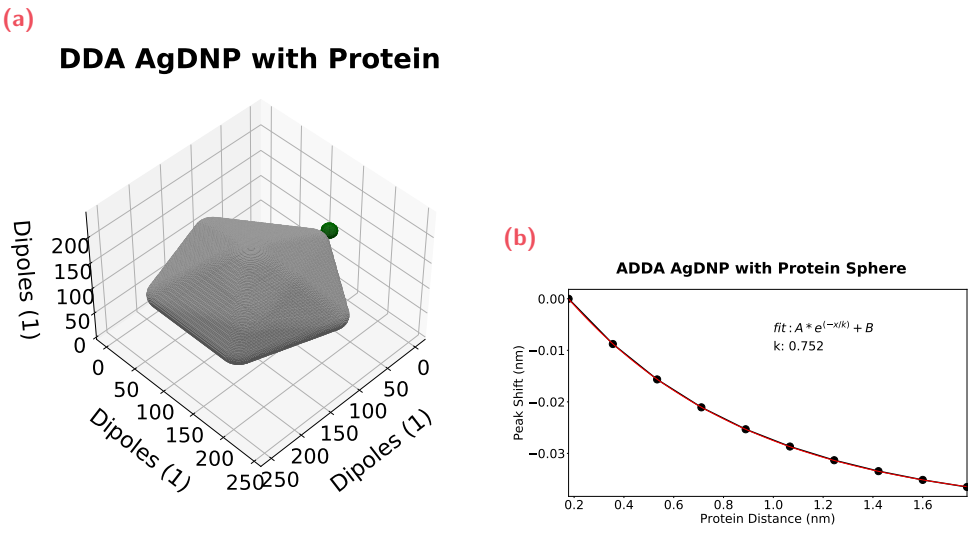

Fig. 2.11.: Discrete Dipole Approximation simulations of *(a)* Silver decahedral nanoparticle with a spherical protein at the tip along the x-axis. *(b)* the LSPR peak position is tracked as the protein is moved further from the surface.

2.2 Chemical Synthesis of Nanosensors

This section discusses the synthesis of colloidal plasmonic nanoparticles. Plasmonic nanoparticles freely diffusing through a liquid are used as optical sensors for biomolecular interactions in this dissertation. In the previous section (Section 2.1) the interaction of light with small nanoparticles, having diameters much smaller than the wavelength of light, has mathematically been derived. It was found that the free-electrons in metallic nanoparticles resonate at specific wavelengths of light, known as Localized Surface Plasmon Resonance (LSPR). The wavelength at which this occurs is dependent on the size, the material, the shape, and lastly the dielectric properties of the surrounding of the nanoparticle. The latter makes these plasmonic particles promising optical sensors, because small changes in its proximity can induce large optical shifts. Metallic nanoparticles can be prepared through various chemical methods. In fact, wet colloidal syntheses have proven to be cheap and flexible to produce differently shaped and sized nanoparticles.[55] Additionally, it is easier to modify and transport the nanoparticles for applications in colloidal systems than when produced through other chemical methods. In this part of the chapter, the chemical syntheses of plasmonic particles are explored. First the one pot syntheses for Silver spherical nanoparticles, and thereafter Silver decahedral nanosensors are synthesized. Namely, Silver decahedra nanoparticles have been found to be promising candidates for optical biosensing from Discrete Dipole Approximation (DDA) studies (Section 2.1.4). Subsequently, the reproducibility of the synthesis is discussed, and we design a new chemical (photo) reactor to remove any user dependent artifacts. Lastly, the biocompatibility and stability of our synthesized nanosensors are examined and we discuss the steps taken to improve those. Here, we discuss strategies of nanosensor coating and surface chemistry to finally obtain a nanosensor usable for in-solution sensing.

2.2.1 One-Pot Synthesis of Spherical Nanoparticles

In this paragraph, the synthesis of colloidal nanoparticles is introduced to comprehend the reactions and the roles of all reactants. The use of colloidal nanoparticles has reports dating back to the 4th century, where they were used to stain glass and medicine. The studies on colloidal nanoparticles has accelerated greatly with advanced analytical techniques in the last century. In the 50s a two reactant one-pot wet reaction was performed by Turkevich, where a Gold salt was reduced by sodium citrate at boiling temperatures.[56] This synthesis has become one of the cornerstones of current colloidal Gold syntheses, since large quantities of metallic nanoparticles could be produced with ease. This spark of interest in the community led to research on new reaction pathways with different reducing agents (i.e. borohydrides, aminoboranes, formaldehyde, hydrazine, polyols, hydrogen peroxide, etc.) and different acceptor metals.[57] Additionally, some of the additives in these reactions have been found to act as stabilizing ligands (i.e. sodium citrate, thiolates, polymers, surfactants (such as CTAB), etc.).[57] Previously in Section 2.1.4, we have mathematically explored different metals and found that Silver has the best optical properties for nanoparticles to obtain an LSPR in the visible spectrum. Thus, the reduction of Silver salt by citrate is of interest to us to form colloidal nanoparticles similar to Turkevich's method. This was first described by Lee and Meisel.[58] The mechanism of the reaction has been proposed to be:[59]

$$4Ag^{+} + C_6H_5O_7Na_3 + H_2O \rightarrow 4Ag^{0} + C_6H_5O_7H_3 + 3Na^{+} + H^{+} + O_2 \uparrow . \quad (2.21)$$

This reaction scheme is very similar to the reduction of Gold salts by citrate, but for Gold a dispute has started recently, whether citrate itself is the main reducing reaction or whether oxidized byproducts of citrate are actually at play.[60] Regardless of what the actually intermediate products or reactants are, metal ions are given an extra electron to become atomic Silver. This Silver floats in solution and forms clusters with other Silver atoms to reduce the thermodynamic free energy. Whenever the rate of reduction is controlled correctly, these nanoparticles can grow steadily and uniformly over time.

Even though widely used, Lee and Meisel's method leads to an ensemble of variously sized and shaped Silver nanoparticles. To obtain more monodisperse Silver nanoparticles, Steinigeweg introduces glycerol into the reaction, which stabilizes the particles against oxidation through its hydroxyl groups.[61] We synthesized $20\,\mathrm{nm}$ Silver spherical nanoparticles (AgSNP), according to his protocol and show the nanoparticle characterization in Figure 2.12. The synthesized nanoparticles

have a peak position similar to Mie calculations, only the width of the LSPR peak is much broader. The mismatch between theory and experiment can be explained by inhomogeneous broadening, which can never be fully circumvented. This is observed in the Transmission Electron Micrograph (TEM) in Figure 2.12b, where various sizes and shapes of nanoparticles are present. The synthesis presented here is not too dissimilar from commercially available syntheses. Higher monodisperse solutions typically are only obtained through filtering methods.

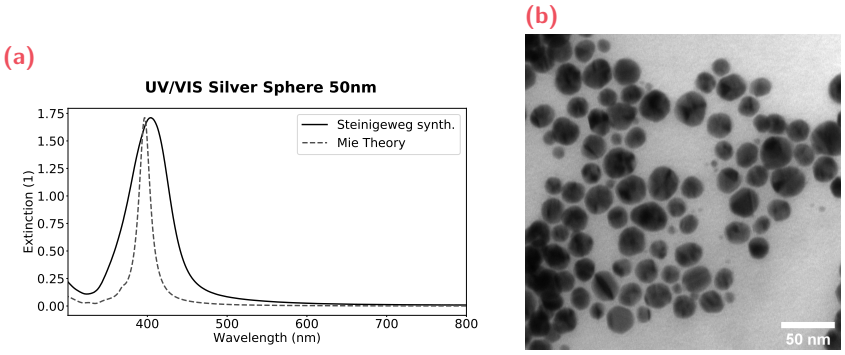

Fig. 2.12.: Synthesis characterization of spherical Silver nanoparticles with *(a)* its UV/VIS spectrum and *(b)* its Transmission Electron Micrograph.

2.2.2 Photo-Assisted Synthesis of Nanoparticles

It was just discussed that Silver ions can be reduced to Silver atoms to form small spherical nanoparticles, and that reactants can also function as stabilizers. Interestingly, some of these stabilizers have energetic preferences for particular crystal structures.[62] When small metallic atoms cluster to form nanoparticles, they typically cluster in a lattice which is preferential for their thermodynamic free energy. Whenever, crystalline nanoparticles are used with specific stabilizing ligands, a deformation of the nanoparticle's shape in one particular lattice plane would occur during growth.[63] These findings resulted in many studies to change the morphology of the metallic nanoparticles to non-spherical ones.[64]

The reduction of metal ions, as in Equation 2.21, does not occur by itself, but relies on energy that is provided into the system. Typically, the energy is provided through heat, however Stamplecoskie et al. describe a photochemical method, where the energy is provided through light absorption.[65] Later other wavelengths of light have been found to convert small spherical nanoparticles into differently shaped higher geometry nanoparticles.[66] However, Pietrobon et al. actually showed first

the conversion of spherical Silver seeds into decahedral nanoparticles, which are nanosensors of choice in this dissertation.[52]

Background on Silver decahedra nanoparticle synthesis

Murshid et al. (colleagues of Pietrobon) reported on the synthesis of Silver decahedra nanoparticles in a one-pot wet synthesis, where Silver ions are reduced by sodium borohydride.[62] Sodium citrate, L-arginine, and polyvinylpyrrolidone (PVP $40\mathrm{K}$) act as stabilizers for the initially formed small Silver nanoparticles. Additionally, L-arginine and sodium citrate also act as photochemical promoter. The activation energy for reduction of sodium citrate is lowered by (optical) activation of a plasmon resonance in the nanoparticle. Effectively, "hot holes" are formed at the surface of the nanoparticle.[67] For L-arginine, the light dependent effect is argued to come from complexing with Silver atoms and binding to sodium citrate.[62] Typically, these stabilizers adsorb to the surface of energetically preferential facets of the nanoparticle. During seeding, the formation of these facets occur randomly and various crystal structures appear. Murshid's protocol is unique in that it utilizes hydrogen peroxide as an etching agent to refine the morphology of the seeds. The various surface stabilizers "protect" certain facets, such that only the Silver atoms on the less-protected surfaces are etched away. Through the combination of etching and light exposure, Silver seeds with a five-fold crystal structure mismatch are predominantly generated, which are the precursor of decahedra nanoparticles, see Figure 2.13. This mismatch in crystal structure is also known as the twinning defect. We synthesize our decahedra nanosensors based on the protocol from Murshid, through light activation at $450\,\mathrm{nm}$.[62] However, our protocol it not exactly the same as in Murshids paper. During a call with Prof. Dr. Vladimir Kitaev, we obtained insights into the synthesis and choice of reactants. The protocol provided down below was transferred during one of those conversations.

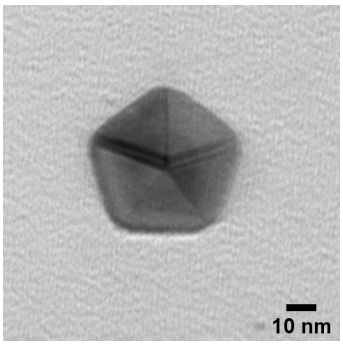

Fig. 2.13.: Transmission Electron Micrograph of a Silver decahedral nanoparticle with five-fold crystal structure mismatch, also known as twinning.

From the conversations with Prof. Dr. Vladimir Kitaev, we also learned that stir bars have inherent nucleation sides. Silver would therefore aggregate on the stir bar, coating it with a fine layer, and reducing the amount of Silver available for nanoparticles to grow. Therefore, stir bars needed to be eliminated, but the reaction mixture should still be mixed thoroughly. Prof. Dr. Vladimir Kitaev and Dr. Fangyuan Song proposed to swirl the reaction vials with a quick wrist movement. However, I found that this causes user-dependence to the synthesis, which will be addressed in Section 2.3. Therefore, I simply provide the final protocol that is used throughout this dissertation to avoid confusion with other protocols that have been explored. Then, we compare our newly synthesized nanosensors with other geometries from literature. Only afterward, I will go deeper into the design considerations of the chemical (photo) reactor, user-effects, and chemical impurities.

Silver Decahedra Synthesis protocol

For the synthesis of Silver decahedra nanoparticles (AgDNP) the following materials are used from Sigma Aldrich: sodium citrate tribasic dihydrate ($99+\%$), polyvinylpyrrolidone (PVP, $M_w = 40K$), L-arginine (TLC, 98%), Silver nitrate (99.9%), sodium borohydride (99%), hydrogen peroxide ($30-32\%$) from VWR, and ultrapure water ($> 18.2\,\mathrm{M\Omega\,cm}$). These chemicals are prepared as stock solutions according to the concentrations from table 2.3, the stocks last roughly 1 week in $4°$. A $20\,\mathrm{mL}$ scintillation vial is filled with the mentioned volumes of the chemicals (up to hydrogen peroxide!) in order of the table, and then tightly capped.

Chemicals	**Molarity** ($\mathrm{mol\,L^{-1}}$)	**Volume** (mL)	**Concentration** ($\mathrm{mg\,mL^{-1}}$)
H_2O	-	14.0	-
Sodium Citrate	0.050	0.520	14.705
PVP	0.050	0.023	2.000
L-arginine	0.005	0.025	0.871
Silver Nitrate	0.005	0.400	0.849
Sodium Borohydride	0.100	0.200	3.783
H_2O_2	10.4	0.300	$30\,\mathrm{wt\%}$

Tab. 2.3.: Table of chemicals and their amounts used in the synthesis of Silver Decahedra nanoparticles.

After the addition of sodium borohydride the solution turns pale yellow. The mixture is vortexed for 30 seconds and left in the dark for $50\,\mathrm{min}$. Then the scintillation vial is placed in a home-built photo reactor on an orbital shaker set to $300\,\mathrm{RPM}$. The mixture is left shaking for $10\,\mathrm{min}$. Hereafter, the vial is uncapped and exposed to blue light from $455\,\mathrm{nm}$ emitting LEDs, and the remaining $300\,\mu\mathrm{L}$ of hydrogen peroxide are added to the mixture. At this point, the vial can be capped again, but not tightly! Pressure is built-up in the vial and could lead to explosions. The reaction is left shaking for at least $30\,\mathrm{min}$ and left illuminated for $14.5\,\mathrm{h}$ overnight.

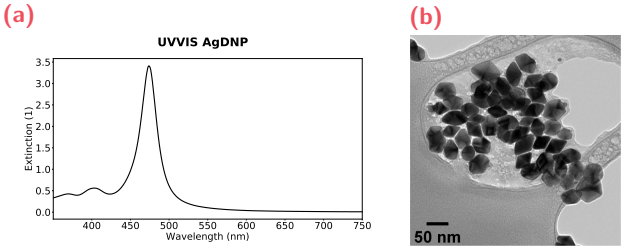

Fig. 2.14.: Characterization of Silver decahedra nanoparticle synthesis through *(a)* a UV/VIS spectrum and *(b)* a Transmission Electron Micrograph.

Silver Decahedra Optical Sensitivity

In this paragraph, the optical sensitivity of the AgDNPs from the synthetic protocol described above is compared to other nanosensors found in literature. First in Figure 2.14, a typical UV/VIS spectrum with a LSPR peak maximum between $470\,\mathrm{nm}$ and $475\,\mathrm{nm}$ (Figure 2.14a), and typical size of $40\,\mathrm{nm}$ to $50\,\mathrm{nm}$ (Figure 2.14b). These values match well with what is reported in Murshids paper and our UV/VIS spectrum also compares well to theirs (number 3), see Figure 2.15.

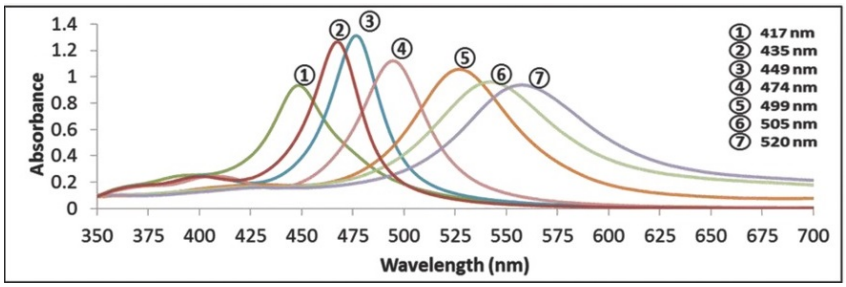

Fig. 2.15.: UV/VIS spectra of Silver decahedra nanoparticles synthesized with various LED sources, adapted from Murshid et al.[62]

To compare with other nanosensors' performances, we measured the sensitivity by addition of $40\,\mathrm{wt}\%$ glycerol/water mixtures in sequence, as seen in Figure 2.14. The refractive indices for the different glycerol/water mixtures are obtained from calibration curves.[68] Additionally, the refractive index of the starting and final glycerol/water mixture (used as UV/VIS blank) have been measured with a Kern & Sohn digital refractometer. Figure 2.16a shows the individual spectra at different refractive indices. Here, the initial solution is mostly water and small additions of the glycerol/water mixture cause the refractive index to increase. Because of these additions, the main LSPR peak decreases in intensity. Effectively, the concentration of AgDNPs is reduced with every addition.

Figure 2.16 shows the sensitivity curve by tracking the dipolar LSPR. Here, we extract a sensitivity value of $220\,\mathrm{nm\,RIU^{-1}}$ ($1220\,\mathrm{meV\,RIU^{-1}}$) with a FOM of 7.8. Then, these experiments have been repeated in triplicate and the results are summarized in Table 2.4, where gray rows are samples measured by us. Additionally, we measured the optical sensitivity of commercial $50\,\mathrm{nm}$ Silver spherical nanoparticles (NanoComposix AGCN50). From this summary, we see that Silver decahedral nanosensors have the highest FOM and excellent sensitivity that we could find in literature. From this summary, it can be observed that even though other nanosensors have high sensitivities, their FWHMs inhibit them from being a good nanosensor, thereby minimizing their FOM.

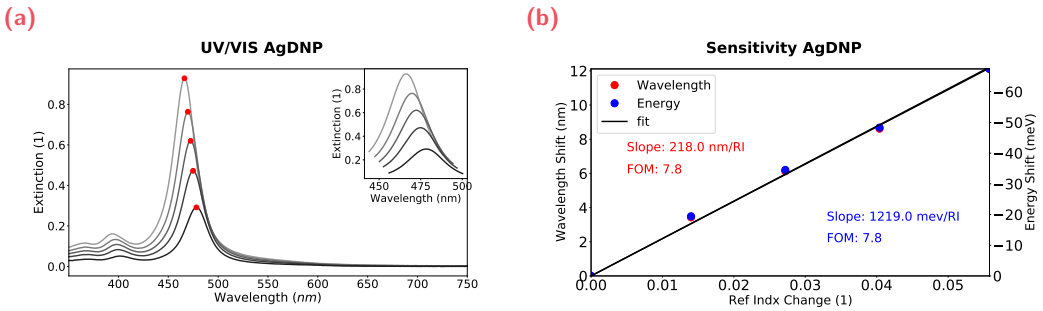

Fig. 2.16.: Sensitivity characterization of Silver decahedra nanoparticles *(a)* UV/VIS spectra *(b)* sensitivity curves.

Metal	**Shape**	**Size nm**	**LSPR Peak** nm **(**eV**)**	**Linewidth** nm **(**eV**)**	**Sensitivity** $\mathrm{nm\,RIU^{-1}}$ **(**$\mathrm{meV\,RIU^{-1}}$**)**	**FOM**	**Ref.**
Au	rod	55 x 16	728	107 (250)	224 (524)	2.1	[69]
Au	cube	77	563	98 (385)	147 (575)	1.5	[69]
Au	bipyramid	103	886	93 (147)	392 (619)	4.2	[69]
Ag	sphere	70	440	100 (650)	115 (736)	1.2	[70]
Ag	cube	84	534	280 (1220)	336 (1461)	1.2	[69]
Ag	triangular plate	84	752	200 (440)	465 (1020)	2.4	[71]
Ag	sphere	50	410	68 (682)	110 (760)	1.6	Ours
Ag	decahedra	43	475	27 (156)	187 (1078)	6.9	Ours

Tab. 2.4.: Table of differently shaped plasmonic nanosensors and comparing their refractive index sensitivities and other characteristics. Gray rows our metallic nanoparticles.

2.3 Optimization and Reproducibility

In this section, we discuss the reproducibility of the synthesis and show the user-independence after photo-reactor optimalization. Dr. Fangyuan Song, a PostDoc in our group, was concerned with establishing the synthesis of Silver decahedral nanosensors (AgDNP) for our lab. His work is based on the synthesis from the group of Vladir Kitaev.[52] At the moment Dr. Fangyuan Song left the group, he transferred the latest version of his protocol to me and to my chagrin user-dependence was one of the greatest issues. Therefore, I was unable to reproduce the optimized particles he designed. This can be observed in Figure 2.17. Three reaction flasks are shown, operated by three different users, are shown in Figure 2.17a. From the color differences, we immediately see the variability in the synthesis process from the user. Namely, these differences could not have come from the precursors, since the identical stock solutions are used. Nor could they come from the amounts that were pipetted, since the pipettes were transferred between the users without adjustment (only new tips were used). Therefore, we could only assume that the variations are due to differences in injection rate, user handling, or shaking. Figure 2.17b shows an example of a UV/VIS spectrum of a failed synthesis. Three characteristics are identified that indicate, whether a synthesis is correct. A peak around $550\,\mathrm{nm}$ hints at the formation of clusters (dimer, trimer, etc.) and the full-width at half maximum (FWHM) of the dipolar resonance is an indication of inhomogeneity, because greater inhomogeneity would lead to a broader FWHM. Lastly, a peak around $415\,\mathrm{nm}$ indicates the presence of unconverted spherical particles. Note that the full interpretation of the $415\,\mathrm{nm}$ peak is a little difficult, since higher order resonances appear at this wavelength as well. The ratio of the dipolar and the quadrupolar peak height can also be used as an indication for the synthesis.

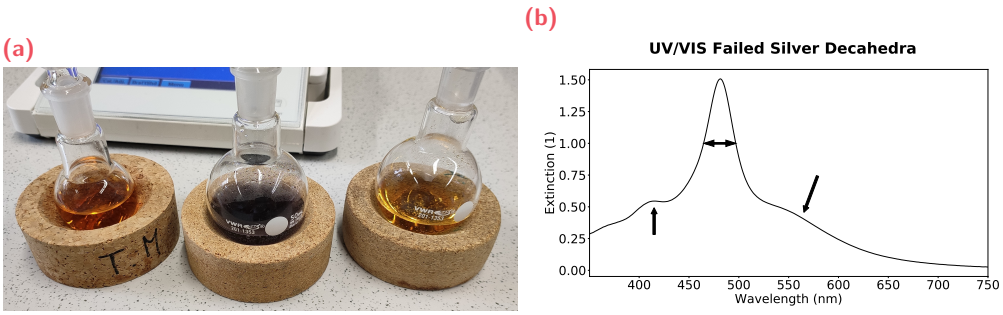

Fig. 2.17.: *(a)* Photograph of reaction mixture after addition of H_2O_2 performed by three different users (left me, middle our technical assitant, and Dr. Fangyuan Song on the right). *(b)* UV/VIS spectrum of a failed Silver decahedra synthesis.

Thus, I set my goal to overcome user dependence by engineering a new chemical (photo) reactor and automizing steps that would introduce variation. First, we talk about the considerations of the photo-reactor design and the iterations that have been made. Then, I show synthesis characterizations of our latest photo-reactor version with data from two independent users. Thereafter, I briefly discuss the effects of impurities on the synthesis.

2.3.1 Photo-Reactor Design and Considerations

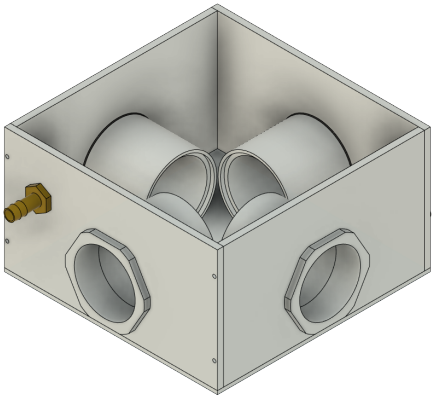

Fig. 2.18.: 3D model of the first photo reactor design to mitigate LED heating and obtain even illumination.

The first photo-reactor design, was considered to illuminate a round bottom reaction flask from 4 sides, see Figure 2.18. The 4 slots on the side were first closed with acrylic panels and later with quartz windows. This way, big cylindrical LED cooling bodies could be slit into the slots, cooling the LEDs, but still allowing the light to hit the reaction flask. Additionally, the photo reactor can be filled with flowing water, such that the temperature of the reaction mixture could be controlled. This was considered, since the LEDs produce quite some heat as an (un)wanted byproduct. At least, it was unclear whether the heat was also driving the reaction or whether it was purely photochemical. This design was made mainly to control the temperature of the reaction mixture. Note that in this photo-reactor model, the intention was to mix the solution with a stir bar. We found that the curved surfaces of the round bottom flask, due to the refraction of the light, together with the stir bar have negative effects on the reaction. Additionally, we learned that with good active

(water) cooling the heat from the LEDs was mitigated, such that there was minimal convection.

Therefore, I designed an up-right LED system that works without a stir bar, with a second reactor design in Figure 2.19a, and the third version in Figure 2.19b. An optimum distance between LEDs and the bottom of the scintillation vial has been found to be at $10\,\mathrm{mm}$. We measured the reaction solution temperature for different distances and at $10\,\mathrm{mm}$ the solution does not heat up more than $0.1\,^{\circ}\mathrm{C}$ above room temperature, while still receiving enough light intensity. The final photo reactor was designed out of Aluminum with water channels in the bottom compartment, such that the LED waste heat is transferred efficiently. There is thus water flowing in a meandering pattern through the box on which the LEDs are mounted with thermal paste. Then, small chimneys are put on top of the LEDs with a vial holder ring at $10\,\mathrm{mm}$ separation from the LED surface. The LEDs are 9-array LEDs (ILH-OW09-DEBL-SC211-WIR200 from Intelligent Light Solutions) with typical peak emission at $455\,\mathrm{nm}$. During operation, we have measured an intensity of $140\,\mathrm{mW\,cm^{-2}}$ at the bottom of the vial (at $10\,\mathrm{mm}$ distance) and $25\,\mathrm{mW\,cm^{-2}}$ at the top of the vial (cap position). This entire photo reactor can be put on a shaker, such that no stir bar or wrist flicking is needed anymore. Additionally, we use a microcontroller to automatically turn off the LEDs after $14.5\,\mathrm{h}$.

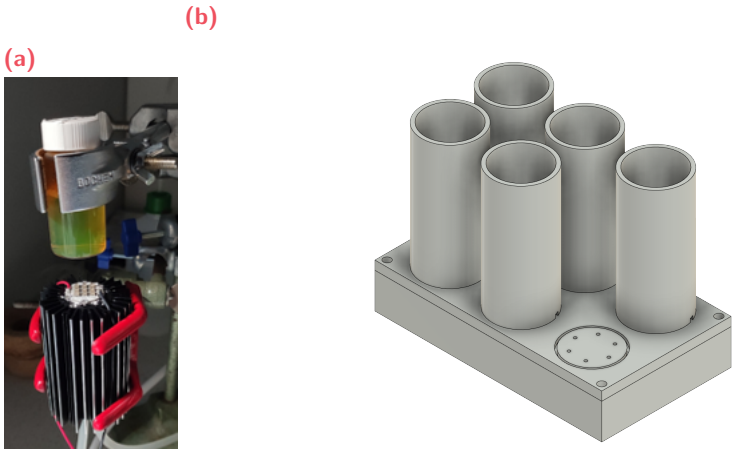

Fig. 2.19.: *(a)* Photograph of our second version of an upright photo reactor design. *(b)* 3D model of the third photo-reactor design used in this work to mitigate user dependence.

AgDNP syntheses, produced over a period of a month, have been measured for two independent users on the upright Aluminum photo reactor, see Figure 2.20. We observed only small variations between the different syntheses with a dipolar LSPR peak distribution falling within a narrow band of only $5\,\mathrm{nm}$, see insets of Figure 2.20a and Figure 2.20b. Foremost, syntheses performed by different users yield similar results. There are minor differences observable in the distribution of the LSPR maximum position, which we attribute to either changes in humidity (drop from $50\,\%$ to $<10\,\%$) or intensity loss in the LEDs due to long-term use. For later use of these nanosensors we have set a quality criterion that the dipolar LSPR peak should lie between $470\,\mathrm{nm}$ and $475\,\mathrm{nm}$. Otherwise, we would simply discard the batch.

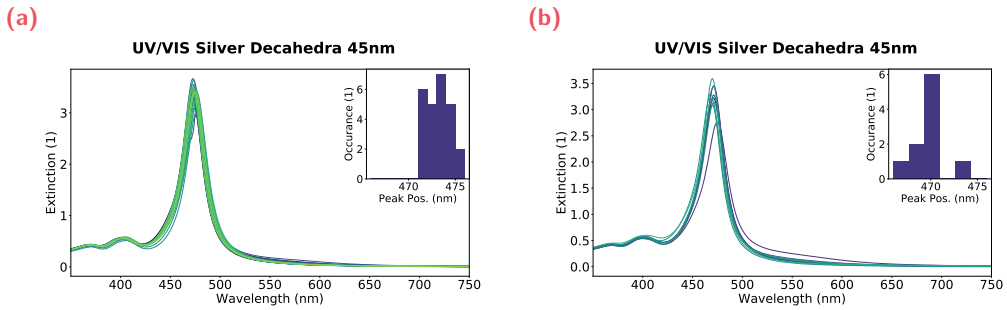

Fig. 2.20.: UVVIS spectra of several synthetic batches of Silver decahedra nanoparticles *(a)* made by me $n = 27$ *(b)* made by our technical assistent $n = 10$. The insets are peak maxima distributions, which fall within a range of $470\,\mathrm{nm}$ to $475\,\mathrm{nm}$.

2.3.2 Iron Impurity Effects on Synthesis

Most nanoparticle syntheses are sensitive to impurities in their reagents. In the call with Prof. Dr. Vladimir Kitaev, he mentioned that their lab would search through many different bottles of hydrogen peroxide until they found one suitable for the synthesis. Most probably, this comes from the fact that the hydrogen peroxide concentrations are slightly different between vendors and depend on the chemical grade. In the AgDNP synthesis, nanoparticle seeds are etched to seeds of only a few dozen atoms with the correct crystal structure. Too high hydrogen peroxide concentration would simply turn all Silver atoms back into Silver ions. Whereas too little hydrogen peroxide concentration might not etch enough, such that the incorrect crystal structures remain. Alternatively, the impurities in the hydrogen peroxide different vastly between vendors, because of the way they produce and purify their materials. We examined the effects of iron impurities on the synthesis,

because we hypothesized that iron might have ended up in our reaction flasks from iron containing reactions and poor cleaning of the glassware. Therefore, we added ferrous and ferric salt in trace concentrations into the mixture. In Figure 2.21, we see UV/VIS spectra of an AgDNP synthesis that were spiked with $1\,\mu\mathrm{L}$ of $1\,\mathrm{mM}$ Fe^{3+}-Citrate (Figure 2.21a) and with $1\,\mu\mathrm{L}$ of $1\,\mathrm{mM}$ Fe^{2+}-Chloride (Figure 2.21b). In both cases, we observe a decrease in the LSPR maximum and a slight blue-shift. This indicates that the iron does have a small effect, most likely reducing the size or the sharpness of the decahedra nanoparticle. Unfortunately, these finding did not explain the failed synthesis. Therefore, we could only hypothesize that the cleaning solution/procedure (overnight HNO_3, H_2O wash and $100\,^{\circ}\mathrm{C}$ drying) has introduced other trace material or nucleation sides. Therefore, we decided to use new glassware for every synthesis.

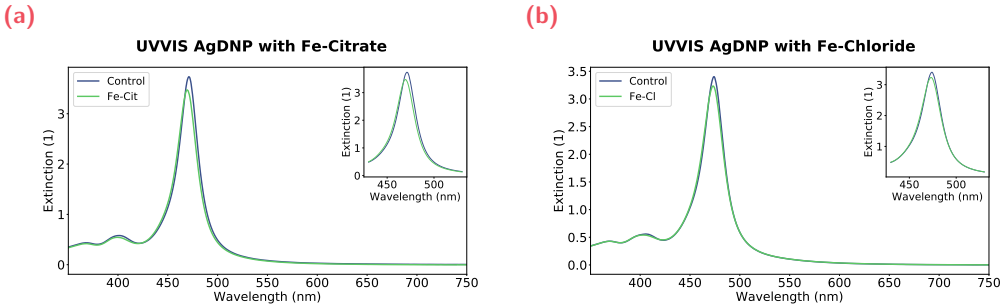

Fig. 2.21.: UV/VIS spectra of several Silver decahedra nanoparticles *(a)* spiked with $1\,\mu\mathrm{L}$ of $1\,\mathrm{mM}$ Fe^{3+}-Citrate *(b)* spiked with $1\,\mu\mathrm{L}$ of $1\,\mathrm{mM}$ Fe^{2+}-Chloride.

2.4 Biocompatibility and Stability

In the previous sections, we laid a theoretical foundation for metal nanoparticle nanosensors and explored different shapes and materials to identify a promising candidate for optical sensing; Silver decahedra nanoparticles (AgDNP). Next, we explored and optimized the chemical synthesis thereof to produce nanosensors with excellent sensitivities and a high Figure-of-Merits (FOM). In this section, our nanosensors are exposed to several commonly-used biological buffers to test their biocompatibilities. After which, methods for improving the biocompatibility are discussed and explored.

2.4.1 Silver Decahedra Nanoparticles in Biological Buffers

In this paragraph, Silver decahedra nanoparticles are exposed to typical biological buffers. These experiments are meant to check the performance and stability of our decahedra nanoparticles. The nanosensors are centrifuged at $10\,870\,\mathrm{g}$ to redisperse them in the desired buffer and after centrifugation up to $15\,\%$ of particles can stay in the supernatant.[62] Therefore, we expect a reduction of the LSPR peak at the beginning of these experiments, simply due to loss of particles in the process. In Figure 2.22, the UV/VIS spectra of AgDNP samples in H_2O, Phosphate Buffer Saline PBS, $50\,\mathrm{mM}$ HEPES saline buffer ($150\,\mathrm{mM}$ NaCl), and $50\,\mathrm{mM}$ Tris saline buffer ($150\,\mathrm{mM}$ NaCl) are shown.

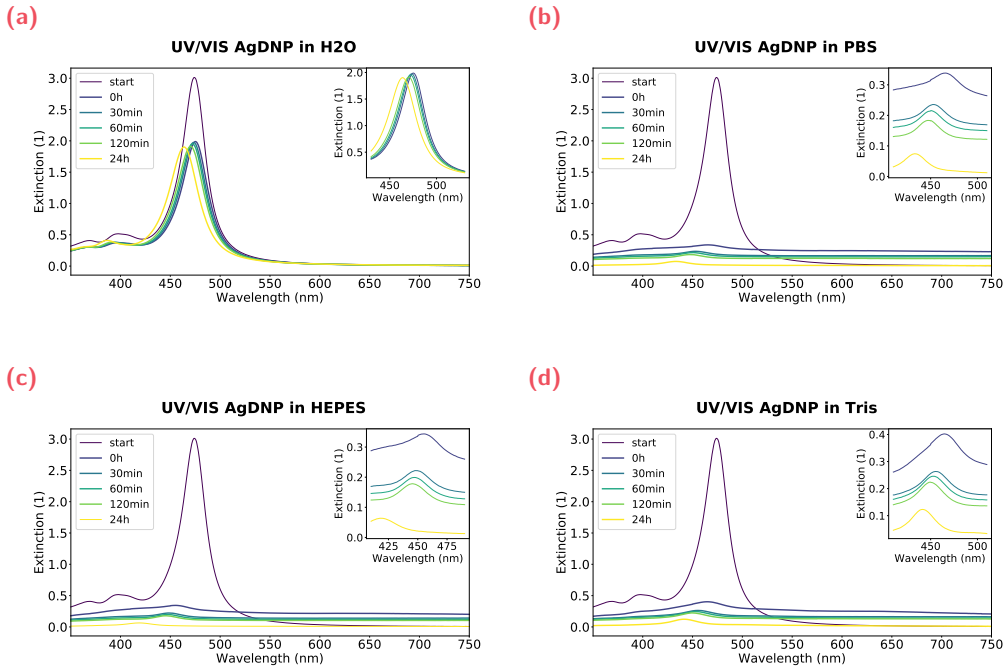

Fig. 2.22.: Time-dependent UV/VIS spectra of Silver decahedra nanoparticles in *(a)* H_2O, *(b)* PBS buffer, *(c)* HEPES buffer, *(d)* Tris buffer. The insets are zooms of the dipolar Localized Surface Plasmon Resonance peak.

In all four subfigures, we observed diminishing of the resonance peak directly at the $0\,\mathrm{h}$ measurement, as expected. In Figure 2.22a, we observe a blue-shift of the plasmon resonance peak over time. When the AgDNPs are redispersed in different media, other than their native solution, we expect that the surface ligands that are used to stabilize the particles are most probably removed from their surfaces. Therefore, allowing the mobile Silver atoms to rearrange themselves to energetically more favorable shapes, making the particles become unstable. Without any ligands

that protect specific crystal facets, the preferred shape is spherical.[72] Thus, we believe that the observed blue-shift indicates the rounding of the edges of our nanosensors, and this can be confirmed in Transmission Electron Microscopy (TEM) Figure 2.23. Unfortunately, in Figure 2.22b, Figure 2.22c, and Figure 2.22d, we observe almost a complete loss of the plasmon resonance. We hypothesize that the addition of NaCl to the solution reduces the Debye-length and therefore brings particles in closer proximity to one other, allowing them to cluster, aggregate and sediment in the cuvette. Despite these poor results, Silver decahedra nanoparticles can still be promising biosensors, because there exist ways to passivate the surface. The TEM micrographs in Figure 2.23 do confirm that AgDNP are rounded when redispersed in H_2O and that they cluster in PBS. The clustering in Figure 2.23c is so severe that one can hardly identify a decahedra nanoparticle anymore.

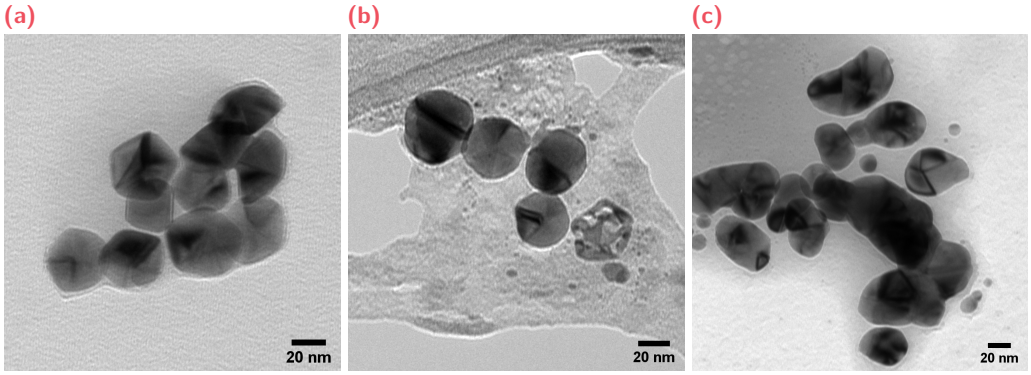

Fig. 2.23.: Transmission Electron Micrographs of Silver decahedra nanoparticles in *(a)* their stock solution, *(b)* H_2O, *(c)* PBS saline buffer.

2.4.2 Gold Coating of Silver Decahedra Nanoparticles

The Conundrum that has presented itself is that Silver has great optical properties, but Silver nanoparticles are not stable in biological buffers. A proposed solution against the degradation of Silver decahedra nanoparticles and Silver nanoparticles in general is to cap the nanoparticles with a small (few nanometers) coating, that is chemically resistant. Silica has been proposed as surface coating, but it typically creates a porous layer, leaving only a shell behind when the particles are put in biological buffers.[73] Murshid proposes a thin Gold layer, even though galvanic replacement sometimes causes dissolution of the Silver atoms, such that only a hollow Gold structure is left. They find that when a Gold solution of less than $10\,\mathrm{mol}\,\%$ is used the surface is not coated uniformly, such that the particles are not chemically resistant and when a Gold solution of more than $20\,\mathrm{mol}\,\%$ is used, the galvanic replacement dominates the reaction and creates hollow nanoparticles.[74] When the addition rate and the molarity of the Gold solution are controlled correctly, uniform layers of Gold can be coated on Silver nanoparticles.[74] In that case, the choice of using Gold as a surface capping agent brings a few benefits. Gold coating of Silver nanoparticles is namely a simple addition reaction and Gold is a plasmonically active material, which should only cause a minimal drop in sensitivity and FOM. Additionally, Gold has well established surface modification chemistry, particularly through the use of thiolates. Lastly, Gold is a rather inert and a less mobile material, which should improve the stability and biocompatibility of the decahedra nanoparticles. My colleague Dr. Jieying Zhou was concerned with establishing the Gold coating protocol of AgDNP for our lab, based on the work of Murshid et al.[74] I simply provide the latest version of the protocol that is used to coat AgDNP with $10\,\mathrm{mol}\,\%$ of Gold solution.

Gold Coating of Silver Decahedra Nanoparticles Protocol

For the synthesis of Gold coated Silver decahedra nanoparticles the following materials are used Gold(III)chloride trihydrate ($> 99.9\,\%$) from Sigma Aldrich, Silver decahedra nanoparticles according to Section 2.2.2, and ultrapure water ($> 18.2\,\mathrm{M\Omega\,cm}$). Additionally, a syringe pump is needed for the slow injection of Gold solution into a decahedra nanoparticle solution.

Prepare $HAuCl_4$ solution for $10\,\mathrm{mol\,\%}$ Gold coating

- Prepare $10\,\mathrm{mM}$ $HAuCl_4$ ($3.938\,\mathrm{mg\,mL^{-1}}$), this can be stored for a month at $4\,^\circ\mathrm{C}$
- Prepare $0.5\,\mathrm{mM}$ $HAuCl_4$ fresh from $10\,\mathrm{mM}$ stock solution
- Add $0.2\,\mathrm{mL}$ $0.5\,\mathrm{mM}$ $HAuCl_4$ to $7.592\,\mathrm{mL}$ water

Gold Coating

- Add $3\,\mathrm{mL}$ of freshly prepared AgDNP solution to scintillation vial
- Add $3\,\mathrm{mL}$ $HAuCl_4$ solution via syringe pump at a rate of $0.25\,\mathrm{mL\,h^{-1}}$ for $12\,\mathrm{h}$
- Keep the reaction mixture stirring at $200\,\mathrm{RPM}$ without light exposure

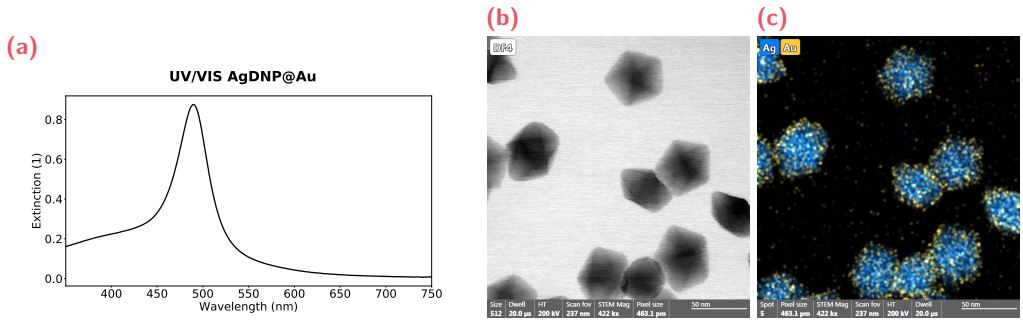

Fig. 2.24.: Characterization of Gold coated Silver decahedra through *(a)* a UV/VIS spectrum, *(b)* a Transmission Electron Micrograph, and *(c)* an Energy Dispersive X-ray image.

In Figure 2.24, a UV/VIS spectrum, Transmission Electron Micrograph (TEM) and Energy Dispersive X-ray (EDX) image of Gold coated Silver decahedra (AgDNP@Au) are shown. Here, it is observed that LSPR of the AgDNP@Au is slightly red-shifted ($490\,\mathrm{nm}$ to $500\,\mathrm{nm}$) compared to the pure Silver decahedra nanoparticle $470\,\mathrm{nm}$ to $475\,\mathrm{nm}$. Additionally, the quadrupolar LSPR around $400\,\mathrm{nm}$ is less pronounce. From the TEM, we observe that the shape is well maintained during the coating, and from EDX images the Gold layer has been found to be roughly $1\,\mathrm{nm}$. The TEM and EDX images have been measured for my colleague Dr. Jieying Zhou during her stay in Scotland at the University of St. Andrews, School of Chemistry (Euan Kay's Lab).

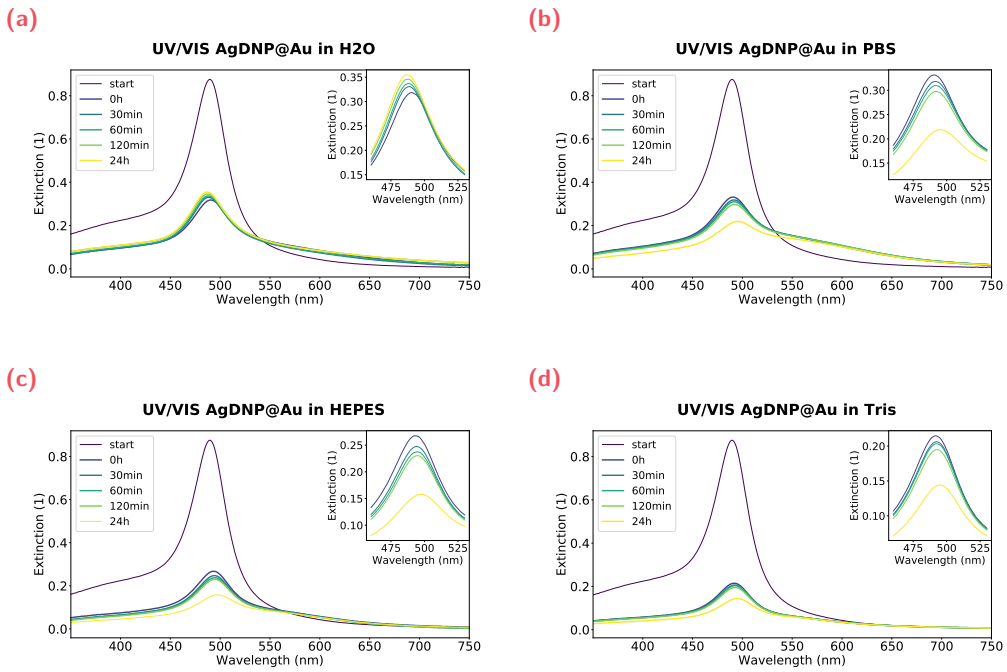

Fig. 2.25.: Time-dependent UV/VIS spectra of Gold-coated Silver decahedra nanoparticles in *(a)* H_2O, *(b)* PBS buffer, *(c)* HEPES saline buffer, *(d)* Tris saline buffer. The insets are zooms of the dipolar Localized Surface Plasmon Resonance peak.

Noteworthy about this synthesis is that the reaction mixture is stirred with a stir bar, even though we earlier found that this has negative effects on the AgDNP synthesis. Efforts to remove the stir bar for the Gold-coating protocol by putting the reaction vial on a shaker have not led to reasonable results. A key observation in these syntheses is that the stir bar gets coated with a small layer of Silver (particles). We believe that this causes batch to batch variation, because the Gold deposition per particle therefore is not the same between different batches. The rate of AgDNP adhesion to the stir bar is different from stir bar to stir bar, and even differs for the

same stir bar from day to day. Also worth of mention, is that this reaction does not seem to scale well.

When trying to coat $6\,\mathrm{mL}$ of AgDNP stock with $6\,\mathrm{mL}$ of Gold-sol at various injection rates, only minimal coating and surface passivation was observed. Therefore, we accepted the loss of AgDNP and variation in the coating thickness. To get comparable results in the end, we monitor the LSPR peak position of the AgDNP@Au and discard every batch with a LSPR peak outside the range of $490\,\mathrm{nm}$ to $500\,\mathrm{nm}$.

In Figure 2.25 AgDNP@Au are redispersed in biological buffers, namely H_2O, Phosphate Buffer Saline PBS, $50\,\mathrm{mM}$ HEPES saline buffer ($150\,\mathrm{mM}$ NaCl), and $50\,\mathrm{mM}$ Tris saline buffer ($150\,\mathrm{mM}$ NaCl). In all subfigures, an initial loss of intensity due to the loss of nanoparticles from the centrifugation and redispersion step is observed (difference between start and $0\,\mathrm{h}$). In Figure 2.25a, we observe a blue shift indicating rounding of the nanosensors. Whereas in Figure 2.25b, 2.25c, and 2.25d, we observe red-shifts and the rise of a shoulder (around $600\,\mathrm{nm}$). This red-shift and shoulder rise indicate clustering of nanoparticles due to the reduced Debye-length. From the UV/VIS we also observe loss of intensity over time. Whereas, we physically observe that the walls of the cuvette turn yellow-red colored with nanoparticles after the experiment. Nevertheless, for all biological buffers the UV/VIS spectra seem to be stable for the first $2\,\mathrm{h}$, indicating that the stability of the nanosensors has been improved due to the Gold coating. This is also confirmed in the TEM micrographs (Figure 2.26) where intact nanoparticles are found even after $24\,\mathrm{h}$. For the PBS sample, we could not observe any nanoparticles in TEM (Figure 2.26c), because of the presence of many salt crystals. Additionally, we believe that most of the AgDNP@Au stuck to the walls of the cuvette.

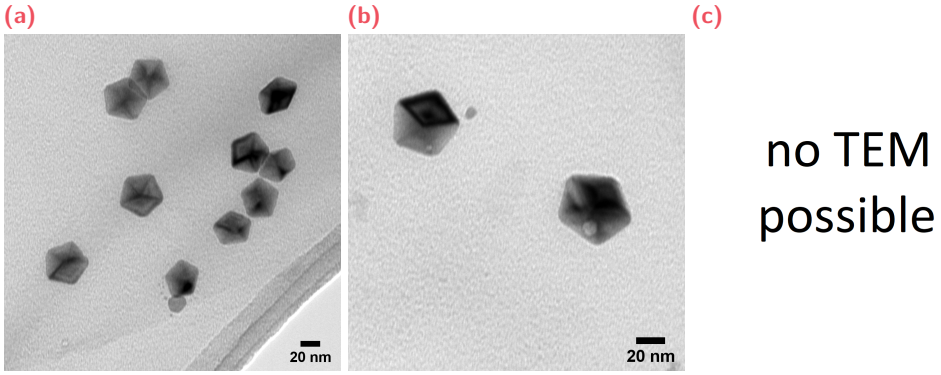

Fig. 2.26.: Transmission Electron Micrographs of Silver decahedra nanoparticles in *(a)* their stock solution, *(b)* H_2O, *(c)* PBS buffer.

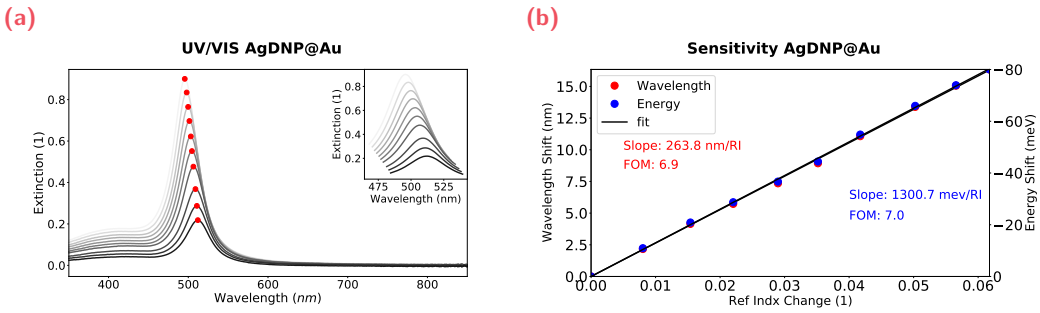

Fig. 2.27.: Sensitivity characterization of Gold coated Silver decahedra nanoparticles *(a)* UV/VIS spectra *(b)* sensitivity curves.

In this paragraph, the sensitivity of AgDNP@Au is compared with the sensitivity value of other nanosensors. Similarly to Figure 2.14, the sensitivity has been measured by addition of a $40\,\mathrm{wt}\%$ glycerol/water mixture and tracking the dipolar LSPR. Figure 2.27a shows the individual UV/VIS spectra at different refractive indices, and Figure 2.16 shows the sensitivity curve by tracking the dipolar LSPR. Here, we extract a sensitivity value of $264\,\mathrm{nm\,RIU^{-1}}$ ($1300\,\mathrm{meV\,RIU^{-1}}$) with a FOM of 7.0. These experiments have been repeated in triplicates, the averaged values are shown in Table 2.5. Gray rows indicate samples measured by us. Here, we observe that the sensitivity is slightly increased for our AgDNP@Au, however the FOM dropped marginally to 6.5. This shows that the addition of Gold only has small effects on the optical performance of the nanosensor, but improves its stability immensely. Compared to other sensitivity and FOM values from literature, our nanosensors have superior performance.

Metal	**Shape**	**Size** nm	**LSPR Peak** nm (eV)	**Linewidth** nm (eV)	**Sensitivity** $\mathrm{nm\,RIU^{-1}}$ ($\mathrm{meV\,RIU^{-1}}$)	**FOM**	**Ref.**
Au@Ag	bars	49 x 25	629	93 (291)	287 (900)	3.1	[69]
Ag@SiO2	Cube	98	450	72 (441)	123 (754)	1.7	[75]
Ag@Au	deca-hedra	45	493	40 (183)	260 (1191)	6.5	Ours

Tab. 2.5.: Table of surface-capped plasmonic nanosensors comparing their refractive index sensitivities and other characteristics. Gray rows our metallic nanoparticles.

2.4.3 Polyethylene Glycol as Surface Stabilizing Ligand

So far, we have seen that capping Silver decahedra nanoparticles (AgDNP) with a thin layer of Gold improves their stability in biological buffers. The Gold coated nanosensors have been found to maintain their shape, but adsorption to plastic and glass walls reduced the concentration over time and caused clustering. This section thus discusses a passivation method of Gold coated Silver decahedra nanoparticles (AgDNP@Au) by covalently binding surface ligands to them. The preferred surface ligand is a long molecule that can act as a steric stabilizer. Polymers are long molecules that come in various sizes, and can be fabricated with active groups at the end of the chain. Poly(ethylene glycol) is a polymer that has a long history, dating back to the 80s, for surface modification because of its water solubility and its low specificity towards interactions with biomolecules.[76] Because the Gold surface is easily modified through thiol chemistry, our choice has fallen on poly(ethylene glycol) methyl ether thiol (mPEG-SH), which covalently binds to the surface of AgDNP@Au.

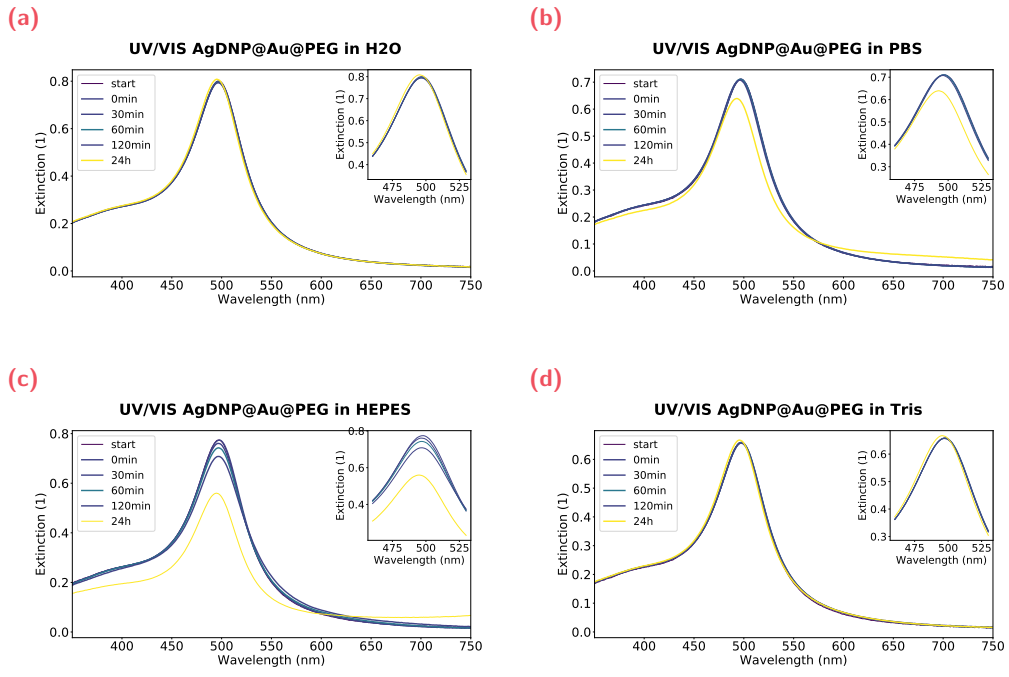

Fig. 2.28.: Time-dependent UV/VIS spectra of Gold-coated Silver decahedra nanoparticles with PEG surface modification (AgDNP@Au@PEG) in *(a)* H_2O, *(b)* PBS buffer, *(c)*50 mM HEPES saline buffer (150 mM NaCl), *(d)* 50 mMTris saline buffer (150 mM NaCl). The insets are zooms of the dipolar Localized Surface Plasmon Resonance peak.

The length and the surface coverage of the polymers determine their conformation, such that proper optimization is needed to get the desired behavior.[77] High amounts of mPEG-SH protect against clustering and deformation, however the polymer molecules then also block the sensing "hotspots", diminishing the efficacy of the nanosensor. Additionally, too high amounts of mPEG-SH can tear the thin Gold layer from the nanosenor. Thus, a fine balance has to be struck between too little and too much PEGylation.

Eventually, we settled on a ratio of $0.1\,\mathrm{nM}$ of nanosensors to $375\,\mu\mathrm{M}$ mPEG-SH ligands. The exploration for optimal mPEG-SH to nanoparticle ratio (especially combined with nitriloacetic acid (NTA), see Chapter 4) has been performed by my colleague: Dr. Jieying Zhou. The entire exploration falls out of the scope of this dissertation and thus, I simply provide the chemical protocol for PEGylation of AgDNP@Au that I adapted for only mPEG-SH, to explore the stability of our nanosensors in various biological buffers. In Figure 2.28, UV/VIS spectra of the AgDNP@Au@PEG coated with mPEG-SH with an average molecular weight of $2\,\mathrm{kDa}$ in various biological buffers is shown. As before, we used H_2O, Phosphate Buffer Saline PBS, $50\,\mathrm{mM}$ HEPES saline buffer ($150\,\mathrm{mM}$ NaCl), and $50\,\mathrm{mM}$ Tris saline buffer ($150\,\mathrm{mM}$ NaCl), and we find that the nanosensors are stable in H_2O (Figure 2.28a) and Tris saline buffer (Figure 2.28d) for up to $24\,\mathrm{h}$. In PBS, the nanosensors are found to be stable for up to $2\,\mathrm{h}$, whereas in HEPES saline buffer, an intensity loss is almost immediate. Nevertheless, in all these biological buffers the stability of AgDNP@Au@PEG is much greater compared to AgDNP and AgDNP@Au. We find in TEM images that the particles remain intact over the duration of $24\,\mathrm{h}$, see Figure 2.29. These micrographs have been taken by washing with H_2O after $24\,\mathrm{h}$ to remove salt from the solution, such that no salt crystals would hinder the imaging process. From these findings, we conclude that the PEGylated nanoparticles are the most stable in Tris buffer saline and therefore, we decided to use Tris buffer saline for further experiments.

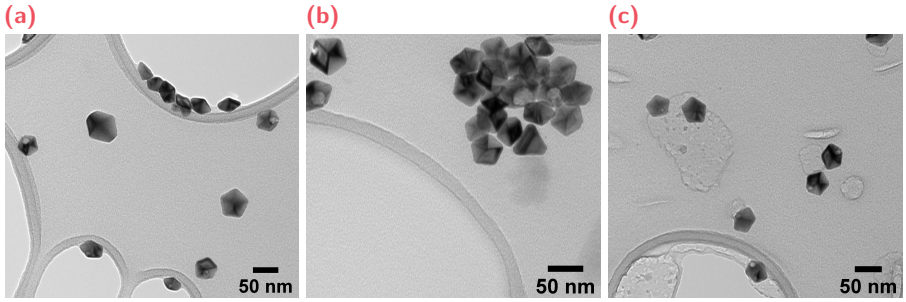

Fig. 2.29.: Transmission Electron Micrographs of poly(ethylene) glycolated Gold coated Silver decahedra nanoparticles kept in *(a)* H_2O, *(b)* Tris saline buffer, *(c)* PBS buffer for $24\,\mathrm{h}$.

PEGylation of Gold Coated Silver Decahedra Nanoparticles Protocol

For the surface ligand modification of attaching poly(ethylene glycol) methyl ether thiol (mPEG-SH) on Gold coated Silver decahedra nanoparticles the following materials are used; mPEG-SH M_w of $2\,\mathrm{kDa}$ ($>95\%$) from BioPharmaPEG, Gold coated Silver decahedra nanoparticles (AgDNP@Au) according to Section 2.4.2, Tween® 20 from Sigma Aldrich and ultrapure water ($> 18.2\,\mathrm{M\Omega\,cm}$).

Prepare Stock Solutions

- Prepare $1\,\mathrm{wt\%}$ aq. Tween® 20 solution. This can be stored at room temperature, shielded from light, but should be refreshed after several uses.
- Prepare $5\,\mathrm{mM}$ mPEG-SH solution in ultrapure water. This can be stored at $-18\,^{\circ}\mathrm{C}$, and lasts for up to a month.

Surface Attachment of mPEG-SH on AgDNP@Au

- Centrifuge $1.2\,\mathrm{mL}$ AgDNP@Au solution at $2500\,\mathrm{g}$ for $30\,\mathrm{min}$
- Coat Eppendorf tubes with $1\,\mathrm{wt\%}$ aq. Tween® 20 solution for $30\,\mathrm{min}$ and dry with compressed air
- Discard supernatant and redisperse the AgDNP@Au in $350\,\mu\mathrm{L}$ ultrapure water
- Measure UV/VIS and adjust LSPR absorption maximum to 1.16 ± 0.04
- Then transfer $350\,\mu\mathrm{L}$ to coated Eppendorf tubes
- Centrifuge all Eppendorf tubes at $10\,870\,\mathrm{g}$ for $10\,\mathrm{min}$
- Discard supernatant and add $26.3\,\mu\mathrm{L}$ of PEG-solution and $323.7\,\mu\mathrm{L}$ of ultrapure water
- Incubate at room temperature, covered in Aluminum foil, while shaking at $300\,\mathrm{RPM}$ overnight.

PEGylated Gold Coated Silver Decahedra Optical Sensitivity

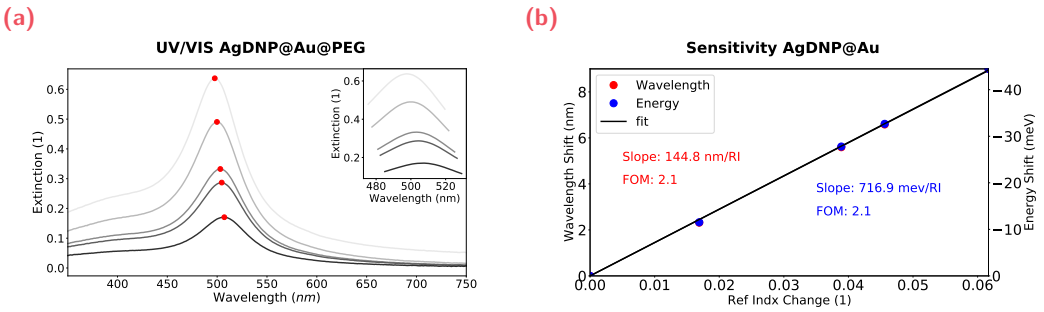

Fig. 2.30.: Refractive index sensitivity of PEGylated Gold coated Silver decahedra nanoparticles *(a)* UV/VIS spectra *(b)* sensitivity curves.

Earlier, we observed that the addition of a thin Gold layer on AgDNP had little effect on the optical performance. Here, we tested the sensitivity of our AgDNP@Au@PEG and compare it with Silica coated Silver cubes, that were used for bio-sensing. In Figure 2.30a, the refractive index of the solution has been changed with additions of a $40\,\mathrm{wt}\%$ glycerol/water mixture. Figure 2.30 shows the sensitivity curve by tracking the dipolar LSPR, where we obtain a value of $145\,\mathrm{nm\,RIU^{-1}}$ ($717\,\mathrm{meV\,RIU^{-1}}$) and a FOM of 2.1 for PEGylated AgDNP@Au.

This time, we observe that the PEG layer has greater effect on the sensitivity of the sensor, most probably since the PEG polymers block off some/part of the particle's hot spots. The PEG layer however has more effect on the FOM of the nanosensors. From literature, we know two physical effects that occur with surface ligands on the surface. First, covalent thiol-Gold bonds perturbs the sea of free electrons in the particle, reducing the amount of free-electrons available to oscillate at resonance. This typically leads to a red-shift in the LSPR. Second, the thiol-binding to the interface modifies the potential, such that chemical interface dampening is increased causing linewidth broadening.[78] We observe that the sensitivity is reduced in our PEGylated nanosensors compared to our AgDNP@Au, most likely because of the first effect, where mPEG-SH inhibits the detection of a dielectric change and fewer electrons are available to sense changes. The efficacy of the PEGylated AgDNP@Au nanosensor is mostly decreased because of the second effect, where the mPEG-SH results in broadening of the LSPR from $40\,\mathrm{nm}$ ($183\,\mathrm{meV}$) to $69\,\mathrm{nm}$ ($341\,\mathrm{meV}$).

All in all, we have discussed the photo-assisted synthesis for decahedra shaped nanosensors, that have been protected with a thin layer of Gold to improve their biocompatibility. Then to further improve the colloidal stability mPEG-SH has been

coated on the surface, still yielding a sensor with high sensitivity and a great FOM compared to literature.

2.5 Conclusion

In this chapter, we discussed optical biosensors, made of metal sized at the nanoscale. From mathematically solving how electromagnetic radiation interacts with small metal nanoparticles, we found that the free-electrons in the nanoparticle oscillate with the incoming light. This oscillation resonance depends on the sensor's material, shape, and the dielectric properties of both the nanosensor and its surrounding, known as the Localized Surface Plasmon Resonance (LSPR).

Then computational models have been employed to describe spherical nanosensors with protein layers of $4\,\mathrm{nm}$ on its surface. The addition of a second layer induced a shift of $1.9\,\mathrm{nm}$ ($14\,\mathrm{meV}$) on a full-width at half maximum (FWHM) of $17.2\,\mathrm{nm}$ ($134\,\mathrm{meV}$). Then optical shifts of the LSPR for different protein masses has been explored, and we observed that small initial protein rings and large second protein rings cause the largest shifts. Additionally, we found that there is a maximum combined size of the protein rings to observe a shift, because the sensitivity of the nanosensor is confined to its surface. We then used Discrete Dipole Approximation to find the sensitivity and figure-of-merit (FOM) of variously shaped nanosensors. From which, a promising nanosensor has been selected; the Silver decahedral nanoparticle (AgDNP).

Experimentally, we have synthesized these AgDNPs, through optimization iterations of their photo-reactor. From which we eventually were able to reproducibly synthesize AgDNP with a sensitivity of $187\,\mathrm{nm\,RIU^{-1}}$ ($1078\,\mathrm{meV\,RIU^{-1}}$) with a FOM of 6.9. These values are the highest compared with literature to date, thus indicating the efficacy of this nanosensor. Subsequently, we tested our AgDNPs in various biological buffers to find that the ligands are desorbed from the nanoparticles surface and that their Debye length is reduced, making them unstable, such that they deform and cluster. The stability is improved by protecting the nanosensors with an approximately $1\,\mathrm{nm}$ Gold layer, which additionally can be surface ligand modified with poly(ethylene glycol) methyl ether thiol (mPEG-SH). Thanks to the surface passivation, we observe high stability for almost up to $24\,\mathrm{h}$ in biological buffers (H_2O and Tris saline) and good stability for up to $2\,\mathrm{h}$ in PBS and HEPES saline buffer.

To conclude, we measure the sensitivity and FOM of our Gold coated Silver decahedra (AgNDP@Au) and find that the surface coating has minimal effect on the sensitivity,

dropping it merely to $260\,\mathrm{nm\,RIU^{-1}}$ ($1191\,\mathrm{meV\,RIU^{-1}}$) with a FOM of 6.5. We thus have shown the search for a promising nanosensor and expected optical outputs through computational models. Where after, we synthesized and optimized this nanosensor and proved that it has high sensitivity, an excellent FOM, and is biocompatible, such that it can be used in our promise to develop a novel system for kinetic biomolecule in-solution sensing.

3 Optical Setup Characterization

To develop a novel device for kinetic measurements of interacting biomolecules, two parts have been identified. Chapter 2 discusses the first component, metallic nanosensors, which have an optical output dependent on the dielectric properties of their surrounding. Additionally, we rationalize through computational methods that the spectral changes for interacting biomolecules in the sensor's proximity ought to be small and fast. This chapter discusses the second component, namely the optical setup, to capture these small and fast optical changes. First, the main components of the optical setup are discussed: an interferometer that is sensitive to small spectral changes, and a confocal microscope that is able to capture approximately one nanosensor at the time. The working principle of the interferometer is mathematically derived, and formulations for the two main methods of operation are introduced: Fourier Transform Spectroscopy and Photon-Correlation Fourier Spectroscopy. From the mathematical descriptions a computational model is composed, based on Monte-Carlo sampling, to explore the experimental parameter space faster. From the computations, it is expected that this setup is able to detect small optical shifts from laser light, but also from scattered light of nanoparticles. The chapter is finalized, by building the actual setup in real-life and characterizing it with static and dynamic laser light. There, the signals are found to be close to the predictions of our computational model. The computational model presented in this chapter has been used as the basis of a patent (Publication No. 2022/214611, Application No. EP2022059308), with the title: "Method, Apparatus and System for Characterizing Transient Interactions between Biomolecules".

3.1 Mathematical Description of an Interferometer

Spectral changes in the Localized Surface Plasmon Resonance (LSPR) of metallic nanoparticles from biomolecular interactions of $30\,\mathrm{kDa}$ proteins has been observed to only change $1.9\,\mathrm{nm}$ on a spectrum with a width of $17.2\,\mathrm{nm}$, see Section 2.1.3. Sensitive optical equipment is needed to capture these optical shifts and interferometers

are such optical devices, because they modulate their output through interference of light. In this section, the mathematical description of an interferometer is derived by describing the way light interacts with its individual components, namely a beamsplitter and mirrors. Even though descriptions of interferometers exist, we use a dual-path Michelson interferometer, which does not have much descriptive literature.[79] Therefore, I deem it useful to mathematically derive how electromagnetic waves are modulated in an interferometer to understand the outputs of spectrally changing light coming from nanoparticles later. For the derivation, I first use a monochromatic plane wave description following insights from Griffiths, that later is generalized into full spectra.[80]

3.1.1 Traveling Through Space

Before a derivation of plane waves interacting with interfaces can be derived, we must first consider what happens to plane waves traveling through space. A plane wave can be described as:

$$\overrightarrow{E}\left(\overrightarrow{r},t\right)=\widetilde{E}_0 e^{i\left(\overrightarrow{k}\cdot\overrightarrow{r}-\omega t\right)} \tag{3.1}$$

$$\overrightarrow{B}\left(\overrightarrow{r},t\right)=\frac{1}{v_1}\left(\overrightarrow{k}\times\overrightarrow{E}\right), \tag{3.2}$$

where ω is the frequency of the wave and v_1 is the phase velocities of the wave in material 1. The wave direction, intensity and frequency are all conserved as it moves through space. Only mathematically, it is interesting to choose the origin and where the time starts. These terms namely introduce a phase-shift. In the following sections, we find that the time dependent part can be neglected as it becomes equal in our evaluations. Only all the phase shifts collected through $\overrightarrow{k}\cdot\overrightarrow{r}$ become important when an expression through spatial coherence is derived.

3.1.2 Electromagnetic Plane Wave at an Interface

The optical components of an interferometer, the mirrors and the beamsplitter, can mathematically be described the same way. A general expression of an incoming plane wave, outgoing reflected wave, and outgoing transmitted wave interacting at an interface can be found. The specific material properties are then later used to find reflection and transmission amounts. Thus, first the generic problem of an electromagnetic plane wave hitting a surface at an arbitrary angle is considered. These derivations can be found in Griffiths, thus I mainly focus on the results.[80]

In Figure 3.1, a monochromatic plane wave with wavevector, $\overrightarrow{k_\mathrm{I}}$ hitting a surface at an angle, θ_I is illustrated. This gives rise to a reflected wave with wavevector, $\overrightarrow{k_\mathrm{R}}$, at angle, θ_R, and transmitted wave with wavevector, $\overrightarrow{k_\mathrm{T}}$, at angle, θ_T.

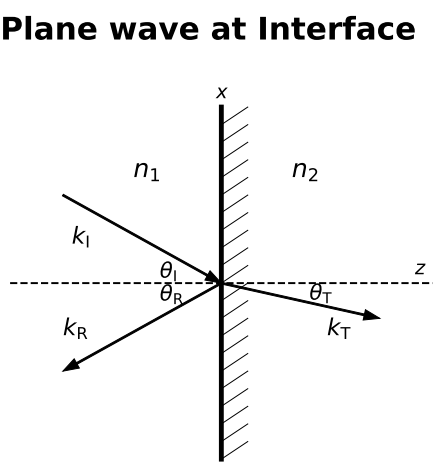

Fig. 3.1.: Illustration of an electromagnetic wave hitting an interface, where a monochromatic plane wave with wavevector, $\overrightarrow{k_\mathrm{I}}$ that hits an interface at angle, θ_I, gives rise to a reflected wave with wavevector, $\overrightarrow{k_\mathrm{R}}$, at angle, θ_R, and transmitted wave with wavevector, $\overrightarrow{k_\mathrm{T}}$, at angle, θ_T.

The electromagnetic wave is written down in complex waveform as:

$$\overrightarrow{E}_{\mathrm{I,R,T}}\left(\overrightarrow{r},t\right)=\widetilde{E}_{0;\mathrm{I,R,T}}e^{i\left(\overrightarrow{k}_{\mathrm{I,R,T}}\cdot\overrightarrow{r}-\omega t\right)} \tag{3.3}$$

$$\overrightarrow{B}_{\mathrm{I,R,T}}\left(\overrightarrow{r},t\right)=\frac{1}{v_{1,2}}\left(\overrightarrow{k}_{\mathrm{I,R,T}}\times\overrightarrow{E}_{\mathrm{I,R,T}}\right), \tag{3.4}$$

where, I, R, and T stand for incident, reflected, and transmitted wave, respectively. The phase velocities are related to the dielectric properties of the medium and follow the relationship: $k_\mathrm{I}=k_\mathrm{R}=k_\mathrm{I}v_1=\frac{v_2}{v_1}k_\mathrm{T}=\frac{n_1}{n_2}k_\mathrm{T}$. Due to conservation of energy, the fields need to be matched at the boundary, with the incident and reflected wave on one side and the transmitted on the other, such that $\overrightarrow{E_\mathrm{I}}+\overrightarrow{E_\mathrm{R}}=\overrightarrow{E_\mathrm{T}}$ and $\overrightarrow{B_\mathrm{I}}+\overrightarrow{B_\mathrm{R}}=\overrightarrow{B_T}$. In doing so, a boundary condition is retrieved that must hold for all x and y at $z=0$ and at all times t. Therefore, everything in the exponent must be equal and the time and frequency dependent part can be divided out to obtain:

$$\overrightarrow{k_\mathrm{I}}\cdot\overrightarrow{r}=\overrightarrow{k_\mathrm{R}}\cdot\overrightarrow{r}=\overrightarrow{k_\mathrm{T}}\cdot\overrightarrow{r},\quad\text{at}\quad z=0\,. \tag{3.5}$$

The system can be oriented freely around the z-axis, because of rotational symmetry, such that the incident wave can be placed in the xz-plane, and from Equation 3.5, the three laws from geometrical optics are obtained. 1) All three electromagnetic waves vectors form a plane, which also includes the surface normal. 2) The angle of reflection is the same as the angle of incident, $\theta_{\mathrm{I}} = \theta_{\mathrm{R}}$. 3) The transmitted angle is related to the refractive index and incident angle as $\frac{\sin\theta_{\mathrm{T}}}{\sin\theta_{\mathrm{I}}} = \frac{n_1}{n_2}$. The latter is also known as Snell's law. Now, the boundary conditions can be written down again without the exponential, because it is equal, such that they become:

$$\epsilon_1 \left(\overrightarrow{E_{0,\mathrm{I}}} + \overrightarrow{E_{0,\mathrm{R}}}\right)_{\mathrm{z}} = \epsilon_2 \left(\overrightarrow{E_{0,\mathrm{T}}}\right)_{\mathrm{z}} \tag{3.6}$$

$$\left(\overrightarrow{B_{0,\mathrm{I}}} + \overrightarrow{B_{0,\mathrm{R}}}\right)_{\mathrm{z}} = \left(\overrightarrow{B_{0,\mathrm{T}}}\right)_{\mathrm{z}} \tag{3.7}$$

$$\left(\overrightarrow{E_{0,\mathrm{I}}} + \overrightarrow{E_{0,\mathrm{R}}}\right)_{\mathrm{x,y}} = \left(\overrightarrow{E_{0,\mathrm{T}}}\right)_{\mathrm{x,y}} \tag{3.8}$$

$$\frac{1}{\mu_1}\left(\overrightarrow{B_{0,\mathrm{I}}} + \overrightarrow{B_{0,\mathrm{R}}}\right)_{\mathrm{x,y}} = \frac{1}{\mu_2}\left(\overrightarrow{B_{0,\mathrm{T}}}\right)_{\mathrm{x,y}} , \tag{3.9}$$

where, $\overrightarrow{B_0} = (1/v)\,\hat{k} \times \overrightarrow{E_0}$, and the last 2 equations are sets of equations for x and y. To continue the derivation, two different cases of how the plane wave is oriented relative to the interface have to be considered. In these cases, we assume that the media are insulating, such that $\rho = 0$ and $\overrightarrow{J} = 0$ in Maxwell's equations (Equations 1.2).

Parallel Polarization (P-polarization)

For parallel polarization, the electric field is parallel to the plane of incidence, such that Equation 3.9 can be simplified to:

$$\epsilon_1 \left(E_{0,\mathrm{I}} \sin\theta_{\mathrm{I}} - E_{0,\mathrm{R}} \sin\theta_{\mathrm{R}}\right) = \epsilon_2 \left(E_{0,\mathrm{T}} \sin\theta_{\mathrm{T}}\right) \tag{3.10}$$

$$0 = 0 \tag{3.11}$$

$$E_{0,\mathrm{I}} \cos\theta_{\mathrm{I}} - E_{0,\mathrm{R}} \cos\theta_{\mathrm{R}} = E_{0,\mathrm{T}} \cos\theta_{\mathrm{T}} \tag{3.12}$$

$$\frac{1}{\mu_1 v_1}\left(E_{0,\mathrm{I}} - E_{0,\mathrm{R}}\right) = \frac{1}{\mu_2 v_2}\left(E_{0,\mathrm{T}}\right) . \tag{3.13}$$

The, earlier obtained, geometrical laws of optics can be used to compute the magnitudes of the electric fields for the reflection and the transmission, $E_{0,\mathrm{R}}$ and $E_{0,\mathrm{T}}$, as:

$$E_{0,\mathrm{R}} = \left(\frac{\alpha-\beta}{\alpha+\beta}\right) E_{0,\mathrm{I}}, \quad E_{0,\mathrm{T}} = \left(\frac{2}{\alpha+\beta}\right) E_{0,\mathrm{I}}\,, \tag{3.14}$$

with $\alpha = \frac{\cos\theta_\mathrm{T}}{\cos\theta_\mathrm{I}}$ and $\beta = \frac{\mu_1 v_1}{\mu_2 v_2} = \frac{\mu_1 n_2}{\mu_2 n_1}$.

Perpendicular Polarization (S-polarization)

The second case is perpendicular polarization, where the electric field is perpendicular to the plane of incidence (out of the paper). Equation 3.9 is then simplified to:

$$0 = 0 \tag{3.15}$$

$$\frac{1}{v_1} E_{0,\mathrm{I}} \sin\theta_\mathrm{I} + \frac{1}{v_1} E_{0,\mathrm{R}} \sin\theta_\mathrm{R} = \frac{1}{v_1} E_{0,\mathrm{T}} \sin\theta_\mathrm{T} \tag{3.16}$$

$$E_{0,\mathrm{I}} + E_{0,\mathrm{R}} = E_{0,\mathrm{T}} \tag{3.17}$$

$$\frac{1}{\mu_1 v_1}\left(-E_{0,\mathrm{I}} \cos\theta_\mathrm{I} + E_{0,\mathrm{R}} \cos\theta_\mathrm{R}\right) = \frac{-1}{\mu_2 v_2}\left(E_{0,\mathrm{T}} \cos\theta_\mathrm{T}\right)\,. \tag{3.18}$$

Again, with the geometrical laws of optics the magnitudes of the electric fields for the reflection and the transmission, $E_{0,\mathrm{R}}$ and $E_{0,\mathrm{T}}$ are calculated. Now as:

$$E_{0,R} = \left(\frac{1-\alpha\beta}{1+\alpha\beta}\right) E_{0,\mathrm{I}}, \quad E_{0,\mathrm{T}} = \left(\frac{2}{1+\alpha\beta}\right) E_{0,\mathrm{I}}\,. \tag{3.19}$$

With a solution to the generic problem of a plane wave hitting an interface, specific solutions for the optical elements of an interferometer can now be determined. First, metallic mirrors and thereafter a specialized mirror, the retroreflector, are discussed. The latter no only reflects, but also displaces the incoming beam, allowing to construct two optical paths in the interferometer. Then, the beamsplitter is discussed, which outputs a reflected and transmitted beam with equal intensity. The beamsplitter and two retroreflectors together build up a dual-path interferometer, and expressions for the modulated output are derived from two different underlying physical principles.

3.1.3 Mirror

First, to describe how electromagnetic waves interact with a mirror, the solution from Section 3.1.2 is utilized. For further derivation let us assume that the mirror is made of metal.[1] Metals are characterized by holding their valence electrons relatively loosely. Therefore, the free current density, $\overrightarrow{J}$, in Maxwell's equations is definitely **not zero**. Thus, the boundary conditions must now include a free surface charge, σ_f, and a free surface current, $\overrightarrow{K_\mathrm{f}}$. Let us recall the Maxwell's equations with surface charge and free surface current:

$$\epsilon_1 E_1^\perp - \epsilon_2 E_2^\perp = \sigma_\mathrm{f} \tag{3.20}$$

$$\overrightarrow{E}_1^\parallel - \overrightarrow{E}_2^\parallel = 0 \tag{3.21}$$

$$\epsilon_1 B_1^\perp - \epsilon_2 B_2^\perp = \sigma_\mathrm{f} \tag{3.22}$$

$$\frac{1}{\mu_1}\overrightarrow{B}_1^\parallel - \frac{1}{\mu_1}\overrightarrow{B}_2^\parallel = \overrightarrow{K_\mathrm{f}} \times \hat{n}\,. \tag{3.23}$$

To formally solve the Maxwell's equations of an incoming plane wave hitting a metal surface, we have to be consider the two polarizations separately. Luckily, they yield the same outcome when $\widetilde{\beta} = \frac{\mu_1 v_1}{\mu_2 \omega}\widetilde{k}_2$ is introduced. The reflected and transmitted fields then become:

$$\widetilde{E}_{0,\mathrm{R}} = \left(\frac{1-\widetilde{\beta}}{1+\widetilde{\beta}}\right)\widetilde{E}_{0,\mathrm{I}}, \quad \widetilde{E}_{0,\mathrm{T}} = \left(\frac{2}{1+\widetilde{\beta}}\right)\widetilde{E}_{0,\mathrm{I}}\,. \tag{3.24}$$

For a perfect conductor $\sigma = \infty$, which leads to $\widetilde{k}_2 = \infty$, the fields then simplify to:

$$\widetilde{E}_{0,\mathrm{R}} = -\widetilde{E}_{0,\mathrm{I}}, \quad \widetilde{E}_{0,\mathrm{T}} = 0\,. \tag{3.25}$$

This last equation teaches us that a perfect conducting metal mirror reflects the incident wave completely, but introduces a π phase shift.

[1] Note, that there exists different types of mirrors that behave differently; dielectric mirrors. Reflections there have more polarization and incident angle dependence.

3.1.4 Hollow Retroreflector

In this paragraph, a special type of mirror is discussed that not only reflects the incoming beam, but also displaces it. These mirrors are known as retroreflectors and come in various types.[81] The retroreflector used in this work consists of 3 mirrors positioned with $90°$ angles between each of them. Essentially, this forms a corner of a perfect cube that ensures that any incoming wave and outgoing wave have the same θ and ϕ angle, but slightly displaces the two waves. The latter is a useful property of retroreflectors, because it allows us to physically separate the waves in the interferometer giving us access to two outputs, hence the name dual-path interferometer. Oppositely, when a "normal" mirror is used, one of the reflected beams usually overlaps with the incoming beam, making it difficult to detect. Additionally, in this work we consider hollow retroreflectors, which have the reflective surfaces on the outside of the corner cube, meaning that the plane wave only travels through air until it bounces off the mirrors. The alternative is a trihedral prism, which leads to unwanted distortions or reflections from the waves traveling through glass. In Figure 3.2, an illustration of a hollow retroreflector reflecting an incoming wave at a displaced distance in two dimensions is shown. Noteworthy is that because the figure is sketched in 2D, only 2 reflections are shown, whereas in reality there are always **3** reflections. Thus, the outgoing wave is $3 \cdot \pi = \pi$ out of phase with the incident wave.

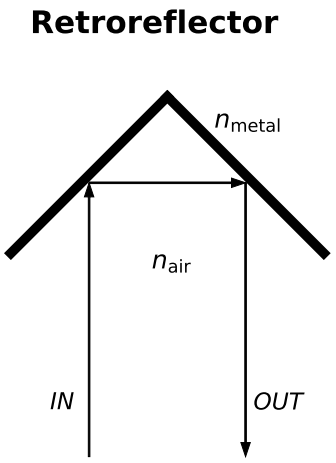

Fig. 3.2.: Schematic representation of a hollow retroreflector, where an incoming plane wave, **IN**, get reflected **three** times, causing the outgoing plane wave **OUT** to be π phase shifted. Note, that in 2D I can only draw two reflections.

3.1.5 Beamsplitter

In this paragraph, the last optical element, the cube beamsplitter, is discussed. Cube beamsplitters are made of two right-angle prisms cemented together with a special optical cement that is semi-transparent. Manufacturers do not disclose the exact composition of their coatings, but for low absorption coatings with little polarization sensitivity for broadband applications, typically hybrid partial-reflection coatings are used.[82] These coatings are a mixture of metals and dielectrics. Note, that other beamsplitters, such as pellicles and plate beamsplitters can have higher transmission efficiencies, but they can introduce unwanted effects, such as vibrations, displaced reflection angles, uneven wavelength dependencies, as well as higher polarization sensitivities. Because of those reasons, we chose to use a cube beamsplitter. Due to the presence of metal in the hybrid partial-reflection cement, it is expected that a phase shift of π between the reflected and the transmitted beam will be induced by the beamsplitter.

In Figure 3.3, a schematic of a cube beamsplitter is shown, where an incoming plane wave, hits the glass surface of the cube and gives rise to a very small back reflection. Then the wave hits an optical cement layer at $45°$, reflecting roughly half of it. The other half of the beam transmits to the other side of the optical cement refracting back to the original incoming angle (along the z-axis in this case). The back reflections and beam displacement are minimized by manufacturers with antireflection coatings and as thin as possible cement layers. These unwanted reflections typically are on the order of $5\,\%$ to $10\,\%$.[83] The choice of the optical cement determines the α and β from Equation 3.14 and Equation 3.19. In an ideal case they cause equal intensity splitting for both polarizations such that:

$$E_{0,\mathrm{R}} = \frac{1}{\sqrt{2}} E_{0,\mathrm{I}}, \quad E_{0,\mathrm{T}} = \frac{1}{\sqrt{2}} E_{0,\mathrm{I}}\,. \tag{3.26}$$

3.1.6 Combined Optical Elements form Interferometer

Spatial Coherence: Phase Tracking

In this section, all the mathematical descriptions for the optical elements that constitute an interferometer are combined to find expressions for the modulated output of the interferometer. Important in this description is that the plane wave has the same functional form everywhere in the interferometer. Only the wave vector will be different. Also, from interactions with interfaces, the wave might pick

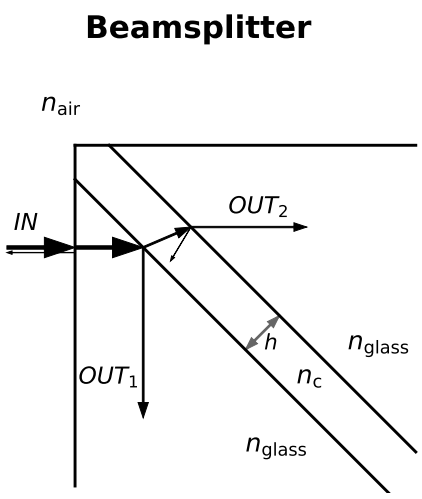

Fig. 3.3.: Schematic representation of a beamsplitter, where an incoming plane wave, **IN**, get separated into two outgoing planes waves **OUT**. Additionally, there are several minor reflections, that in-real life are minimized by coatings.

up phase shifts. To describe an interferometer through spatial coherence, all the phase-shift that a plane wave collects, moving through the interferometer, have to be bookkept. In Figure 3.4, a schematic representation of a dual-path Michelson interferometer is shown, where an incoming wave is firstly split by a beamsplitter. Thereafter, travels the two outgoing waves towards retroreflectors that reflect the beam back with a small displacement. The back-traveling waves recombine at the beamsplitter (offset to where they originally were split), giving rise to two outgoing plane waves. We aim to use this dual-path Michelson interferometer for our optical device, because it experimentally grants us access to both outgoing waves. In traditional common-path interferometers, one of the outgoing paths overlaps with the incoming beam, such that one loses access to it. With two outputs available, both signals can be analyzed, granting more information, but I will come back to this in later sections in this chapter.

Let us start with an incoming plane wave from the left that hits the beamsplitter. I will focus only on the $\overrightarrow{E}$-field only, since the $\overrightarrow{B}$-field simply follows it. The incoming wave picks up some phase from traveling (through the glass) to the position in the beamsplitter, where it is split. Luckily, the phase up to this point is not so important, since it will carry over to both of the split waves and since it relies on our choice of the origin. Therefore, we choose the origin to be exactly at the split, such that we start with $0°$ phase shift. We use the plane wave description for the electromagnetic wave and move the time dependency into a new prefactor $\widetilde{E_0'}$.

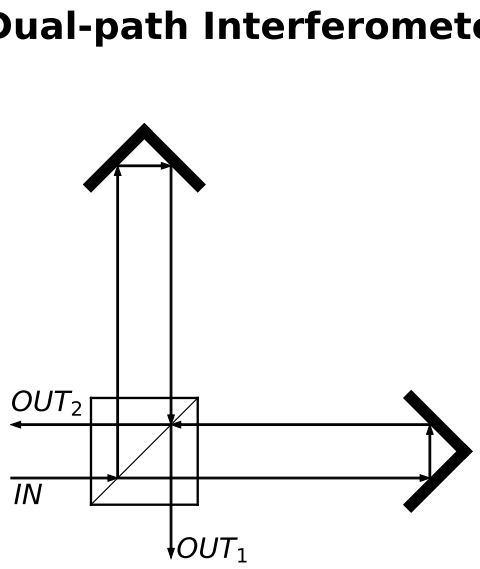

Fig. 3.4.: Schematic representation of an interferometer, where an incoming plane wave is split into two separate portions. These travels through different parts of the setup, obtaining different phases, that results in interference when they combine again.

Moreover, the prefactor of the plane wave will accumulate phase shifts at any new position $\overrightarrow{r}$ from interactions with interfaces and from traveling through space. We thus can write:

$$\overrightarrow{E}\left(\overrightarrow{r},t\right)=E_0e^{i\left(\overrightarrow{k}\cdot\overrightarrow{r}-\omega t\right)}=\widetilde{E_0}e^{i\overrightarrow{k}\cdot\overrightarrow{r}}\,. \tag{3.27}$$

Let us do the bookkeeping for all the phases of the beam going up into the interferometer arm, as illustrated with in Figure 3.5. First, the wave reflects off of the beamsplitter giving it a π phase shift, E_1. Next, the wave travels upwards through the glass to the glass air interface, picking up a phase $k_{\mathrm{g}}L_{\mathrm{g,L}}$, captured in E_2, with the prefactor of the plane wave E_2 being E_1. Then the wave travels up through the arm ($k_{\mathrm{air}}L_{\mathrm{A}}$), bounces off the mirror (π), displaces a distance from the mirrors ($k_{\mathrm{air}}L_{\mathrm{M}}$), bounces two more times (2π), travels downwards through the interferometer arm ($k_{\mathrm{air}}L_{\mathrm{A}}$), and finally travels through the glass to the beamsplitting interface ($k_{\mathrm{g}}L_{\mathrm{g,S}}$). At this point the beam will be split again by the beamsplitter into $E_{\mathrm{OUT1,A1}}$ and $E_{\mathrm{OUT2,A1}}$. The latter picks up another phase shift of π, because it reflects off of the beamsplitter. In contrast to $E_{\mathrm{OUT1,A1}}$, which is transmitting through. Therefore, we observe that the two outputs are a factor of π separated in phase. In this derivation k_{g} is the angular wavenumber in glass, k_{air} is the angular wavenumber in air, and L_{x} are lengths as defined in Figure 3.5 with x being the subscript to indicate which length. We start the bookkeeping for all the phases that the wave picks up as:

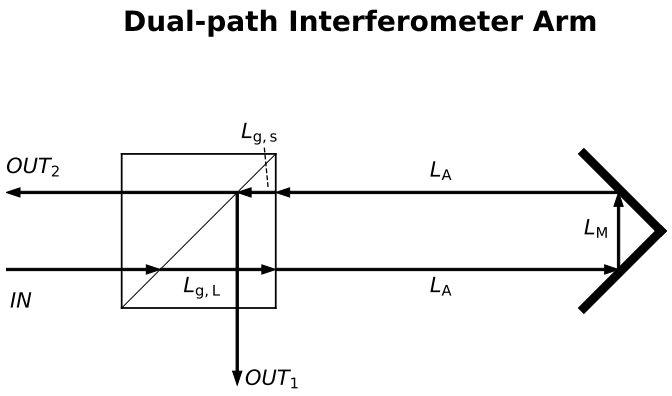

Fig. 3.5.: Schematic representation of part of an interferometer to track all the phase shifts from interface interactions and traveling through space.

$$E_1 = \frac{1}{\sqrt{2}}\widetilde{E_0}e^{i\pi} \tag{3.28}$$

$$E_2 = \frac{1}{\sqrt{2}}\widetilde{E_1}\cdot e^{ik_{\mathrm{g}}L_{\mathrm{g,L}}} = \widetilde{E_0}e^{i\pi}\cdot e^{ik_{\mathrm{g}}L_{\mathrm{g,L}}} \tag{3.29}$$

$$E_3 = \frac{1}{\sqrt{2}}\widetilde{E_0}e^{ik_{\mathrm{g}}L_{\mathrm{g,L}}+i\pi}\cdot e^{ik_{\mathrm{air}}L_{\mathrm{A}}} \tag{3.30}$$

$$E_4 = \frac{1}{\sqrt{2}}\widetilde{E_0}e^{ik_{\mathrm{g}}L_{\mathrm{g,L}}+ik_{\mathrm{air}}L_{\mathrm{A}}+\pi}\cdot e^{ik_{\mathrm{air}}L_{\mathrm{M}}} \tag{3.31}$$

$$E_5 = \frac{1}{\sqrt{2}}\widetilde{E_0}e^{ik_{\mathrm{g}}L_{\mathrm{g,L}}+ik_{\mathrm{air}}(L_{\mathrm{A}}+L_{\mathrm{M}})+i\pi}\cdot e^{i3\pi} \tag{3.32}$$

$$E_6 = \frac{1}{\sqrt{2}}\widetilde{E_0}e^{ik_{\mathrm{g}}L_{\mathrm{g,L}}+ik_{\mathrm{air}}(L_{\mathrm{A}}+L_{\mathrm{M}})+i4\pi}\cdot e^{ik_{\mathrm{air}}L_{\mathrm{A}}} \tag{3.33}$$

$$E_7 = \frac{1}{\sqrt{2}}\widetilde{E_0}e^{ik_{\mathrm{g}}L_{\mathrm{g,L}}+ik_{\mathrm{air}}(L_{\mathrm{A}}+L_{\mathrm{M}})+i4\pi}\cdot e^{ik_{\mathrm{g}}L_{\mathrm{g,S}}} \tag{3.34}$$

$$E_{\mathrm{OUT1,A1}} = \frac{1}{2}\widetilde{E_0}e^{ik_{\mathrm{g}}\left(L_{\mathrm{g,L}}+L_{\mathrm{g,S}}\right)+ik_{\mathrm{air}}(2L_{\mathrm{A}}+L_{\mathrm{M}})+i4\pi} \tag{3.35}$$

$$E_{\mathrm{OUT2,A1}} = \frac{1}{2}\widetilde{E_0}e^{ik_{\mathrm{g}}\left(L_{\mathrm{g,L}}+L_{\mathrm{g,S}}\right)+ik_{\mathrm{air}}(2L_{\mathrm{A}}+L_{\mathrm{M}})+i5\pi}\,. \tag{3.36}$$

A similar exercise can be done for the other interferometer arm, which one lies in the direction of the incident beam. Since the plane wave transmits through the beamsplitter, it does **not** pick up the initial π phase shift. Eventually, similar expressions are obtained, but missing that initial π phase offset, resulting:

$$E_{\mathrm{OUT1,A2}} = \frac{1}{2}\widetilde{E_0}e^{ik_{\mathrm{g}}\left(L_{\mathrm{g,L}}+L_{\mathrm{g,S}}\right)+ik_{\mathrm{air}}(2L_{\mathrm{A}}+L_{\mathrm{M}})+i4\pi} \tag{3.37}$$

$$E_{\mathrm{OUT2,A2}} = \frac{1}{2}\widetilde{E_0}e^{ik_{\mathrm{g}}\left(L_{\mathrm{g,L}}+L_{\mathrm{g,S}}\right)+ik_{\mathrm{air}}(2L_{\mathrm{A}}+L_{\mathrm{M}})+i3\pi}\,. \tag{3.38}$$

These expressions become more interesting, when the length of one arm is allowed to change. In this case, let us assume that we can extend or retract the second arm with a distance L_{c}, making $L_{\mathrm{A}} = L_{\mathrm{A}} + L_{\mathrm{c}}$, such that:

$$E_{\mathrm{OUT1,A2}} = \frac{1}{2}\widetilde{E_0}e^{ik_{\mathrm{g}}\left(L_{\mathrm{g,L}}+L_{\mathrm{g,S}}\right)+ik_{\mathrm{air}}(2L_{\mathrm{A}}+L_{\mathrm{M}}+\mathbf{2}\boldsymbol{L_{\mathrm{c}}})+i4\pi} \tag{3.39}$$

$$E_{\mathrm{OUT2,A2}} = \frac{1}{2}\widetilde{E_0}e^{ik_{\mathrm{g}}\left(L_{\mathrm{g,L}}+L_{\mathrm{g,S}}\right)+ik_{\mathrm{air}}(2L_{\mathrm{A}}+L_{\mathrm{M}}+\mathbf{2}\boldsymbol{L_{\mathrm{c}}})+i3\pi}\,. \tag{3.40}$$

At this point, plane waves descriptions arriving at the beamsplitter after travelling through both interferometer arms have been found. Both of them picked up numerous phase shifts, and because Maxwell's equations are additive, both electric fields can simply be summed to find the total electric field after recombination at the beamsplitter. The first outgoing electric plane wave then become:

$$
\begin{aligned}
E_{\mathrm{OUT1}} &= E_{\mathrm{OUT1,A1}} + E_{\mathrm{OUT1,A2}} && (3.41)\\
&= \frac{1}{2}\widetilde{E_0}\left(e^{-ik_{\mathrm{g}}\left(L_{\mathrm{g,L}}+L_{\mathrm{g,S}}\right)+k_{\mathrm{air}}(2L_{\mathrm{A}}+L_{\mathrm{M}})+i4\pi}\right.\\
&\qquad \left.+e^{-ik_{\mathrm{g}}\left(L_{\mathrm{g,L}}+L_{\mathrm{g,S}}\right)+k_{\mathrm{air}}(2L_{\mathrm{A}}+L_{\mathrm{M}}+2L_{\mathrm{c}})+i4\pi}\right) && (3.42)\\
&= \frac{1}{2}E_0 e^{-i\omega t}\left(e^{-i(k_{\mathrm{g}}L_{\mathrm{g}}+k_{\mathrm{air}}L_{\mathrm{air}})}+e^{-i(k_{\mathrm{g}}L_{\mathrm{g,int}}+k_{\mathrm{air}}L_{\mathrm{air}}+2k_{\mathrm{air}}L_{\mathrm{c}})}\right), && (3.43)
\end{aligned}
$$

where $L_{\mathrm{g}} = L_{\mathrm{g,L}} + L_{\mathrm{g,S}}$ and $L_{\mathrm{air}} = 2L_{\mathrm{A}} + L_{\mathrm{M}}$. We, now, have the electric field, but the unit we actually measure with our detectors is the intensity of the beam. We should thus take a look at the absolute value of the electric field as:

$$
\begin{aligned}
I_{\mathrm{D1}} &= E_{\mathrm{OUT1}} \cdot \overline{E_{\mathrm{OUT1}}} && (3.44)\\
&= \frac{1}{4}E_0^2 e^{-i\omega t}\left(e^{-i(k_{\mathrm{g}}L_{\mathrm{g}}+k_{\mathrm{air}}L_{\mathrm{air}})}\right.\\
&\qquad \left.+e^{-i(k_{\mathrm{g}}L_{\mathrm{g}}+k_{\mathrm{air}}L_{\mathrm{air}}+2k_{\mathrm{air}}L_{\mathrm{c}})}\right)\\
&\qquad \cdot\left(e^{+i(k_{\mathrm{g}}L_{\mathrm{g}}+k_{\mathrm{air}}L_{\mathrm{air}})}\right.\\
&\qquad \left.+e^{+i(k_{\mathrm{g}}L_{\mathrm{g}}+k_{\mathrm{air}}L_{\mathrm{air}}+2k_{\mathrm{air}}L_{\mathrm{c}})}\right) && (3.45)\\
&= \frac{1}{4}E_0^2\left(2+e^{-i2k_{\mathrm{air}}L_{\mathrm{c}}}+e^{i2k_{\mathrm{air}}L_{\mathrm{c}}}\right) && (3.46)\\
&= \frac{1}{4}E_0^2\left(2+2\cos\left(k_{\mathrm{air}}2L_{\mathrm{c}}\right)\right) && (3.47)\\
&= \frac{1}{2}E_0^2\left(1+\cos\left(k_{\mathrm{air}}2L_{\mathrm{c}}\right)\right). && (3.48)
\end{aligned}
$$

All the terms cancel except for the distance term, L_{c}, that changes the length of one of the interferometer arms. In Equation 3.48, this distance is found to modulate the intensity over periods of $2k_{air}L_{\mathrm{c}} = 2\pi\widetilde{\nu}_0\left(2L_{\mathrm{c}}\right) = 2\pi\widetilde{\nu}_0\delta$, with δ as the path-length difference between the two arms. A similar expression is obtained for the intensity of the outgoing wave, which due to the π phase shift oscillates oppositely to the intensity on detector 1. The intensities then become:

$$I_{\mathrm{D1}} = \frac{1}{2} E_0^2 \left(1 + \cos\left(2\pi \widetilde{v}_0 \delta\right)\right) \tag{3.49}$$

$$I_{\mathrm{D2}} = \frac{1}{2} E_0^2 \left(1 - \cos\left(2\pi \widetilde{v}_0 \delta\right)\right) \ . \tag{3.50}$$

Throughout this derivation, I have neglected that there are two different polarizations, because in Section 3.1.3 we found that there is no difference between polarizations when reflecting off of metal surfaces. In our interferometer derivation, we have chosen optical elements (made of metal) that behave the same for both S- and P-polarization. Therefore, we expect to find this modulated output from an interferometer independent of polarization.

Plane Wave becomes Sinusoid in Interferogram Space

Thus far, a description for a plane wave going through an interferometer has been obtained, where the output intensity turns into a cosine with the path-length difference between the two arms and the plane wave frequency in its argument. I want to discuss how one can think about this in terms of photons and spectra. This reasoning, namely, becomes important for the development of the computational model later in this chapter. The plane wave that has been used, only had one frequency ω (in other words, only one wavenumber $\widetilde{\nu_0}$). We could potentially say that this plane wave with only a single wavenumber is one single photon travelling through the interferometer. Let us first assume this, to see whether this is correct. Namely, this way we can construct spectra, consisting of multiple photons by summing them all together, thanks to the additive nature of electromagnetics. The intensity can then be described as a sum over several wavenumbers $\widetilde{\nu_{\mathrm{i}}}$ as:

$$I_{\mathrm{D1}} = \sum_i \frac{1}{2} E_{0,\mathrm{i}}^2 \left(1 + \cos\left(2\pi \widetilde{v_{\mathrm{i}}} \left(2\delta\right)\right)\right) \tag{3.51}$$

$$I_{\mathrm{D2}} = \sum_i \frac{1}{2} E_{0,\mathrm{i}}^2 \left(1 - \cos\left(2\pi \widetilde{v_{\mathrm{i}}} \left(2\delta\right)\right)\right) \ , \tag{3.52}$$

where $\sum_i E_{0,i}^2 = \langle I \rangle$ can be written, resulting in:

$$I_{\mathrm{D1}} = \frac{1}{2}\langle I\rangle + \sum_i \frac{1}{2} E_{0,\mathrm{i}}^2 \cos\left(2\pi\widetilde{v}_{\mathrm{i}}\left(2\delta\right)\right) \tag{3.53}$$

$$I_{\mathrm{D2}} = \frac{1}{2}\langle I\rangle - \sum_i \frac{1}{2} E_{0,\mathrm{i}}^2 \cos\left(2\pi\widetilde{v}_{\mathrm{i}}\left(2\delta\right)\right)\ . \tag{3.54}$$

This expression can be transformed into an integral, whenever many photons are considered, as:

$$I_{\mathrm{D1}} = \frac{1}{2}\langle I\rangle + \int \frac{1}{2} E_{0,\widetilde{\mathrm{v}}}^2 \cos\left(2\pi\widetilde{v}\left(2\delta\right)\right) d\widetilde{v} \tag{3.55}$$

$$I_{\mathrm{D2}} = \frac{1}{2}\langle I\rangle - \int \frac{1}{2} E_{0,\widetilde{\mathrm{v}}}^2 \cos\left(2\pi\widetilde{v}\left(2\delta\right)\right) d\widetilde{v}\,. \tag{3.56}$$

This results looks very similar to a cosine Fourier Transform with the argument $\frac{1}{2}E_{0,\widetilde{\mathrm{v}}}^2$. This argument is intrinsically an amplitude factor indicating how much prevalence one certain wavenumber has. This amplitude is directly related to the number of photons that are present at that wavenumber. Alternatively, the cosine Fourier Transform is written as the real part of a normal Fourier Transform such that:

$$I_{\mathrm{D1}} = \frac{1}{2}\langle I\rangle + \frac{1}{2}\langle I\rangle \mathfrak{Re}\left\{\mathcal{F}\left[s\left(\widetilde{v}\right)\right]\right\} \tag{3.57}$$

$$I_{\mathrm{D2}} = \frac{1}{2}\langle I\rangle - \frac{1}{2}\langle I\rangle \mathfrak{Re}\left\{\mathcal{F}\left[s\left(\widetilde{v}\right)\right]\right\}\ . \tag{3.58}$$

Here we define a spectrum as the sum of individual photons with $A\left(\widetilde{\nu}_{\mathrm{i}}\right)$, an amplitude factor describing how many photons are present at wavenumber $\widetilde{\nu}_{\mathrm{i}}$. In the continuous case this amplitude factor becomes the spectrum, $s\left(\widetilde{\nu}\right)$, such that:

$$\sum_i^{N_{\mathrm{photons}}} A\left(\widetilde{\nu}_{\mathrm{i}}\right)\cos\left(2\pi\widetilde{\nu}_{\mathrm{i}}2\delta\right) = \int s\left(\widetilde{\nu}\right)\cdot\cos\left(2\pi\widetilde{\nu}2\delta\right)d\widetilde{\nu} = \mathfrak{Re}\left\{\mathcal{F}\left[s\left(\widetilde{\nu}\right)\right]\right\}\ . \tag{3.59}$$

Spectrum is Sum of Single Photons

To quantitatively prove that this description for a spectrum is valid, I simulate an arbitrarily shaped spectrum. We compute the Fourier transform thereof via a Fast Fourier Transform (FFT) algorithm and compare that to a summation of cosines with wavenumbers distributed according to the spectrum. For the latter, we perform Monte-Carlo sampling of the spectrum to obtain the correct distribution of photon wavenumbers to use in $\cos(2\pi\tilde{\nu}_i 2\delta)$ as a function of path-length difference, δ.[2] In Figure 3.6, a double peaked input spectrum is chosen (Figure 3.6a) and the corresponding interferograms from FFT and Equation 3.48 (Figure 3.6b) with $10\,000$ photons are compared. The residuals show that indeed we obtain the same result, indicating that a spectrum can be described as a sum of single photons. This loosely proves that our assumption of saying that every plane wave is one photon is not completely wrong.

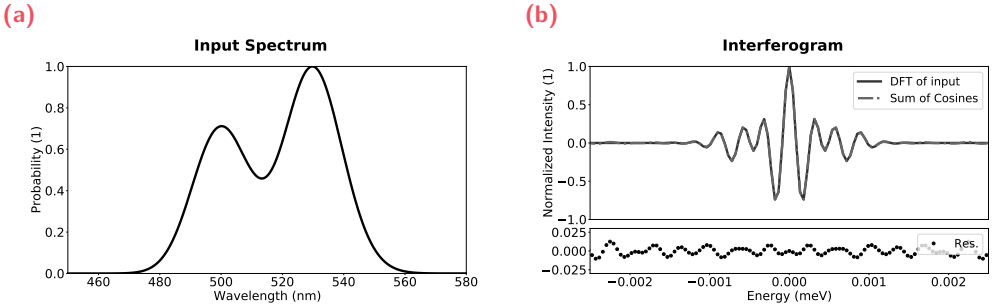

Fig. 3.6.: Description of a spectrum by the sum of its individual photons with *(a)* a double peaked input spectrum and *(b)* the discrete Fourier Transformed interferogram and the interferogram from Equation 3.59 as a sum of the individual photons.

Temporal Coherence: Wiener-Khinchin Theorem

In this paragraph, we discuss temporal coherence in an interferometer. We have just seen that interference can mathematically be described through spatial coherence. However, there I left the time-factor in the exponent of the plane-wave quietly on the side. Nevertheless, this does not disprove the derivation we just performed. It rather opens another view on how interferometers work, and that is through time-related phase shifts. The path-length difference between the two plane waves causes a time-delay, τ, between them, when they combine again at the beamsplitter. We could compute the time-average of the intensity at the detector, and find that

[2] see section 3.5.1 about Monte-Carlo sampling

this expression looks very similar to a first order auto-correlation. Then the Wiener-Khinchin theorem can be used to relate the spectrum to the Fourier transform of the auto-correlation.[84] The Wiener-Khinchin theorem namely states that the auto-correlation of $S(\widetilde{\nu}, t)$ is equal to the Fourier transform of the absolute square of $S(\widetilde{\nu}, t)$. Let us write down the combined electric field as a superposition of the two individual arm paths:

$$E_{\mathrm{OUT1,A1}} = \frac{1}{2} E_0(t) \tag{3.60}$$

$$E_{\mathrm{OUT1,A2}} = \frac{1}{2} E_0(t-\tau) \tag{3.61}$$

$$I_{\mathrm{OUT1}}(t) = (E_{\mathrm{OUT1,A1}} + E_{\mathrm{OUT1,A1}})\,\overline{(E_{OUT1,A1} + E_{\mathrm{OUT1,A1}})} \tag{3.62}$$

$$I_{\mathrm{OUT1}}(t) = \frac{1}{4}\left(I(t) + I(t-\tau) + E_0(t)\cdot\overline{E_0(t-\tau)} + \overline{E_0(t)}\cdot E_0(t-\tau)\right) \tag{3.63}$$

This instantaneous intensity is not very useful by itself. Thus, let us take the time-average, where we find that the time-average of a shifted intensity is intrinsically the same, and $S(\tau) \equiv \left\langle E_0(t)\cdot\overline{E_0(t-\tau)}\right\rangle$ defined through Wiener-Khinchin theorem, and $s(\tau)$ being the normalized spectrum.

$$\langle I_{\mathrm{OUT1}}(t)\rangle = \frac{1}{4}\left(\langle I(t)\rangle + \langle I(t)\rangle + \left\langle E_0(t)\cdot\overline{E_0(t-\tau)}\right\rangle + \left\langle\overline{E_0(t)}\cdot E_0(t-\tau)\right\rangle\right) \tag{3.64}$$

$$\langle I_{\mathrm{OUT1}}(t)\rangle = \frac{1}{4}\left(2\langle I(t)\rangle + \left\langle E_0(t)\cdot\overline{E_0(t-\tau)}\right\rangle + \left\langle\overline{E_0(t)}\cdot E_0(t-\tau)\right\rangle\right) \tag{3.65}$$

$$\langle I_{\mathrm{OUT1}}(t)\rangle = \frac{1}{4}\left(2\langle I(t)\rangle + S(\tau) + S^*(\tau)\right) \tag{3.66}$$

$$\langle I_{\mathrm{OUT1}}(t)\rangle = \frac{1}{2}\left(\langle I(t)\rangle + \mathfrak{Re}\left\{\mathcal{F}\left[S(\widetilde{\nu}, t)\right]\right\}\right) \tag{3.67}$$

$$\langle I_{\mathrm{OUT1}}(t)\rangle = \frac{\langle I(t)\rangle}{2}\left(1 + \mathfrak{Re}\left\{\mathcal{F}\left[s(\widetilde{\nu}, t)\right]\right\}\right) \tag{3.68}$$

3.2 Fourier Transform Spectroscopy

Having found mathematical expressions for the output modulated by an interferometer, the interferometric techniques utilized throughout this dissertation can be discussed. First, in this section Fourier Transform Spectroscopy (FTS), an optical technique used in many different fields, which utilizes the interference of light instead of dispersion optics to measure spectra, is discussed. Typicall,y in FTS the entire spectrum is passed through an interferometer and the intensities are modulated by changing the path-length difference of the interferometer. In the previous section, we have worked through the mathematical derivation of how a known spectrum affects the output intensity for a given path-length difference. These equations (Equation 3.69) can thus be used inversely to obtain the full spectrum, when the modulated intensities are measured with known path-length differences. These modulated intensities are known as the interferogram and FTS captures them to perform the inverse Fourier transforms to obtain the full spectrum. The advantages of FTS are that it can measure broad spectral ranges with fast measurement time and high signal-to-noise (S/N).

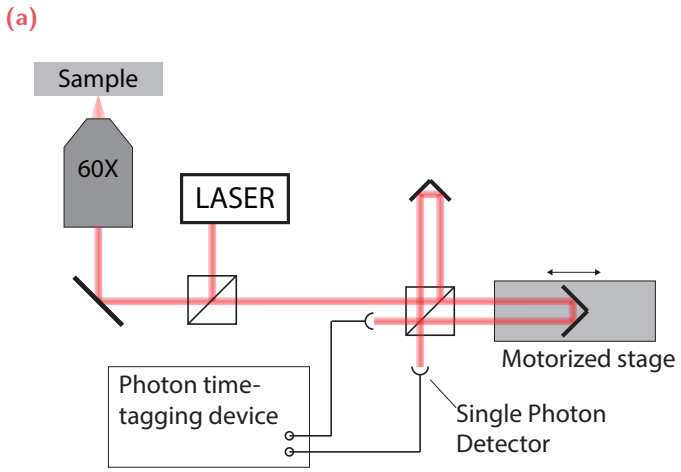

Fig. 3.7.: Schematic representation of a Fourier Spectroscopy Setup. Light is captured through an object and then redirected into an interferometer with one moveable arm. After the light recombines at the beamsplitter, it is sent to two Single Photon Detectors, that record all the arrival times of the photons.

In our setup, illustrated in Figure 3.7, we modulate the intensities by enlarging or decreasing the distance to one of the retroreflectors with a motorized stage. This stage sweeps in a continuous linear movement, during which photons are counted in the two output paths of the interferometer. Note, that we use photon counting detectors oppose to intensity detectors, and that we obtain two outputs. Both are

atypical in FTS experiments. After the experiment, in post-process, small time-bins are defined to represent one single path-length difference. With small enough bins, the path-length difference can be assumed constant. Photon arrival times are then sorted into these bins and the number of photons per bin is counted.

Intensity Correction in 2 Detector FTS

In our setup, the light beams are split into two physically different paths, allowing for the detection of the two outputs of the interferometer. Typically, FTS utilized only one output and one detector. Therefore, I have shown the complete derivation of both detector intensities of a dual-path interferometer in the previous section, obtaining Equation 3.69. We found that the intensities are modulated based on the spectrum and the path-length difference. Additionally, whenever one detector intensity would increase, the other detector intensity would decrease because of conservation of energy. Thus, the following expressions are obtained:

$$I_{\mathrm{a}}(t) = \frac{1}{2} I_0(t) \left[1 + \mathfrak{Re}\left\{\mathcal{F}\left[s\left(\widetilde{\nu}, t\right)\right]\right\}\right] \tag{3.69a}$$

$$I_{\mathrm{b}}(t) = \frac{1}{2} I_0(t) \left[1 - \mathfrak{Re}\left\{\mathcal{F}\left[s\left(\widetilde{\nu}, t\right)\right]\right\}\right] . \tag{3.69b}$$

In Equation 3.69, $Re\left\{FT\left[s\left(\widetilde{\nu}, t\right)\right]\right\}$ is the mathematical representation of the interferogram, and $\frac{1}{2} I_0(t)$ is a time-dependent prefactor. In most FTS applications, the total intensity does not change over time, such that $I_0(t) = I_0$. However, this is not always true. Especially, the signals shown in this work are characterized by fast fluctuations. Thanks to our dual detector setup, we are able to correct for intensity fluctuations by calculating the ratio of the difference over the sum of the individual signals.

$$I_{\mathrm{a}}(t) + I_{\mathrm{b}}(t) = I_0(t) \tag{3.70a}$$

$$I_{\mathrm{a}}(t) - I_{\mathrm{b}}(t) = I_0(t) \cdot \mathfrak{Re}\left\{\mathcal{F}\left[s\left(\widetilde{\nu}, t\right)\right]\right\} \tag{3.70b}$$

$$\frac{I_{\mathrm{b}}(t) - I_{\mathrm{b}}}{I_{\mathrm{a}}(t) + I_{\mathrm{b}}(t)} = \mathfrak{Re}\left\{\mathcal{F}\left[s\left(\widetilde{\nu}, t\right)\right]\right\} \tag{3.70c}$$

3.2.1 Chromatic Aberrations in FTS

In this section, chromatic aberrations in FTS, that we observe experimentally, are discussed. Localized Surface Plasmon Resonances (LSPR) rely on a driving light to establish them, therefore we thought of using a broad light source, broader than the LSPR. In initial tests with this broad band source, we observed wavelength dependent effects in FTS experiments, shown in Figure 3.8. Interferograms obtained through reflection off of a mirror going into the interferometer from a NKT supercontinuum white light laser (Fianium 15) with a Laser Line Tunable Filter (LLTF) contrast filterbox are shown in Figure 3.8a for several different wavelengths. The LLTF turns the supercontinuum spectrum into spectra of $1\,\mathrm{nm}$ with variable center wavelengths. It uses volume Bragg gratings to disperse the light, and the rotation of the grating determines the center wavelength. From these data the envelope functions are used to obtain the maximum position, also known as the white fringe position, through Gaussian fitting (Figure 3.8b). By tracking the white fringe position as a function of wavelength, we measure a white fringe shift of $23.2\,\mu\mathrm{m\,eV}^{-1}$, see Figure 3.8c. We hypothesize that this effect most likely comes from the optical components that are used to construct the interferometer. However, exchange of the beamsplitter cube for different components, such as a plate beamsplitter or pellicle, only resulted in less stability without mitigating the effect. The retroreflectors have not been replaced, since they are hollow and should thus have less effect. Additionally, there are not many other optics available that can replace the retroreflectors without compromise. In FTS literature, one can find mention of phase-effects causing aberrations in FTS measurements and several methods are proposed to treat the effect.[85, 86]

From these findings we must conclude that experimentally there is not a constant white fringe positions. Therefore, we will introduce a wavelength-dependent phase term into the original equations (Equation 3.59) to describe this effect mathematically. From the derivation, we find a simple trick that can be used to correct for chromatic aberrations in post-process. Let us introduce a wavelength-dependent zero position as: $\delta = \widetilde{\delta} + \delta_0\left(\widetilde{\nu}\right)$. Let us first consider the Fourier Transform of a spectrum with only one photon:

$$\mathcal{F}\left\{\sigma\left(\widetilde{\nu}\right)\right\} = \int \sigma\left(\widetilde{\nu}\right) \cdot \cos\left(2\pi\widetilde{\nu}\left(\widetilde{\delta} + \delta_0\left(\widetilde{\nu}\right)\right)\right) d\widetilde{\nu} \tag{3.71a}$$

$$= \cos\left(2\pi\widetilde{\nu_0}\left(\widetilde{\delta} + \delta_0\left(\widetilde{\nu_0}\right)\right)\right) \tag{3.71b}$$

$$= \cos\left(2\pi\widetilde{\nu_0}\widetilde{\delta} + \phi\right), \tag{3.71c}$$

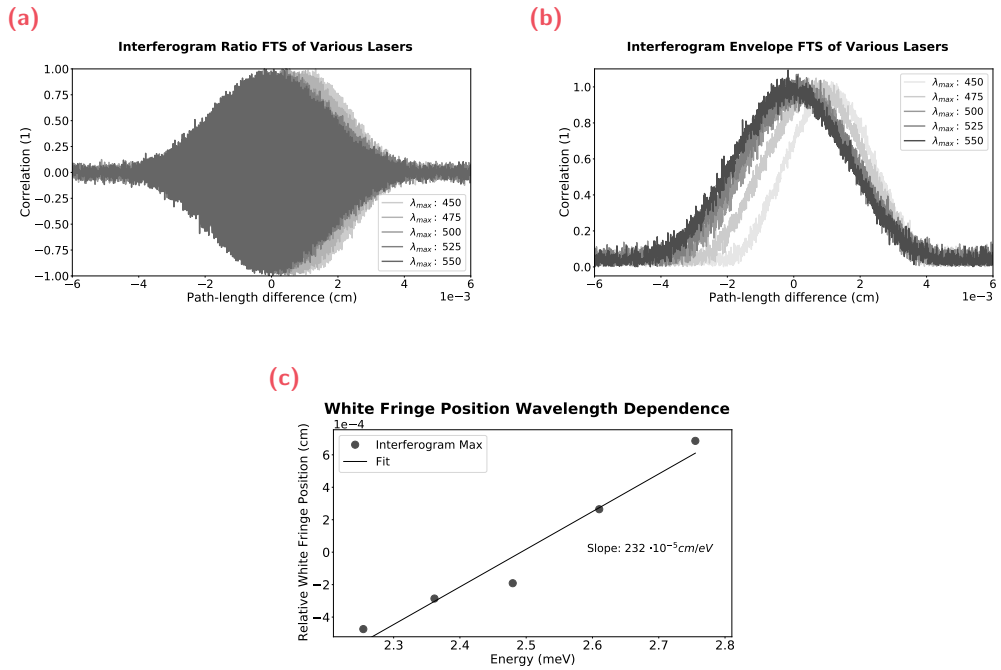

Fig. 3.8.: Experimental observation of chromatic aberrations in Fourier Transform Spectroscopy with *(a)* shifting maxima in the interferograms as a function of spectral peak, *(b)* the envelope functions of the interferograms from *(a)*, and *(c)* the shift plotted as a function of wavelength.

where the wavelength dependent offset is turned into a wavelength dependent phase shift, ϕ. Typically, a FTS user is not interested directly in the interferogram, but rather in the spectrum. This is obtained through Fourier transformation. To obtain the spectrum of the cosine spectrum, we consider Euler's identity, $\cos(\theta) = \frac{e^{i\theta}+e^{-i\theta}}{2}$, and compute the full (complex) Fourier Transform as:

$$\mathcal{F}\left\{\cos\left(2\pi\widetilde{\nu_0}\widetilde{\delta}+\phi\right)\right\} = \frac{1}{2}\mathcal{F}\left\{e^{i\left(2\pi\widetilde{\nu_0}\widetilde{\delta}+\phi\right)}\right\} + \frac{1}{2}\mathcal{F}\left\{e^{-i\left(2\pi\widetilde{\nu_0}\widetilde{\delta}+\phi\right)}\right\} \tag{3.72a}$$

$$= \frac{e^{i2\pi\widetilde{\nu_0}\phi}}{2}\mathcal{F}\left\{e^{i2\pi\widetilde{\nu_0}\widetilde{\delta}}\right\} + \frac{e^{-i2\pi\widetilde{\nu_0}\phi}}{2}\mathcal{F}\left\{e^{-i2\pi\widetilde{\nu_0}\widetilde{\delta}}\right\} \tag{3.72b}$$

$$= \pi\left(e^{i2\pi\widetilde{\nu_0}\phi}\Delta\left(\widetilde{\nu}-\widetilde{\nu_0}\right) + e^{-i2\pi\widetilde{\nu_0}\phi}\Delta\left(\widetilde{\nu}+\widetilde{\nu_0}\right)\right) \tag{3.72c}$$

where $\Delta\left(\widetilde{\nu}\right)$ is the Dirac Delta function. We quickly simplify the equation by dropping the delta function that peaks at negative wavenumbers, since this does not have any physical significance, such that:

$$\mathcal{F}\left\{\cos\left(2\pi\widetilde{\nu_0}\widetilde{\delta}+\phi\right)\right\}=\pi e^{i2\pi\widetilde{\nu_0}\phi}\Delta\left(\widetilde{\nu}-\widetilde{\nu_0}\right)\,. \tag{3.73}$$

Now, we use Euler's identity again to turn the imaginary exponent back into a real and an imaginary part. The next key realization is that for FTS spectra, one is interested in the absolute value of the Fourier Transform (sometimes also called the magnitude spectrum), since negative spectra do not carry physically meaning. The absolute value of imaginary numbers is computed as $|z|=|a+i\cdot b|=\sqrt{a^2+b^2}$. Hereafter, the Pythagorean identity $\sin^2\left(\theta\right)+\cos^2\left(\theta\right)=1$ is used to simplify the prefactor of the delta function and observe that the phase-dependent factor drops from the equation. Thus, we observe that (absolute) Fourier Transforms in FTS (interferometry in general) remove phase information. This is perhaps an undeliberate correction of chromatic aberrations in FTS, such that chromatic aberrated interferograms can be transformed into non-chromatic aberrated spectra as:

$$\begin{aligned}
|\mathcal{F}\left\{\cos\left(2\pi\widetilde{\nu_0}\widetilde{\delta}+\phi\right)\right\}| &= |\pi\left(\cos\left(2\pi\widetilde{\nu_0}\phi\right)+i\cdot\sin\left(2\pi\widetilde{\nu_0}\phi\right)\right)\delta\left(\widetilde{\nu}-\widetilde{\nu_0}\right)| && \text{(3.74a)}\\
&= \pi\cdot\delta\left(\widetilde{\nu}-\widetilde{\nu_0}\right)\sqrt{\left(\cos^2\left(2\pi\widetilde{\nu_0}\phi\right)+\sin^2\left(2\pi\widetilde{\nu_0}\phi\right)\right)} && \text{(3.74b)}\\
&= \pi\cdot\delta\left(\widetilde{\nu}-\widetilde{\nu_0}\right)\,. && \text{(3.74c)}
\end{aligned}$$

Chromatic Aberrations cause Asymmetry

In other FTS experiments, we observed asymmetric interferograms. Here, we observed that when spectra are sufficiently narrow ($<30\,\mathrm{nm}$ or $<100\,\mathrm{meV}$) this effect is basically non-observable. However, for broader spectra, this becomes very clear, and we hypothesize that it also comes from chromatic aberrations. Prior Photon Correlation Fourier-Spectroscopy literature has never mentioned observations of asymmetric interferograms, since their spectra were sufficiently small. FTS literature does mention asymmetric interferograms and phase-correction thereof, typically by measuring a narrow and stable signal.[87, 88, 85, 86] Having identified a relationship between white fringe position and center wavelength, together with a

mathematical incorporation in the interferometer intensity output equations, asymmetric interferograms can now be corrected. Figure 3.9 shows, two experimentally measured FTS interferograms with spectra of $50\,\mathrm{nm}$ linewidth (Figure 3.9a) and of $100\,\mathrm{nm}$ linewidth (Figure 3.9b). These spectra have been measured from reflections off of a mirror going into the interferometer. The super continuum white light laser from NKT was utilized together with the VARIA filterbox to produce spectra with variable linewidths at $500\,\mathrm{nm}$ center wavelength. Next, we used Monte-Carlo simulations with the spectrum as input to determine theoretical (symmetric) interferograms (Figure 3.9c and Figure 3.9d). With a phase offset based on Equation 3.71 implemented into our Monte-Carlo simulation, we obtain asymmetric interferograms that qualitatively are a like the experimentally measured ones (Figure 3.9e and Figure 3.9f). Next, we perform double (absolute) Fourier Transformations on the asymmetric interferograms to remove the phase shift induced by chromatic aberrations. This simply turns the interferogram into the spectrum with its phase information removed (Equation 3.74), which then is turned back into a symmetric interferogram. The resulting interferograms match nicely with the non-chromatic aberrated FTS interferograms (Figure 3.9g and Figure 3.9h), having low residual noise. Therefore, we called it the double (absolute) Fourier Transformation. We thus, have shown that with a simple mathematical trick, asymmetry can be removed from FTS experiments.

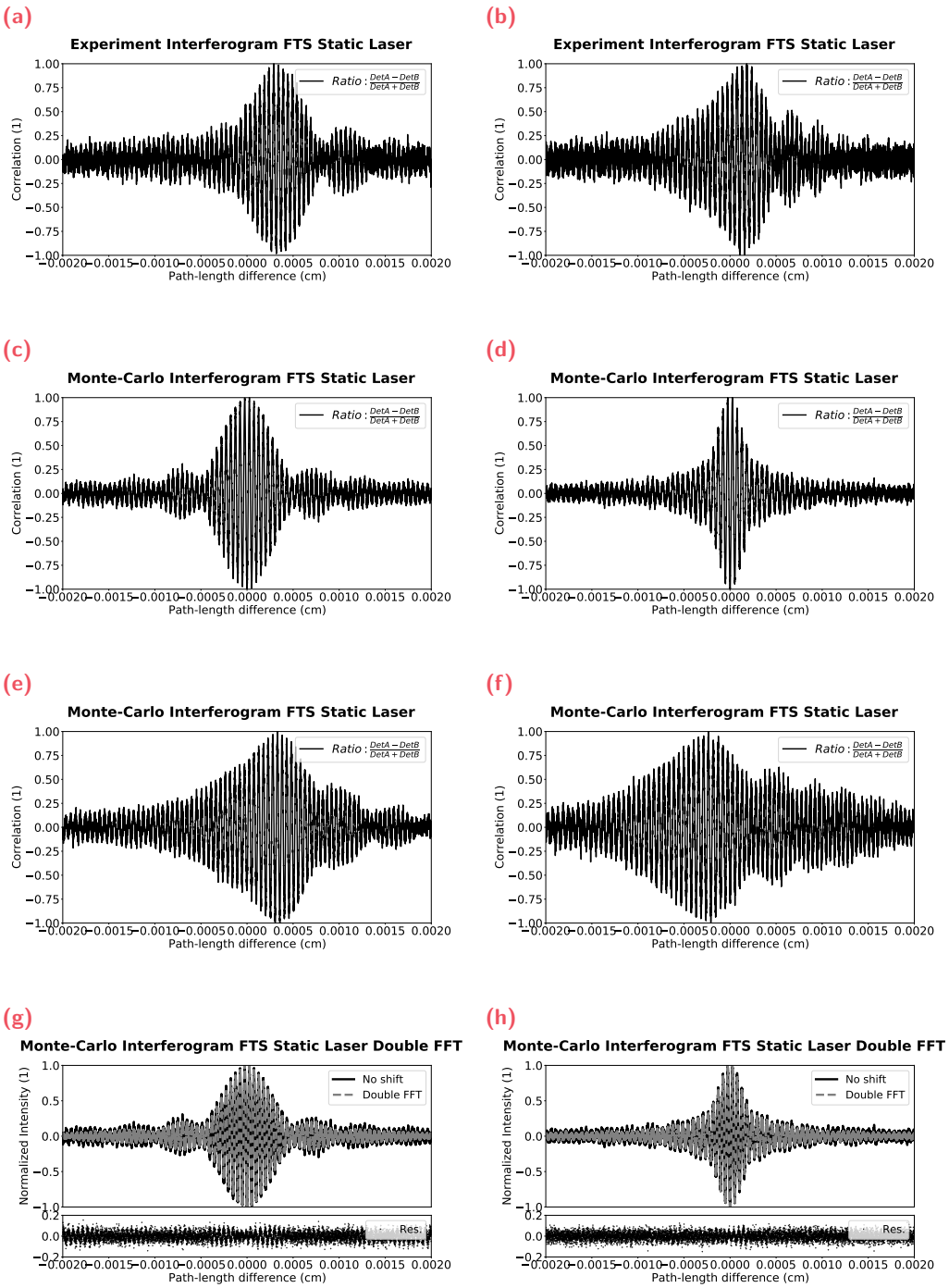

Fig. 3.9.: Double Fourier transform trick to obtain symmetric interferograms . In *(a)* and *(b)* experimentally measured interferogram of a spectrum with 50nm and 100nm width, respectively. In *(c)* and *(d)* Monte-Carlo simulation of interferogram of a spectrum with 50nm and 100nm width, respectively. In *(e)* and *(f)* Monte-Carlo simulation of interferogram **with chromatic phase offset** of a spectrum with 50nm and 100nm width, respectively. In *(g)* and *(h)* comparisons between double Fourier transformed *(e)* & *(f)* and non-chromatic aberrated interferograms *(c)* & *(d)*, respectively.

3.3 Fluorescence Correlation Spectroscopy

Before, the second interferometric technique utilized throughout this dissertation can be discussed, a small detour must be made to discuss Fluorescence Correlations Spectroscopy (FCS), a technique that analyzes the diffusion of fluorophores in solution. Namely, understanding of this technique is helpful for understanding a later part in this dissertation. FCS was introduced to study the fluctuations of freely diffusing molecules in solution.[89, 90, 91] Intensity signals are obtained from fluorophores diffusing through a small focal volume, however these signals are rather difficult to interpret directly. Therefore, FCS signals are typically analyzed by calculating intensity correlation curves. These give statistical insights into diffusion events, like rotational or translational diffusion, but also triplet state kinetics. FCS took really off in the 1990s, due to improvements in the equipment and the use of confocal setups that reduce the effective volume from which light is captured from (focal volume).[92, 93] In Figure 3.10, a schematic of a typical FCS setup is shown, where small fluorescent molecules freely diffuse in a liquid. A high Numerical Objective (NA) objective is used to focus laser light into the liquid. The molecules absorb and emit fluorescent light whenever they pass through the focused laser light. The resulting burst of light is captured and directed to a detector, where the laser light is first filtered out to obtain pure fluorescence intensity signals. These intensity fluctuations, statistically analyzed, can give insights into the working of systems in their native environment.

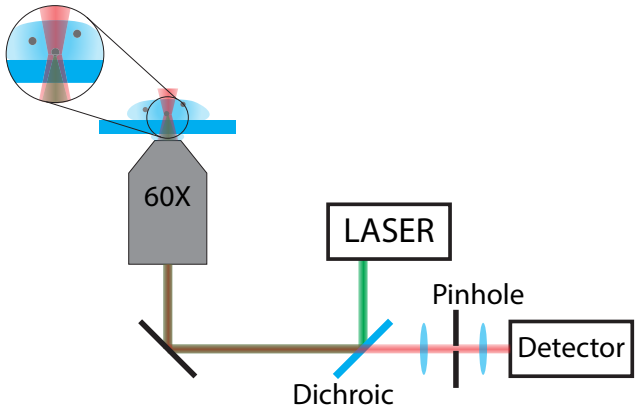

Fig. 3.10.: A confocal Fluorescence Correlation Spectroscopy setup to capture intensity fluctuations from fluorophores freely diffusing in a liquid.

For our application of kinetic interaction sensing of biomolecules with plasmonic nanoparticles, we are interested in measuring signals in solution, similar to FCS, to eliminate unwanted effects from the substrate. In that case, we can probe the

protein interactions as natively as possible. Therefore, we will use the confocal part of the FCS setup as part of the optical device developed in this dissertation. Only, we need to alter the detection scheme a little to get greater spectral sensitivity than FCS, see section 3.4 later.

Figure 3.11 shows theoretical intensity time traces as would be obtained in an FCS experiment. In Figure 3.11a, small fluctuations from the mean value are observed, which seem to occur randomly. However, there are still typical times, τ, associated with the fluctuations, since they come from molecules passing through the focus of the laser. The slower the molecules diffuse, the longer the fluctuation would be stretched. Additionally, the height of the fluctuation compared to the mean is an indication for the amount of molecules in the laser focus.

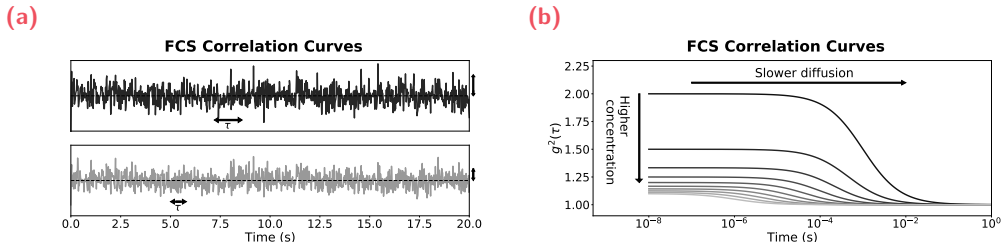

Fig. 3.11.: Typical Fluorescence Correlation Spectroscopy data with **(a)** the time traces on the detector and **(b)** the correlations functions of those time traces with indicators how diffusion constants and fluorophore concentrations affect the curves.

In Figure 3.11b, theoretical auto-correlation curves from different intensity traces are shown. Here, the slower diffusing fluorophores staying longer in the focal volume that cause stretched fluctuation become visible. Namely, the auto-correlations are stretched to longer time-separations accordingly. Additionally, higher concentrations of fluorophores lead to more fluorophores being present in the focal volume at the same time, causing fewer fluctuations. This reduces the height of the auto-correlation curves, and therefore becomes a direct indication of the number concentration of fluorophores in the solution. In this example, the top of Figure 3.11a would correspond to the slowest auto-correlation curve in Figure 3.11b, whereas the bottom time trace would correspond to the auto-correlation curve with the fastest diffusion. These auto-correlation functions are computed by comparing the time traces with a displaced version of itself, with displacement factor τ, as:

$$g^{(2)}(\tau) = \frac{\langle I(t)\, I(t+\tau)\rangle}{\langle I(t)\rangle \langle I(t+\tau)\rangle} = \frac{1}{\langle I(t)\rangle^2} \int_{-\infty}^{\infty} I(t)\, I(t-\tau)\, dt\,. \tag{3.75}$$

Elson and Magde present a full derivation of the auto-correlation for isotropic three-dimensional diffusion through a Gaussian laser focus.[90, 89] I will not repeat the derivation here, since it is lengthy. However, I do want to touch on their method in the calculation. Namely, they describe the detected photons at a certain time, $n(t)$, to consist of some mean average $\langle n \rangle$ and some fluctuations $\delta n(t)$, such that $n(t) = \langle n \rangle + \delta n(t)$. The number of photons is directly related to the intensity by: $I(t) = n(t)/\Delta t$, with Δt being a time interval. In Figure 3.11a, this already has been observed, where fluctuation are seen on top of an average stable background signal. This rationalizes their consideration to split the intensity fluctuations into two parts. Interestingly, this split splits the auto-correlation function into two parts as well:

$$g^{(2)}(\tau) = 1 + g^{(2)}_{\text{fluc}}\,. \tag{3.76}$$

Elson and Magde find that a constant background of photons, $\langle n \rangle$, leads to a value of 1 in the auto-correlations, and that the fluctuations, $\delta n(t)$, lead to a measurable signal $g^{(2)}_{\text{fluc}}$. We will come back to this separation, when we discuss the solution Photon-Correlation Fourier Spectroscopy theory, because this insight is important for that derivation as well. In FCS, however, people like to find an expression of $g^{(2)}_{\text{fluc}}$ related to the fluorophore properties to extract information from the system. The focal volume of the laser is actually ellipsoidal gaussian, where the long axis (from objective into the sample) is much longer than the two short axes.[89] In that case a simple approximation can be made, where the z-axis is ignored:

$$g^{(2)}(\tau) = 1 + \frac{1}{< N >}\frac{1}{1+\tau/\tau_{\text{D}}}, \tag{3.77}$$

with $< N >$ being the average occupation number in the focal volume and τ_{D} is the average dwell time through the laser focal volume. This is a 2-dimensional diffusion auto-correlation fitting function for FCS. For Fickian diffusion the mean-square displacement scales linearly with time, and the displacement observed is from one side of the focal volume to the other side. With diffraction-limited optics the focal width is described as $\omega_{\text{xy}} = 2r_{\text{xy}} = \frac{1.22\lambda}{NA}$, with NA being the numerical aperture. This way, τ-values, extracted from FCS experiments, can be directely related to the diffusion coefficients as:[3]

$$\omega^2_{xy} = 4D\tau_D\,. \tag{3.78}$$

The diffusion coefficient can be related to the Stokes-Einstein relation to find other parameters of the system such as temperature or fluorophore size;

[3]The prefactor 4 in Equation 3.78 is due to 2D diffusion.

$$D = \frac{k_{\mathrm{b}} T}{6\pi\eta r}\,, \tag{3.79}$$

with k_{b} the Boltzmann constant, T the temperature, η the viscosity of the liquid, and r the radius of the molecule. Therefore, FCS is a powerful analysis technique for in-solution characterization. Additionally, the fluorophores are not chosen, but rather "show up" in the measurement, such that there is no user-selection bias. We aim to utilize these benefits from FCS to study light coming from nanosensors diffusing freely in solution. In this section, the reader may have observed the words "fluorophore", "molecule", and "fluorescence" a lot, which are not mentioned as much in other parts. This is the terminology used in FCS, however the methodology is not just confined to fluorescence. Any fluctuating light, coming from particles diffusion through a small focal volume can be analyzed with FCS.

Discrete Correlations

Early FCS theory is developed for continuous signals. However, we use Single Photon Detectors (SPD), which output photon numbers and arrival times instead of intensities. These detectors combined with a time-tagging device record the occurrences of photons with very high timing-precision ($\sim \mathrm{ps}$). Photon arrival times indicate when a photon was detected, and the number count for that specific time point goes up one. With linear time-bins and counting the number of photons per bin, we would obtain intensity traces similar to the continuous signals from before. The problem with this method is that one cannot find correlation events faster than the width of the bin, even though they might be present. One could be tempted to make the bin sizes smaller, but at some point the signal is lost with only one or zero photons per bin. Thus, the data has to be analyzed differently to access faster time-scales. Since photon numbers are directly related to intensity, the easiest method is to compute all the time-separations between all possible photon pairs and then sort those into time-separation (τ) bins. This intrinsically is the counting version of the auto-correlation. To do this for traces with high photon counts is computationally expensive. Therefore, multi-tau algorithms were invented that only compute a few time lags at full-resolutions, and then keep dividing the amount of computations in half over and over to minimize computation with very little resolution loss. In this work Laurence's algorithm is used, which is an optimized counting a search algorithm for the computation of correlation functions.[94] Regardless, all these methods rely on counting the photon pairs such that:

$$g^{(2)}(\tau) = \frac{\langle I(t)\, I(t+\tau)\rangle}{\langle I(t)\rangle \langle I(t+\tau)\rangle} = \frac{n\left(\{(i,j) \ni t_{\mathrm{i}} = u_j - \tau\}\right)(T-\tau)}{n\left(\{i \ni t_{\mathrm{i}} \leq T-\tau\}\right) n\left(\{j \ni u_{\mathrm{ji}} \geq \tau\}\right)} \tag{3.80}$$

where, T is the total measurement time, $n\left(\{i \ni t_i = t\}\right)$ is the number counting operator on all photons i and j that have arrival time t_{i} equal to t. Whenever this counting operation is performed on all t_{i} within a small range of Δt, we obtain the intensity $I_{1,2}(t)$.

3.4 Photon-Correlation Fourier Spectroscopy

Having discussed FCS, the second interferometric spectroscopy method used throughout this dissertation can be introduced: Photon-Correlation Fourier Spectroscopy (PCFS). PCFS is an interferometric technique that, similarly to FCS, analyzes fluctuating signals. FCS looks at intensity space to learn something about the sample, whereas PCFS looks at both intensity and spectral space. The power of PCFS is that spectral fluctuations can be turned into spectral correlations with a temporal range spanning over orders of magnitude, especially with high signal-to-noise (S/N) towards the ns-regime.[95, 96, 97] Typical intensity-binning methods simply lack the readout speed in this regime, therefore we believe that photon-correlation methods are needed. Foremostly, since we expect fast spectral fluctuations from plasmonic nanoparticles caused by fast biomolecular interaction events in their proximity. Therefore, we view the use of PCFS' power to analyze the spectral space as a valid path forward. Here, we discuss two implementations of PCFS; single-emitter PCFS that analyzes spectral fluctuations in general, and solution-PCFS that analyzes decouples spectral fluctuations of a diffusing single emitters from its ensemble. The latter is based on combing FCS together with regular PCFS, therefore we needed the detour about FCS theory first.

3.4.1 PCFS Equations

First, the governing equations of PCFS are introduced. In Figure 3.12, a schematic of a PCFS setup is shown. The reader might find the setup very similar to the FTS setup shown in Figure 3.7, only with an additional pinhole installed this time. Both setups actually are similar, since the difference lies in the way the interferometer moves and how signals are analyzed. In FTS the interferometer arm is extended or retracted with a continuous linear movement. In PCFS however, there is a stepwise movement

through the interferogram, and at every step the stage is slowly oscillating back and forth. This oscillation needs to be larger then a few interference fringes to be able to measure the envelope of the (FTS) interferogram. This envelope is known as the PCFS interferogram.

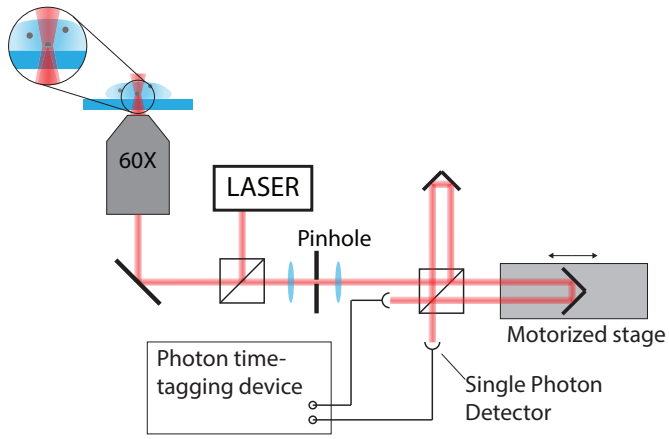

Fig. 3.12.: Schematic representation of a Photon-Correlation Fourier Spectroscopy Setup. Light is captured through an object and then redirected into an interferometer with one moveable arm. After the light recombines at the beamsplitter, it is sent to two Single Photon Detectors, that record all the arrival times of the photons.

For the derivation of PCFS, the cross-correlation of the intensity signals on the two detectors, being passed through the interferometer, is of interest;

$$g^{\times}(\delta,\tau)=\frac{\langle I_{\mathrm{a}}(t)\rangle\langle I_{\mathrm{b}}(t-\tau)\rangle}{\langle I_{\mathrm{a}}(t)\,I_{\mathrm{b}}(t-\tau)\rangle}\,. \tag{3.81}$$

From Equation 3.69 a relationship between the spectrum and the intensities on either detector has been found, which were:

$$I_{\mathrm{a}}(t)=\frac{1}{2}I_0(t)\left(1+\mathfrak{Re}\left\{\mathcal{F}\left[s(\tilde{\nu},t)\right]\right\}\right) \tag{3.82}$$

$$I_{\mathrm{b}}(t)=\frac{1}{2}I_0(t)\left(1-\mathfrak{Re}\left\{\mathcal{F}\left[s(\tilde{\nu},t)\right]\right\}\right)\,. \tag{3.83}$$

Let us plug in these definitions for the intensities on both detectors and expand the denominator first. Additionally, we take advantage of the fact that averages are distributive. To continue the derivation, we would need to implement a mathematical description for our oscillating movement, also called "dither". Dr. Andrew Beyler has a very in-depth explanation in his dissertation about the effect of the dither on the

final PCFS Equation.[97] However, I would like to focus on the most simple case, a triangular dither, since this is the dither that we implemented experimentally. This allows us to simplify the equation, by noting that the dither is symmetric and runs over a few interference fringes ($A_{dither} \gg 1/\nu_0$), causing any time-average over the Fourier transform of the spectrum to go to zero, such that:

$$g^{\times}(\delta,\tau) = \frac{\langle I_1(t)\, I_2(t+\tau)\rangle}{\langle I_1(t)\rangle \langle I_2(t+\tau)\rangle} \tag{3.84}$$

$$= \frac{\langle I_1(t)\, I_2(t+\tau)\rangle}{\langle I_0(t)\,(1+\mathfrak{Re}\{\mathcal{F}[s(\widetilde{\nu},t)]\})\rangle \langle I_0(t+\tau)\,(1-\mathfrak{Re}\{\mathcal{F}[s(\widetilde{\nu},t+\tau)]\})\rangle} \tag{3.85}$$

$$= \frac{\langle I_1(t)\, I_2(t+\tau)\rangle}{\langle I_0(t)\rangle \langle I_0(t+\tau)\rangle}\,. \tag{3.86}$$

Now, the numerator can be expanded, where the intensity averages are decoupled from spectral-time averages, because we assume that spectral fluctuations are not correlated with intensity fluctuations;

$$g^{\times}(\delta,\tau) = \frac{\langle I_0(t)\, I_0(t+\tau)\,(1+\mathfrak{Re}\{\mathcal{F}[s(\widetilde{\nu},t)]\})\,(1-\mathfrak{Re}\{\mathcal{F}[s(\widetilde{\nu},t+\tau)]\})\rangle}{\langle I_0(t)\rangle \langle I_0(t+\tau)\rangle} \tag{3.87}$$

$$= \frac{\langle I_0(t)\, I_0(t+\tau)\rangle}{\langle I_0(t)\rangle \langle I_0(t+\tau)\rangle} \langle 1+\mathfrak{Re}\{\mathcal{F}[s(\widetilde{\nu},t)]\} - \mathfrak{Re}\{\mathcal{F}[s(\widetilde{\nu},t+\tau)]\} - \mathfrak{Re}\{\mathcal{F}[s(\widetilde{\nu},t)]\}\cdot\mathfrak{Re}\{\mathcal{F}[s(\widetilde{\nu},t+\tau)]\}\rangle \tag{3.88}$$

$$= \frac{\langle I_0(t)\, I_0(t+\tau)\rangle}{\langle I_0(t)\rangle \langle I_0(t+\tau)\rangle} (1 - \langle \mathfrak{Re}\{\mathcal{F}[s(\widetilde{\nu},t)]\}\cdot\mathfrak{Re}\{\mathcal{F}[s(\widetilde{\nu},t+\tau)]\}\rangle) \tag{3.89}$$

$$= g^{(2)}(\tau)\,(1 - \langle \mathfrak{Re}\{\mathcal{F}[s(\widetilde{\nu},t)]\}\cdot\mathfrak{Re}\{\mathcal{F}[s(\widetilde{\nu},t+\tau)]\}\rangle)\,. \tag{3.90}$$

Now, the convolution theorem is used to derive the PCFS equation. Note that Dr. Andrew Beyler talks about the mis-use of the convolution theorem here, because the Fourier Transforms might not be evaluated at the same path-length difference. Additionally, he mentions that the last equation is a convolution of the real part of a Fourier Transform, which makes the math a little more complicated. To his first point, it is correct that the Fourier Transforms are not evaluated at the same $< \delta >$ if you use any arbitrary dither waveform (which he does). However, because of

our choice of a symmetric and periodic waveform, our averaged Fourier Transforms are evaluate at the same averaged interferometer position. As to his second point, expanding the cosine transforms, results in both cosine and sine Fourier Transforms, but the sine transforms vanish again, because of their odd nature and the integration over symmetric dither waveforms. Therefore, we are allowed to use the convolution theorem here given our symmetric dither waveform. Nevertheless, in his derivation a prefactor of $\frac{1}{2}$ comes about, which I simply add to Equation 3.91. This prefactor is a normalization factor that keeps the interferograms between -1 and 1, which otherwise would be incorporated into the definition of $s\left(\widetilde{\nu},t\right)$. Since, we typically normalize our interferograms and spectral correlation, this prefactor carries less meaning anyways. I would direct any reader to the dissertation of Dr. Andrew Beyler for more insights in the derivation of the PCFS equations, because he keeps many assumptions open for arbitrary shape or function.[97] Finally, the cross-correlation is given by:

$$g^{\times}\left(\delta,t\right)=g^{(2)}\left(\tau\right)\left(1-\frac{1}{2}\mathfrak{Re}\left\{\mathcal{F}\left[p\left(\zeta,\tau\right)\right]\right\}\right), \tag{3.91}$$

where, we have introduced the spectral correlation, $p\left(\zeta,\tau\right)$ with ζ the energy separation and τ the time-separation. From this equation one can see that PCFS analyzes both the intensity **and** spectral fluctuations to obtain spectral correlations. The spectral correlation is defined as a correlation of the spectrum over energy and time:

$$p\left(\zeta,\tau\right)\equiv\left\langle\int s\left(\widetilde{\nu},t\right)s\left(\widetilde{\nu}+\zeta,t+\tau\right)d\widetilde{\nu}\right\rangle, \tag{3.92}$$

where, τ is the time separation and ζ is the energy separation. The spectral correlation oppose to the spectrum is a useful measure, because of its temporal resolution. Typical integrative method would not be able to reslove fast enough spectral fluctuations, simply due to the lack of information (number of photons). With PCFS, through statistical means, spectral fluctuations in the sub-millisecond time regime can be analyzed. Similar to how intensity fluctuations in the sub-millisecond time regime could be analyzed with FCS. Therefore, PCFS is a very powerful technique to analyze fast and small spectral fluctuations, when other techniques lack the resolution.

3.4.2 Solution Photon-Correlation Fourier Spectroscopy

In this section, the derivation of the solution-PCFS (sPCFS) equations, which were first explained by Marshall et al., are discussed.[98] Solution-PCFS is a version of the interferometric technique PCFS, that analyzes spectral fluctuations of freely diffusing particles in solution. Here, the contributions of the averge single photon are decoupled from the background ensemble. The setup and analysis are similar to PCFS. Only now, the mathematical formulas have to be rewritten to include the categorization of photons pairs in the correlation curves.

Recall the splitting of the auto-correlation curves by Elson and Magde in equation 3.76. Visually this is shown in Figure 3.13, where a typical FCS auto-correlation curve can be split into 2 categories: photon pairs coming from the ensemble and photon pair coming from the average single particle. From Elson and Magde we have seen that the average photon numbers, $\langle n \rangle$, and the fluctuation thereof, $\delta n\,(t)$ gave rise to a constant background signal 1 and a time dependent decay, $g^{(2)}\,(t)$, respectively. In solution-PCFS, we will make the same split. Only now, the spectral component of these two categories is considered as well. Steady background light will come from multiple particles (ensemble) in the background of the focal volume, whereas the short fluctuations come from single particles (average single) diffusing through the focal volume. Statistical reasoning also teaches us that, it is unlikely that photon pairs with long time-separation (τ) would come from the same particle, therefore the opposite must be true, such that they come from different particles (ensemble). Following that same reasoning, is must thus be true that photon pairs with short time-separation are more likely to come from the same particle.

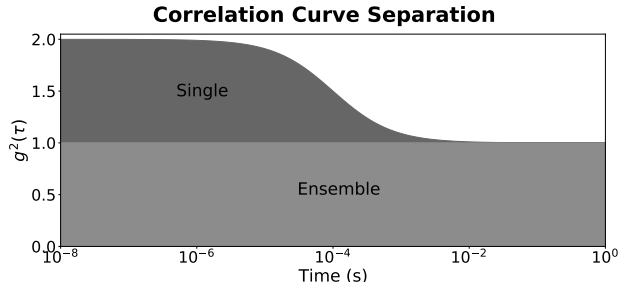

Fig. 3.13.: A auto-correlation curve from Fluorescence Correlation Spectroscopy, with separation of photon pairs coming from the ensemble and from the average single particle.

$$g^{(2)}\,(\tau) = 1 \qquad + g^{(2)}_{\text{fluc}}\,(\tau) \tag{3.93}$$

$$g^{\times}\,(\delta, \tau) = g^{\text{ens}}\,(\delta, \tau) + g^{\text{single}}\,(\delta, \tau) \tag{3.94}$$

In Equation 3.93, a split auto-correlation for FCS is shown and the same logic is apply to the cross-correlation in sPCFS. Next, the PCFS equation is filled in for every individual category, following Equation 3.91, with $g^{(2)}$ equal to the split value from the auto-correlation. Lastly, all of this is combined with the use of the additive nature of the Fourier Transform to obtain the solution-PCFS equation as:

$$g^{\text{ens}}(\delta,\tau) = 1 \cdot \left(1 - \frac{1}{2}\mathfrak{Re}\left\{\mathcal{F}\left[p_{\text{ens}}(\zeta,\tau)\right]\right\}\right) \tag{3.95}$$

$$g^{\text{single}}(\delta,\tau) = g^{(2)}_{\text{fluc}}(\tau) \cdot \left(1 - \frac{1}{2}\mathfrak{Re}\left\{\mathcal{F}\left[p_{single}(\zeta)\right]\right\}\right) \tag{3.96}$$

$$g^{\times}(\delta,\tau) = g^{(2)}_{\text{fluc}}(\tau) + 1 - \frac{1}{2}\mathfrak{Re}\left\{\mathcal{F}\left[p_{\text{ens}}(\zeta) + \left(g^{(2)}_{\text{fluc}}(\tau)\right) p_{\text{single}}(\zeta)\right]\right\} \tag{3.97}$$

$$g^{\times}(\delta,\tau) = g^{(2)}(\tau) - \frac{1}{2}\mathfrak{Re}\left\{\mathcal{F}\left[p_{\text{ens}}(\zeta) + \left(g^{(2)}(\tau) - 1\right) p_{\text{single}}(\zeta)\right]\right\}. \tag{3.98}$$

Through the governing sPCFS equation, spectral correlations can be obtained for both the average single nanoparticle and the ensemble. The spectral correlations, similar to derived for single-emitter PCFS, offers insights into spectral dynamics that are faster than measurable with integrative methods. sPCFS has the additional advantage that spectral diffusion of the average single particle is decoupled from ensemble events through diffusion weighting. This way fast and small diffusion events of a single emitter can be statistically isolated, resulting in better signal to noise (S/N) ratios. Typically the ensemble component is measured in the PCFS interferogram at large time-separation, causing $\left(g^{(2)}(\tau) - 1\right) \approx 0$. Then the average single spectral correlation is computed by subtraction of the obtained ensemble component and weighting it with the auto-correlation.

3.5 Computational Feasibility Study

In this section, I lay out a computational model based on Monte-Carlo simulations to study the performance and examine the parameter space of the techniques (FTS and PCFS) from Section 3.2 and Section 3.4. This way, expected outputs from spectrally shifting light can be obtained to check the setup's viability, before building it in real-life to measure spectral shifts from nanosensors, measuring biomolecules. The model is constructed by simulating simple Poissonian light sources, i.e. lasers, from which the photon energies are determined through Monte-Carlo sampling. Time-invariant and time-varying spectra are simulated to find the method's capability of retrieving the input timing information.

3.5.1 Monte-Carlo Sampling for Sparse Interferometry

The model presented in this section is based on the interferometer math derived in Section 3.1.6. Two key points from that section are:

- a spectrum is a distribution of photons with specific energies
- one single photon with specific energy turns into a cosine in interferometer space

We will use these two findings and a mathematical way of describing a single photon as a Dirac delta function to build an inexpensive computational model by using Monte-Carlo sampling, since Monte-Carlo sampling allows us to statistically probe our method, without the need of explicit electromagnetic simulations, i.e. Finite Element Methods, Finite Difference Time Domain, or Ray tracing. These explicit methods are computationally more expensive and typically work with only 1 wavelength. This way expected outputs for both our interferometry methods, FTS and PCFS, can be obtained with the use of a few well-chosen distributed photons. Let me first explain Monte-Carlo sampling before the actual model can be constructed.

Monte-Carlo Sampling

Monte-Carlo methods are based on random sampling to obtain numeric results.[99] In our case, we will make use of random draws from probability density functions (PDF) and their corresponding cumulative density functions (CDF), that represent the chance of that event occurring. In Monte-Carlo approaches, uniformly distributed random numbers are generated, which are used as input in the inverse CDF. The

inverse CDF is a transfer function that translates a value between 0 and 1 back to units of the PDF. This way, any arbitrary probability distribution can be sampled through the means of the inverse CDF. Let us consider an example.

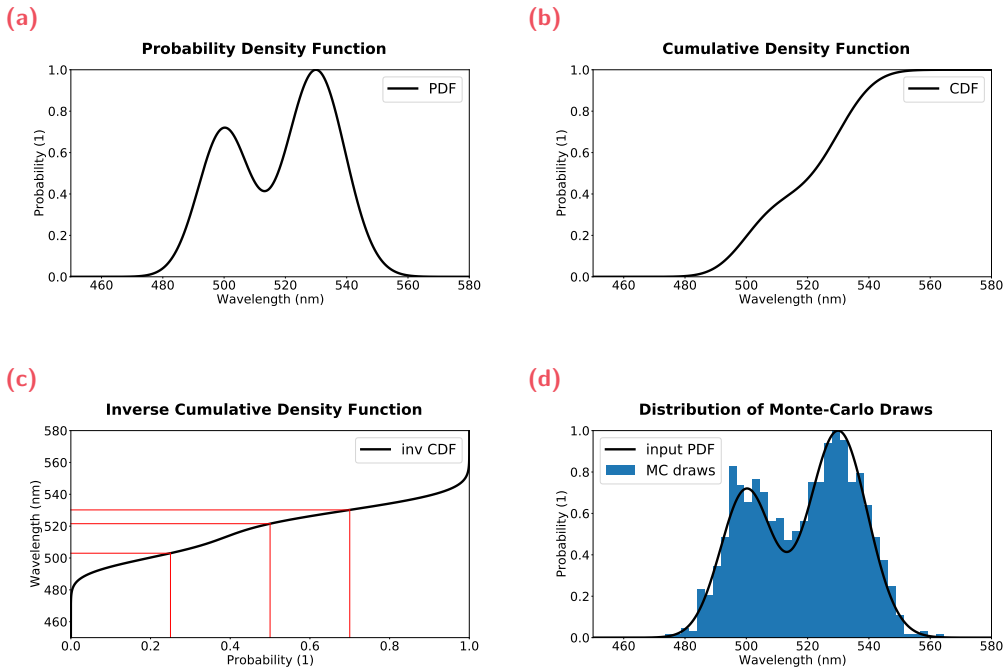

Fig. 3.14.: Example of Monte-Carlo sampling, where *(a)* a Probability Density Function (PDF) is converted to *(b)* a Cumulative Density Function (CDF), and *(c)* the inverse-CDF. Uniformly distributed random samples [0,1] are converted into units of the PDF in *(c)*, resulting in the correct probability distribution *(d)*.

Figure 3.14 shows the process of Monte-Carlo sampling. In Figure 3.14a, a PDF is shown consisting of two Gaussian peaks. Next, the CDF needs to be determined from the PDF. This can be done mathematically for most functions, but for some this cannot be done. Computationally, a CDF is calculated by iteratively summing over all the values in the PDF array and then normalizing it, see Figure 3.14b. Therefore, computationally, any function can be turned into a CDF. Next, the axes of the CDF curve are flipped, to generate a transfer function from between 0 and 1 (x-axis) to units of the PDF (y-axis), see Figure 3.14c. Now, when a uniformly distributed random number generator provides values between 0 and 1, those random numbers can be translated into values from the PDF. As an example, I show 3 numbers between 0 and 1 that turn into values between $450\,\mathrm{nm}$ and $580\,\mathrm{nm}$. Computationally, the CDF is an array and randomly generated numbers most likely fall in between the values of the array. Therefore, linear interpolation is implemented to retrieve continuously distributed values. In Figure 3.14d, this sampling scheme has been

used for 1000 uniformly distributed random numbers to feed them into the inverse CDF to generate a distribution that resembles the input PDF. The benefit is that Monte-Carlo sampling is computationally inexpensive and that outcomes are based on probabilities. The statistical power of the output increases with increasing number of draws.

Monte-Carlo Interferometry model

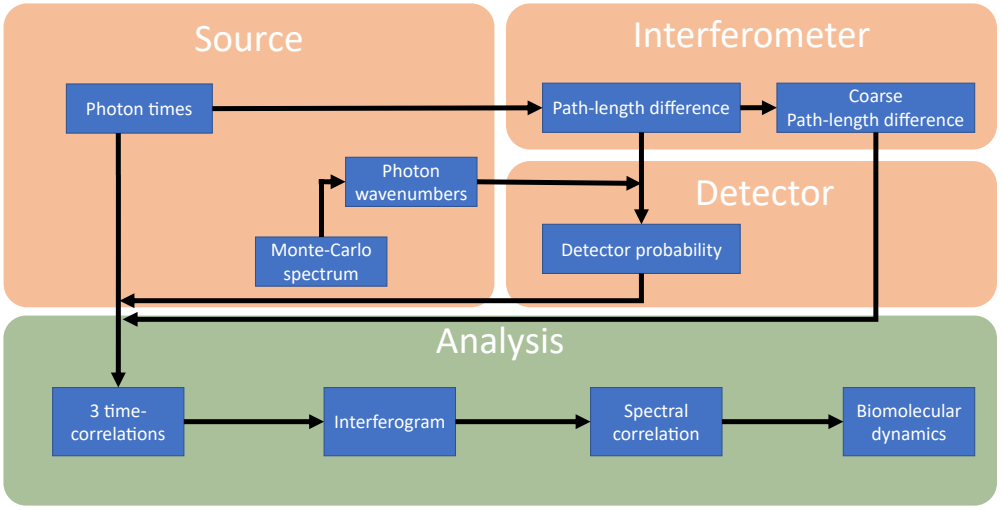

Fig. 3.15.: A flow chart of the computational model based on Monte-Carlo sampling to generate photons with random arrival times and photon energies. Whose characteristics together with computational settings are used to determine probabilities of detection on two detectors. Adapted from Cui et al. 2022.[100]

Now that Monte-Carlo sampling is explained, the computational model can be discussed. Figure 3.15 gives an overview of all the steps taken to compute the detection probabilities from photon characteristics and computational settings. As we move on through this chapter, more and more small parts will be added and explained in this scheme. Nevertheless, the main parts of this computation are a source that generates a stream of photons with energies and arrival times. This is fed into the "computational" interferometer, which generates detector probabilities, based on path-length differences and dither/scanning. Then the probabilities are collapsed into real detection events, which are output by the model together with the arrival times that were given to the photon initially. Finally, this information is passed to the analysis script, which is identical for simulations and experiments, since the outputs are designed to be the same. This computational model allows for the probing of the

interferometric parameter space by statistically choosing only the photons that are of interest, thereby limiting the need for expensive broad wavelength range searches. Let us discuss the source and computational interferometer a bit more in detail.

In the model, photons are characterized by two units: spectral energies and arrival times. These values are randomly assigned through Monte-Carlo sampling, based on the settings of the computation. The two characteristics of the photons are used together with settings of the computation (i.e. PCFS or FTS, interferometer steps, and integration time etc.) to compute detection probabilities. These probabilities are then turned into actual detection events also with the use of MC-sampling. The computational settings are implemented in such a way that they represent experiments knobs. Before detection probabilities can be computed, a couple of intermediate values have to be determined first. The photon arrival times are translated into interferometer positions, because the path-length differences of the interferometer are known from the settings we choose. Next, these interferometer positions, together with the spectral energies, can be used via Equation 3.69 to obtained "collapsed" cosines (in other words a value between 0 and 1) that indicate the probability of detection of a specific photon on either detector 1 or detector 2. Because of conservation of energy, we have seen that when one detector gets all the intensity, the other one gets nothing. Through MC-sampling, the collapsed cosines are translated into actual detection events, where the model returns the photon with its arrival time and the detector it was detected on. The model is constructed this way, because then we obtain the same output as obtained experimentally.

Output Analysis

In this part, the analysis of the photon stream with arrival times and detector occurrences is discussed. Firstly, the analysis depends on what type of simulation/-experiment has been performed. In our case, we distinguish between three different kinds; FTS, PCFS, and sPCFS.

FTS Analysis

To analyze FTS photon streams, the stream is binned into linear spaced time bins per detector, resulting in intensity time traces. These time traces are then summed and subtracted to eventually determine the ratio thereof, according to Equation 3.70. From this ratio, the Fourier Transform is calculated through Discrete Fourier Transform (DFT), which results in the FTS spectrum. This is the basic FTS analysis scheme, where the spectra, dependent on the experiment or desired output, can then be used for further analysis, such as peak-following, averaging, etc.

PCFS Analysis

For PCFS analysis, the auto- and cross-correlations are computed at every interferometer stepping point via Laurence.[94] We compute the auto-correlation as the combined signal of all arrival times, and the cross-correlation is computed as the averaged cross-correlation of $A \times B$ and $B \times A$. Mathematically they are identical, however due to the approximations of the algorithms, there exist minor differences between them. With the correlation functions known, the corrected-cross correlation can be calculated via Equation 3.91. The corrected-cross correlations basically form a 3-dimensional dataset of time dependent PCFS interferograms (envelopes) with time-separations and path-length differences on the axes. The path-length differences are obtained from the settings of the experiment, where we saved at what $\langle\delta\rangle$ the photon stream was measured. From the 3D dataset, PCFS interferograms can be taken at desired time-separations, which in turn can be Fourier Transformed ($\delta \rightarrow \zeta$) via Fast Fourier Transform (FFT) algorithms into spectral correlations. This results in 3D spectral correlations with energy differences and time as axes. The spectral correlations can then be used for further analyses, such as peak-height extraction, Full Width at Half-Maximum analysis, etc.

sPCFS Analysis

The analysis of sPCFS is similar to PCFS analysis, in that it computes the auto-, corr-, and corrected-cross correlations for different path-length differences. However, for further analysis, a subtraction of the ensemble photon-pairs must be performed according to Equation 3.98. The ensemble is chosen at time-separations longer than the typical diffusion time to obtain a 3D dataset of sPCFS interferograms with path-length difference and time-separation on the axes. These sPCFS interferograms can again be Fourier Transformed with respect to path-length difference to obtain a 3D spectral correlation dataset of the average single nanoparticle with energy- and time-separation as axes. These spectral correlations can also be used for further analyses similar to PCFS.

3.5.2 Static Laser Simulation

Let us use the computational model to simulate light coming for a static laser, which does **not** show any intensity fluctuations **and no** spectral fluctuations. This is a simple case, where there is only a light source that is expected to have no dynamics. This is a good check to see whether spectral linewidths match with expectations and because experimentally a laser is used to align the interferometer

and perform quick checks whether the optical device is working correctly. For this model, the photons that "are emitted" by the laser are considered to come from one (time-invariant) spectrum (PDF). Additionally, we implement that the photon arrival times are independent of each other, since we assume that our laser source is Poissonian.[101] To characterize the photons in this computational model, we thus perform Monte-Carlo sampling on an input spectrum (spectral PDF) and generate uniformly distributed random numbers as arrival times (independent events). These photons are then fed into the generic machinery as described above to generate detection probabilities to then return arrival times and detector occurrences. Figure 3.16 shows a FTS simulation of a static laser light source. The chosen input spectrum for the laser is shown in Figure 3.16a and the FTS interferogram from Monte-Carlo simulation is shown in Figure 3.16b. Lastly, the spectral correlations are computed from the input spectrum directly and from the Fourier transform of the simulated FTS spectrum, see Figure 3.16c. From the residuals of the difference of the two spectral correlations, we observe that the FTS simulation output matches closely with what is expected.

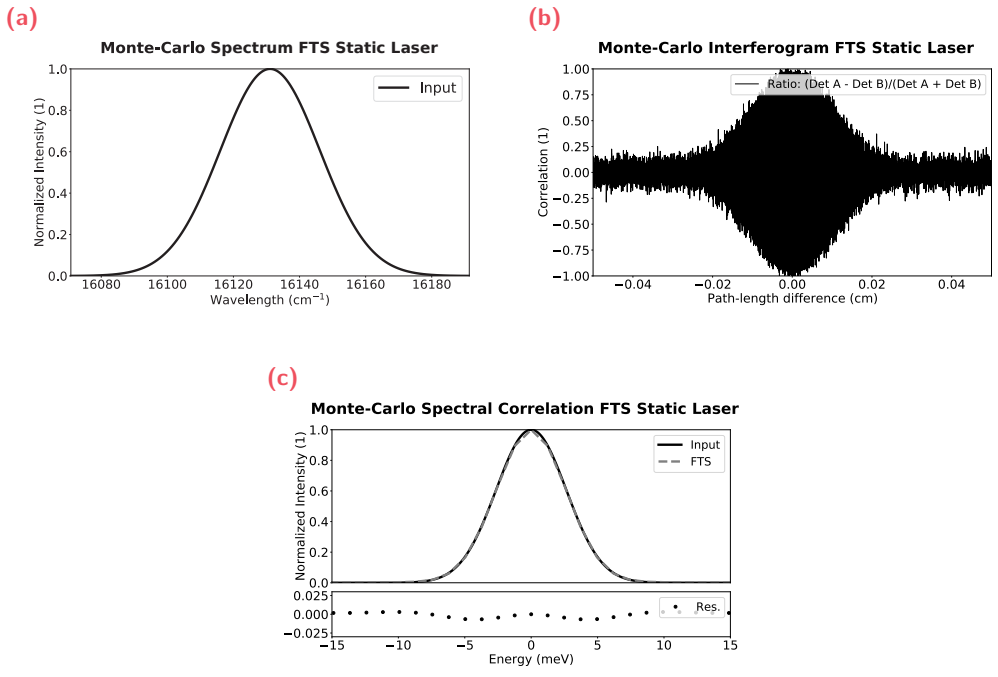

Fig. 3.16.: Fourier Transform Spectroscopy computation of a static laser with *(a)* input spectrum, *(b)* the interferogram from the model, and *(c)* the spectral correlations from the model compared with the spectral correlation from the input spectrum.

Next, we simulate a PCFS experiment, by chaning only a few simulation settings, that uses the same input spectrum as the FTS simulation, see Figure 3.17. Now,

auto- and cross-correlations are computed at different path-length differences, see Figure 3.17b. These intensity correlations are combined with the use of Equation 3.91 into the corrected cross-correlations:

$$g^{\times}_{\mathrm{corr}}(\delta,t) = 2\left(g^{\times}(\delta,t)/g^{(2)}(\tau) - 1\right) = \mathcal{F}\left[p(\zeta,\tau)\right] \tag{3.99}$$

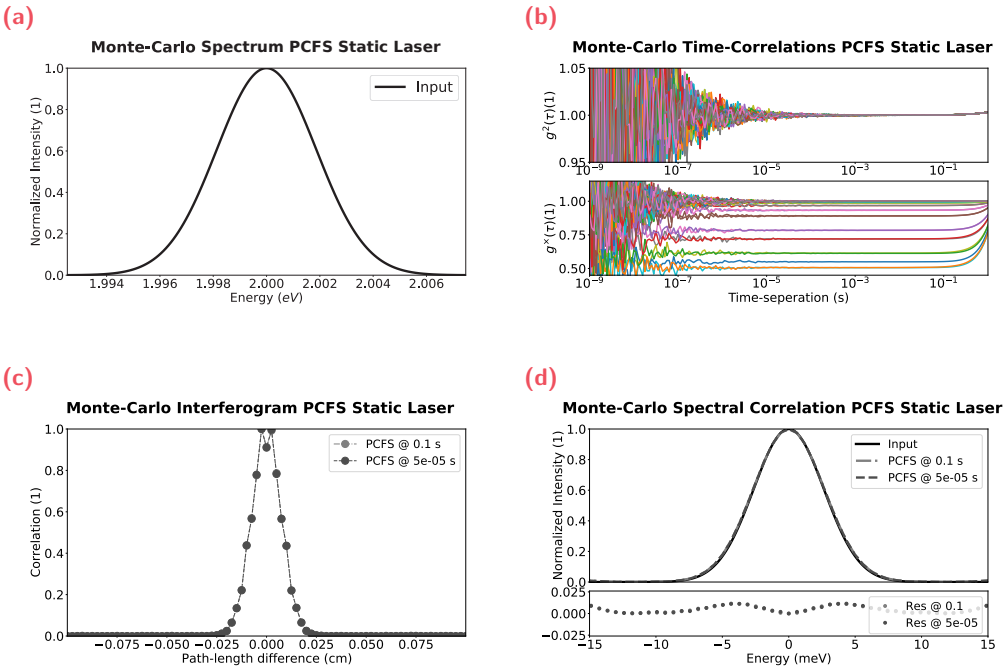

Fig. 3.17.: Photon-Correlation Fourier Spectroscopy computation of an intensity and spectrally static laser with *(a)* input spectrum, *(b)* intensity correlations, *(c)* the PCFS interferogram[4], and *(d)* spectral correlation direct from *(a)* and from Monte-Carlo simulation.

This corrected cross-correlation is essentially the envelope of the FTS interferogram, here defined as the PCFS interferogram, which can be shown at specific time-separations ($0.5\,\mathrm{s}$ and $50\,\mu\mathrm{s}$), see Figure 3.17c. This representation is useful, since the spectral correlations are obtained through Fourier transformation, as seen in Figure 3.17d. Additionally, here, we compare the direction calculation of the spectral correlations (Equation 3.92) of the input spectrum with the data outputted by our computational model, and from the residuals we find good agreement, indicating that our computational model works for static spectra. The reader might also have spotted a rise around $1\,\mathrm{s}$ in the cross-correlations in Figure 3.17b. This rise is part of a greater oscillation that is an artifact from the small periodic movement around each

[4] A dip at 0 path-length difference is observed, which likely comes from sampling issues at the white fringe position, because the model does not produce any background photons.

interferometer position, called the dither. The dither is needed for PCFS experiments to obtain the envelope of the interferogram. In the following section, computations of PCFS experiments without dither are explored and used to show the integral part of the dither to the method.

The Effect of the Absence of Dither

This paragraph takes a small detour to explain what the effect of the dither is. The dither, a small periodic motion performed around static points in the interferogram, is key to PCFS measurements. Here, I will show its importance by showing simulations **without** dither (Figure 3.18a) that can be compared to earlier simulations **with** dither (Figure 3.17). For a fair comparison, the same input spectrum is used as in the simulation with dither. Again, the auto- and cross-correlations are computed at various interferometers points, see Figure 3.18b. Already, we observe that the cross-correlations do not deviate from 1, whereas they did earlier (Figure 3.17b). Therefore, the corrected cross-correlations become $1 - 1 = 0$ for all τ, such that the PCFS interferogram in Figure 3.18c also remains zero and flat for all path-length differences. Therefore, the spectral correlations in Figure 3.18d result in flat lines lying at zero.

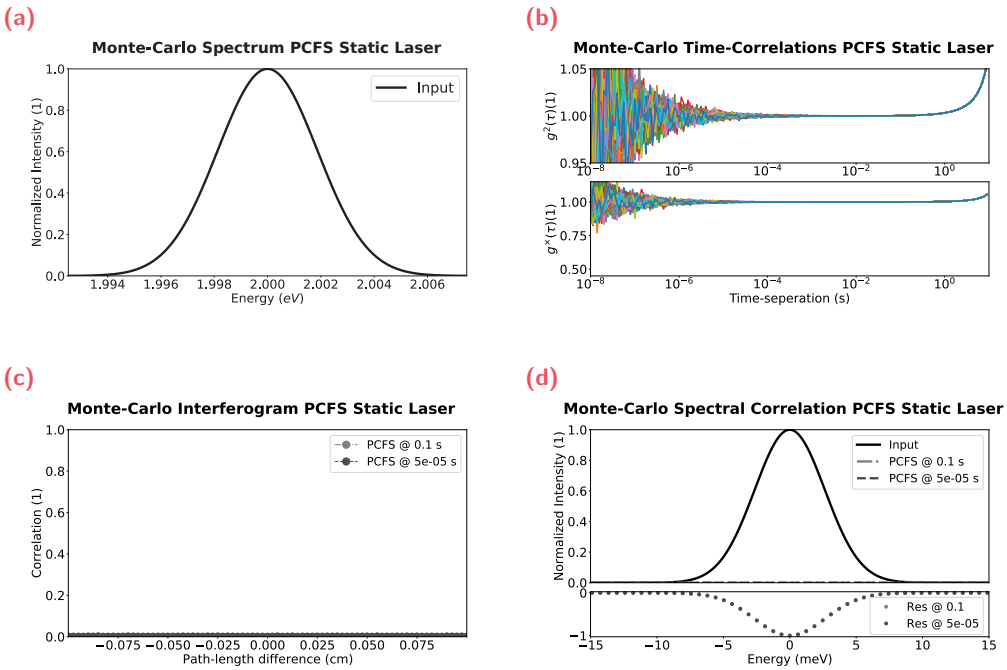

Fig. 3.18.: Photon-Correlation Fourier Spectroscopy computation of a static laser **without dithering** with *(a)* input spectrum, *(b)* intensity correlations, *(c)* the PCFS interferogram, and *(d)* spectral correlation direct from *(a)* and from Monte-Carlo simulation.

For these simulation **only** the dither was disabled, such that the detector occurrence probabilities are computed at fixed interferogram positions. As observed in Figure 3.18, PCFS analysis fails when the dither is not present. This is due to the fact

that the rate of photons being directed to either detector 1 or detector 2 remains constant for the entire measurement at that path-length difference. This results in intensity traces that remain constant and flat (Figure 3.19a), which in turn results in constant and flat cross-correlations. The amplitude of the cross-correlation might differ, but the algorithm that we use outputs normalized correlation curves. This is due to the fact that the correlation algorithm cannot differentiate between two flat intensity traces with amplitudes 0.25 & 1 and two intensity traces with amplitudes 0.5 & 0.5. In both cases cross-correlations computation results in flat lines with an amplitude of 0.25 and is therefore normalized to be 1. A small periodic movement introduces the flow of photons from detector 1 to detector 2 (or reversed) over time, since it intrinsically is moving over a fringe in the interferogram. Thus changing the detection probabilities (contrast) over time, resulting in sinusoidal time traces with amplitudes related to the change contrast (Figure 3.19b). In Figure 3.19 examples of intensity time traces for computations **without** and **with** dither are shown.

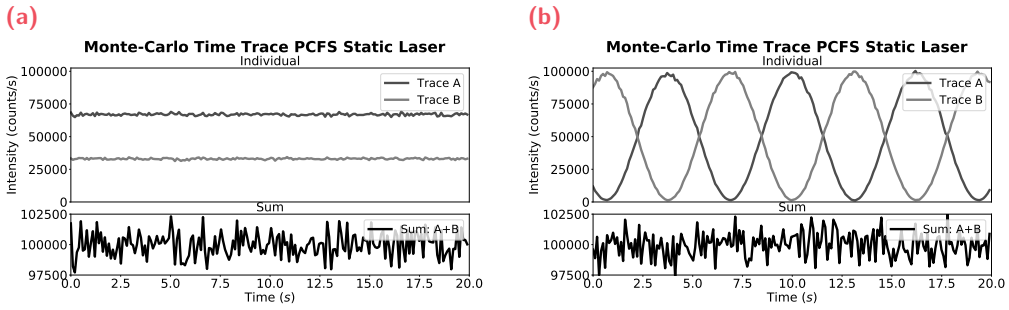

Fig. 3.19.: Time traces at maximum contrast for Photon-Correlation Fourier Spectroscopy computation of a static laser *(a)* **without** dithering and *(b)***with** dithering.

3.5.3 Dynamic Laser Simulation

In this section, we examine the output of our computational model for spectra that show dynamics, since eventually we are interested in using this proposed setup experimentally, for kinetic measurements of dynamic spectra from nanosensors. We, thus, expand our computational model to explore the parameter space to get a grasp of what signals to expect. Having established that our model correctly outputs data for spectrally and intensity static laser light, a reasonable next step is to look at dynamically changing spectra of a laser. Here, we examine pure spectral dynamic by keeping the photon rate constant. To define the dynamic model, we use two distinct spectra, that we consider as individual optical states that the system can reside in. First, periodically switching between the two states is implemented and examined, thereafter a system with exponentially distributed switching times is implemented. Brokmann et al. have explored a simulation of spectral jumps in quantum dots.[102] Their implementation of the model is slightly different to ours, because they consider a continuous changing path-length difference and random spectral fluctuation starting for a known center peak.

Periodic Switching

The part covers the periodic switching between two distinct spectra, which we will call optical states. The width of the spectrum of both states is implemented to be the same, only the center peak position is different, see Figure 3.20a. A very small shift of only $0.1\,\mathrm{nm}$ ($0.7\,\mathrm{meV}$) on a full-width at half maximum (FWHM) of $\sim 1\,\mathrm{nm}$ ($\sim 4.4\,\mathrm{meV}$) is simulated to switch state every $130\,\mathrm{ms}$. We simulated the spectra to shift from $450.0\,\mathrm{nm}$ to $450.1\,\mathrm{nm}$, which is important because we observe that the spectra in the visible might only have small FWHMs in wavelength space, but their energy space FWHM is much broader compared to spectra in the infrared. The energy space photon distribution is important, since this is where the interferometer modulates over ($\widetilde{\nu_0}$ in Equation 3.50).

The intensity correlations in Figure 3.20b hint at spectral dynamics around $100\,\mathrm{ms}$ because of small ripples formation. The signal-to-noise (S/N) however of a single cross-correlation is not enough to clearly extract the dynamics. This is also observed in the spectral correlations in Figure 3.20c, where no dynamics are observed by eye. Therefore, we analyzed the FWHM of the spectral correlations as a function of time in Figure 3.20d. This gives more statistical power and is better able to capture the center peak shift. The main idea of FWHM analysis is that at short time-separations only photon pairs are observed coming from the same identical optical state, whereas

at larger time-separations photon pairs with photons coming from both optical states could be counted. This would make the spectrum appear broader, and thus the FWHM changes. In the simulation, we see half an oscillation at $63 \pm 5\text{ms}$ and a full oscillation at $122 \pm 10\text{ms}$, close to the $130\,\text{ms}$ that was implemented. Additionally, we observe that the maxima and minima diminish over time and average towards the half-way point. This is due to logarithmic bin sizes that are used in the computation of the correlations. The bin size increases at larger time-separations and thus greater portions of the sinusoid (spectral switching) are taken, resulting in more averaging.

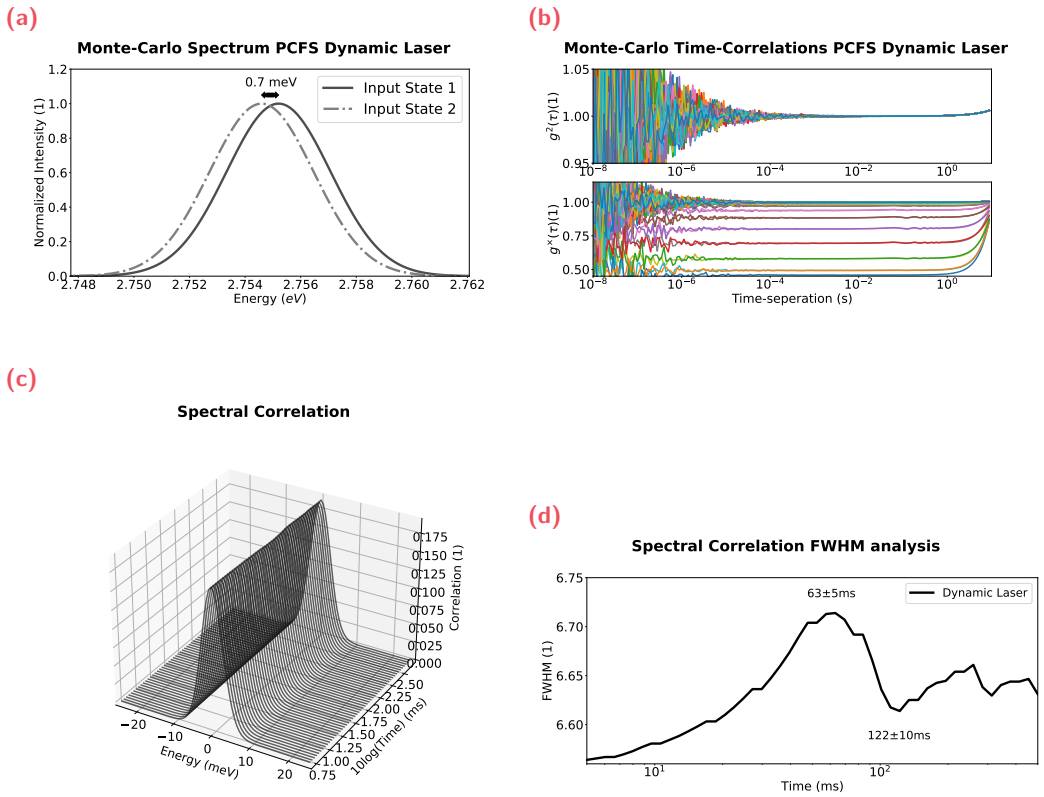

Fig. 3.20.: Photon-Correlation Fourier Spectroscopy computation of a dynamic laser with periodic switching every $130ms$. With *(a)* the input spectra of both states, *(b)* the intensity correlations, *(c)* the spectral correlations, and *(d)* the full-width at half maximum (FWHM) of the spectral correlation as a function of time.

2-State Rate Switching

In this following section, two state switching is implemented via exponentially distribution switching times. Biological events are rarely regularly timed, but rather rely on probabilities to decay into the other state. In the introduction (Section 1.1), I have discussed biomolecular interactions of two proteins forming a complex. Here, we use the exact same model system, however we describe the 2 optical states separately as S_{unbound} and S_{bound}, which represent the spectra of an optical sensor sensing unbound and bound biomolecules, respectively. The equilibrium equation then becomes:

$$S_{\mathrm{unbound}} \underset{k_{\mathrm{off}}}{\overset{k_{\mathrm{on}}}{\rightleftharpoons}} S_{\mathrm{bound}} \tag{3.100}$$

where, k_{on} is the probability to go from the unbound to the bound state and k_{off} is the probability to fall back from the bound to the unbound state. The probability distribution, P_{on} and P_{off}, from this 2-state equilibrium process can be found from solving the differential equation for the concentrations, and are obtained as: $P_{\mathrm{on}}(t) = e^{-k_{\mathrm{on}} \cdot t}$ and $P_{\mathrm{off}}(t) = e^{-k_{\mathrm{off}} \cdot t}$.

For the simulations, switching times are obtained from these alternating distributions to fill an array up to the duration of the simulation. In our Monte-Carlo sampling method, the photon energies are drawn from the corresponding spectrum (State bound or State unbound) based on the photon arrival time compared to the array with switching times. Additionally, the switching time array is also obtained through Monte-Carlo sampling by $t_{\mathrm{on/off}} = k_{\mathrm{on/off}} \cdot ln(R_{\mathrm{val}})$, where R_{val} is a random value from a uniform distribution in the range of $[0, 1]$. Note that the natural logarithm is the inverse of the exponential probability function. This is thus the mathematical calculation of the inverse CDF from an exponential PDF.

In Figure 3.21, a PCFS simulation is shown with rate dependent switching between two input states (Figure 3.21a). The on and off rates are set equal, such that $k_{\mathrm{on}} = k_{\mathrm{off}} = 1 \cdot 10^3 \mathrm{s}^{-1}$. This value was chosen to test whether sub-ms switching events would be measurable with PCFS. From this simulation, no obvious wrinkles or width changes in the intensity and spectral correlations (Figure 3.21b and Figure 3.21c) are observed. However, with FWHM analysis of the spectral correlations an exponential decay is observed, see Figure 3.21d. The FWHM at short time separations is related to the average FWHM of input state spectra, whereas the FWHM at long time separations reflect photons pair sampled from both states, making the obtained FWHM broaden. By fitting an exponential function, the $\mathrm{on} + \mathrm{off}$ rates are found to be $k_{\mathrm{obs}} = k_{\mathrm{on}} + k_{\mathrm{off}} = 1.5 \pm 0.2 \cdot 10^3 \mathrm{s}^{-1}$, which is close to the input rates we set. We hypothesize that the difference comes from photon numbers and

sampling, and that the extracted rate value would be closer with more photons. We also observe more noise at shorter time-separations than in the periodic switching event. This is due to fact, that the kinetics in this example are a factor of 10 faster and that the S/N for the intensity correlations is photon rate dependent. With more photons the S/N could be improved and most likely the kinetics could be made another factor of 10 to 100 faster. In the following paragraph, we will go deeper into the fitting function and the values that can be extracted from it.

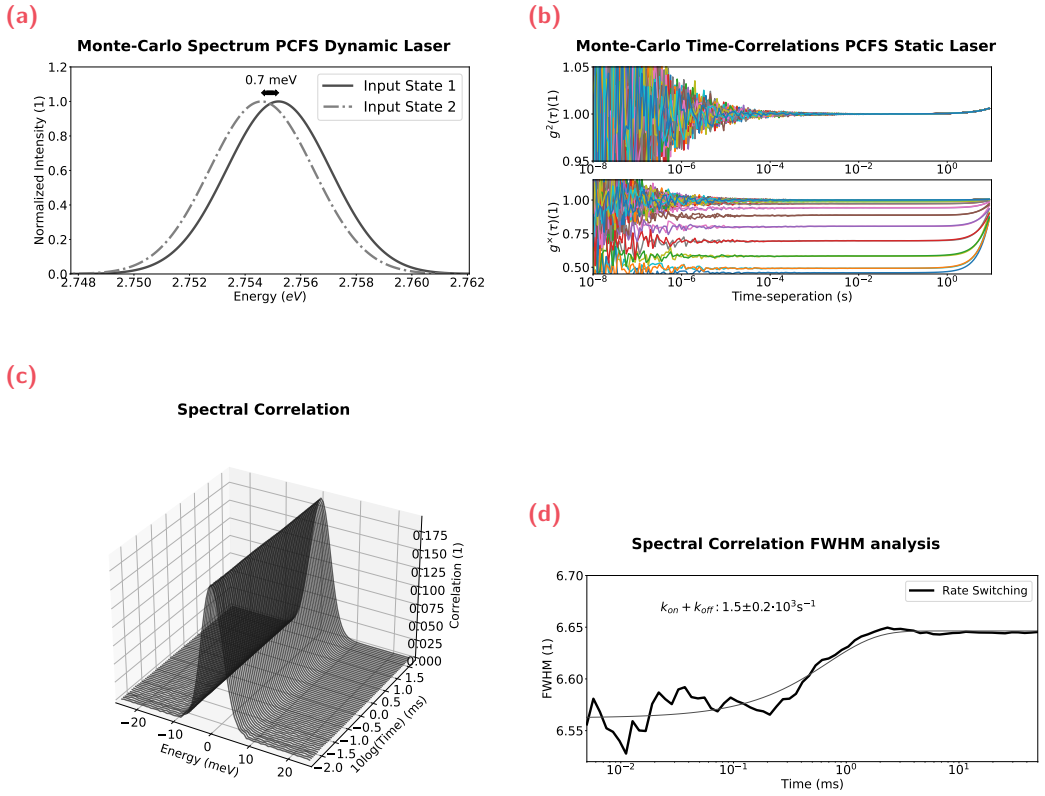

Fig. 3.21.: Photon-Correlation Fourier Spectroscopy computation of a spectrally dynamic laser with switching events governed by a simple two-state rate equation with $k_{on} = k_{off} = 1 \cdot 10^3 \mathrm{s}^{-1}$. In *(a)* the input spectra of both states, *(b)* the intensity correlations, *(c)* the spectral correlations, and *(d)* the full-width at half maximum (FWHM) of the spectral correlation as a function of time are shown.

Rate Fitting Function

In this section, the exponential fitting function for 2-state equilibrium equation is discussed. A generic decaying exponential model can be used (Equation 3.101) to extract information. This exponential function comes from solving a differential equation of the concentrations of state bound and unbound. However, the fitting

parameters A, B and k can also be expressed in terms of k_{on} and k_{off} by considering a simplified 2-state system.

$$\mathrm{Exp\_fit}\,(t) = A \cdot e^{-k_{\mathrm{obs}} \cdot t} + B \tag{3.101}$$

To find expressions for the fitting parameters, the two spectra are assumed to be spectrally more distinct from each other, such that when a state switch happens all photons must come from that state. To do so let us consider a simple case where the spectrum is artificially narrow, effectively being described as a Dirac delta-like function. We assume them delta-like, since we would like to give both state an amplitude, which is related to the amount of photons that are emitted from that state. Dirac delta functions make for a convenient model system, since they remain Dirac delta functions in spectral correlation space, whereas Gaussians or other functions with some width would broaden in spectral correlation space.

Let us first find an expression for k_{obs}, which describes the probability of finding photon pairs coming from the same state. Therefore, it must be that $k_{\mathrm{obs}} = k_{\mathrm{on}} + k_{\mathrm{off}}$, since one only arrives into the original state after going to the other and back.

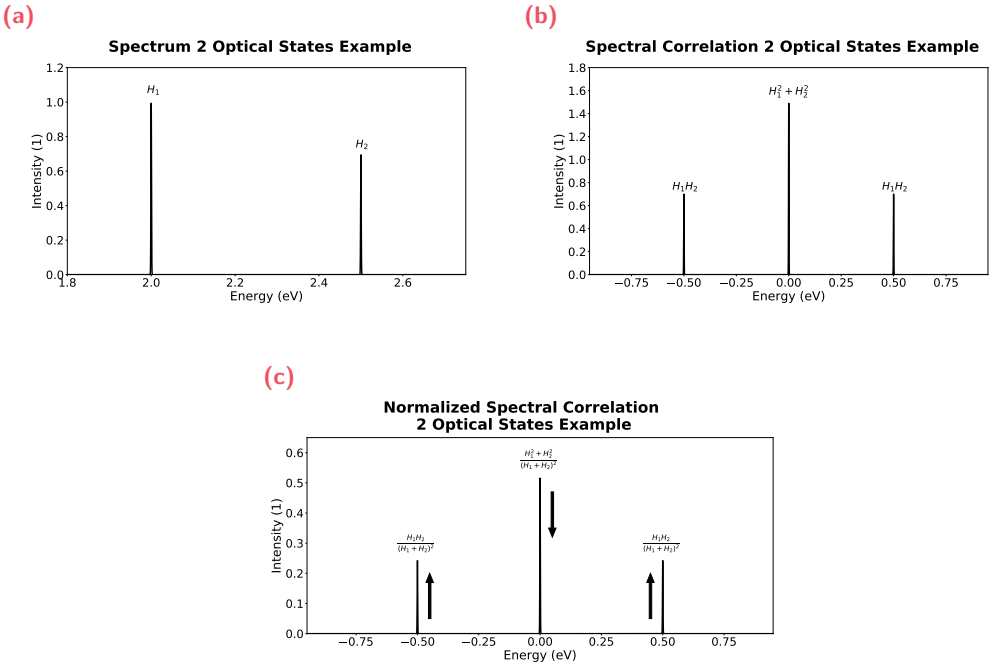

Fig. 3.22.: Example of a spectrally distinct 2-state model. In *(a)* the spectrum, *(b)* the spectral correlation, *(c)* the normalized spectral correlation with arrows indicating height changes from short τ to long τ.

To describe A and B, let us define a spectrum with two states having a height of H_1 and H_2, respectively. The spectral correlation of a spectrum with 2 Dirac peaks has 3 Dirac peaks in spectral space and their heights are described by $H_1 \cdot H_2$, $H_1^2 + H_2^2$, and $H_1 \cdot H_2$, in order. When the spectral correlations are normalized, they become $\frac{H_1 \cdot H_2}{(H_1+H_2)^2}$, $\frac{H_1^2+H_2^2}{(H_1+H_2)^2}$, and $\frac{H_1 \cdot H_2}{(H_1+H_2)^2}$, respecively. At short time-separations the photons can be assumed to only come from one state, which for a normalized spectral correlation results in a single peak of height 1 at an energy-separation of 0. Therefore, the 3 peaked spectral correlations introduced in the beginning becomes 0, 1, and 0 at short time-separations. Therefore, we can establish that the side peaks grow from 0 to $\frac{H_1 \cdot H_2}{(H_1+H_2)^2}$ and that the center peak shrinks from 1 to $\frac{H_1^2+H_2^2}{(H_1+H_2)^2}$.

Now, we consider that amount of photons, and therefore the height of the Dirac delta function, are proportional to the time spent in either state. We can thus infer that $\frac{k_{\mathrm{on}}}{k_{\mathrm{off}}} = \frac{H_1}{H_2}$, where we can define the $K_{\mathrm{d}} = \frac{k_{\mathrm{on}}}{k_{\mathrm{off}}}$. This relationship between K_{d} and the peak heights can be plugged into the descriptions of the three-peaked spectral correlations. Here, we find that the side peaks grow from 0 to $\frac{K_d}{(1+K_d)^2}$ and that the center peak shrinks from 1 to $\frac{K_{\mathrm{d}}^2+1}{(1+K_{\mathrm{d}})^2}$. Looking back at Equation 3.101, for analysis of the center peak height, we can turn A into $1 - B$, because of normalization, and $B = \frac{K_{\mathrm{d}}^2+1}{(1+K_{\mathrm{d}})^2}$. Whereas for the side peaks A turns into $-B$, and $B = \frac{K_{\mathrm{d}}}{(1+K_{\mathrm{d}})^2}$. Noteworthy, in all of this math state bound **cannot** be distinguished from state $\mathrm{unbound}$ without prior knowledge, therefore the definitions of k_{on} and k_{off} are not unique and could actually be swapped.

Luckily in actual biomolecular systems the on rate is protein-concentration dependent, whereas the off rate is independent of protein concentration. For protein dynamics typically other rate constants are defined as k_{d} and k_{a}. They are related to the on and the off rates as:

$$k_{\mathrm{off}} = k_{\mathrm{d}} \tag{3.102}$$

$$k_{\mathrm{on}} = k_{\mathrm{a}} \cdot [P] \tag{3.103}$$

with $[P]$ being the protein concentration in M^{-1}. All of this math gives us a handle on extracting rate kinetics from spectral correlations. However, in the examples discussed earlier, we observed that the shifts are rather small compared to the width of the spectra. Therefore, we cannot resolve the theoretical three peaks anymore, but rather observe a change in FWHM. The change in FWHM is directly related to the math derived here, but also on the FWHM of the spectra of the two states and the magnitude of the shift. Therefore, when performing FWHM analysis, we cannot obtain a clean fitting model as derived here. Luckily, we have also found that obtaining a value for K_{d} from the height or the width is not really needed. Namely,

we can obtain $k_{\mathrm{on}} + k_{\mathrm{off}}$, and for proteins on rate is protein-concentration dependent, such that when we measure a protein concentration series, we would be able to extract K_{d}.

3.6 Experimental Characterization of the Optical Setup

Thus far, we have discussed the physical principle of interferometry and derived governing equations for Fourier Transform Spectroscopy (FTS) and Photon-Correlation Fourier Spectroscopy (PCFS). With this knowledge, a computational model has been build to explore the parameter space of spectrally shifting signals, that represent metallic nanosensors observing biomolecular interactions with fast kinetics. In this last section, we actually build the proposed setup from Figure 3.12 and a list of all the components used is presented in Appendix A.6. We then use various laser sources to test the performance of our real-life setup and compare it with the outputs of the computational model from Section 3.5. First, static spectra from various lasers are analyzed. After which, a white-light laser source with a filter box, that can sweep the spectrum periodically and aperiodically, is used to obtain kinetic PCFS data.

3.6.1 Static Spectra from Various Lasers

Photon Correlation Fourier Spectroscopy on Static Laser

Similar to how we started our computational model, we test our setup with intensity and spectrally static laser spectra. Namely, lasers have long coherence lengths, meaning that their fringes and the interferogram stretch over several 10ths of cm. Thus, they are a good choice for initial experiments. Here, a gas laser (green HeNe/GrHeNe) with an emission wavelength of $543\,\mathrm{nm}$ from Newport (N-LGR-393) is tested. In Figure 3.23, the PCFS analysis is shown by computing intensity correlation curves for every path-length difference, Figure 3.23a. Then, the corrected cross-correlations are computed to form the 3D PCFS interferogram, which are shown as time slices in Figure 3.23b. Lastly, the spectral correlation is calculated from the PCFS interferogram, see Figure 3.23c. From this measurement, we find that the gas laser has a coherence of a few decimeters, which in spectral space results in a narrow spectral correlation. This in term would mean that the laser has a very pure laser line (a narrow spectrum).

Next, a supercontinuum white light laser (superK FIANIUM FIU-15) from NKT is used together with two different filterboxes to reduce the width of the spectrum. The superK itself spans the entire visible and infrared spectrum. A spectrum this broad would result in a coherence length so small, that our mechanical stage, used to change the path-length difference, would not be able to perform the steps need to resolve the interferogram. This is because such a broad spectrum would result

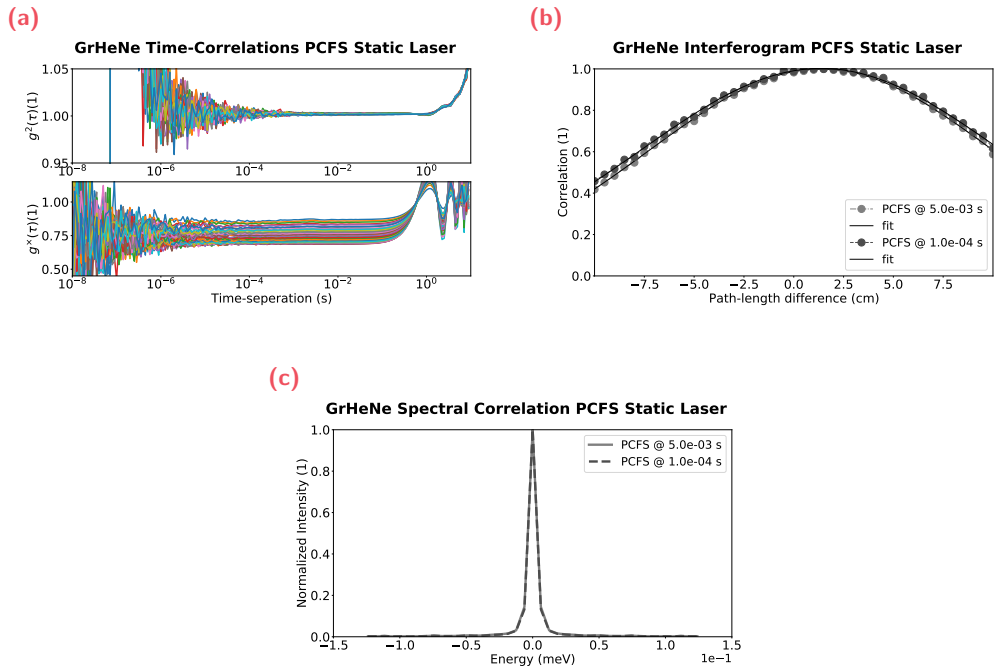

Fig. 3.23.: Photon-Correlation Fourier Spectroscopy (PCFS) experiment of a green HeNe laser. In *(a)* the intensity correlations curves, *(b)* the PCFS interferogram from the corrected cross-correlation, *(c)* the spectral correlations.

in an interferogram with only a handful of fringes. First, the Laser Line Tuneable Filterbox (LLTF contrast) made by Photon Etc. is used. This is a customized filterbox for the superK laser, that turns the broad white light into narrow laser lines. The LLTF disperses the light through a volume Bragg grating and captures it with another volume Bragg grating to return a collimated beam. Volume Bragg gratings are pieces of optic that have a periodic modulation of the refractive index, causing diffraction. The diffracted wavelength is angle dependent can be tuned by rotating the gratings. In summary, the LLTF filterbox allows us to shift the output center wavelength by rotation of its built-in grating.

Second, the superK VARIA tunable filterbox is used, which consist of tunable short- and long-pass filter. These filters are mechanically positioned in the laser beam to change their cut-off wavelength, thereby allowing to change both the center wavelength and the bandwidth of the spectrum. Both laser-filterbox combinations have been analyzed through PCFS to extract spectral FWHM values from fitting the PCFS interferograms with Gaussians. In Appendix A.12, I go deeper into the fitting equations and how they can be calculated for different spectra. In Table 3.1, the FWHMs for the three laser (systems) are shown and compared with their specifications. Here, we observe that experimental FWHMs agree well with the

FWHM from the lasers' specifications. We however observe a greater mismatch for the VARIA filterbox, which is explained by the fact that the short- and long-pass filters in the filterbox have cut-on and -off tolerances of $\sim 5\,\mathrm{nm}$. An increase of $2.5\,\mathrm{nm}$ to each side of the optical band would result in an expected value of $63.2\,\mathrm{meV}$.

	Green HeNe	superK LLTF	superK VARIA
Experimental FWHM	$3.7 \pm 0.2\,\mu\mathrm{eV}$	4.52 ± 0.04 meV	55.4 ± 0.7 meV
Specified FWHM	$4.1\,\mu\mathrm{eV}$	$4.2\,\mathrm{meV}$	$42.1\,\mathrm{meV}$

Tab. 3.1.: Table with Full-Width at Half Maximum (FWHM) data obtained from Photon-Correlation Fourier Spectroscopy (PCFS) experiments on static laser(systems). The experimental values are obtained by fitting the PCFS interferogram with Gaussians and are compared with the specifications of the laser(systems).

Fourier Transform Spectroscopy on Static Laser

Next, we investigated the correctness of the spectral correlations by overlaying them with Fourier Transform Spectroscopy data and data obtained from a handheld spectrometer (Thorlabs CCS100/M) as shown in Figure 3.24. In this experiment the super continuum white light laser was used together with the NKT VARIA to create a spectrum at$500\,\mathrm{nm}$ with a bandwidth of $50\,\mathrm{nm}$. Measurements where the raw data is obtained, are shown in Figure 3.24a. With the handheld spectrometer a spectrum is measured and with FTS we obtain the interferogram, whereas for PCFS the envelope of the interferogram is obtained. From these data spectral correlations are computed, shown in Figure 3.24b, where we observe that the spectral correlations of all three methods match quite well. Interestingly, background noise in the FTS measurement results in a pedestal (broad triangle) that offsets spectral correlation slightly. The shape of these spectral correlations is expected, since the input spectrum looks like a rectangular function, whose spectral correlation is a triangular function.

Here, I also want to stress the importance of the fitting models that are used to extract data from the PCFS interferograms. When this PCFS interferogram is fitted with a rectangular function, a linewidth of $72 \pm 1\mathrm{meV}$ is obtained, whereas when the PCFS interferogram is fitted with a Gaussian function a FWHM of $164 \pm 3\mathrm{meV}$ is extracted. Theoretically, the linewidth is expected to be $248\,\mathrm{meV}$. The origin of this mismatch might lay in the asymmetry caused by chromatic aberrations or in the definition of the fitting function. Appendix A.12 goes deeper into how the fitting function are defined and obtained. Nevertheless, we find that the spectral correlations do nicely match and these can be used to extract linewidth information without making assumptions of the spectrum.

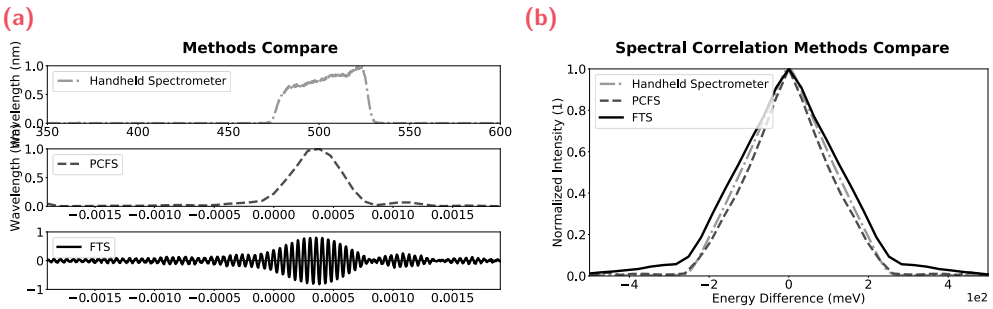

Fig. 3.24.: A comparison between spectral correlations obtained through PCFS, FTS, and a handheld spectrometer *(a)* with their raw data and *(b)* the spectral correlations computed from the raw data in *(a)*.

For broader spectra, the chromatic aberrations cause greater asymmetry in the interferograms. As seen in Section 3.2 the asymmetry does not affect FTS spectra, however, for PCFS data we observe a greater mismatch between the spectral correlations when compared to other methods. In Appendix A.10 data is presented showing this mismatch. So far, we have not worked on a rigorous mathematical method to correct PCFS interferogram asymmetry, however in Appendix A.11 we present a method that matches the PCFS interferogram to the FTS envelope of a double Fourier Transformed FTS interferogram.

3.6.2 Dynamic 2-State Spectrum

In this paragraph, we mimicked a spectrum with two distinct optical states by rotating the volume Bragg grating in the LLTF filterbox. This allows us to shift the spectral output of the laser system from $540\,\mathrm{nm}$ to $545\,\mathrm{nm}$ periodically as fast as the grating can move. The LLTF is specified to produce spectra with FWHMs $<1\,\mathrm{nm}$, therefore the two optical states are clearly separated, similar to our two Dirac delta functions *Gedankenexperiment* of Section 3.5.3. For the next experiment, the spectral switching is determined by a control program that rotates the grating with rate-equation probabilistics, therewith mimicking a natural 2-state system. The random time for the switching event is generated from exponential distributions similar to in Section 3.5.3. Note that for the rate switching experiment, the spectral states have been moved closer to each other to $450.0\,\mathrm{nm}$ and $450.1\,\mathrm{nm}$, respectively. In this case, the two states overlap for a large portion of their spectrum, similar to the nanoparticle spectra obtained from Mie calculation from Section 2.1.3.

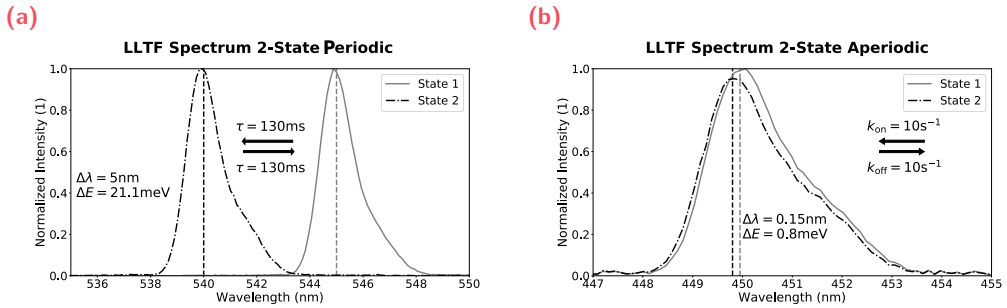

Fig. 3.25.: Spectra of a spectrally dynamic 2-state systems. In *(a)* periodic shifting is induced between $540\,\mathrm{nm}$ to $545\,\mathrm{nm}$. In *(b)* optical state switching from $450.0\,\mathrm{nm}$ and $450.1\,\mathrm{nm}$ with switching times that are exponentially distributed.

Dynamic 2-State Spectrum Periodic

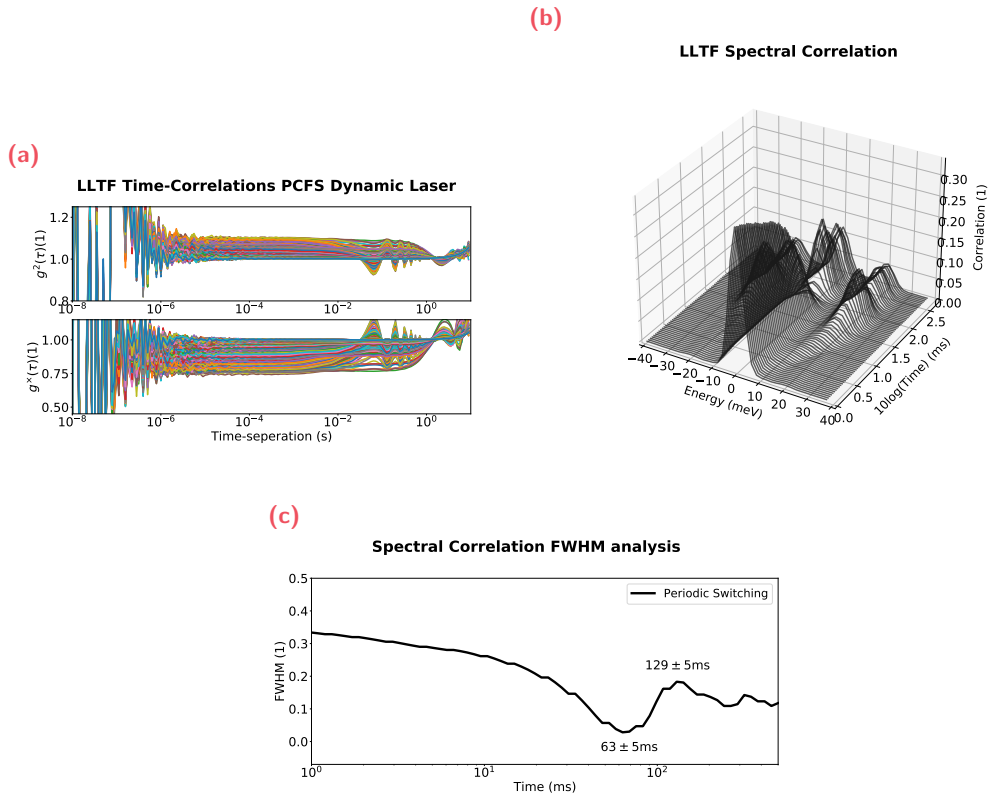

Fig. 3.26.: Photon-Correlation Fourier Spectroscopy (PCFS) experiment of a periodic switching laser system. In *(a)* the intensity correlations curves, *(b)* the 3D spectral correlation, and *(c)* a section of the spectral correlations at $0\,\mathrm{meV}$ energy separation with typical oscillation frequency of $130\,\mathrm{ms}$.

In Figure 3.26, we performed a PCFS experiment on a dynamic laser system that switches from $540\,\mathrm{nm}$ to $545\,\mathrm{nm}$. The specifications of the filterbox state that a $65\,\mathrm{ms}$ stabilization time is needed for a $5\,\mathrm{nm}$ spectral shift. We would thus expect oscillations to have a periodicity of $2 \cdot 65 = 130\mathrm{ms}$, since we try to switch at the maximum allowed speed. In Figure 3.27a we observe both oscillating auto- and cross-correlation, which indicate that the induced spectral fluctuations are not entirely decoupled from intensity fluctuates. This could be explained from the fact that the spectrum of the supercontuum laser is not entirely flat. Nevertheless, the spectral fluctuations are much larger in amplitude, indicating that the main signal comes from spectral fluctuations. In Figure 3.27b, the 3D spectral-(time)-correlations are shown, where we observe at short times 1 peak and at long times 3 peaks. 3 peaks in the spectral correlation correspond to 2 peaks in the spectrum. For the distance between the peaks we find $\sim 20\,\mathrm{meV}$, indicating the energy difference between the

two states, which theoretically should be $21\,\mathrm{meV}$. Additionally, we observe there is only 1 center peak at short time-separations and that two side peaks arise at larger time-separations. When the side peaks arise, the center peak is observed to diminish. Lastly, we find that at very long time-separations the 3 peaks seem to approach a steady state, which is explained due to the logarithmical time-bins in the correlations functions, whereas the oscillation is purely linear in time. Lastly, a section as a function of time at $0\,\mathrm{meV}$ energy-separation is shown in Figure 3.27c. Here, the oscillations are better observed, and a half period occurs at $63 \pm 5\mathrm{ms}$ and a full period at $129 \pm 5\mathrm{ms}$, which are close to the specifications of the LLTF. These results can be compared with our computational model from Figure 3.20 and might explain the earlier seemingly arbitrary choice of $130\,\mathrm{ms}$. Here, we conclude that the computational and experimental behaviors are very similar, thus proving the efficacy of our computational model and with that also the ability of PCFS to resolve sub-ms spectral dynamics.

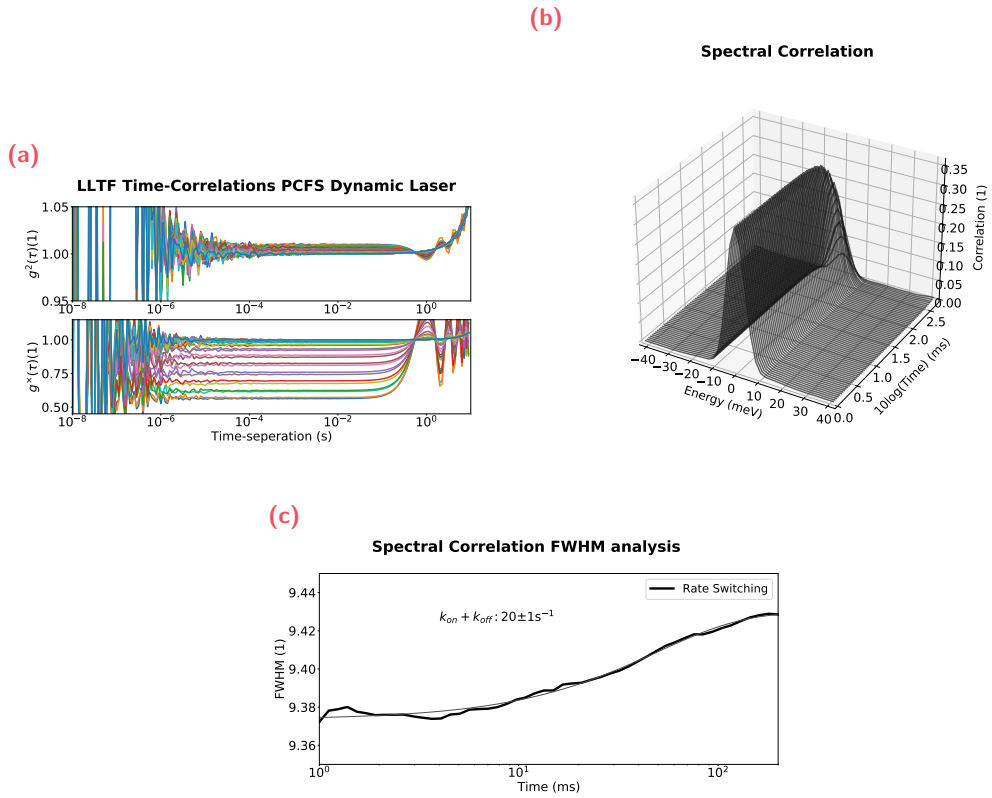

Fig. 3.27.: Photon-Correlation Fourier Spectroscopy (PCFS) experiment of an aperiodic switching laser system. In *(a)* the intensity correlations curves, *(b)* the 3D spectral correlation, and *(c)* FWHM analysis of the spectral correlations as a function of time with typical dynamics at $0.2\,\mathrm{s}^{-1}$.

Lastly, a PCFS experiment on a switching laser system that switches according to rate equations probabilistics is performed, see Figure 3.27. The values of k_{on} and k_{off} could be chosen freely, and we wanted to prove that our optical setup can measure very fast shifts. However, we are limited by the ability of the LLTF to rotate fast enough. For example, the specifications mention that a $0.1\,\mathrm{nm}$ steps needs $20\,\mathrm{ms}$ of stabilization time. Additionally, to get maximum contrast we would like to keep $k_{\mathrm{on}} = k_{\mathrm{off}}$, see Section 3.5.3. Therefore, we implemented rate switching probabilities of $k_{\mathrm{on}} = k_{\mathrm{off}} = 10\,\mathrm{s}^{-1}$ with optical states at $450.0\,\mathrm{nm}$ and $450.1\,\mathrm{nm}$. In Figure 3.27, a PCFS experiment is performed on this dynamic 2-state system. This time in the intensity correlations curves, no dynamics can be easily observed, see Figure 3.27a. Neither, do the 3D spectral (time)-correlations (Figure 3.27b) give more direct insight. Most likely a shift of only $0.1\,\mathrm{nm}$ on a spectral FWHM of $1\,\mathrm{nm}$ is too small such that advance analysis technique is needed. The reader might confuse the dither

effect at $1\,\mathrm{s}$ for the 2-state dynamics, however this feature is almost 3 orders of magnitude removed from where we expect the dynamics of the 2-state system to occur. Therefore, the FWHM of the spectral-(time)-correlations as a function of time have been analyzed to observe the spectral shift. This has been fitted with an exponential decay, according to Section 3.5.3, to obtain: $k_{\mathrm{on}} + k_{\mathrm{off}} = 18 \pm 1\mathrm{s}^{-1}$, which agrees nicely with the input settings. Note, that our systems obtains good enough signal-to-noise (S/N) down to $1\,\mu\mathrm{s}$ to $10\,\mu\mathrm{s}$, but that for these experiments we were limited by the shifting ability of the laser system. Additionally, we observe that the S/N are similar between computation and experiment such that we believe that sub-millisecond spectral shifts ought to be measurable.

3.7 Conclusion

In this chapter, we have discussed the second part needed for in-solution sensing: the optical setup. Here, we have seen that the combination of two existing optical devices (a confocal microscope and an interferometer) can form a new optical device (a Photon-Correlation Fourier Spectroscopy (PCFS) setup), which is able to measure both intensity **and** spectral fluctuations of particles freely diffusing in solution. Then we derived governing equations for three modes of operation; Fourier Transform Spectroscopy (FTS), PCFS, and solution PCFS, by solving Maxwell's equations for the optical components that the optical setup is composed of. For FTS we found that the way we construct our setup, allows us to intensity correct signals, which is atypical for FTS experiments.

From the governing equations, a computational model based on Monte-Carlo sampling is introduced, which is computationally cost-efficient and allowed us to explore the "experimental" parameter space quicker. We simulated Poissonian light sources **without** and **with** dynamics, which in the dynamic case switched $0.1\,\mathrm{nm}$ on a spectrum with full-width at half maximum (FWHM) of $1\,\mathrm{nm}$ every $130\,\mathrm{ms}$. The obtained output was close to our implementation at $122 \pm 10\mathrm{ms}$. We then explored aperiodic switching through exponential distribution probabilistics, which was simulated with on and off rates as $k_{\mathrm{on}} = k_{\mathrm{off}} = 1 \cdot 10^3 \mathrm{s}^{-1}$. We retrieved $k_{\mathrm{obs}} = k_{\mathrm{on}} + k_{\mathrm{off}} = 1.5 \pm 0.2 \cdot 10^3 \mathrm{s}^{-1}$, again in good agreement with our input.

The chapter is finalized by characterizing the optical setup in real-life, where we used spectrally static laser light to find that the extracted linewidths agree well with the specifications of the laser systems. Finally, we use a supercontinuum white light laser and filterboxes to induce dynamically shifting spectra, where we first examined periodic switching. We found that the measured dynamics lines up with the specifications ($130\,\mathrm{ms}$) of the filterbox at $129 \pm 5\mathrm{ms}$. Lastly, we mimicked a 2-state switching system that follows exponential probabilities, where we moved a spectrum $0.1\,\mathrm{nm}$ on a FWHM of $1\,\mathrm{nm}$, and extracted $k_{\mathrm{obs}} = k_{\mathrm{on}} + k_{\mathrm{off}} = 18 \pm 1\mathrm{s}^{-1}$, close to our input parameters of $k_{\mathrm{on}} = k_{\mathrm{off}} = 10\mathrm{s}^{-1}$.

Overall, in these experiments, the signal-to-noise (S/N) has been found to be good and remain good down to $1\,\mu\mathrm{s}$ to $10\,\mu\mathrm{s}$. Additionally, we found that our computational model with its S/N compares well with experiments. Experimentally, we were limited to $\sim 100\,\mathrm{ms}$ dynamics, but we found through simulation that sub-ms dynamics can be easily retrieved with our optical setup. This makes us confident that small optical shifts from nanosensors sensing biomolecular dynamics in their proximity from Chapter 2 can be measured with our optical setup. The ratio of shift

compared to the FWHM of the spectrum is namely comparable to the experiments in this current chapter. In summary, we have shown deep theoretical understanding of the optical setup that we built, and demonstrated its working both computationally and experimentally. Where, in the latter, we show the ability to find fast rate kinetics of small shifts from broad spectra.

4 Nanoparticle Spectroscopy

In this chapter, simulations and experiments of in-solution sensing are presented. The aim of these experiments is to establish a method that can obtain kinetic information of fast and transient interacting biomolecules. For this, we utilize the small metallic nanoparticles from Chapter 2 as freely diffusing optical nanosensors, which are sensitive to their dielectric environment. Their optical output is captured in our custom-built device from Chapter 3, which offer high temporal and spectral resolution. The front-part of the optical setup is based on Fluorescence Correlation Spectroscopy (FCS), which is an optical technique that analyzes intensity fluctuations of nanoparticles diffusing through a laser focal volume. Due to the inclusion of an interferometer in the detection scheme of our setup, we are also capable of measuring spectral fluctuations of these nanoparticles. This setup is known as Photon-Correlation Fourier Spectroscopy. Because freely diffusing nanoparticles are used as biosensors, our signals include diffusion and intrinsic spectral effects that have to be understood first before in-solution bio-sensing can be achieved.

In the first half of this chapter, the nanoparticle diffusion and intrinsic spectral effects are mapped, such as the spectral differences between the average single and the ensemble. First, the computational model from Section 3.5, based on Monte-Carlo (MC) sampling, is expanded to simulate light bursts from particles diffusing through a focal volume. Then we prove that with a dual-path interferometer, Fourier Transform Spectroscopy (FTS) can be performed on fluctuating signals. Hereafter the second mode of operation of the optical setup, Photon-Correlation Fourier Spectroscopy (PCFS) is simulated to give insight into the difference between the linewidths of the average single nanoparticle and the ensemble. The expansion of the computational model in this chapter is also found in the patent (Publication No. 2022/214611, Application No. EP2022059308), with the title: "Method, Apparatus and System for Characterizing Transient Interactions between Biomolecules". These computational findings are then backed-up with experiments on Cadmium Selenide Quantum Dots (CdSe QDs) to understand the intrinsic spectral differences between the average single nanoparticle and the ensemble with the use of solution Photon-Correlation Fourier Spectroscopy analysis. With this analysis, spectral effects can be separated from any diffusion effects. Then, scattered light and photoluminescence

of plasmonic nanoparticles are examined with PCFS, where the pros and cons of both light methods are discussed and compared.

The second half of this chapter discusses biomolecular sensing simulations and experiments. From the learnings of the first half of the chapter, a new method is introduced, which used two continuous wave (CW) laser diodes to drive the scattered light of the nanosensors. We use our computational model with light bursts from diffusing nanoparticles and include the possibility for the nanoparticle to have two optical states. Then, the nanoparticle is simulated to switch between optical states with exponential probabilistics, similar to natural binding and unbinding events of simple biomolecules. The simulations are assisted with experiments, where the local sensitivity of the plasmonic nanoparticles is used to observe diffusion of analyte passing by the sensor. Here, bio-like molecules, such $8\,\mathrm{nm}$ oil micelles, $15\,\mathrm{nm}$ SiO_2 nanoparticles, and $12\,\mathrm{nm}$ by $40\,\mathrm{nm}$ DNA origami, are used as analyte of which the diffusion is observed. Then a fast and transient interacting protein pair is examined, and the chapter is finalized with FTS measurements on a strong binding protein pair.

4.1 Intensity Fluctuations from Nanoparticles

In the previous chapter (Chapter 3), a specialized optical setup for measuring both intensity and spectral fluctuations has been introduced. In this setup, light is captured of particles that freely diffuse in solution. When a particle passes through a laser focal volume, a burst of light is generated, either through photoluminescence or scattering, which goes into optical setup. The light is analyzed with an interferometer that gives high spectral resolution and single photon detectors that give high temporal resolution. Previously, the characterization was purely done through coherent laser light and spectral fluctuations were induced with special filterboxes. In this section, incoherent light of diffusing nanoparticles is detected with our setup, causing intensity fluctuations as well as spectral fluctuations due to inhomogeneous broadening.

First, we examine this computationally. We expand the model from Section 3.5 to include nanoparticle diffusion. With this expanded model, we show that Fourier Transform Spectroscopy (FTS) can be performed on intensity fluctuating signals, when a dual-path interferometer and the intensity correction math from Section 3.2 are used. Then we show computationally that Photon-Correlation Fourier Spectroscopy (PCFS) on nanoparticle light bursts gives insight in the spectral linewidth of the average nanoparticle and the ensemble. The spectral fluctuations due to inhomogeneous broadening can be isolated with solution Photon-Correlation Fourier Spectroscopy (sPCFS) analysis, which decouples spectral and intensity fluctuations.

These computational findings are then compared to experiments on Cadmium Selenide Quantum Dots (CdSe QDs). Previously, the Bawendi group characterized QDs syntheses by examining their fluorescent light in PCFS experiments.[103, 104] Therefore, we use CdSe QDs to test our setup and analysis pipeline, before we can examine the particles of interest; plasmonic nanoparticles (Chapter 2). This section finishes with PCFS and FTS experiments on these metallic nanoparticles, using both scattered and luminescent light to understand their diffusion and intrinsic spectral effects. The findings from those experiments form important considerations for the subsequent sensing experiments.

4.1.1 Computational Model with Diffusing Nanoparticles

In this section, the computational model is expanded by changing how the light source produces a photon stream. In a true PCFS experiment, light that is analyzed, does not come from a Poissonian light source, but rather from freely diffusing

nanoparticles that occasionally diffuse through a laser focal volume. When the particle diffuses through a focal volume, a burst of light is generated that enters the optical setup. Importantly, this light can no longer be assumed to be Poissonian (independent events), since it now depends on the presence of a particle in the focal volume. The burst of light can have different physical origins, but for the simulations the true origin is not so important. We simply consider the particle to emit light when it enters the focus on the objective, and stops emitting when it moves out of the focal volume.

To simulate the full extent of particles moving in and out of a focal volume, one would have to perform Molecular Dynamics (MD) simulations to find trajectories of particles undergoing Brownian Diffusion. Within the MD simulation box, a subvolume can be defined that, where particles start emitting photons when they enter and stop when they leave the subvolume again. We, however, skip the MD simulations entirely, since they are computationally expensive, especially when they need to be performed for various path-length differences. Alternatively, one could perform one MD simulation, and reuse it over and over. However, this would probably lead to artifacts.

We opted for a more computationally inexpensive Monte-Carlo style approach, where we consider the statistical time it takes for a particle to move through the focal volume (dwell time). We simply define $t_{\mathrm{dwell}} = \frac{w_{\mathrm{f}}^2}{6D}$, with w_{f} being the width of the focal volume and D the diffusion coefficient of a particular nanoparticle. The diffusion coefficient is based on the Einstein-Stokes equation $D = \frac{k_{\mathrm{b}}T}{6\pi\eta r}$, with k_{b} being the Boltzmann constant, T the temperature, η the dynamic viscosity, and r the hydrodynamic radius of the particle. Then, individual dwell times are computed for an ensemble of particles with normal distributed radii.

In our simulations, we assume a spherically symmetric focal volume, such that we do not have to consider from which direction the particle is moving.[1] For the entire duration of the dwell time the particle is simulated to emit light. We do note that the behavior of one single particle could differ vastly from reality with these assumptions, however both FTS and PCFS measurements rely on statistics of many particles. This ensures that obtained information about individual behavior is generalized anyhow. Thus, do the generalized descriptions of diffusion not affect the expected finding of FTS and PCFS simulations. In Appendix A.5, I discuss the comparison of the presented model with MD simulations. If the reader is interested in applying the presented computational model for Fluorescence Correlation Spectroscopy, it should

[1] A statistical adaptation could be implemented for ellipsoidal focal volumes as well, where w_{f} would not be uniform, but has some distribution to statistically represent an ellipsoid.

be noted that the particle diffusion characteristics might differ from experiments, because of the assumptions we make here (spherical focal volume and generalized diffusion behavior). For the desired behavior of the computational model in this chapter, this generalized model suffices, especially since particle diffusion characteristics are corrected through sPCFS analysis (Equation 3.98).

We thus can update the flowchart of the computational model from Section 3.5. Figure 4.1 gives the full overview of all the steps taken to compute the detection probabilities from photon characteristics and computational settings. The added features now include photon arrival time selection from particle diffusion and spectral dynamics. How particle diffusion is accommodated in this model, is already discussed above, where the appear times of the nanosensors are independent events, but the emission of photons is given as a set time, based on the dwell time to cross the spherical focal volume. The second added part, is something that already has been discussed in Section 3.5.3, which allowed us to simulate spectral dynamics. We, however, never updated the flowchart to include this part. To accommodate spectral dynamics, multiple MC spectra for every particle are computed, which represent the different optical states they can reside in. In the case of sensing, discuss in the second half of this chapter, these optical states resemble either nanosensors with proteins bound on their surface or nanosensors without anything in their vicinity. The model then computes switching times based on probabilistics that we define. Then, based on the photon arrival time, photon energies of a specific optical state are chosen. This way, we can introduce spectral switching events on top of particle diffusion. This complete model then allows us to simulate freely diffusing nanosensors that change their spectra due to sensing events.

First, FTS simulations are shown on only intensity fluctuating signals due to nanoparticle diffusion, where due to the dual-interferometer setup better signal-to-noise spectra are obtained than in traditional FTS. Then PCFS experiments are shown on the same intensity fluctuating signals, where with sPCFS analysis the spectral differences between the average single nanoparticle and the ensemble are exposed.

Computation of Fourier Transform Spectroscopy on Diffusing Nanoparticles

First, we examine Fourier Transform Spectroscopy (FTS) of the intensity fluctuating nanoparticle signal. With this technique we can only obtain spectral information over the entire duration of the experiment, therefore single particle spectral contributions are combined into one, known as the ensemble. For FTS experiments, one arm of the interferometer is swept in a continuous linear motion from one side of the white

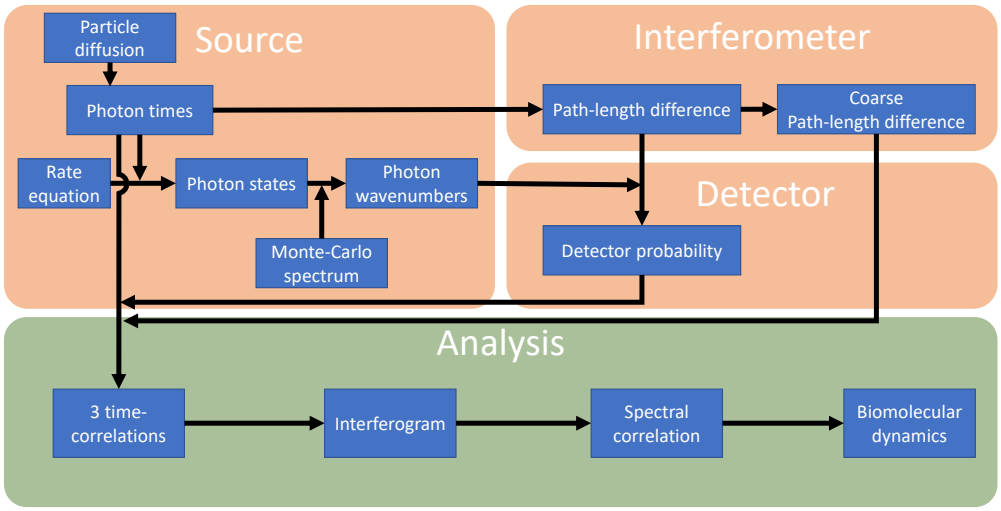

Fig. 4.1.: Updated flow chart of the computational model based on Monte-Carlo sampling to generate photons with random arrival times and photon energies. Whose characteristics together with computational settings are used to determine probabilities of detection on two detectors. Adapted from Cui et al. 2022.[100]

fringe to the other. The output intensity is modulated by interference and is known as the FTS interferogram. This section is meant to show the reader the benefits of having a dual-path FTS setup by comparing the signal-to-noise (S/N) in spectra captured with 1 versus 2 detectors. The math derived in Equation 3.70 is used to correct for intensity fluctuation to reduce the S/N for the 2 detector setup. Figure 4.2 shows a MC simulation of particles having an identical spectrum. The light coming from the particles produces bursts of light, such that the intensity fluctuates heavily, as seen in Figure 4.2b. The sum signal (Figure 4.2c) and the difference signal (Figure 4.2d) are computed from the intensity traces to then calculate a clean FTS interferogram as the ratio, see Figure 4.2e. The dual-path interferometer intensity ratio interferogram is compared to one single intensity interferogram from Figure 4.2b by Fourier transforming, see Figure 4.2f. Here, a great improvement in S/N is observed, due to the elimination of intensity fluctuation from the spectral fluctuations in the FTS interferogram. With this method, clean ensemble spectra can be obtained from freely diffusing nanoparticles in solution.

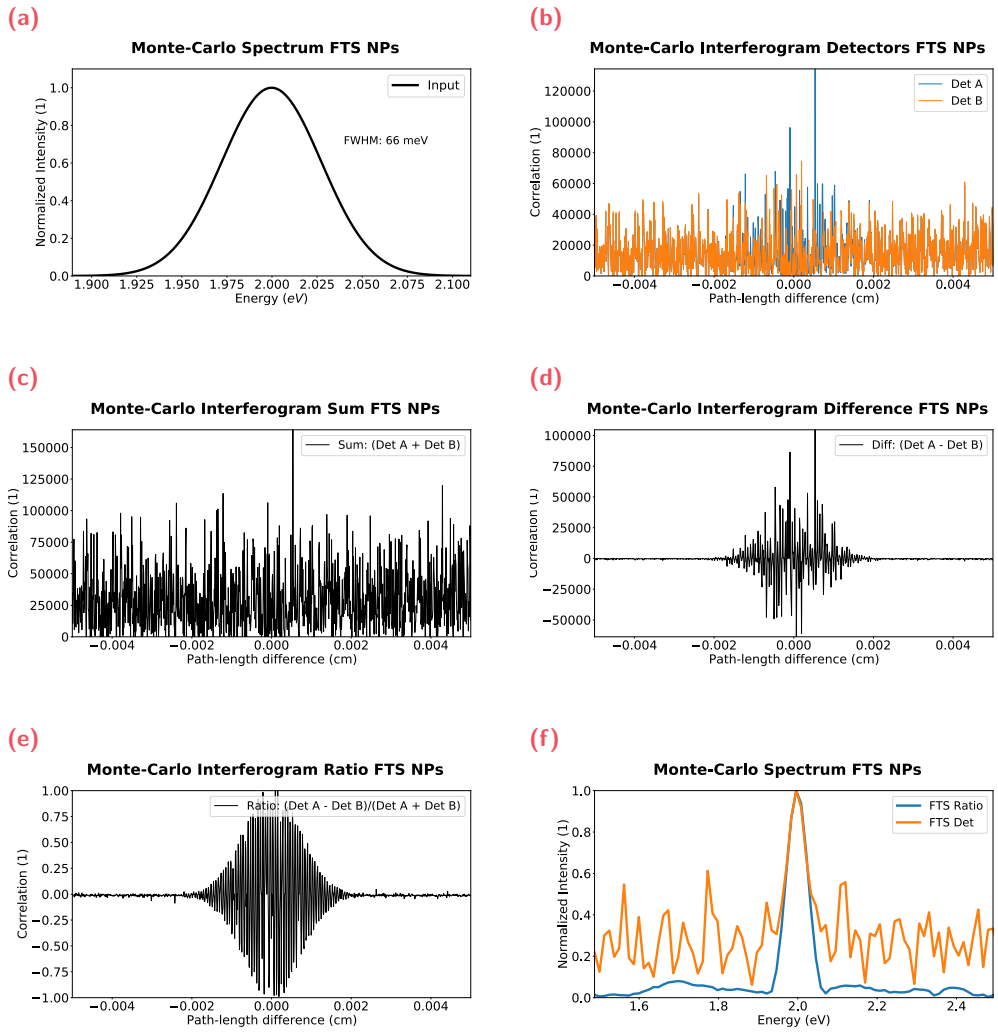

Fig. 4.2.: Fourier Transform Spectroscopy computation of nanoparticles with a static spectrum. In *(a)* the input spectrum, *(b)* the intensity measured per detector, *(c)* the sum of both detector signals, *(d)* the difference of both detector signals, *(e)* the ratio of the difference over the sum, *(f)* the FTS spectra after Fourier transform of *(a)* and *(e)*.

In reality, however, particles almost never have the exact same spectrum and inhomogeneous broadening is always present. Therefore, we simulated nanoparticles with a spectral FWHM of $65\,\mathrm{meV}$ and normal distributed center peak positions following the size of the particle. This way bigger particles take longer to diffuse through the focal volume, but also have a more red-shifted spectrum, similar to the size effects we know from Mie theory. For this simulation we use 1000 particles, and when their spectra are summed the ensemble spectrum is obtained with a spectral FWHM of $96\,\mathrm{meV}$, shown in Figure 4.3a. Note that these two spectra are indicative and have **not** used as input for the simulation. After FTS simulation, we calculate the ratio intensity trace following Equation 3.70 to obtain a clean FTS interferogram, see Figure 4.3b. By Fourier transforming this interferogram the FTS spectrum is obtained (Figure 4.3c). The MC output is compared with the implemented input by computing the spectral correlations, as in Figure 4.3d. Here, we observe that the FTS spectral correlation linewidth of $127\,\mathrm{meV}$ is close, but slightly narrower than the input spectral correlation FWHM of $136\,\mathrm{meV}$. We hypothesize that this difference comes from the amount of particles that has been sampled, and the difference could be reduced by simulating more photons and more particles. We also observe that with FTS, we only obtain the ensemble FWHM.

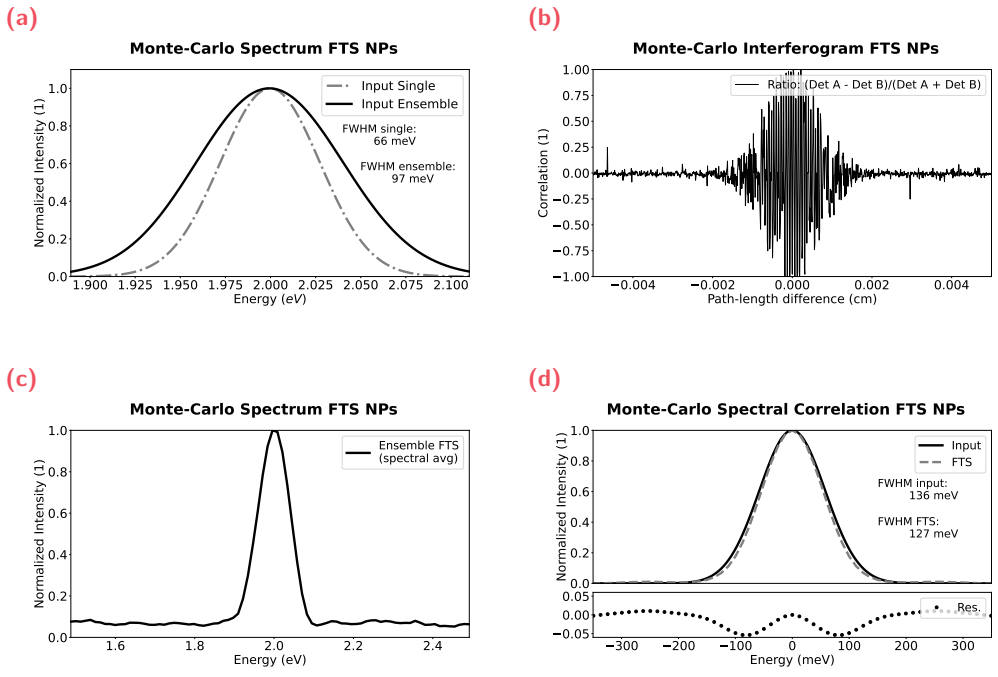

Fig. 4.3.: Fourier Transform Spectroscopy computation of nanoparticles. With *(a)* the input spectra of both states, *(b)* the intensity correlations, *(c)* the spectral correlations, and *(d)* the full-width at half maximum (FWHM) of the spectral correlation as a function of time.

Computation of Photon-Correlation Fourier Spectroscopy on Diffusing Nanoparticles

In the previous subsection, a simulation is shown of particles emitting bursts of light, each having their own spectrum. In the FTS operation mode, the obtained data could only be translated into the ensemble spectrum. Here, the same computational model is used, but in the PCFS operation mode, such that observations can be made about the linewidths of both the average single nanoparticle and the ensemble. Thus, the same input as in the FTS simulations (Figure 4.3) is used of single particle spectra with a FWHM of $65\,\mathrm{meV}$. The center peak position of each particle spectrum is normal distributed based on its radius, resulting in an ensemble linewidth of $96\,\mathrm{meV}$. In Figure 4.4, the input spectra of an average particle and the ensemble are shown. Note that these two spectra are **not** used as input for the simulation. After simulating photon streams, the intensity correlations are computed from the output of the computational model, as shown in Figure 4.4b. Then, time-separation slices are taken to produce two PCFS interferograms, one at $10\,\mu\mathrm{s}$ and one at $100\,\mathrm{ms}$. The latter one is chosen to be past the typical diffusion time of the nanoparticles through the laser focal volume. To recall Chapter 2, photon pairs with time separations smaller than the typical diffusing time can be assumed to come from the same particle, whereas photon pairs with time separations longer than the diffusion time must come from different particles. Therefore, the latter pairs can be assumed to represent the ensemble, whereas the photons pairs at $10\,\mu\mathrm{s}$ represent the average single nanoparticle. Through solution PCFS analysis, the FWHM of the ensemble and the average single particle are obtained by separation of the photon pairs weighted by the diffusion curve. The spectral correlations are then computed through Fourier transformation of the PCFS interferograms resulting in Figure 4.4d. Here, we see that the average single nanoparticle has the spectral correlation FWHM of $87\,\mathrm{meV}$ and the ensemble has $135\,\mathrm{meV}$. If we assume that the spectrum is Gaussian, these spectral correlation linewidths translate to spectral FWHMs of $62\,\mathrm{meV}$ and $95\,\mathrm{meV}$, respectively. Alternatively, we can use the PCFS interferograms and fit them with a Gaussian fitting model to extract the FWHM. When this is done, a FWHM of $59.3 \pm 0.5\mathrm{meV}$ for the average single and $96 \pm 1\mathrm{meV}$ for the ensemble are extracted. All these linewidth values agree very well with the input of the simulation. The slight differences are again attributed to photon and particle numbers that were used.

With the extended computational model, we have shown that FTS experiments can be performed on fluctuating intensity signal coming from nanoparticle diffusing through a focal volume. Here, the dual-path interferometry setup allows for the

decoupling of intensity and spectral fluctuations. However, the FTS experiments only resulted in ensemble spectral information. To obtain spectral information of the average single nanoparticle, PCFS experiments on the same input have been simulated. Through solution-PCFS analysis, photon pairs have been separated, weighted by the typical diffusion of the nanoparticles through the focal volume. This way, we obtained spectral correlations for both the ensemble and the average single nanoparticle, that matched with the input parameters of the computation. The results of these computational studies indicate that our down-stream analysis is working and helps with the deciphering of experimental observations, which are discussed in the following sections. There, FTS and PCFS experiments are discussed on nanoparticles of different materials. These results are compared with other techniques to ensure that we understand the diffusion and intrinsic spectral effects of the metallic nanosensors in our PCFS setup. This information is needed to account for their effects, before in-solution sensing is possible.

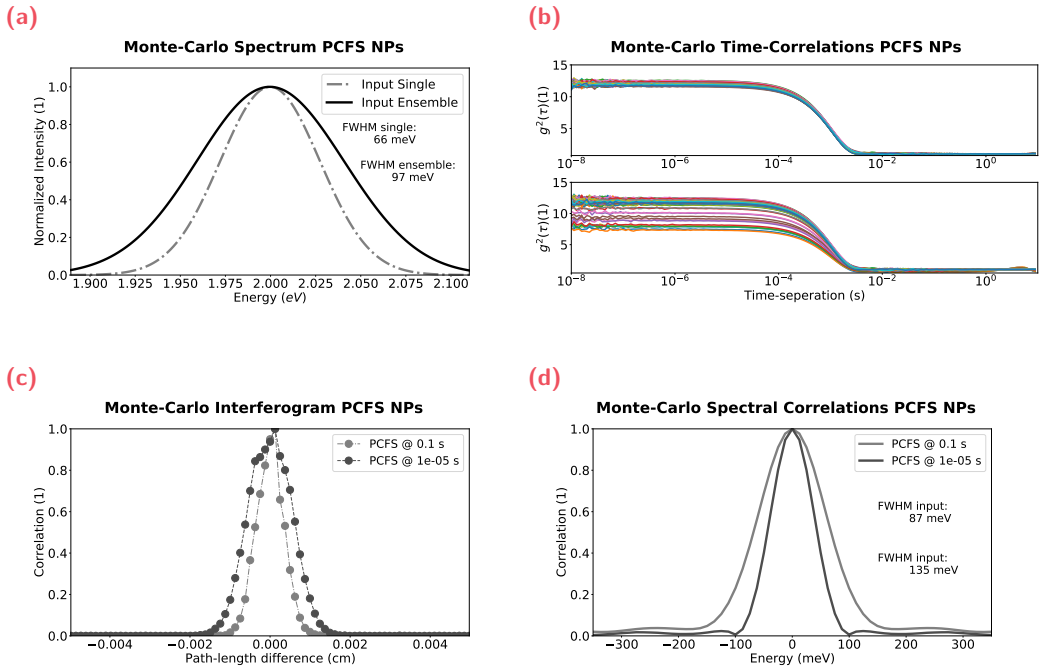

Fig. 4.4.: Photon-Correlation Fourier Spectroscopy computation of a dynamic laser with periodic switching every $130ms$. With *(a)* the input spectra of both states, *(b)* the intensity correlations, *(c)* the spectral correlations, and *(d)* the full-width at half maximum (FWHM) of the spectral correlation as a function of time.

4.1.2 Darkfield Spectroscopy Setup

Before we continue, with experiments on our custom-built optical setup, we take a small detour to discuss another optical setup that can measure nanoparticle spectra. This setup can be used as a comparative technique to ours, which can extract single nanoparticle spectra of particles deposited on a substrate. It has two modes of operation; fluorescent mode and dark-field scattering.

Figure 4.5 shows a schematic of the dark-field spectroscopy setup. This setup is built, by modifying an Olympus BX53 upright microscope. We split the outgoing light with a $90:10$ beampslitter (Thorlabs BSX10R) to relay the $90\,\%$ towards an Andor spectrometer (Kymera 193i, equipped with an iXon 897 EMCCD). The relay system was built with 2 200mm achromatic doublet lenses (Thorlabs AC254-200-A-ML) and 3 Silver mirrors (Thorlabs PF10-03-P01). Everything was connected together using Thorlab's cage system building blocks, such as rods, cage plates, kinematic mirror mounts, etc.

First, we will discuss the dark-field (DF) scattering mode. In this mode of operation, a special beamsplitter that blocks the light of an excitation/driving source is used. It is special in the sense that it only stops the light in the center of the beam with a so-called dark-field spider (Olympus U-MDF3). The light that is not stopped is focussed with a numerical aperture objective onto a substrate with nanoparticles on the surface. Most of the light is transmitted through the sample, but particles on the surface scatter the light back at various angles. On the way back into the DF spectroscopy setup, an additional light stop after the dark-field beamsplitter cube is used to filter out the excitation/driving light. This way, the substrate appears bright and only scattering objects appear white, hence the name dark-field.

We then relayed the scattered light to an Andor spectrometer, where a blazed grating disperses the light on an EMCCD camera. With a calibration lamp (Newport 6035), each pixel position can be translated to a specific wavelength. This way we can determine the spectrum of the scattered light. To obtain the true Localized Surface Plasmon Resonance spectrum, we need to correct for the driving light spectrum, as seen previously in Equation 2.4. In an experiment, we would measure the scattering spectrum of the particles and that of the driving light for something neutral like a scratch on a glass slide. In post-process the LSPR spectrum is then calculated by dividing with the driving light spectrum.[105, 106]

Alternatively, this setup can be used in fluorescent mode, where we replace the darkfield beamsplitter with fluorescent filters (Olympus U-FWBS or U-FWGS) to look at photoluminescence of nanoparticles. In that case, the excitation light is filtered

spectrally instead of mechanically.[2] With this setup, both QDs (fluorescent mode) and plasmonic nanoparticles (DF mode) can be examined to obtain single particle spectra. We aim to compare DF spectroscopy measurements with measurements on our custom-built optical setup as a control. This way we can eliminate setup artifacts and get a better understanding of the diffusion and intrinsic spectral effects of the plasmonic nanosensors in our setup.

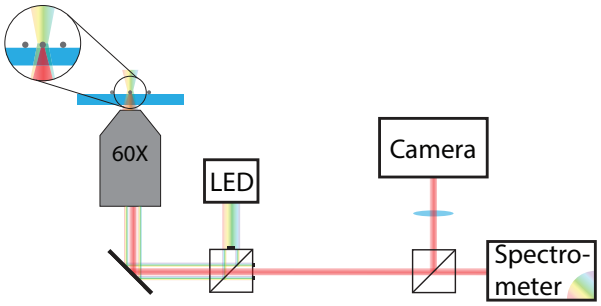

Fig. 4.5.: Schematic of a dark field spectroscopy setup. A modified olympus BS53 microscope, where the output light is split and relayed onto a Andor Kymera spectrometer.

4.1.3 Cadmium Selenide Quantum Dots Experiment

In this section, we discuss PCFS experiments performed on semiconductor nanoparticles, sometimes also called Quantum Dots (QDs). Semiconductor nanoparticles can be very interesting, because of the ability to tune their fluorescent emission wavelength. Typically, the emission wavelength is set by the bandgap of the material, but due to spatial confinement of the electron-hole pair the wavelength can be tuned. The nanoparticles, that we use, are made of Cadmium Selenide core with a Zinc Sulfate shell (CdSe@ZnS) from Sigma Aldrich (product number: 900219). For simplicity, I mostly call them by their core composition. With these CdSe QDs, we aim to observe inhomogeneous broadening effects of the spectra. As we have shown with simulations, we can isolate the average single nanoparticle spectral correlation from the ensemble spectral correlation through sPCFS analysis. These particles allow us to test our setup and see if the diffusion correction experimentally is working correctly to eliminate any setup-related artifacts. In previous PCFS literature, typical values spectral linewidths of $50 - 70\mathrm{meV}$ for average single QDs and $100\mathrm{meV}$, for an ensemble have been found.[103] We can thus firstly use these values as a rough

[2] Technically when the fluorescent mode is used, it no longer is a dark-field spectroscopy setup, however we still use this term to indicate to the reader that the same setup is still being used.

guide for our findings, however later we use the DF spectroscopy setup in fluorescent mode to obtain the same information of the exact sample that we are using.

Photon-Correlation Fourier Spectroscopy on Cadmium Selenide Quantum Dots

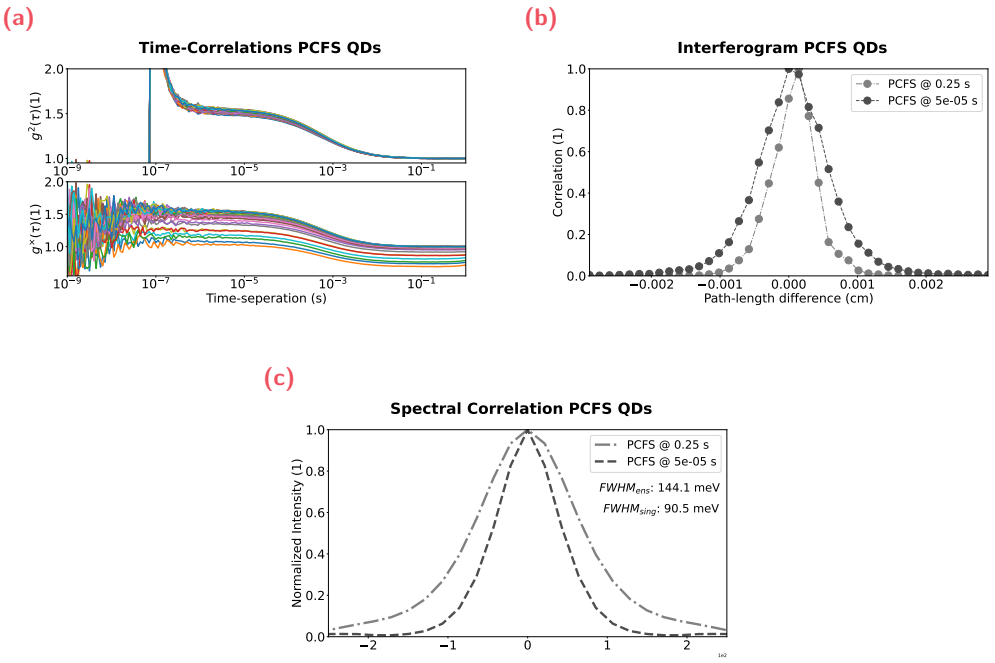

Fig. 4.6.: Photon-Correlation Fourier Spectroscopy of Cadmium-Selenide@Zinc-Sulfide Quantum Dots. With *(a)* intensity correlations at various interferometer positions, *(b)* the PCFS interferogram at $10^{-}5\mathrm{s}$ (avg. single) and $10^{-}1\mathrm{s}$ (ensemble), and *(c)* the spectral correlations, where the full-width at half maximums (FWHM) are compared.

In Figure 4.6, we show data of a PCFS measurement on CdSe QDs. In Figure 4.6a, we find the intensity correlations at various interferometer positions. Here, we observe a few differences from our particle simulations.

Firstly, we observe a sharp drop-off at $77\,\mathrm{ns}$. This drop-off is explained due to the detector dead time, which from specification needs 77 ns to be able to measure a new photon event. Secondly, we observe a rise at time-separations just before the detector dead time. This is an artifact known as afterpulsing. The single photon detectors, used in our optical setup, work at high bias voltages above the breakdown voltage. This allows for an avalanche effect upon detection of a single photon, however sometimes electrons get trapped in trap-states, that trigger artificial detection events

much later after the real detection event. Alternatively, the detector can also emit a photon because of this high bias voltage, which travels back into the setup to trigger a detection event on the other detector. Nevertheless, these curves can still be used to compute corrected cross-correlations, since the afterpulsing artifact dies off after a few microseconds. Only special care needs to be taken when time-separations in the afterpulsing pedestal want to be analyzed.

The corrected cross-correlations form PCFS interferograms, which we plotted at $5 \cdot 10^{-5}$ and $2.5 \cdot 10^{-1}$, see Figure 4.6b. The PCFS interferograms can be fitted with Gaussian functions to extract $67.5 \pm 0.9\mathrm{meV}$ and $110 \pm 3\mathrm{meV}$ for the FWHM of the average single QD and the ensemble spectra, respectively. From calculating the FWHM of the spectral correlations, see Figure 4.6c, we find $91\mathrm{meV}$ and $144\mathrm{meV}$, which translates to $64\mathrm{meV}$ and $102\mathrm{meV}$ assuming a Gaussian lineshape for the average single and ensemble, respectively. These values are of the same order of magnitude that we find in other reports.

Dark-Field Spectroscopy on Cadmium Selenide Quantum Dots

A comparison with literature is fair, but not definitive, since the range of linewidths is rather broad. The DF spectroscopy (in fluorescence mode) allows us to measure the exact same QD sample, but then spincoated on a substrate for direct comparison. For DF spectroscopy experiments, we spincoated $50\,\mu\mathrm{L}$ of diluted QD solution on coverslips (Thorlabs CG15KH1) at $3000\,\mathrm{RPM}$ that were cleaned in acetone, isopropylalcohol, and ultrapure water in this order while being sonicated for $30\,\mathrm{min}$ each. Thereafter, the coverslips are oxygen-plasma treated to ensure better adhesion of the QDs. In Figure 4.7b, we see spectra of individual QDs obtained in DF spectroscopy. These spectra are then converted into spectral correlations for the every single QD, but also for the ensemble (sum of all single spectra), see Figure 4.7c. Here, we extract linewidths of $97\mathrm{meV}$ for the average single and $122\mathrm{meV}$ for the ensemble with $N = 48$, which translates to a spectral FWHM, assuming a Gaussian lineshape, of $68\mathrm{meV}$ for the average single and $86\mathrm{meV}$. The average single FWHM matches nicely with the PCFS experiment from Figure 4.6. The ensemble value however is slightly off, most probably due to the limited number of QDs that were analyzed in the DF spectroscopy.

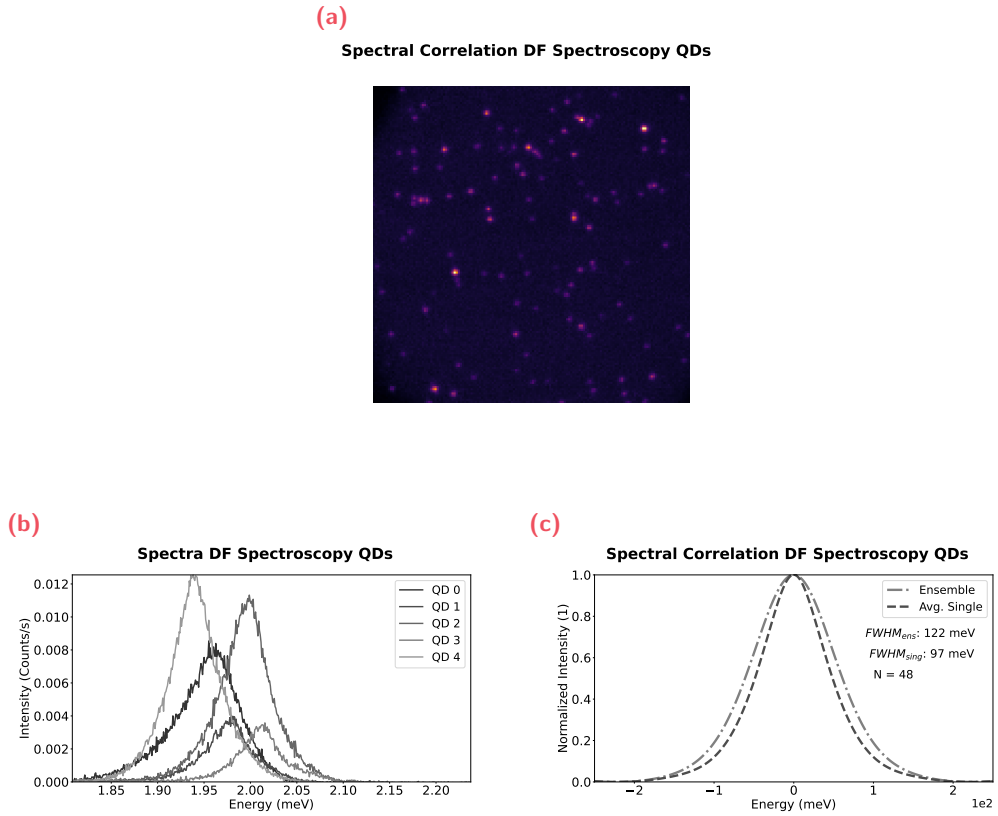

Fig. 4.7.: Darkfield Spectroscopy measurement of Cadmium-Selenide@Cadmium-Sulfide Quantum Dots (QDs) in Fluorescent mode. With *(a)* spectra of individual QDs, and *(b)* the spectral correlations of the average single and ensemble QDs, where the full-width at half maximums (FWHM) are compared.

4.1.4 Scattering Light of Plasmonic Nanoparticles Experiment

Thus far, we have compared photoluminescence of QDs of measurements on our PCFS setup and DF spectroscopy and found that they overlap nicely. These experiments give us confidence in our optical setup, and thus we move on to the nanoparticle of our choice, namely plasmonic nanosensors, which we later aim to use as in-solution biosensors. In chapter 2, we have worked through the mathematics of how electromagnetic waves interact with a metallic nanoparticle and found that a resonance of the free electrons occurs at a specific frequency of the incoming wave. There also exists a resulting outgoing electromagnetic wave and this is the signal of the plasmonic nanosensors we measure in our optical setup.

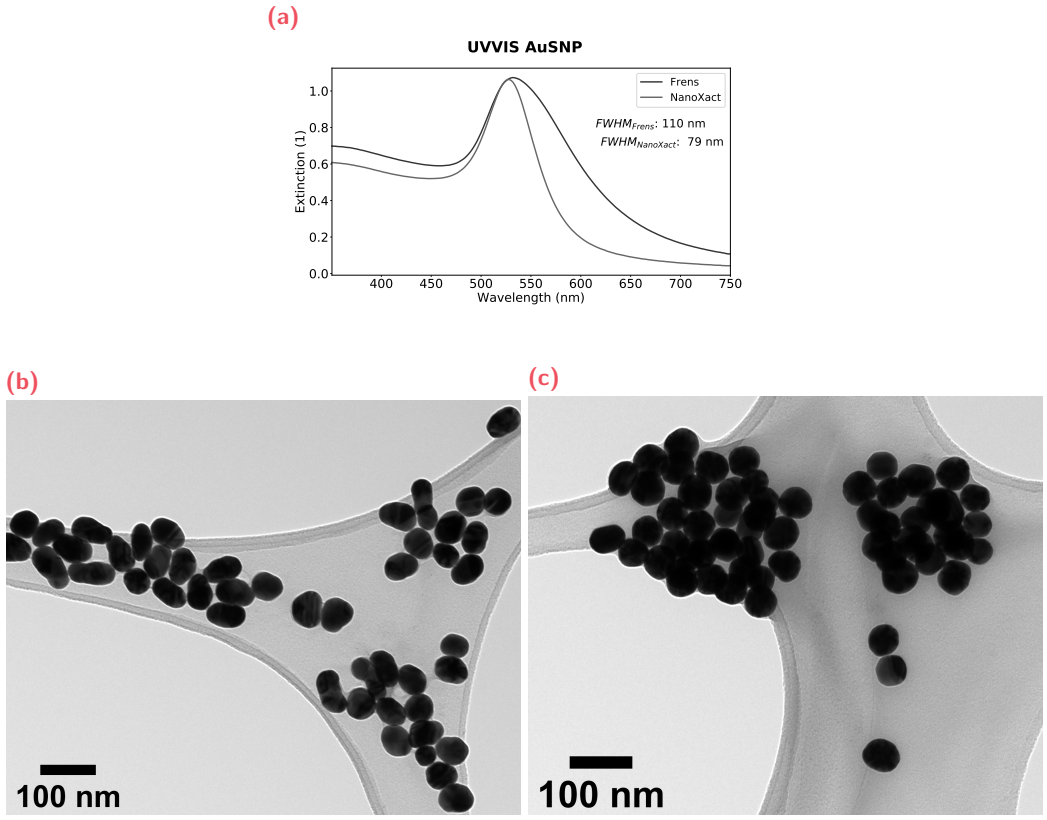

Fig. 4.8.: Characterization of Gold spherical nanoparticles (AuSNP). Through UVVIS spectra for *(a)* homemade AuSNPs, and *(b)* bought ultra-pure AuSNPs. Additionally, characterized through Transmission Electron Microscopy of *(c)* homemade AuSNPs, and *(d)* bought ultra-pure AuSNPs.

In Section 2.1, we have talked about absorption, scattering and extinction of metallic nanoparticles. Even tough they are related, they slightly differ and in the following experiments, we find ourselves comparing them occasionally. For instance the

UV/VIS data are the extinction spectra, whereas the FTS, PCFS, and DF spectroscopy experiments measure the scattering light of the nanosensors. All these comparisons are used to understand the diffusion and intrinsic spectral effects of plasmonic nanoparticles. Here, we also examine two different physical origins of the light, namely scattering and photoluminescence of these particles, where the benefits and disadvantages of both methods are discussed and compared. We also note that the single/ensemble information we obtain is a great indicator for synthesis optimization of metallic nanoparticles.

In the following experiments, we first examine Gold spherical nanoparticles as a model system. The synthesis is well-known and optimized and these particles are readily available to purchase. Therefore, we compare homemade Gold spheres (AuSNP) and commercial ultra monodisperse AuSNPs. The homemade AuSNPs are synthesized according to Frens' protocol for $50\,\mathrm{nm}$ in diameter.[107] The ultra monodisperse AuSNPs were obtained from NanoComposix under the name NanoXact (Product number: AUCN50-50M). In Figure 4.8a we see UV/VIS spectra of the homemade and commercial particles and observe that the homemade ones have a much broader spectrum, resulting in a FWHM of $110\,\mathrm{nm}$, whereas the commercial particles have a linewidth of $79\,\mathrm{nm}$. We hypothesize that this comes due to inhomogeneous broadening and this agrees with observations in TEM images, where the NanoXact AuSNPs are more uniformly shaped and size-distributed, see Figure 4.8b. Our homemade AuSNPs on the other hand have various shapes and actually predominantly seem to be elongated, see Figure 4.8c. These two particle batches are therefore perfect test samples for our PCFS setup, since we would expect the homemade particles to have different single/ensemble values and the commercial particles we expect to have much closer single/ensemble linewidths.

Scattering Photon-Correlations Fourier Spectroscopy on Gold Spherical Nanoparticles

In this section, we compare the AuSNPs as a test sample on our PCFS setup to understand the scattering signals of freely diffusing nanoparticles. Here, we first perform PCFS experiments on the homemade AuSNPs. As discussed in Section 2.1 plasmonic particles need to be excited/driven with a broadband light source. For this, we use a super continuum white light laser (NKT SuperK FIU-15) coupled to a filterbox (superk VARIA), which turns the white light spectrum into a smaller spectrum with variable center wavelength and bandwidth. To drive the AuSNPs, we set the VARIA to a center wavelength of $560\,\mathrm{nm}$ with a bandwidth of $180\,\mathrm{nm}$.

Homemade AuSNPs

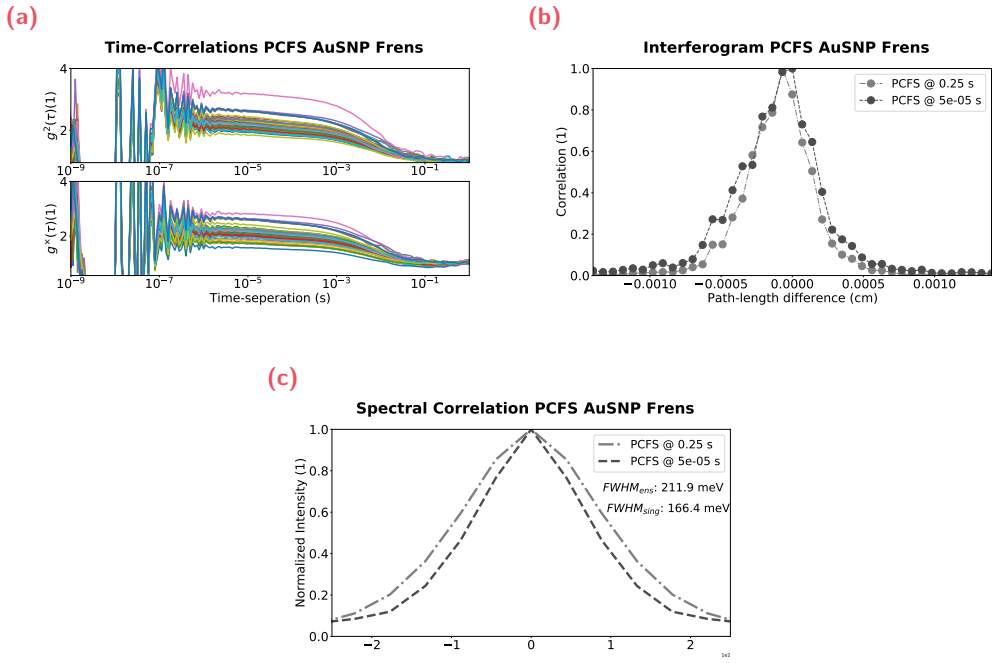

Fig. 4.9.: Photon-Correlation Fourier Spectroscopy (PCFS) experiment on homemade Gold spherical nanoparticles (AuSNP). In *(a)* the intensity correlations and *(b)* PCFS interferogram. Through Fourier transformation are *(c)* the spectral correlation obtained.

In Figure 4.9, we see the PCFS measurement with the auto- and cross-correlations in Figure 4.9a. These curves look different from the simulation and the fluorescent signals presented earlier in this chapter. Here, we find repeating spikes every $12.5\,\mathrm{ns}$, which overlap with the pulses of the white light laser operating at a repetition rate

of $80\,\mathrm{MHz}$. Additionally, we observe that the auto-correlation's occupation number (height of the curve) fluctuates more than the fluorescent QDs. Later in this section, we will discuss the reason for this in greater detail. From the correlation curves, the PCFS interferograms are computes, as shown in Figure 4.9b at two different time-separation. One is chosen at time-separations past the typical nanoparticle diffusion and the other well before, such that they represent the ensemble and the average single nanoparticle PCFS interferogram, respectively. Through sPCFS analysis with Gaussian fitting of the PCFS interferograms, we extract FWHMs of $129 \pm 4\mathrm{meV}$ and $159 \pm 4\mathrm{meV}$ for the average single and ensemble, respectively.

By Fourier transforming the PCFS interferograms, we find the spectral-correlation (Figure 4.9c). Here, we observe an average single FWHM of $166\,\mathrm{meV}$ and an ensemble of $212\,\mathrm{meV}$, which for Gaussian lineshapes translates to $117\,\mathrm{meV}$ and an ensemble of $150\,\mathrm{meV}$. These linewidth values are relatively close to each other, and the linewidth values indicate that the assumption of a Gaussian lineshape is not incorrect. We do however obtain a mismatch between the linewidth values of the UV/VIS experiment and this PCFS experiment. First, this comparison is not entirely fair, since we are comparing extinction with scattering data, however they should behave similarly. Second, the scattering PCFS data here is using a driving light that has a spectrum too, which is not being corrected for. Later in this section, we discuss the driving light correction of scattering PCFS experiments. We hypothesize that these two reasons cause the mismatch between the UV/VIS data and the scattering PCFS data.

Commercial AuSNPs

Having measured the homemade AuSNPs, we now measure the commercial AuSNPs, for which we hypothesize that the inhomogeneous broadening is less present. In Figure 4.10 a PCFS measure of the commercial AuSNPs (NanoComposix AUCN50-50M) is shown. In Figure 4.10a, the auto- and cross-correlations for different path-length differences are shown, where similar to the homemade AuSNPs we observe that the auto-correlation's occupation number (height of auto-correlation) varies a lot for measurements at different path-length differences. Next, in Figure 4.10b the PCFS interferograms at the same time-separations as for the homemade AuSNPs are shown, representing the average single and ensemble nanoparticles. For this sample, we extract linewidths of $117 \pm 4\mathrm{meV}$ and $135 \pm 5\mathrm{meV}$ for the average single and ensemble, respectively, from Gaussian fitting of the PCFS interferogram. The spectral-correlation are shown in Figure 4.10c, where the FWHM for the average single is $154\mathrm{meV}$ and that for the ensemble is $177\mathrm{meV}$. These translate to $109\mathrm{meV}$ and $125\mathrm{meV}$ for the spectral FWHM, assuming Gaussian lineshapes.

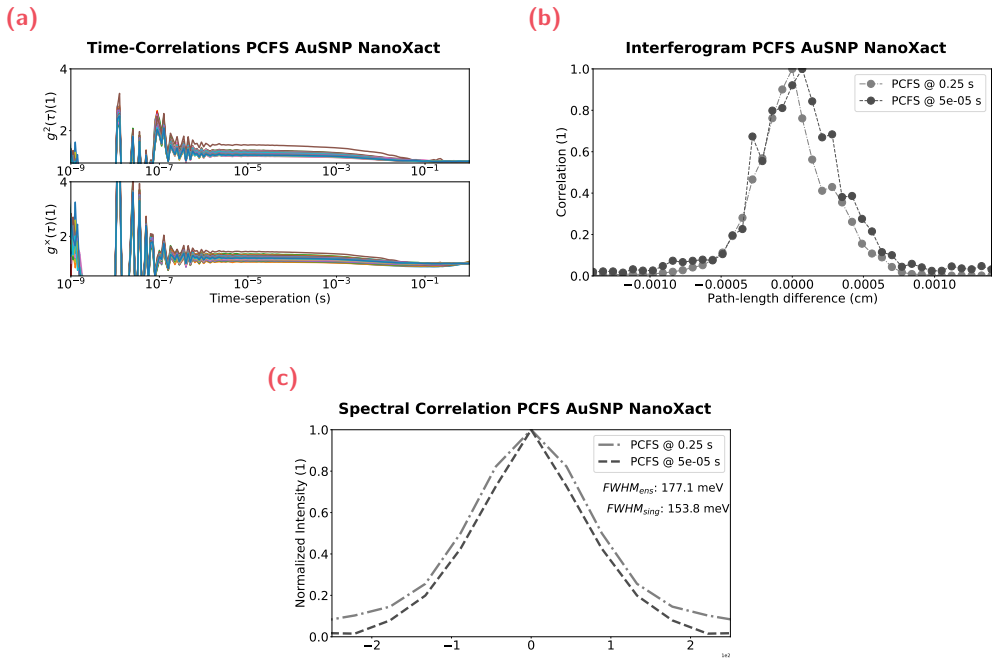

Fig. 4.10.: Photon-Correlation Fourier Spectroscopy (PCFS) experiment on commercial Gold spherical nanoparticles (AuSNP). In *(a)* the intensity correlations and *(b)* PCFS interferogram. Through Fourier transformation are *(c)* the spectral correlation obtained.

When we compare the linewidth values of our homemade AuSNPs with the commercial AuSNPs, we find that the commercial ones have slightly better monodispersity. Interestingly, however, the linewidth values and the ratios thereof lie very close at $87\,\%$ and $81\,\%$ for the commercial and the homemade particles, respectively. The huge difference in the UV/VIS spectra must thus be explained by something else than inhomogeneous broadening. We hypothesize that the slightly elongated shape of our homemade AuSNPs causes two LSPR resonances, where one is slightly red-shifted. The spectrum thus has become more rod-shaped than pure spherical.

Fourier Transform Spectroscopy on Gold Spherical Nanoparticles

The previous PCFS experiments give us insight in the average single and ensemble linewidths, however we are unable to make definitive conclusions about whether the LSPR linewidths are representative of the extracted linewidth values from PCFS. The main reason for this is that in the scattering light of metallic nanoparticles is dependent on a light driving the resonance. The scattering spectrum is therefore not unique and depends on the driving light spectrum, mainly because electric field

amplitude for the plasmon resonance has a wavelength dependence through $E_0(\lambda)$. Usually we treat E_0 constant over the entire spectrum, when we plot cross-section, but in experiment the scattered light is amplifies the driving light.[3]

FTS measurements output absolute spectra, which can be measured for both the plasmonic nanoparticle and the driving light to then calculate the pure LSPR spectrum. In the FTS measurements of homemade AuSNPs and commercial AuSNP as used previously for PCFS, we can actually calculate the pure LSPR spectrum, see Figure 4.11. Intensity-fluctuation corrected FTS interferograms are shown in Figure 4.11a and Figure 4.11b for homemade and commercial AuSNPs, respectively. These FTS interferograms are Fourier transformed to obtain the scattering spectra and the driving light spectra (interferograms not shown), see Figure 4.11c and Figure 4.11d.

Lastly, we compute the pure LSPR spectrum by dividing the scattering spectrum with the driving light spectrum as $s_{\mathrm{LSPR}}(\lambda) = s_{\mathrm{scat}}(\lambda)/s_{\mathrm{DL}}(\lambda)$. The scattering LSPR spectra in Figure 4.11e and Figure 4.11f, compare much better to the previously obtained UV/VIS extinction spectra (Figure 4.8a). The vast difference between the scattering spectra and the LSPR spectra make it thus difficult for us to say something definitive about the relationship between the obtained PCFS linewidth and the LSPR linewidths. In the following section, we discuss what a driving light correction method would look like for scattering PCFS experiments in order to obtain true LSPR linewidth information.

[3]Note, that in the literature some use the word "convoluted" here, which is not a true convolution rather a multiplication.

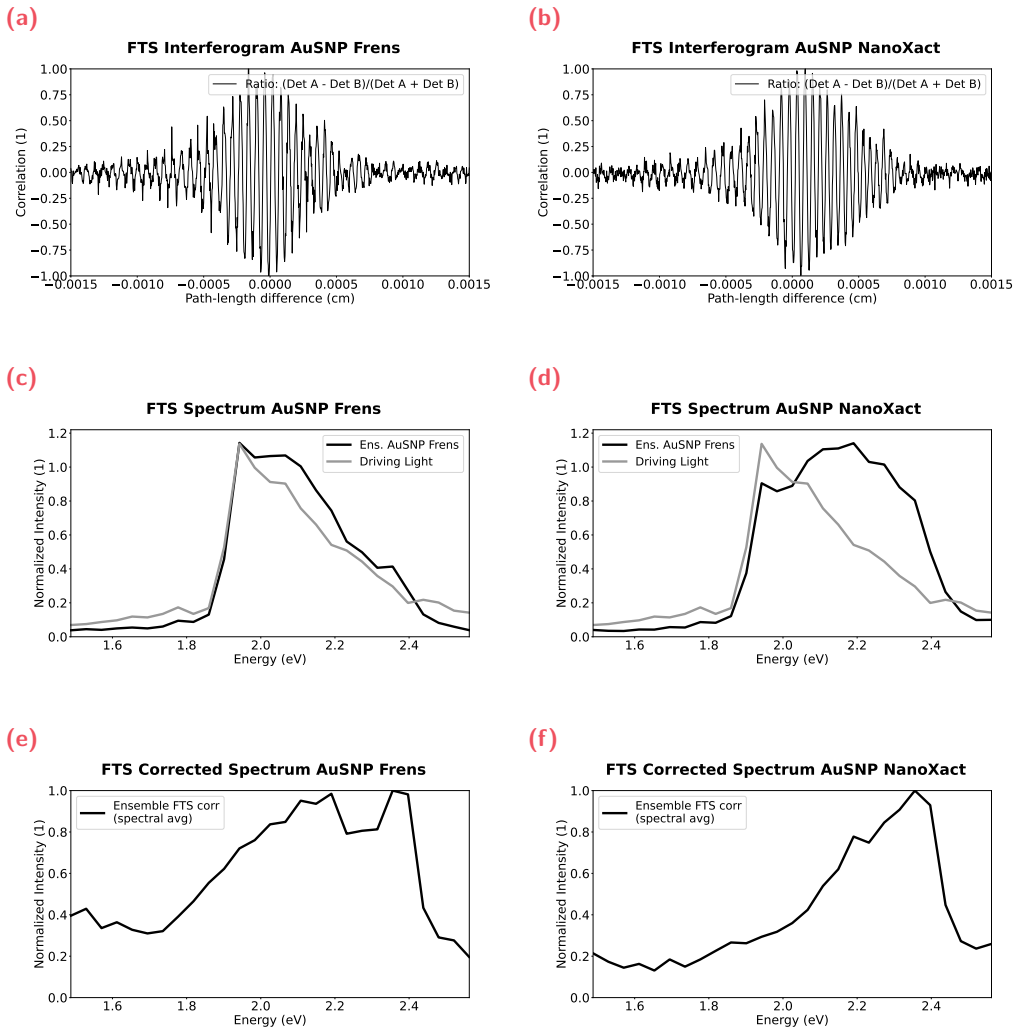

Fig. 4.11.: Fourier Transform Spectroscopy (FTS) on Spherical Gold Nanoparticles (AuSNP). Home-made AuSNP according to Frens' protocol with *(a)* FTS interferogram, *(c)* FTS spectra, and *(e)* corrected spectrum from division. Commercial AuSNP from Nanocomposix with *(b)* FTS interferogram, *(d)* FTS spectra, and *(f)* corrected spectrum from division.

To find the correct linewidths of scattering metallic nanoparticles in PCFS experiments, we would also need to perform a driving light correction. From FTS, we have seen that $s_{LSRP}(\lambda) = s_{NP}(\lambda)/s_{DL}(\lambda)$. Let us thus try to see what happens when this is plugged into the PCFS equation, Equation 3.91. For readability, I drop the wavelength and time dependence of the spectra in the following derivation.

$$
\begin{aligned}
g^{\times}(\delta,t) &= g^{(2)}\left(1-\frac{1}{2}\mathcal{F}\left\{s_{\mathrm{LSRP}} * s_{\mathrm{LSRP}}\right\}\right) && (4.1)\\
&= g^{(2)}\left(1-\frac{1}{2}\mathcal{F}\left\{s_{\mathrm{NP}}/s_{\mathrm{DL}} * s_{\mathrm{NP}}/s_{\mathrm{DL}}\right\}\right) && (4.2)\\
&= g^{(2)}\left(1-\frac{1}{2}\mathcal{F}\left\{s_{\mathrm{NP}}\cdot(s_{\mathrm{DL}})^{-1} * s_{\mathrm{NP}}\cdot(s_{\mathrm{DL}})^{-1}\right\}\right) && (4.3)\\
&= g^{(2)}\left(1-\frac{1}{2}\left(S_{\mathrm{NP}} * S_{\mathrm{DL,inv}}\cdot S_{\mathrm{NP}} * S_{\mathrm{DL,inv}}\right)\right) && (4.4)
\end{aligned}
$$

Here, we use S_{i} as the inverse Fourier transform of the spectrum s_{i}, with i a subscript to indicate which spectrum. Regardless to which space we transform, we remain with an unremovable convolution. We would actually like to write the solution as a function of the individual spectral correlations, $p_{\mathrm{NP}}(\zeta,\tau)$ and $p_{\mathrm{DL}}(\zeta,\tau)$ following Equation 3.92. Our best assumption so far is to ignore this convolution and write the spectral correlation as $p_{\mathrm{LSPR}}(\zeta,\tau) = p_{\mathrm{NP}}(\zeta,\tau)/p_{\mathrm{DL}}(\zeta,\tau)$. This however does not guarantee correct linewidth values. We have explored the possibility of correcting the spectral correlations with FTS measurements of the ensemble and the driving light. However, so far these efforts have not led to reasonable results. In Appendix A.11 goes deeper into corrections for scattering PCFS measurement.

We have however come up with experimental settings that one can use to obtain results closest to the true LSPR resonance spectral correlations. For this, any reflection of the driving light should be minimized, and the scattered light of the sample should be maximized by choosing correct optical elements. Correct alignment of the setup helps improving these two remarks. Additionally, experimentally, the driving light should be modulated to be as flat as possible, such that $E_0(\lambda) \approx E_0$ for all wavelengths. Lastly, one should pick a driving light that is broader than the expected LSPR linewidth, with a rule of thumb of a factor 2 to 2.5.

4.1.5 Comparative Measurements to Extract Single/Ensemble Linewidths

Thus far, we tested our setup with fluorescent light from CdSe QDs and found correct agreement of the obtained PCFS linewidths with literature and the comparative technique: dark-field (DF) spectroscopy. Then, we looked at PCFS measurement of AuSNPs and found linewidths that were indicative of the effects that we observed in UV/VIS and TEM, however we realized that true LSPR linewidths could not be obtained with scattering PCFS in its current state. In this section, we first explore whether the ratio of linewidth values obtained earlier actually represents the true inhomogeneity of the AuSNP samples. Thereafter, we explore an alternative physical origin of light of metallic nanoparticles as comparative technique. These measurements are used to gain insight in the behavior of metallic nanoparticles to identify a viable path towards in-solution sensing.

Dark-Field Spectroscopy on Gold Spherical Nanoparticles

The first comparative technique to our PCFS findings, similar to how we compared the QDs, is DF spectroscopy. Our aim of these experiments is to see whether at least the ratio between single and ensemble linewidths have the same trend. That would indicate PCFS's effectiveness of determining linewidth values of scattered light without the need of driving light correction.

To measure the nanoparticles, cover glasses (Thorlabs CG15NH1) have been sonicated for $30\,\mathrm{min}$ in acetone, isopropyl alcohol, and ultrapure water, successively. Thereafter, the cover glasses have been oxygen-plasma treated for $10\,\mathrm{min}$. A cover glass was spincoated (Laurell WS-650MZ-23NPPB) at $3000\,\mathrm{RPM}$ with $50\,\mu\mathrm{L}$ of nanoparticle solution. Driving light spectra of the lamp are measured by scratching a cover glass with sandpaper. DF measurements of particles in solution were performed by putting nanoparticle sample into a rectangular capillary (Vitrocom 3524-050). Note that these particles are freely diffusing, but since their concentration is high enough, we still obtain an ensemble spectrum.

In Figure 4.12 driving light correction spectra obtained through DF spectroscopy of homemade and commercial AuSNP in solution are shown. These results look similar to the UV/VIS measurements in Figure 4.8a, where the ensemble spectrum of the commercial AuSNPs is much narrower than the homemade ones. The peak positions and linewidths do not fully overlap, and we hypothesize that this is due to the comparison of extinction data with scattering data.

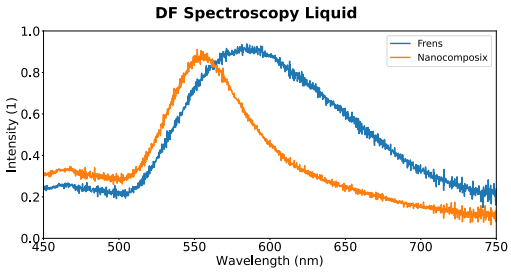

Fig. 4.12.: Darkfield spectroscopy of Gold spherical nanoparticles (AuSNP) in solution. Commercial (Nanocomposix) are compared with homemade (Frens) AuSNPs. The driving light spectrum is obtained by scratching a cover slip, which is used as divisor of the measured raw spectra to obtain the scattering spectrum.

In Figure 4.13 driving light corrected DF spectroscopy spectra of several AuSNP on a glass substrate are shown. Here we observe that the DF spectra are not single peaked and do not resemble the ensemble LSPR spectrum. In Figure 4.13a for our homemade AuSNPs, we only observe one nanoparticle having a similar spectrum to the ensemble obtained with UV/VIS and FTS, namely NP0. All the nanoparticle spectra have variously different spectra. We hypothesize that three things could be happening in these experiments. First, the (slightly) greater inhomogeneity or the elongated shape of the homemade AuSNPs caused multiple resonances and different peak positions. The second effect could be that these particles cluster due to electrostatic attraction when they are removed from their suspension. In this case, dimers, trimers, and multimers would form which typically have multiple resonances and red-shifted peaks.[108, 109] Third, the nanoparticles are sensing the presence of the substrate and their orientation on it caused the LSPR resonance to shift.

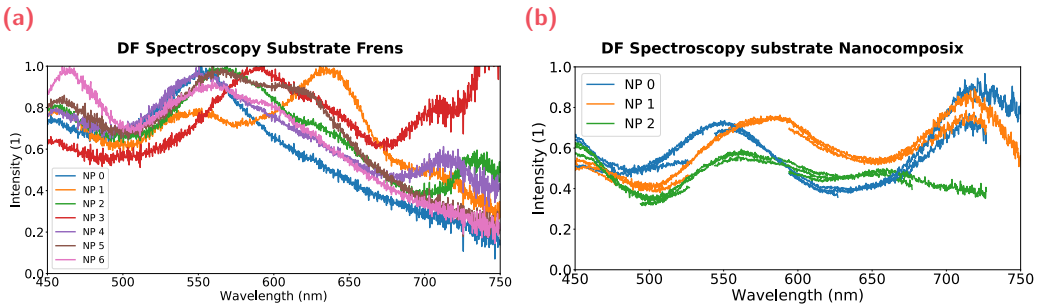

Fig. 4.13.: Darkfield spectroscopy measurements on Gold spherical nanoparticles (AuSNP) on a substrate. *(a)* Spectra of homemade AuSNPs and *(b)* spectra of commercial AuSNPs.

We thus measured the commercial AuSNPs, as shown in Figure 4.13b. Here we expect less inhomogeneity, thus we could prove or disprove one of the hypotheses

above. We observe similar multi-peaked spectra as with the homemade AuSNPs. Additionally, we measured different parts of the spectrum separately to check whether the stitching algorithm was causing this, however that was not the case. We thus must conclude that these particles cluster when trying to spincoat them or that the substrate has measurable effects causing the LSPR to differ vastly from in-solution measurements. We therefore cannot use DF spectroscopy as a comparative technique for our scattering PCFS measurement on AuSNPs. For that reason, we searched for an alternative method, and that presented itself as photoluminescence of metallic nanoparticles. This way, in-solution measurements with pure LSPR spectra can be used. Before we discuss this method, a small section is dedicated to investigate how big substrate effects can be for plasmonic nanoparticles.

Substrate Measurements compared to Solution Measurements

As a comparative technique for our PCFS experiments, we have spincoated nanoparticles on a substrate. For the QDs sample, we have not observed any strange behavior and the comparison could be done with ease. For metallic nanoparticles, however, we observed strange behavior of multi-peaked LSPRs that would indicate clustering or substrate effects. In this section, we explore the effects of a substrate computationally and compare our finding to the work of Martinsson et al.[110]

As discussed in Chapter 2, metallic nanoparticles are sensitive to dielectric changes in their proximity. When they are spincoated on a substrate, we can expect different behavior from when they are suspended in solution. Firstly, the refractive index is expected to be different, because in solution, particles will mostly be surrounded by water. On the other hand, spincoated particles are surrounded by air and a substrate. Martinsson et al. published computational work of different shaped plasmonic nanoparticles on substrates.[110] He uses a different computational method called Finite Difference Time-Domain (FDTD) and finds that the substrate is affecting the spectra and the sensitivity of the nanoparticles. Namely, instead of sensing analyte, they are now sensing the presence of the substrate. Additionally, the substrate physically prohibits analyte from diffusing into the sensing volume of the nanosensor. As a result, both of these effects reduce the effectiveness of the sensor. Interestingly, he finds that spherical nanoparticles are the least affected by the substrate.

His findings would suggest that our DF spectroscopy measurements on the AuSNPs are valid, since they should not be affected by the substrate as much. This would hint that clustering due to electrostatic interactions is an issue when our nanoparticles are removed from the suspension. Martinsson's results however teach us that nanoparticles with corners, such as our preferred nanosensor; the decahedral nanoparticle, are more affected by the substrate. Therefore, we sought out a different comparative method, which we found in photoluminescence of plasmonic nanoparticles. This is discussed in the following section.

The reason why we did not observe any substrate effects with the fluorescent QDs is due to the fact that they are less sensitive to the presence of a substrate an other QDs in their proximity. They are less sensitive to dielectric changes, but exhibit other phenomena in the presence of a substrate. These effects also only result in small spectral changes in the QD spectrum.

We were interested in seeing whether Discrete Dipole Approximation (DDA) computation gives similar results as FDTD for particles in the presence of a substrate. In Figure 4.14, we have used the surface mode of ADDA to compute sensitivity curves

for a $40\,\mathrm{nm}$ Silver cubic nanoparticles (AgCNP) on a glass surface ($n = 1.5$) with dielectric constants from Johnson and Christy.[39] We have also explored the surface mode for Silver decahedral nanoparticles (AgDNP), however those computations has thus far not been successful because of technical reasons. For a decahedron on a substrate, the orientation becomes more important, as well as the polarization direction of the incoming light. For a cubic nanoparticle, this has been much easier to simulate, due to its symmetry. Therefore, we present the spectra of a AgCNP in solution and on a glass substrate in Figure 4.14. Here, we observe that the resonances (both dipolar and quadrupolar) shift due to the substrate. Additionally, the amplitudes of both resonances change, being reduced for the AgCNP on a substrate. Lastly, in Figure 4.14b, we computed the sensitivity by tracking the dipolar resonance as a function of refractive index change. Here, we observe a diminished sensitivity from $194\,\mathrm{nm\,RIU^{-1}}$ ($1160\,\mathrm{meV\,RIU^{-1}}$) to $111\,\mathrm{nm\,RIU^{-1}}$ ($636\,\mathrm{meV\,RIU^{-1}}$) when a substrate is introduced. This means that the sensitivity of a Silver cube nanoparticle on a substrate is reduced by $45\,\%$. Martinsson et al. found a reduction of $28\,\%$, which could be explained by the different electromagnetic simulation tool (DDA vs. FDTD) or the different dielectric constants that have been used or because of different corner rounding.

The unwanted spectral effects due to the presence of a substrate and clustering make it difficult to get a comparative single particle technique to our PCFS measurements. We therefore went through the literature in search of other in-solutions techniques and only found a different physical origin of metallic nanoparticle light: photoluminescence. In the following section, scattered light and photoluminescent light of plasmonic nanoparticles is compared to give insight into single/ensemble linewidths.

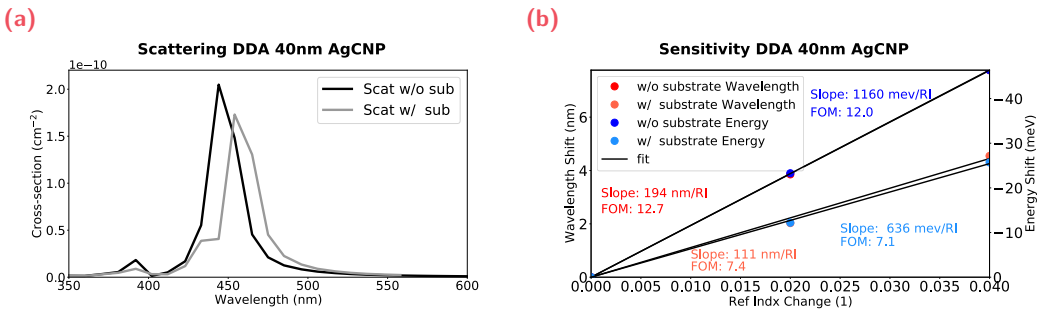

Fig. 4.14.: Discrete Dipole Approximation computations of Silver cubic nanoparticles (AgCNP). *(a)* the cubic nanoparticle shape with slightly rounded edges, *(b)* the cross-sections of a AgCNP in solution ($n = 1.33$) and on a substrate ($n = 1.5$), and *(c)* the sensitivity curves calculated by tracking the main (dipolar) resonance as a function of refractive index change.

4.1.6 Photoluminescence of Plasmonic Nanoparticles

In the previous sections, we have discussed PCFS experiments on scattering signals of metallic nanoparticles. We then explored different techniques to compare the linewidth values obtained through sPCFS analysis, but found that substrate effects and clustering due to electrostatic interactions made these comparisons very difficult. We are therefore in need of another in-solution technique. From literature, we found an alternative method to obtain light from metallic nanoparticles; photoluminescence (PL).

Surface Enhanced Raman Spectroscopy (SERS) has always measured broad background signals under the resonant Raman peaks, when metal substrates were used. It was only later hypothesized that these substrates themselves are causing this background due to intrinsic photoluminescence. Then Wilcoxon et al. showed that small Gold clusters have greater photoluminescence quantum efficiencies over planar Gold surfaces and that the physical process comes from interband electron-hole pair recombination.[111] This started the interested in photoluminescence of plasmonic nanoparticles and Mohamed et al. showed that the PL intensity scales linear with size, similar to how intensity of QDs scales.[112] Tcherniak et al. compared the scattering and PL spectra of Gold nanorods to find that they look the similar, showing that the PL emission is linked to the LSPR.[113] Since the LSPR and the PL seem to be linked, we could use the PL of metallic nanosensors to compare to our scattered PCFS data. Namely, that results in LSPR spectra that do not need to be driving light corrected.

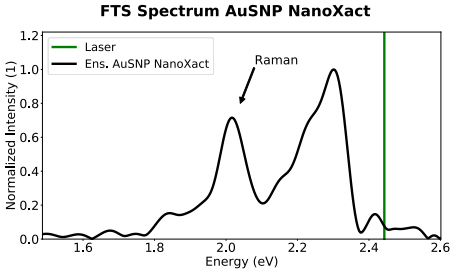

Fig. 4.15.: Fourier Transform Spectroscopy spectrum of photoluminescence of AgDNP in water, where we observe the LSPR peak at $2.3\,\mathrm{eV}$ and an additional Raman peak from OH-stretching of the water molecules at $2.0\,\mathrm{eV}$. The nanoparticle is excited with a laser at $2.443\,\mathrm{eV}$, making the Raman peak appear at energies of $412\,\mathrm{meV}$ to $422\,\mathrm{meV}$ in agreement with literature.[114]

The PL emission process, however, is less efficient than scattering, having Quantum Efficiencies of around $10^{-4} - 10^{-5}$.[111] Due to the lower emission efficiencies, high excitation powers are needed, and other photoluminescent processes can be

excited as well. For instance, we have observed a Raman peak of the vibrational mode (OH-stretching) from water in our PL experiments at energies of $412\,\mathrm{meV}$ to $422\,\mathrm{meV}$, see Figure 4.15, that matches with literature.[114] In order to perform PL experiments on metallic nanoparticles, we would need to use a long-pass filter to remove the excitation filter and a short-pass filter to remove the Raman peak from water. This effectively narrows the width of the spectra we can observe to $\sim 400\,\mathrm{meV}$.

Fourier Transform Spectroscopy spectrum of photoluminescence of AgDNP in water, where we observe the LSPR peak at $2.3\,\mathrm{eV}$ and an additional Raman peak from OH-stretching of the water molecules around $2.0\,\mathrm{eV}$. The nanoparticle is excited with a laser at 2.443 eV, making the Raman peak appear at energies of $412\,\mathrm{meV}$ to $422\,\mathrm{meV}$ in agreement with literature.[114]

Auto-correlation Height Fluctuations

Before we move onto PL experiments of plasmonic nanoparticles, a short section is dedicated to the fluctuation differences in the auto-correlations between PL and scattering experiments. The reader might have noticed that the auto-correlation curves in Figure 4.6a show less variation in their amplitude than the auto-correlations in Figure 4.10a. We hypothesize that this variation is explained due to intensity fluctuations in the measured photon rates, caused by the light bursts of the nanoparticles. Previously, in Equation 2.4, we have found that the scattering cross-section scales as V^2. This means that small variations in the size distribution cause intensity fluctuations, which in term cause auto-correlation fluctuations. On the other hand, photoluminescence is determined by different factors, such as quantum yield and absorption cross-section.[115] Most of these factors do not have a dependence on size, except for the absorption cross-section. From Equation 2.4, we have found that the absorption cross-section scales at V. We believe that because of this reason, the fluctuations in the amplitude of the correlation curves are more dominant in scattering signals than in photoluminescent ones. We thus summarize:

$$I_{scat} \propto V^2, \qquad I_{PL} \propto V\,. \tag{4.5}$$

In the next section, scattering light and photoluminescent light coming from plasmonic particles are compared. With the use of PL to aim to obtain LSPR spectra, such that driving light correction is not needed. Additionally, since these are in-solution measurements, we do not expect clustering and substrate effects to be present. This way, we can compare linewidths of the average single nanoparticle and the ensemble that are obtained with scattering and PL.

4.1.7 Comparison Scattering and Photoluminescence of Gold Coated Decahedra Nanoparticles

Here, we discuss the comparison between photoluminescence (PL) and scattering of Gold coated Silver decahedra (AgDNP@Au). UnPEGylated AgDNP@Au synthesized with the protocol in Section 2.4.2 have been concentrated by a factor of 5 to 10 and the supernatant was used as dispersion media. A long-pass (FELH0500) and a short-pass (FES0550) filter have been used to filter out the excitation laser and the Raman peak in photoluminescence. These filter have been rotated relative to the incoming beam to change their cut-off wavelength to span a range of $\approx 400\,\mathrm{meV}$.

For the scattering experiments, these filter remained in the setup to create a driving light spectrum with the same bandwidth. A super continuum white light laser (NKT superK FIU-15) with a filterbox (superK VARIA) were tuned to create a driving light spectrum with a center wavelength of $500\,\mathrm{nm}$ and bandwidth of $150\,\mathrm{nm}$. For the PL experiments, a 80mW laser diode (Thorlabs PL450B) with a wavelength of $450\,\mathrm{nm}$ in combination with a clean-up filter (Thorlabs FBH450-10) have been used for the PL experiment.

In Figure 4.16 scattering PCFS data is shown in the left column and PL PCFS data is shown in the right column. In Figure 4.16a and Figure 4.16b, the auto- and cross-correlations at various path-length differences are shown. Here, we observe (as expected) more fluctuations in the amplitude of the correlation functions for the scattering light. Through sPCFS analysis PCFS interferograms are obtained for the average single nanoparticle and the ensemble chosen at a time-separation well before and well past the typical diffusion of the nanoparticles, respectively. This is shown in Figure 4.16c and Figure 4.16d. By fitting the scattering interferograms with Gaussian fits, we extract linewidth values of $150 \pm 10\mathrm{meV}$ and $183 \pm 2\mathrm{meV}$ for the average single nanoparticle and the ensemble, respectively. For the PL interferograms we obtain $135 \pm 3\mathrm{meV}$ and $138 \pm 1\mathrm{meV}$ as FWHM values for the average single and the ensemble, respectively. We observe a similar single/ensemble linewidth ratio of $0.77\,\%$ from the spectral correlations linewidths in Figure 4.16e for scattering light of AgDNP@Au with $199.8\,\mathrm{meV}$ and $259.9\,\mathrm{meV}$ for the average single and the ensemble, respectively. In Figure 4.16f we find a linewidth of $184.5\,\mathrm{meV}$ for the average single nanoparticle and a linewidth of $194.8\,\mathrm{meV}$ for the ensemble, resulting in a ratio of $0.95\,\%$.

From these measurements, we find that the PL data indicates high monodispersity in this sample, whereas the scattering light seems to indicate slightly less monodispersity. We hypothesize that three things could be affecting these linewidth ratios. First, the ensemble linewidth value for scattering light is influenced by the driving light due to unwanted reflections in the setup. Namely, there is no spectral or

mechanical filtering (other than the pinhole) happening in the optical setup. These reflections would only affect the ensemble linewidth values, since sPCFS analysis filters out Poissonian distributed photon pairs. We do observe that the average single linewidths of scattering and PL are much closer to each other. Second, the volume effect, as discussed in the previous section, could skew the photon energy distribution to mostly represent large particles. In that case, both the average single and the ensemble linewidths would be affected and simply have different values, because they represent a different (sub)-population of the sample. Lastly, the

driving light could affect the observed spectrum, however, when the average single and ensemble linewidths are close to each other this effect could lead to incorrect linewidth values, but the ratio should be conserved.

In this first half of this chapter, we have tested our optical setup first computationally by including light bursts of nanoparticles diffusing through a focal volume. Then we experimentally tested our setup with a known sample; Cadmium Selenide Quantum Dots. In those experiments, we measured the photoluminescence and found good agreement with literature and with a comparative technique called: dark-field (DF) spectroscopy. We then analyzed PCFS data of scattering nanoparticles freely diffusing in solution and compared them with DF spectroscopy measurements. Here, unwanted substrate and clustering effects are observed, such that we explored the photoluminescence (PL) of plasmonic nanoparticles as an in-solution alternative to scattering. For nanoparticle synthesis optimization with scattering light, proper mathematical understanding of how to perform driving light correction in PCFS is still needed. PL of metallic nanoparticles however seems a promising alternative that does not need this correction. These investigations have helped us understand the diffusion and intrinsic spectral effects of plasmonic particles in both scattering and PL better. We realize that for in-solution sensing, the exact FWHM information might actually not be needed. In the next section, we discuss in-solution sensing experiments through PCFS of metallic nanosensors and how we change the driving light spectrum to our advantage with the learning from the first half of this chapter.

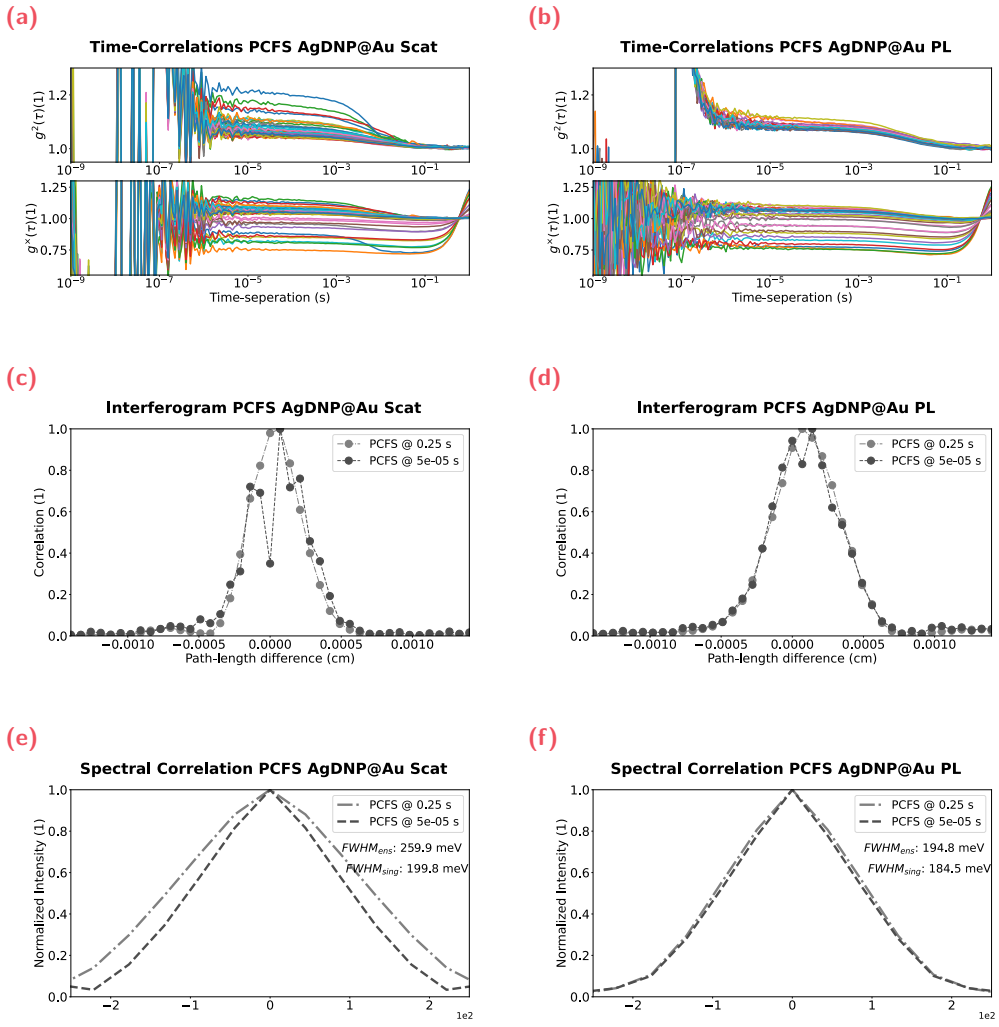

Fig. 4.16.: Photon-Correlation Fourier Spectroscopy measurements of Gold coated Silver decahedra nanoparticles (AgDNP@Au) comparing scattered and photoluminescent (PL) light. In *(a)* and *(b)* the intensity correlations are shown for scattering and PL, respectively. In *(c)* and *(d)* the PCFS interferograms are shown for scattering and PL, respectively. Lastly, in *(e)* and *(f)* the spectral correlations of the average single and the ensemble for both scattering and PL are shown, respectively.

4.2 Biomolecular Sensing

In this section sensing experiments with metallic nanoparticles as freely diffusing nanosensors are measured on a custom-built optical setup. The setup offers high temporal and spectral resolution and can extract the average single particle spectral dynamics through diffusion correction of auto- and cross-correlations. This setup is known as Photon-Correlation Fourier Spectroscopy (PCFS) and in this section a slight modification to the excitation/driving light is made from finding of experiments described in the first half of this chapter. The experiments in this chapter are meant to show the capabilities of our combined method (nanosensors & optical setup) to detect biomolecules and their interaction partners.

We start the section with the expansion of an MC computational model to simulate fast, and transient binding interactions observed by diffusing nanosensors. Then 2 laser scattering is introduced as alternative excitation/driving light method. Thereafter, we show experiments of the detection of bio-like molecules in the proximity of the nanosensors. Then a fast interacting protein pair is examined and lastly a strong binding protein pair is measured in FTS mode.

4.2.1 Fast Kinetic Sensing Computationally

In this section, we combine all the parts of previous simulations into one big computational model that resembles sensing of nanoparticles diffusing through a laser focal volume. In this model, the photons are generated in bursts of light as if they were emitted from nanoparticles diffusing through a focal volume. For this, we assume a spherical laser focal volume and compute the dwell time of the particles with the use of Fickian diffusion. The particles emit light for the entire duration of the dwell time and the nanoparticles' appearance in the focal volume is Poissoinian distributed. Then, for every emitted photon a photon energy is selected with MC sampling of two distinct optical states (spectra), which are computed from Mie-theory. Exponential probabilistics are used to switch between the two optical states, such that they resemble simple natural binding and unbinding events.

In Figure 4.17 simulation data is shown with switching rates set to $k_{\mathrm{on}} = k\mathrm{off} = 1 \cdot 10^{5}\mathrm{s}^{-1}$, which represent fast interaction kinetics only a factor 100 slower than the Smoluchowski limit.[116, 117] The two optical states in Figure 4.17a are computed from Mie Theory, as previously seen in Section 2.1.2. The spectra for the two optical state represent a spherical Silver nanoparticle with one single protein ring of $4\,\mathrm{nm}$ and a spectrum of that same construct but with two protein rings, as previously seen

in Figure 2.6. The intensity correlations after simulation are shown in Figure 4.17b and the spectral correlations in Figure 4.17c are computed through sPCFS analysis, where diffusion effects of the particles are removed. This way the spectral dynamics of the average single nanoparticle can be extracted. To obtain greater statistical power, the FWHM of the spectral correlations as a function of time is shown in Figure 4.17d. These data are fitted with an exponential decay according to Equation 3.101, which returns $k_{on} + k_{off} = 1.7 \pm 0.2 \cdot 10^5 \mathrm{s}^{-1}$.

The results of the computational model agree well with the input parameters. This shows that through sPCFS spectral dynamics can be unveiled of the average single nanoparticle at sub-ms timescales. This simulation suggests that correlation studies on photon streams with spectral shifts of less than $10\,\%$ of their FWHM, occurring sub-ms timescales can be resolved with good signal-to-noise (S/N) ratio. These findings give us great confidence in the method, especially since earlier S/N ratios have been found to agree well between simulation and experiment (Section 3.5.3 and Section 3.6.2).

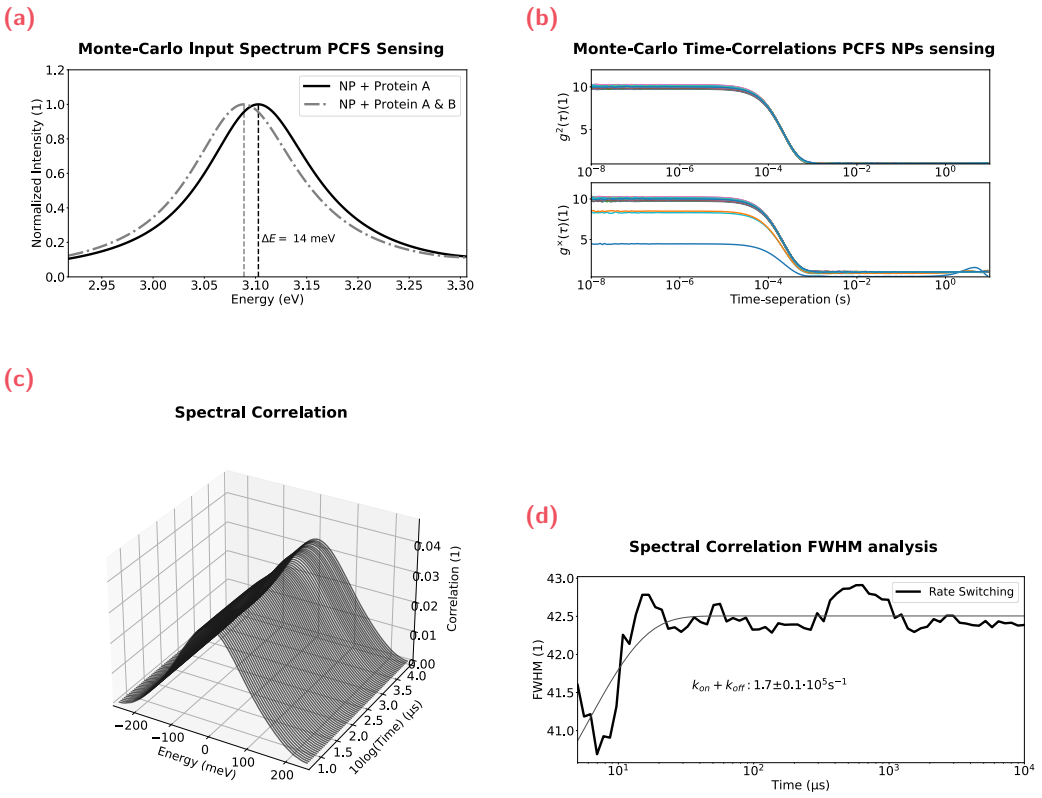

Fig. 4.17.: Photon-Correlation Fourier Spectroscopy computation of nanoparticles with protein rings surrounding them dynamically switching between having only 1 ring or 2 rings through exponentially distributed switching times. In *(a)* the input spectra calculated with Mie-theory, *(b)* the intensity correlations, *(c)* the spectral correlations, and *(d)* the full-width at half maximum (FWHM) of the spectral correlation as a function of time showing sub-ms dynamics.

4.2.2 2 Laser Continuous Wave Scattering

Having seen that spectral shifts calculated with Mie Theory, that represent biomolecular interactions sensing events, resulted in measurable outputs simulated with our Monte-Carlo method makes us more confident that real life experiments would have observable outcomes. In this last part of this dissertation, experiments on biomolecular sensing of freely diffusion nanosensors measured with our home-built PCFS setup are discussed. There are however a few learning points from Section 4.1.4 that have not been elaborated yet, since they were not needed for the linewidth comparisons between the average single and the ensemble.

First, we found that a pulsed laser created spikes in the auto-correlation that can be observed down to $1\,\mu$s. It is important to know that the observation thereof heavily depends on the bin width of the auto- and cross-correlations. We therefore believe that continuous wave (CW) lasers were needed to ensure artifact free detection down to $1\,\mu$s. The $1\,\mu$s-regime is of importance for bio-sensing, because Baaske et al. measured characteristic diffusion times of biomolecules with Gold nanorods that are placed a substrate on this order of magnitude.[118] If we are to measure fast and transient biomolecular interactions that occur at the diffusion limit, this regime should be measurable. Additionally, to test whether our combined method is working, we would first try to observe simple diffusion, before measuring biomolecular interactions.

The main problem with CW light sources is that there do not exist many that output a broad spectrum and that can be confined spatially to form a focal volume for PCFS experiments. However, we hypothesized that to observe spectral shifts that reflect biomolecular dynamics in the proximity of the nanosensor, we do not need the LSPR linewidth information. We only need a spectrum that reflects the spectral shifts, and for this we decided to explore the use of single wavelength laser diodes to form a comb-like spectrum. Upon a sensing event, the scattering spectrum of the nanoparticle will shift, causing the relative intensities of the "comb" to change. We could then track spectral dynamics from these relative intensity changes, similar to the *Gedankenexperiment* in Section 3.5.3.

The simplest "comb" that can be formed consists of 2 laser diodes. We realized that at least two lasers should be used, since the relative intensity change between the two lasers tells something about spectral changes and thus sensing events. Whereas, when only one laser is used, one cannot distinguish between intensity fluctuations due to particle diffusion or spectral fluctuation due to sensing. The reasoning here is similar to why a ratio of detector intensities in dual-path FTS is able to obtain

particle dynamics free spectra (Section 3.2). We expect the intensity of both lasers to change relative due to spectral shifts in the LSPR spectrum and equally due to particle diffusion. Then with sPCFS analysis, the diffusion effects from the average single particle are corrected for, leaving only the spectral dynamics.

Figure 4.18 shows the concept of 2 laser scattering for biomolecular sensing, where two lasers are used to generate scattered light from freely diffusing nanosensors. In Figure 4.18a an extinction spectrum (should actually be scattering, however they are similar in shape) is illustrated with 2 laser shown at their laser lines. We decided to use laser diodes at $488\,\mathrm{nm}$ (Sharp GH04850B2G) and $520\,\mathrm{nm}$ (Thorlabs CPS520), which are positioned left and right of the LSPR peak maximum. We expected a two-peaked spectrum to have a three-peaked spectral correlation, whose peak amplitudes would vary as a function of time due to spectral dynamics, see Figure 4.18b. The amplitude of these spectral correlation peaks as a function of time reflect biomolecular sensing events observed through metallic nanosensors diffusing in solution. The characteristic biomolecular rate constants can then be extracted with the use of fitting models.

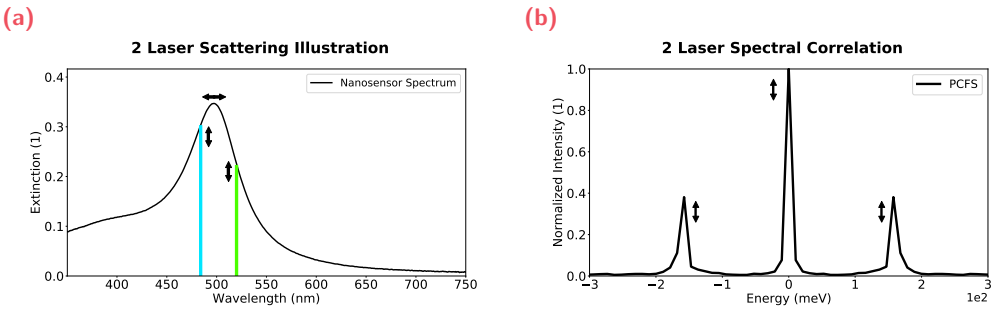

Fig. 4.18.: The concept of 2 laser scattering for biomolecular sensing with *(a)* an illustration of the position of 2 lasers compared to the plasmon resonance peak. *(b)* the spectral correlation as a results of 2 lasers, of which the amplitude is indicative of biomolecular sensing events.

2 Laser Scattering Analysis

In this section the analysis of 2 laser scattering data is discussed by looking at data of a sample with only nanosensors. Here the pipeline of computational steps is explained that is used to turn the spectral correlation data into bio-sensing curves. As we have seen in earlier simulations and experiments both in Chapter 2 and Chapter 3, raw spectral correlation curves do not obviously show the spectral dynamics and sometimes the FWHM of the spectral correlation was analyzed. Having a 3-peaked

spectral correlation with peak widths that are not expected to change, we have to employ something else and will turn to the relative amplitudes of the peaks.

In Figure 4.19 data is shown of a sample consisting of just nanosensors. Important to note is that for all the experiments presented in this last part, we had to concentrate the stock solutions of the AgDNP@Au@PEG particles by a factor of 5 to 10 We found out that when the amplitude of the auto-correlation curves lies around 1.3 to 2 with 1.5 being the preferred value, we obtain good results and are not hindered by scattering fluctuations that scale as V^2. Additionally, we believe that this volume effect is minimized in experiments with AgDNP@Au@PEG, because of the many centrifugation steps in the protocols, which filter out small seeds and bigger particles/clusters.

In Figure 4.19b, the spectral correlation of a 2 laser scattering experiment is shown with the typical 3 peaks, named "Side", "Zero", and "Side", respectively. We would want to use the amplitude of the Side and the Zero peaks, however we observed variation when taking a line section of the side peak. Most likely, this variation is caused by the number of data points in our spectral correlation. This causes the actual position of the side peak to fall in between two data point, resulting seemingly in "spectral fluctuations" in the side peak. Therefore, we decided to compute the areas under the peak, by integrating the curves in between the black vertical lines. This area under the curve we then treat as being the amplitude of that peak to obtain ore statistical power and reduce artifacts due to the low number of data points in the spectral correlations. We also made sure that the spectral fluctuations did not come from the laser diodes themselves to analyzing reflected light off of a mirror. This is shown in Appendix A.14.

The areas under the curves for the Zero and the Side (which we later simply name Zero and Side peaks) are shown in Figure 4.19c, where because of symmetry only one Side peak is plotted. Before we go deeper into discussing these curves, let us recall Section 3.5.3, where we discussed the *Gedankenexperiment* of two Dirac Delta-like functions that act as two distinct optical states. This example translates well to a 2 laser scattering experiment. In the 2 laser scattering experiment, however, the amplitude will not completely go to zero after switching, but only slightly reduces. From the Gedankenexperiment we learned that the Zero and the Side peak are not decoupled from each other. Whenever one increases in amplitude, the other decreases, because the integral over the entire energy space should be conserved. This is observed in Figure 4.19c, where we see the Side peak behaves oppositely to what the Zero peak does. Now we have a better understanding of where these come from and what they represent, we can discuss their shapes.

We hypothesize that the Zero and Side peaks of a sample with just nanosensors should be flat as a function of time. This is expected because there should not be spectral dynamics due to the absence of sensing events. Unfortunately in Figure 4.19c, we found that these peaks are not constant over time. We have however formulated views on what the intrinsic dynamics in these curves could be caused by. Let us start at short time-separations and look at the Zero peak (the Side does the exact opposite). In the range of $0.1\,\mu\mathrm{s}$ to $1\,\mu\mathrm{s}$ a steep decline is observed in the Zero peak, which we believe is caused by afterpulsing of the single photon detectors we use. These detectors can trap electrons after a real detection event that result in a cascade of unreal detection events much later after the original event. Typically, this effect is intensity dependent and the shape is conserved based on the detector. Appendix A.11.2 shows more on the characterized of the afterpulsing. A second dynamical event in Figure 4.19c is observed around $100\,\mu\mathrm{s}$, causing a small drop in amplitude. We hypothesize that this could be caused by two effects; either rotational diffusion of the nanosensor or surface ligand mobility. Then lastly, towards $1\,\mathrm{ms}$ to $10\,\mathrm{ms}$ an increase in the Zero peak amplitude is observed. These values get close to the diffusion time of the nanoparticle of $\tau = 1\,\mathrm{ms}$. Therefore, less photon pairs are available in sPCFS analysis resulting in higher noise.

Something that stands out in Figure 4.19c is that the shapes of the curves look identical, but their absolute values are different, despite coming from the same sample batch. Therefore, we investigated whether the differences of the curves (quasi derivatives) are conserved. We compute the discrete differences of the spectral correlation, $dP\left(\zeta\right)$, as:

$$dP\left(\zeta\right)\left[\tau_{\mathrm{i}}\right] = P\left(\zeta\right)\left[\tau_{\mathrm{i}}+1\right] - P\left(\zeta\right)\left[\tau_{1}\right]\,, \tag{4.6}$$

where $P\left(\zeta\right)$ is the (discrete) spectral correlation, τ_{i} is the index indicative of time-separation τ . In Figure 4.19d we find that the shapes of the difference curves match well and from the residuals (Zero 1 minus Zero 2 and Side 1 minus Side 2) we conclude that the shapes must be conserved for samples from the same sample batch. The existence of intrinsic spectral effects/dynamics and the fact that the difference curves match nicely for measurements of the same particle batch, sparked the idea to use a reference measurement for background subtraction as:

$$dP\left(\zeta\right)_{\mathrm{analyte}} = dP\left(\zeta\right)_{\mathrm{sample}} - dP\left(\zeta\right)_{\mathrm{reference}}\,, \tag{4.7}$$

where $dP\left(\zeta\right)_{\mathrm{i}}$ is the difference curve of the spectral correlation with i an indicator for which measurement. These measurements can be a "reference" which only has nanosensors, or a "sample" which has nanosensors and analyte, or "analyte" which

is the background corrected signal. Throughout the rest of this chapter, I mostly present $dP\,(\zeta)$ analyte as the residuals of the $dP\,(\zeta)$ curves to not confuse the reader too much with all the analysis steps. Performing a background correction to remove intrinsic characteristic is used in other methods as well, such as the use of a blank in UV/VIS experiments.

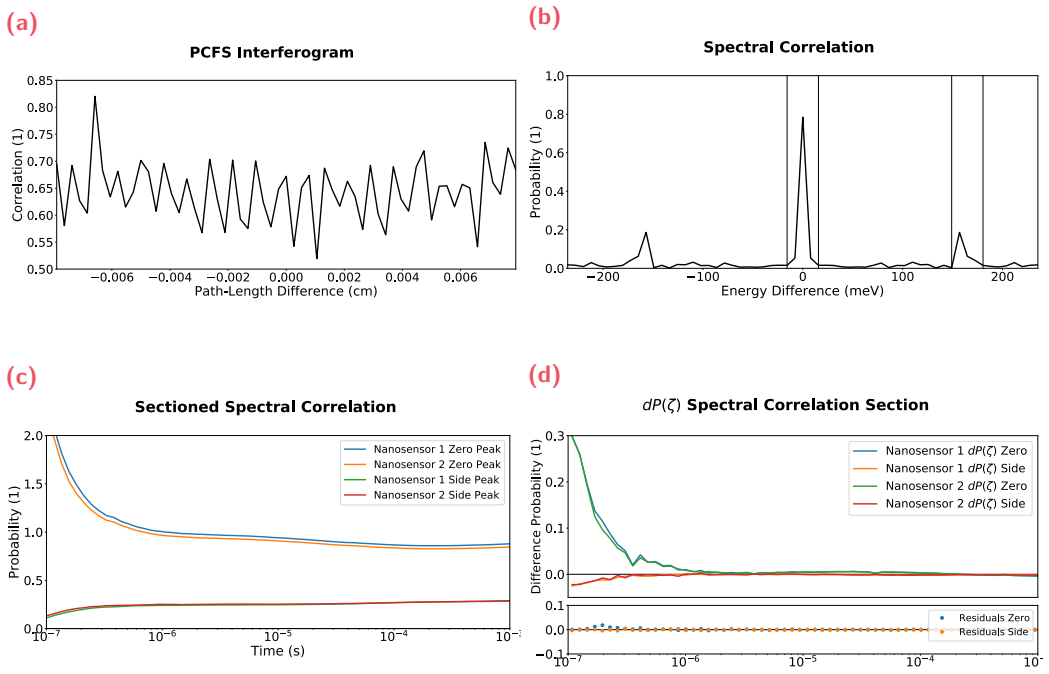

Fig. 4.19.: An example of a 2 laser scattering experiment of nanosensor sample with *(a)* the PCFS interferogram, *(b)* the spectral correlations, *(c)* the area under the curve of the "zero" and the "side" peak as a function of time, and *(d)* the differences of a curve in *(c)* along the time-axis with residuals calculated as: Zero 1 minus Zero 2 and Side 1 minus Side 2.

2 Laser Scattering Experiments of freely Diffusing Nanosensors Speed-Up

In this section, I want to touch on the measurement time needed to obtain the data of Figure 4.19. Namely, I believe that the overall duration of a single measurement is too long to be useful for in-solution sensing experiments. However, in order to resolve the spectral correlations in Figure 4.19b. Specific parameters were chosen to obtain the PCFS interferograms.

The PCFS interferogram consist of 60 data points as seen in Figure 4.19a. The spacing of the PCFS interferogram points is chosen specifically (with steps of $1.33\,\mu\mathrm{m}$) to resolve a spectral correlation up to energy differences of $130\,\mathrm{meV}$ (difference

between the two laser diodes). Second the amount of data points (60) are needed to at least obtain 3 data points for every peak in the spectral correlation. Thirdly, the measurement time for each data point is determined to be 100 s in order to capture the diffusion of the nanoparticles in the auto-correlations and to make sure that the dither does not affect the cross-correlation. Namely, we want to select the ensemble value at 0.25 s to perform sPCFS analysis without obtaining artifacts from either diffusion or the dither. All of these settings combined, result in the duration of $\sim 2\,\mathrm{h}$ (including sample loading and stabilization times) for one single 2 laser scattering experiment.

In the previous section, I mentioned that the Zero and Side peaks are not (completely) decoupled from each other. Therefore, we thought of a way to speed up these 2 laser scattering experiments, where only the Zero peak is measured. In that case only 12 data points of 100 s are needed, reducing the total measurement time to $\sim 30\,\mathrm{min}$. We tested whether this is a feasible path forward by comparing data of 2 h and 30 min experiments measured on the same nanosensor batch. We computed the difference curves of the Zero peaks with Equation 4.6, which are shown in Figure 4.20. Furthermore, we observe that they overlap nicely and from the residuals $(dP\,(\zeta)_{\mathrm{fast1}} - dP\,(\zeta)_1)$ we conclude that there is no observable difference, making the speed-up method a viable path forward.

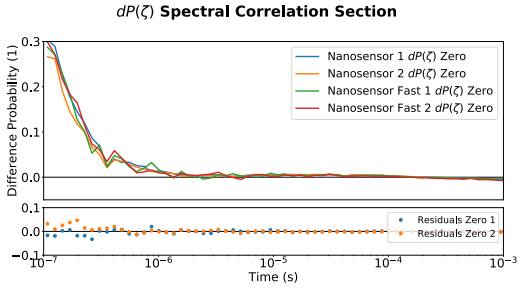

Fig. 4.20.: A comparison of the area under the curve of the zero peak of a 2 laser scattering experiment on just nanosensors between a 2 h experiment and 30 min (Fast) experiment with residuals calculated as: Zero Fast 1 minus Zero 1 and Zero Fast 2 minus Zero 2.

4.2.3 2 Laser Scattering Experiments of Freely Diffusing Nanosensors with Various PEG Lengths

In this section we changed the length of the PEG ligand on the nanoparticle, since we wanted to understand what is causing the intrinsic dynamics in the integrative Zero and Side peak curves around $100\,\mu s$. We have two working hypotheses about what could cause dynamics. First, we hypothesize that the movements of the flexible PEG polymer chain attached to surface of the nanosensor are leading to visible dynamic by moving in and out of the sensing volume. Second, we hypothesize that the dynamics could be caused by rotational diffusion of the nanoparticles.

Thus, we experimented with different PEG lengths and changed the NaCl concentration of the Tris buffer saline, where the nanosensors are dispersed in. Changing the PEG length would have an effect on the hydrodynamic radius of the nanoparticle, therefore itself is not enough to be quantifiable. From literature, it is however known that PEG polymers stretch in high salt concentrations and retract in low salt concentrations.[119] With these experiments we tried to see whether this stretching and coiling could have visible effects.

For these experiments we modified the PEG-coating protocol of Section 2.4.3, where we kept the molar concentration of the PEG addition the same, but the PEG variant has been exchanged to; $SH-PEG800$ (Sigma-Aldrich 729108), $SH-PEG2000$ (Sigma-Aldrich 729140), $SH-PEG6000$ (Sigma-Aldrich 729159), or $SH-PEG10000$ (Sigma- Aldrich 743011). Here, the number represents the average molecular weight and is proportional to the polymer chain length. The end-to-end lengths of the polymer is given by the Flory-radius as:

$$R_{\mathrm{F}} = b\left(\frac{aN}{b}\right)^{\nu}, \tag{4.8}$$

where $b = 0.73\,\mathrm{nm}$ is the Kuhn length and $a = 0.28\,\mathrm{nm}$ is the monomer size.[119] N is the number of monomers and can be calculated from the molecular weight directly as $N = M_{\mathrm{w}}/M_{\mathrm{monomer}}$, where the monomer weight is $M_{\mathrm{monomer}} = 44\,\mathrm{kDa}$.[119] Lastly, ν is a magnitude parameter for the solvent and lies between $1/2 - 3/5$, where $1/2$ is the high salt regime.[119] The particles and PEG have been dispersed in Tris buffer saline.

In Figure 4.21, 2 laser scattering data is shown for samples consisting of pure nanosensors with various PEG ligand lengths in $150\,\mathrm{mM}$ NaCl. In Figure 4.21a the Zero peak of the spectral correlation is plotted as a function of time and the intrinsic dynamics are fitted with an exponential curve. The obtained diffusion times are

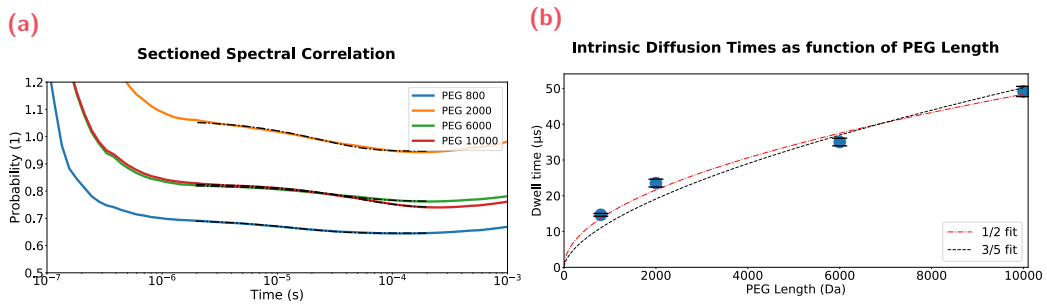

Fig. 4.21.: 2 laser scattering measurement of pure nanosensors with various PEG lengths in Tris buffer saline with the *(a)* area under the curves of the Zero peak, where the intrinsic diffusion is fitted with exponential functions. *(b)* the extracted diffusion times are plotted in a graph as a function of PEG length.

plotted as a function of PEG length in Figure 4.21b, where we observe that the diffusion time increases with increasing PEG length. These results neither confirm nor reject one of the two working hypotheses, which can also be done with the addition of salt.

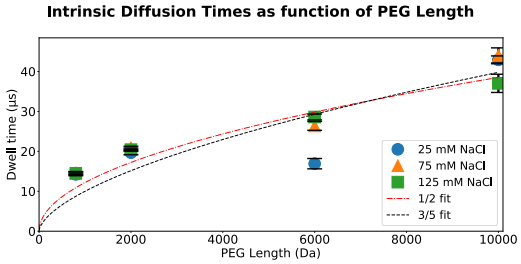

Fig. 4.22.: 2 laser scattering measurement of pure nanosensors with various PEG lengths in Tris buffer saline with different salt concentrations. The intrinsic diffusion times have been obtained from fitting the Zero peaks with exponential decays and are plotted in a graph as a function of PEG length.

We thus tested nanosensors with various PEG lengths on their surface in buffers with different salinity, see Figure 4.22. The dynamics have been obtained from the Zero peaks by fitting with exponential fits around in the $100\,\mu$s range. Here, we observe that the nanosensors with PEG6000 on their surface do not follow the previous established trend. We hypothesize that this could come from a pipetting error, where not enough $PEG-SH$ volume was added during coating. For the other nanosensors with different PEG lengths, we observe that when small PEG lengths are used, that the behavior seems to be NaCl concentration independent. Unfortunately, due to the large spread and the outlier behavior of the PEG6000, these results do not give more insight into the actual mechanism that could cause the intrinsic dynamics. Note that the actual salt concentration, especially towards higher

salinity, might be erroneous due to the fact that additions of a high salt stock were used to create them. Therefore, we resort to using the difference curves ($dP\,(\zeta)$) with a control measurement, since we have previously seen that this dynamics is at least conserved for the same sample batch. Trying to model this intrinsic dynamic without knowing the true underlying mechanistics could lead to artifacts, especially when experimental errors already have shown to be able to affect the diffusion times.

4.2.4 2 Laser Scattering Experiments on Freely Diffusing Nanosensors with Solution Analyte

Oil Micelles

In this section we explore whether our nanosensor can detect analyte, with both freely diffusing in solution. For this we synthesized oil micelles with a protocol from Baaske et al.[118] A mixture of $4\,\%$ soybean oil (Sigma-Aldrich S7381), $16\,\%$ Brij-O10 (Sigma-Aldrich P6136) and $80\,\%$ ultrapure water have been mixed and heated to $80\,^{\circ}\mathrm{C}$ for $10\,\mathrm{min}$, while being stirred at $2000\,\mathrm{RPM}$. Subsequently, the mixture is cooled to room temperature and from Dynamic Light Scattering (DLS) measurements (see Appendix A.13) an average size of $8.28 \pm 0.09\mathrm{nm}$ has been determined. These micelles are chosen as study material, since they are easy to synthesize, should not non-specifically bind to the nanosensor (following Baaske's findings), and mimic biomolecules of a size of $\sim 250\,\mathrm{kDa}$.

In Figure 4.23a, the integrated Zero peaks are shown for three measurement; a control with just nanosensors, a sample with micelles, and a sample with diluted micelles $(1:1)$. For these experiments, $30\,\mu\mathrm{L}$ of AgDNP@Au@PEG in Tris saline buffer ($300\,\mathrm{mM}$ NaCl) were used with $10\,\mu\mathrm{L}$ of micelles. Here, we observe clear differences between the control and the samples with micelles in them. Additionally, we find that when the sample of micelles is slightly diluted the deviation from the control becomes less, indicating that there are less sensing events during the experiment.

As discussed in the previous section, to control for any intrinsic dynamics and offsets the difference curves are computed, see Figure 4.23b. Here, the residual curves are obtained by subtracting $dP\left(\zeta\right)_{\mathrm{control}}$ from $dP\left(\zeta\right)_{\mathrm{sample}}$. Essentially, the residuals represent the background corrected difference curves. Since these difference curves are quasi-derivatives, we expect flat lines of the residuals when the dynamics in the control and the sample are identical. However, we expect a deviation in the residuals in the form of a bump or a valley, when there are dynamical differences between the sample and the control. Whether the residuals form a bump or a valley depends on the direction of the shift and what happens to the initial spectrum. Typically, these sensing events induce red-shifts of the LSPR spectrum and when, for instance, the initial intensity of the $488\,\mathrm{nm}$ is higher than the $520\,\mathrm{nm}$ laser, we expect the formation of a valley. We also expect that a difference in dynamics would manifest itself as a function that starts flat and ends flat on the time axis, because there is only 1 single typical time associated with the dynamics.

In the residuals of Figure 4.23b we observe a minimum at $0.18 \pm 0.01 \mu s$, indicating the steepest difference between the micelle sample and the control. This value is the same as one would obtain from exponential fitting of the $dP\,(\zeta)$, therefore we can compare this value directly with finding from Baaske et al., who found a diffusion time of $0.25\,\mu s$ to $1.0\,\mu s$ for $8\,\mathrm{nm}$ oil micelles measured with Gold nanorods.[118] We expect that the diffusion times are on the same order of magnitude for different nanosensors, however as discussed in Chapter 2 nanosensors with sharper corners do confine the electromagnetic waves stronger creating smaller sensing volumes.[54] This would explain the minimal deduction in the diffusion time that we measure compared to Baaske et al. Additionally, they mention that variability in the nanosensors' sensing volumes result in different diffusion times. In our method however we measure ensemble statistics, which should average the variability in the sensing volume of the nanosensor within one sample.

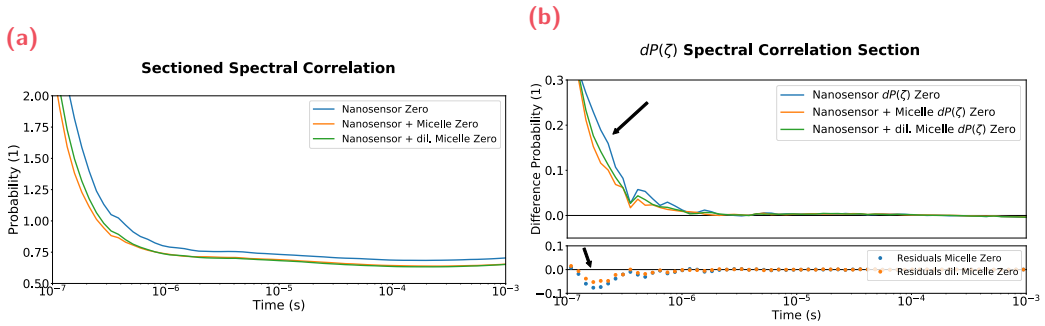

Fig. 4.23.: 2 laser scattering measurement of $8\,\mathrm{nm}$ oil micelles with *(a)* the intensity of the spectral correlation zero peak as a function of time, *(b)* the difference curve of the zero peak with residuals.

SiO_2 Nanoparticles and DNA Origami

In this section, we experiment with 2 different types of freely diffusing analyte: SiO_2 nanoparticles and DNA origami. Both of these are chosen as analyte, because of their refractive index and their surface charge that should prohibit unspecific binding to the nanosensor's surface. The size of these analytes is rather larger than common biomolecules, such that they compare to $\sim 1.5\,\mathrm{MDa}$ biomolecules. The Silicon Dioxide nanoparticles are $10\,\mathrm{nm}$ to $20\,\mathrm{nm}$ in size (Sigma-Aldrich 637238) and were redispersed in ultrapure water with a concentration of $1\,\mathrm{mM}$. The particles were sonicated for $20\,\mathrm{min}$ to make sure that they disperse well. The solution looked milky, but after transfer into a different vial, residue was observed to stick to the walls of the vial. This final concentration in the measurement might therefore actually be not

that precise. For the DNA origami we used a helix bundle of $\sim 12\,\mathrm{nm}$ by $\sim 40\,\mathrm{nm}$ called 20HB with a concentration of $10\,\mathrm{mM}$ to $100\,\mathrm{mM}$.[120] This was kindly gifted to me by Karoline Kadletz from the ITERM institute of Helmholtz Munich.

In Figure 4.24 $30\,\mu\mathrm{L}$ of concentrated AgDNP@Au@PEG in Tris buffer saline ($150\,\mathrm{mM}$ NaCl) is mixed with $10\,\mu\mathrm{L}$ SiO_2 and DNA origami, respectively. In Figure 4.24a, the integrated Zero peak is shown as a function of time. We observe that both the Zero peaks of SiO2 and the DNA origami, behave differently from the control. From the difference curves ($dP\,(\zeta)$) in the residuals of Figure 4.24b, we find maxima for both the SiO_2 and the DNA origami that are slightly offset with respect to each other. For the DNA origami we extract $0.20 \pm 0.02\mu\mathrm{s}$ and for the SiO_2 nanoparticles we find $0.23 \pm 0.03\mu\mathrm{s}$. We would expect the DNA origami to have a slower diffusion due to is bigger volume, but we do note that this DNA origami is a rather long rod, whose dynamics is more complex than a simple sphere. Unfortunately, due to batch-to-batch differences, it is difficult to compare the absolute diffusion times with previous experiments, since variations in the nanosensor syntheses might cause sensing volumes to be slightly different as well. Interestingly, however, is that we observe approximately the same diffusing times for $8\,\mathrm{nm}$ oil micelles, $10\,\mathrm{nm}$ to $20\,\mathrm{nm}$ SiO_2 nanoparticles, and DNA origami of $\sim 12\,\mathrm{nm}$ by $\sim 40\,\mathrm{nm}$. Baaske et al. report similar findings, that measurements of vastly different sizes of biomolecules resulted in similar diffusion measured with Gold rods. They even find that some bigger biomolecules diffuse faster than smaller ones, hypothesizing that it has to do with the variability in the sensing volumes of the rods or interactions between nanosensors and biomolecule.[121] Here it is also important what surface chemistry has done to the nanosensor, since that would affect the interactions too.

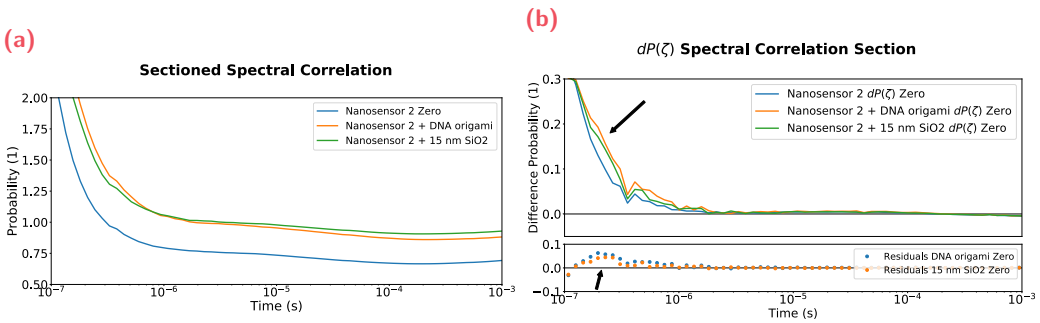

Fig. 4.24.: 2 laser scattering measurement of $10\,\mathrm{nm}$ to $20\,\mathrm{nm}$ SiO_2 nanoparticles and DNA origami (20HB) of $\sim 12\,\mathrm{nm}$ by $\sim 40\,\mathrm{nm}$ *(a)* the intensity of the spectral correlation zero peak as a function of time, *(b)* the difference curve of the zero peak with residuals.

These experiment indicate that our setup is able to measure the diffusion of analyte molecules when the sensor itself is also freely diffusing in solution. We do note that these measurements are taken at timescales overlapping with the afterpulsing pedestal. However, we tried to minimize artifacts by using the same nanoparticle batch, by using the same nanosensor concentration, and by setting photon count rate the same, for both sample and control. We hypothesize that the direction of detection (negative for micelles and positive for SiO_2 and DNA origami) could come from differences in the initial spectrum, causing by batch-to-batch variations. Alternatively, the conformation of the PEG ligands on the surface could be different due to differences in salinity. This would change the effective refractive index before a sensing event, such that the absolute shift and even the direction could be different between the experiments presented here and earlier. Namely, the addition of micelle solution causes the final concentration of NaCl to drop, potentially affecting the surface ligands' conformation.

4.2.5 2 Laser Scattering Experiments Nanosensors TAD-NCBD

Having done experiments on freely diffusing analyte and proving that detectable events are observed in the obtained data, we moved on to proteins. In this section, we tried measuring a fast-transient binding pair, which has an association rate close to the diffusion limit. Here, we studied the transactivation domain (TAD) of the tumor suppressor protein p53 and the nuclear coactivator binding domain (NCBD) of the CREB-binding protein (CBP). These proteins have been produced and purified by Dr. Peijian Zou from the STB institute, inspired by the sequences of Kim et al.[122] We modified the sequences to remove the fluorescent tag and working with his-TAD and freely diffusing NCBD. Both of these proteins are flexible and bind through multiple binding sites, where TAD wraps around NCBD through major conformational changes.[122]

For these experiments, we used nitrilotriacetic acid (NTA) (ProChimia HS-C11EG3-NTA) and NiCl in a slightly modified PEG-coating protocol to bind to the His-tag of TAD. We replaced the PEG addition of Section 2.4.3 with $40\,\mathrm{mol}\,\%$ NTA and $60\,\mathrm{mol}\,\%$ PEG800 (Sigma-Aldrich 729108) and added a $2\,\mathrm{h}$ incubation step of $10\,\mu\mathrm{M}$ NiCl final concentration. The optimizations of the molar ratios and concentrations have been performed by my colleague Dr. Jieying Zhou. We loaded the nanosensors in Tris saline buffer ($150\,\mathrm{mM}$ NaCl) with TAD in a final concentration of $0.32\,\mu\mathrm{M}$, mixed it well and added NCBD in a final concentration of $1.6\,\mu\mathrm{M}$.

In Figure 4.25 data of a 2 laser scattering experiment on TAD and NCBD is shown. According to Kim et al. at $150\,\mathrm{mM}$ NaCl the $K_\mathrm{D} = 29.9\,\mu\mathrm{M}$, $k_\mathrm{a} = 0.232 \cdot 10^9 \mathrm{M\,s}$, and $k_\mathrm{d} = 6.93 \cdot 10^3 \mathrm{s}^{-1}$.[122] This would mean that for the concentration of NCBD that we use $k_\mathrm{obs} = k_\mathrm{a} \cdot [\mathrm{NCBD}] + k_\mathrm{d} = 371 + 6930 = 7301 \mathrm{s}^{-1}$. We would thus expect dynamics to show up around $10^{-4}\mathrm{s}$ if protein interactions are occurring.

In Figure 4.25a, the integrative Zero peak is shown as a function of time, from which we computed the difference curves as seen in Figure 4.25b. In this figure, we observe that the sample with TAD behaves differently from the pure nanosensor control sample. Therefore, in the residuals (TAD minus control) we find a maximum around $0.18 \pm 0.01\mu\mathrm{s}$, which would indicate sensing of freely diffusing TAD. For the sample with NCBD, we observe a minimum when the residuals (NCBD minus TAD) are computed. These residuals however result in a flat line when the control sample is used (NCBD minus TAD). After the experiment, we hypothesized that the concentration of NCBD that was used was too little. From calculation with the use of KD from Kim et al., we expect that only 1 out of 20 NCBD-TAD pairs have formed on the nanosensor's surface. In that case, our sensors' spectra would

be dominated by one single optical state (unbound), resulting in too little photon statistics to properly resolve it any binding events.

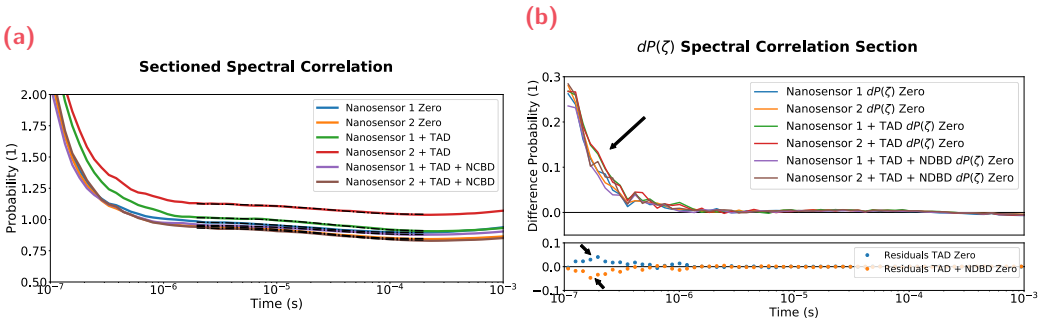

Fig. 4.25.: 2 laser scattering measurement of TAD and NCBD, a transient protein interaction pair. *(a)* the intensity of the spectral correlation zero peak as a function of time, *(b)* the difference curve of the zero peak with residuals (TAD minus control & NCBD minus TAD).

As a control to test that the His-tag binding works correctly, we fitted the intrinsic nanosensor dynamics with exponential fits in Figure 4.25a. Here, we observe an increase in diffusion when TAD and TAD & NCBD are added to the nanosensors, indicating that the proteins do bind to them. Independent of the true underlying physical principle, this data proved that His-tag binding of proteins does change something to the system. These findings are summarized in Table 4.1. No statistical difference is found between TAD and TAD & NCBD, indicating that our hypothesis of too low NCBD concentrations plausible.

Sample	**Diffusion Time**
Control	$26.0 \pm 0.7\mu$s
TAD	$35 \pm 1\mu$s
TAD & NCBD	$33 \pm 1\mu$s

Tab. 4.1.: A table with extracted diffusion times of the intrinsic nanosensor dynamics upon binding of TAD and NCBD.

4.2.6 Fourier Transform Spectroscopy High Affinity Protein Pair

This chapter is finalized by discussing experiments performed on a high affinity protein pair: TbPEX19 and pTbPEX38. This is a novel binding pair found by our collaborators from the STB institute at Helmholtz Munich. Special thanks to Dr. Stefan Gaussmann, who gave us these proteins and informed us that they have a high affinity. For these measurements we used AgDNP@Au@NTA made with the

same modified protocol as presented in Section 2.4.3 dispersed in Tris buffer saline (150 mM NaCl).

PCFS experiments as shown in previous sections can unfortunately not be used to obtain kinetic information of high affinity protein pairs. This is due to the fact that the binding and unbinding occurs slower than the typical diffusion time of the nanosensors through our laser focus. Therefore, statistically we do not observe these events, however with FTS, we can measure time-resolved spectra over hours to at least prove that 2 laser scattering is sensitive enough to detect protein-protein interactions. First, we check the surface attachment and the protein pair binding with time-resolved UV/VIS spectra. Here, we perform sequential additions of His-tagged TbPEX19 and pTbPEX38 to a cuvette with nanosensors and track the LSPR peak position as a function of time. First, the His-tagged TbPEX19 is expected to attach to the nanoparticle surface through Ni-NTA interactions. Then the pTbPEX38 is supposed to bind TbPEX19. We use Bovine Serum Albumin (BSA) as a control, which is commonly used as a non-specific binding site blocker.[123] In our case however, we utilize it as an unspecific binding site seeker, which would indicate whether the binding of the protein pair is specific or not. Note that UV/VIS time-resolved experiments for protein-protein interaction studies were initiated by my colleague Dr. Jieying Zhou. The UV/VIS data presented here has been obtained by myself, but is rather a replicate of results she obtained earlier.

In Figure 4.26 the LSPR peak position as a function of time from fitting the UV/VIS spectra with a Lorentizian functions is shown. The peak position at $T = 0$ has been taken as $\Delta E = 0$. For the first 30 min, the peak position of the LSPR of a pure nanosensor sample is monitored as a control. After those 30 min, 0.16 µM final concentration of TbPEX19 has been added to the cuvette. A direct LSPR peak shift is observed, with a characteristic time of a few minutes. Then after another 30 min, either 1.6 µM final concentration pTbPEX38 (indicating with an arrow in Figure 4.26a) or BSA (Figure 4.26b) has been added. Here, we observe that pTbPEX38 induced an additional LSPR shift, whereas BSA does not seem to cause any effect. This indicates that TbPEX19 and pTbPEX38 bind specifically. Note that during the entire experiment, the LSPR blue shifts (also observable in the first 30 min without proteins). We later found from TEM images that the particular batch of AgDNP@Au used, was not coated correctly with Gold, leaving small areas of Silver exposed on the surface. This caused the nanosensors to become unstable and blueshift in biological buffers.

The UV/VIS experiments indicate that the nanoparticle construct functions correct for specific protein-protein interaction sensing. To show that protein-protein interaction

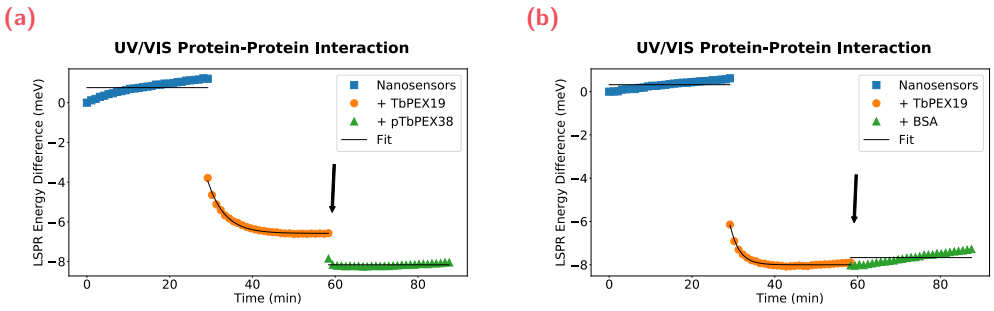

Fig. 4.26.: Time-resolved UV/VIS measurement of TbPEX19 and pTbPEX38 binding, a strong binding pair. A control has been performed with TbPEX19 and BSA. pTbPEX19 has been added at 30 min and the 2nd protein at 60 min.

sensing is possible with 2 laser scattering experiments, we therefore reproduced the UV/VIS experiments of Figure 4.26 on our custom-built optical setup. With FTS, interferograms have been measured as a function of time by scanning one arm of the interferometer continuously. These FTS interferograms have then been converted into spectra of which the ratio (low energy over high energy) of the two laser peaks has been calculated. This time-resolved ratio is shown in Figure 4.27, where 0.16 μM final concentration of TbPEX19 was added to a capillary (Vitrocom 3524-050) after 15 min of the start of the experiment. Then after another 30 min, pTbPEX38 was added in a final concentration of 1.6 μM. The FTS spectra are obtained every 160 s in order to obtain good enough S/N. In Figure 4.27 we observe qualitatively the same behavior as in Figure 4.26.

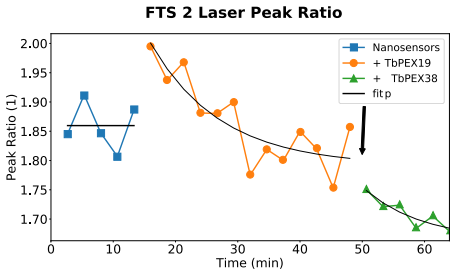

Fig. 4.27.: Time-resolved Fourier Transform Spectroscopy measurement of a strong binding pair: TbPEX19 and pTbPEX38 binding.

The experiments and findings in this chapter indicate that the detection of diffusing analyte and measurements of protein-protein interactions are possible with our novel proposed method of in-solution sensing. This would open a new path towards fast-transient biomolecular sensing, where both the biomolecules and the optical nanosensor are freely diffusing in solution, while being at thermal equilibrium.

4.3 Conclusion

In this chapter, we have discussed the combination of the nanosensor from Chapter 2 and the optical setup presented in Chapter 3 for in-solution sensing experiments. In the first half of the chapter, we performed simulations and experiments to characterize the behavior of our nanosensor in our optical setup. This information was needed, before in-solution sensing experiments could be performed, to understand the intrinsic diffusing and spectral effects of the Silver decahedra nanoparticles (AgDNP).

First, the Monte-Carlo (MC) computational model from earlier chapters was expanded to include light bursts of particle diffusing in and out of a laser focus. Here, we proved that Fourier Transform Spectroscopy (FTS) measurements can be performed on intensity fluctuating signals due to our choice of a dual-path interferometer, as discussed in Section 3.2, resulting in better S/N spectra. Then we simulated Photon-Correlation Fourier Spectroscopy (PCFS) experiments to find differences in the single and ensemble spectral linewidths through solution PCFS (sPCFS) analysis. We extracted linewidths of $59.3 \pm 0.5\mathrm{meV}$ and $96 \pm 1\mathrm{meV}$ for the average single and the ensemble, respectively, which are close to the input settings of $65\,\mathrm{meV}$ for the average single nanoparticle linewidth and $96\,\mathrm{meV}$ for the ensemble linewidth.

Then, we tested photoluminescence of Cadmium Selenide Quantum Dots (CdSe QDs), where we extracted linewidths of $67.5 \pm 0.9\mathrm{meV}$ and $110 \pm 3\mathrm{meV}$ for the average single and ensemble, respectively. These findings were compared with a comparative technique, where individual spectra of spincoated CdSe QDs on a substrate are measured. Here, a FWHM of $68\,\mathrm{meV}$ for the average single and an ensemble FWHM of $86\,\mathrm{meV}$ are obtained for ($N = 48$) particles. These values match nicely, and slight differences are explained by the limited number of single particle spectra in the comparative technique.

With the optical setup tested and calibrated with photoluminescence it was time to measure the scattering light of the nanosensors of Chapter 2. We observed high monodispersity in two samples of Gold spherical nanoparticles (AuSNP), of which one was homemade and the other was purchased. Spectral differences were attributed to the elongated shape of the homemade nanoparticles and when single particle spectra were tried to be obtained with the comparative method, we noticed clustering and substrate effects to inhibit our comparison. Therefore, photoluminescent light was used as a comparative study to the scattering light, since both could be measured in solution. We observed that the average single

nanoparticle linewidths for both scattering and photoluminescence were close, and hypothesized that sPCFS analysis allows for the correct observation of the average single nanoparticle. The linewidths of the ensembles were not matching, which we think could come from unwanted reflections or driving light effects for the scattering case. These findings hint that PCFS can be used as a tool to study single/ensemble linewidth discrepancies to potentially optimize chemical syntheses. Herein, is the use of photoluminescent light an easy approach, even though the quantum efficiencies are low. Scattering light could potentially be used, but more research is needed to obtain true nanoparticle spectra.

In the second half of this chapter, in-solution sensing experiments are discussed. This part starts off with the MC computational model that is used to simulate freely diffusing nanosensors that switch between two optical states (protein bound and protein unbound) at sub-ms time scales. We observe dynamics of $k_{\text{obs}} = k_{\text{on}} + k_{\text{off}} = 1.7 \pm 0.2 \cdot 10^5 \text{s}^{-1}$, with input parameters of $k_{\text{on}} = k_{\text{off}} = 1 \cdot 10^5 \text{s}^{-1}$. The signal-to-noise (S/N) ratios of these simulations and the overlap of S/N in Chapter 3 between simulation and experiment, make us confident that sub-ms dynamics can be observed with our method.

Experimentally, with the learning of the first half of this chapter, we updated the excitation/driving light part of our optical setup. Nanosensors freely diffusing in solution are illuminated with two continuous wave (CW) laser diodes, of which the relative intensity changes are tracked as a function of time in spectral correlation space. We found that intrinsic spectral dynamics of pure nanosensors were making interpretation difficult, but that these dynamics were conserved within the same sample batch. Therefore, we suggested to look at difference curves (quasi-derivatives) of the spectral correlations and the residuals after subtraction of control experiments.

Then we measured the diffusion times of freely diffusing analyte passing through the sensing volume of the nanosensor for three different cases: oil micelles, SiO_2 nanoparticles, and DNA origami. We measured diffusion times of $0.18 \pm 0.01 \mu\text{s}$, $0.23 \pm 0.01 \mu\text{s}$, and $0.20 \pm 0.02 \mu\text{s}$, respectively. These findings are comparable with diffusion times of analyte passing by a Gold rod found in literature.[118] Additionally, these researchers acknowledge the fact that the diffusion times of biomolecules with vastly different sizes all seem to fall within a very narrow range.[121]

Having sensed the presence of freely diffusion nanoparticles, we move on to protein binding pairs. First a fast-transient protein pair is examined, and we are only able to observe the binding of the first protein to the nanoparticle surface. We hypothesize that the concentration used of the second proteins is too far away from optimal values, such that only 1 out of 20 is bound on the surface of the nanoparticle. This

statistically does not give us enough photon pairs to resolve binding and unbinding events. Therefore, we test a strong binding protein pair in Fourier Transform Spectroscopy mode and find that binding of the second protein does indeed cause enough spectral change to be measurable. The findings presented in this chapter pave a new path towards optical sensing in-solution with the potential to resolve fast and transient binding kinetics.

5 Discussion and Conclusion

In the first part of this chapter, the optical method presented in this dissertation for in-solution sensing is discussed with respect to its potential shortcomings and still open questions. Estimations are given for the kinetic rate parameters, concerns due to optical heating are discussed, and thoughts on the size and type of biomolecules are given. Then technical improvements for the current optical setup are discussed. Thereafter a few experiments are proposed, which in my view are paths to continue this research. Then, this chapter is finalized with aa general conclusion of this whole dissertation.

5.1 Scattering PCFS for Synthesis Optimization

In the first half of Chapter 4, experiments on scattering light of diffusing plasmonic nanoparticles are discussed. Here, we found that the driving light affects the obtained linewidths and that potentially volume dependent intensity fluctuations are caused. For scattering PCFS to become a useful technique for syntheses optimizations, a proper mathematical understanding is needed of how the true LSPR spectrum can be obtained. With the computational model presented in this dissertation, the parameter space of driving light to LSPR linewidth ratio can be examined. Additionally, the effects caused by the shape of the driving light can be investigated. Experimentally, consecutive measurements of FTS and PCFS can be used to obtain absolute driving light information, such could perhaps be used in a mathematical model as correction. Currently, I would suggest to use photoluminescence of plasmonic nanoparticles, since these experiments seem to behave similarly to photoluminescence experiments on quantum dots, which have been proven to work.

5.2 Measurement Range of In-Solution Sensing Method

In the second part of Chapter 4, we have discussed an optical method that can be used for in-solution sensing. This section estimates the range of rate parameters

that can potentially be measured with the method presented in this work. For our method to obtain the highest signal $k_{\mathrm{on}} \approx k_{\mathrm{off}} \approx \frac{1}{2} k_{\mathrm{obs}}$. In terms of K_{D}, we would need to measure at concentration close to it, since that ensures that half of the biomolecules are bound and the other half in unbound. If we were to measure far from this balance, then the signal would simply be dominated by one single state, such that any dynamic events would fall within the noise of the measurement and thus cannot be observed.

Dissociation Rate

Let us estimate the dissociation rate first. The fastest time that can be measured with the current setup is limited to the detector dead time, because this feature shows up in the auto-correlations that are used in the computation of the PCFS interferograms and spectral correlations. The detector dead time is approximately $\sim 100\,\mathrm{ns}$. For the slowest time that can be measured, we are limited by the dynamics of the particle moving through the focal volume, because association or dissociation events cannot statistically be measured once the nanosensor is out of the focal volume. Therefore, this limit is given by $\sim 1\,\mathrm{ms}$, and since $k_{\mathrm{d}} = k_{\mathrm{off}} \approx k_{\mathrm{obs}}$ we can estimate:

$$10^{3}\mathrm{s}^{-1} < k_{\mathrm{d}} < 10^{9}\mathrm{s}^{-1}\,. \tag{5.1}$$

Association Rate

For the association rate, similar reasoning can be used as for the dissociation rate, such that $10^{3}\mathrm{s}^{-1} < k_{\mathrm{on}} < 10^{9}\mathrm{s}^{-1}$. The association rate is related to the on-rate by $k_{\mathrm{a}} = k_{\mathrm{on}} / [P]$ with $[P]$ the molar protein concentration. Therefore, we need to estimate the molar concentrations of the biomolecules at study. A lower limit of biomolecule concentration is given in relation to the nanosensor concentration. Let us assume that approximately $10 - 100$ initial biomolecules are bound to the surface of the nanosensor. To observe the dynamics, we want half of them bound, such that we expect $5 - 50$ biomolecules per nanosensor. The nanosensor concentration is determined from the focal volume[1], such that on average 1 nanosensor is present in the focal volume, resulting in a number concentration: $10^{19}\mathrm{NPs}/\mathrm{m}^{3}$. Therefore, we estimate a lower protein concentration of $5 - 50 \cdot 10^{19}\mathrm{proteins}/\mathrm{m}^{3} \approx 10^{-}7\mathrm{mol\,L}^{-1}$. The upper molar protein concentration is given by the protein solubility and the influence on the dynamics because of crowding. Let us assume the worst case, where the entire focal volume is filled with proteins. For this we assume a spherical

[1] The focalvolume is on the order of $10^{-16}\mathrm{liter}$

molecular size of $4\,\mathrm{nm}$, which is a protein of roughly $30\,\mathrm{kDa}$, such that the volume occupied by one protein is $4 \cdot 10^{-27}\mathrm{m}^3$. Therefore, the number concentration of maximum allowed proteins becomes $2.5 \cdot 10^{26}\mathrm{proteins/m}^3$, which is equal to a molar concentration on the order of $10^2\mathrm{mol\,L}^{-1}$. This upper limit lies well above most of the protein solubility concentrations, therefore we take $1\,\mathrm{mol\,L}$ as upper limit to calculate the association rate, such that:

$$10^3\mathrm{s}^{-1} < k_{\mathrm{on}} < 10^9\mathrm{s}^{-1} \tag{5.2}$$

$$10^3\mathrm{mol}^{-1}\,\mathrm{L}^{-1}\,\mathrm{s}^{-1} < k_{\mathrm{a}} < 10^{16}\mathrm{mol}^{-1}\,\mathrm{L}^{-1}\,\mathrm{s}^{-1}\,. \tag{5.3}$$

However, more realistically, due to either too little or too high protein concentrations:

$$10^5\mathrm{mol}^{-1}\,\mathrm{s}^{-1} < k_{\mathrm{a}} < 10^{14}\mathrm{mol}^{-1}\,\mathrm{s}^{-1}\,. \tag{5.4}$$

The upper end of $10^{14}\mathrm{mol}^{-1}\,\mathrm{s}^{-1}$ is rather unreal, since the association rate is limited by the diffusion of the proteins. This is also known as the Smoluchowski limit and typically lies around values of $10^{10}\mathrm{mol}^{-1}\,\mathrm{s}^{-1}$.[116] We thus adjust the upper limit as:

$$10^5\mathrm{mol}^{-1}\,\mathrm{s}^{-1} < k_{\mathrm{a}} < 10^{10}\mathrm{mol}^{-1}\,\mathrm{s}^{-1} \tag{5.5}$$

Dissociation Rate Constant

For the in-solution sensing method, we want to operate roughly at K_{D} values, such that half of the proteins are bound and the other half unbound. Therefore, the same reasoning as for the computation of the molar protein concentrations for k_{a} can be used to compute the dissociation rate constant. The lower limit is given by the nanosensor concentration ($10^{19}\mathrm{NPs/m}^3$), where we want $10 - 100$ proteins on the surface, leading to a molar protein concentration of $\approx 10^{-}7\mathrm{mol\,L}^{-1}$. And for the upper limit, we consider the maximum solubility of proteins, which from simple sphere stacking leads to $10^2\mathrm{mol\,L}^{-1}$, but due to solubility most likely will stop around $10^0\mathrm{mol\,L}^{-1}$. Therefore, optimistically, K_{D} values are expected to fall within:

$$10^{-7}\mathrm{mol}^{-1}\,\mathrm{L}^{-1} < k_{\mathrm{D}} < 10^0\mathrm{mol}^{-1}\,\mathrm{L}^{-1}\,, \tag{5.6}$$

and more pessimistically, we expect them to fall in:

$$10^{-5}\mathrm{mol}^{-1}\,\mathrm{L}^{-1} < k_{\mathrm{D}} < 10^{-2}\mathrm{mol}^{-1}\,\mathrm{L}^{-1}\,. \tag{5.7}$$

5.3 Potential Concerns of Current Method

5.3.1 Plasmonic Heating

Plasmonic sensors are great heating devices, because almost half of their extinction spectra consist of absorption, see Figure 2.3. Therefore, these particles are used in *in-vivo* cancer treatment, where the particles enter the cell and upon illumination heat-up tremendously to kill the cell.[**huang2012**]Thermal heating is a known issue for plasmonic sensing.[**taylor2008**] Namely, the added heat can influence the biomolecular interactions, and therefore we have to discuss this effect for the method presented in this dissertation as well. We measured the intensity of our 2-laser scattering experiments to be on the order of $100\,\mathrm{nW}$, and assume a diffraction limited spot of $250\,\mathrm{nm}$ in width. From DDA simulations, we obtain an absorption cross-section of $\sigma_{\mathrm{abs}} \approx 0.012\mu\mathrm{m}^{-2}$, see Appendix A.3. Therefore, hypothetically, all incident power can be absorbed by the nanoparticle. Let us use the following equation from Baffou for heating of plasmonic particles in solution at steady-state:[124]

$$\Delta T = \frac{Q}{4\pi\kappa_{\mathrm{s}} a}\,, \tag{5.8}$$

with Q the added optical energy, κ_{s} the thermal conductivity of the environment and a the radius of the particle. Using the thermal conductivity of water $0.6089\,\mathrm{W\,m^{-1}\,K^{-1}}$ and a nanoparticle size of $40\,\mathrm{nm}$, we find that $\Delta T =\sim 0.3\,\mathrm{K}$. Noteworthy, is that this calculation is the worst-case scenario, since our nanosensors are freely diffusion and never stay in the most intense part of the beam for long. Additionally, most plasmonic heating systems use Gold, because of its higher absorption cross-section, because of our choice for Silver the absorption is much less. Thus, we can assume that the thermal effect from light absorption are neglectable for the method presented in this work.

5.3.2 Range of Biomolecular Sizes

This part discusses which sizes of biomolecules can be detected with optical method presented in this dissertation. Let us first consider measurable proteins by assuming they are sphere-like. In Section 2.1.3 protein ring formation on the surface of a sphere, and in Section 2.1.4 protein sensing at the tip of a Silver decahedra nanoparticle are discussed. From these two sections, it becomes clear that the plasmonic nanosensors only are able to sense the presence of biomolecules close to the surface. Additionally, it has been found that these sensing volumes are on the

order of $1\,\mathrm{nm}$ to $5\,\mathrm{nm}$. This is problematic for the presented method, because when the sensing volume is occupied by protein A with a too large size, interactions with B will never be observed. This makes the method of this dissertation especially useful for biomolecules with sizes smaller than $50\,\mathrm{kDa}$. Note that too small molecules do not change the dielectric environment enough such that they are also not observable, such that the measurable range will lie between $10\,\mathrm{kDa}$ to $50\,\mathrm{kDa}$.[2]

Throughout this dissertation, we approximated biomolecules as sphere-like objects, however proteins do not necessarily have to fold into spheres. Especially, interacting proteins pairs might fold completely different, since they would want to occupy each other's binding pockets. This is actually beneficial for our optical method, since that means that initial proteins do not occupy the sensing volume as much until they bind. Therefore, the upper range of $50\,\mathrm{kDa}$ might actually be higher, because of protein structure that has been neglected for those estimations. Promising proteins to study are proteins which lack intrinsic structure, such as intrinsic disordered domain proteins, which would extend out as long chains, but coil up upon binding.

5.3.3 Type of Biomolecules

The type of biomolecules that can be studied with this method are predominantly cytosolic proteins. These proteins can namely be expressed in E. Coli cultures to be purified after. In the correct buffer, the cytosolic proteins should be folding correctly, such that their measured kinetics should be similar to *in-vivo*. Unfortunately, a large class of proteins, membrane bound proteins, currently fall outside the measurable biomolecules for our method. The main reason for this is that membrane bound proteins need support of a membrane to fold correctly.

A proposed method to measure membrane bound proteins with our method is to form a supported lipid bilayer around the nanosensors with proteoliposomes from overexpressing cells. Richards et al. describe a chemical triggering method for cells to produce liposomes with membrane proteins on them, known as blebs.[125] These blebs can then be incorporated into a supported lipid bilayer on a SiO_2-substrate. PEGylated lipid vesicles are used in the formation of the supported lipid bilayer to form a cushion, such that correct the membrane proteins can fold correctly. This method would allow studying membrane bound protein interactions as well, however the effect on the sensing capabilities due to the formation of a lipid bilayer around the particle have to be investigated. Chances are that the lipid bilayer is too thick, resulting in no observable signal changes from the nanosensors.

[2]The lower range is estimated from optical shifts presented in Section 2.1.3.

Alternatively, lipid nanodiscs can be used as small membrane domains that can be attached to the surface of our nanosensor. Lipid nanodiscs are lipid bilayers that are surrounded by amphipathic molecules that contain the size of the lipid bilayer today to nano sizes. Membrane bound proteins can then sit and within the disc in a stable lipid bilayer. When both constructs are used, the supported lipid bilayer and the lipid nanodics, the distance between the interaction event and the sensing volume must be considered. As we have shown in this dissertation, the sensing volume is only a few nanometers in size.

5.3.4 Measuring in Afterpulsing Pedestal

In Section 4.2.4 biomolecular sensing events of oil micelles have been shown and discussed. It has been mentioned that these the observed changes fall within a measurement artifact, the afterpulsing pedestal. Even though average intensity, nanosensor concentration, and nanosensor batch have been controlled for, one could still argue that intensity fluctuation characteristic might differ between the experiments that could lead to the observation in those experiments. In this section, two solutions are proposed to get rid of the afterpulsing pedestal, such that it no longer can affect the observations.

Additional Single Photon Detectors

PCFS analysis relies on using the auto-correlation as an intensity correction on the spectral cross-correlations. Unfortunately, the auto-correlation suffers from afterpulsing effects due to retriggering of detection events from trapped electrons. Therefore, previously, cross-correlations far from the white fringe have been used as auto-correlations for Quantum Dot samples.[95, 96] This is a viable method, when average intensities across the sample are stable and steady. However, we observed that scattering signals do fluctuate more than fluorescent signals, such that instantaneous auto-correlations are needed for correction. To remove the afterpulsing effect, two additional single photon detectors can be used on the signal before it enters the interferometer. The signal should be split with a $50:50$ beamsplitter to direct half of it into the interferometer to do PCFS as described in this dissertation and the other $50\,\%$ can be used to determine the instantaneous cross-correlation that can be used for intensity correction. In that case, another $50:50$ beamsplitter is needed that guides the already split light onto two single photon detectors. In this proposed setup, 4 cross-correlations are computed, 2 on the intensity signal before

entering the interferometer and 2 after leaving the interferometer. The downside of this solution is that $50\,\%$ of the signal for interference is lost, which could be acceptable when the system is not intensity starved, which is the case for scattering light.

Different Types of Detectors

Another option to remove the afterpulsing feature from the auto-correlations is by using different detectors. The afterpulsing pedestal is namely an artifact of single photon detectors. There exist other detectors which do not have an afterpulsing pedestal. For example linear intensity detectors have only low gain, such that there are no trapped electrons, however these need high intensity signals to actually output a detection event. Superconducting Nanowire Single Photon Detectors (SNSPD) also have low dead times and no afterpulsing. Hybrid detectors are also sold, which operate in between a photon-multiplier tube and single photon detectors. One would have to find the exact specifications that are needed for the biomolecular interactions that are to be studied.

5.4 Future Directions

5.4.1 Measurement of Proteins

Having shown sensing events of oil micelles as biological analyte in Section 4.2.4, the simple next step would be to use the nanosensors to measure the diffusion of proteins in solution. These experiment can give insight into the protein-nanosensor interactions. It is namely known that certain proteins adsorb to surfaces in non-specific interactions. It is good to know whether the unspecific adsorption leads to diminished sensing capabilities due to obstruction of the sensing volume. Additionally, experiments are needed that can indicate whether the unspecific adsorption of proteins is short- or long-lasting. These insights are definitely needed before biomolecular interaction studies can be performed.

5.4.2 Measurement at Thermal Equilibrium

Measurement of interacting biomolecules at thermal equilibrium is an important promise of our optical method. In order to resolve diffusion limited kinetics, systems

have to be at thermal equilibrium. Surface Plasmon Resonance (SPR) measurements are for instance limited in the kinetics that can be measured due to microfluidics. In those experiments, fast kinetics cannot be distinguished from flow/diffusion effects. Our in-solution method is designed to measure at thermal equilibrium and therefore has the potential to measure diffusion limited kinetics.

Nanosensors on substrate or tethered to substrate

The proposed experiments in this paragraph might speak against some of the motives initially given for this work, however they still could be useful as a proof of principle, since they reduce the degrees of freedom. Here, I am proposing to perform thermal equilibrium protein-protein experiments of nanosensors attached to a substrate. Either the nanosensors are adsorbed to the substrate or they could be tethered through Siloxane-$\mathrm{PEG}-\mathrm{SH}$. The hope is that in these experiments, pure Gold coated Silver decahedra can be used with just $\mathrm{NTA\text{-}PEG}$ on their surface and no other surface ligands. With the proposed method, one single nanosensor can be studied and its interactions with biomolecules and/or the interactions of NTA his-tagged proteins on its surface with freely diffusion proteins. To obtain ensemble statistics, multiple particles can be viewed by moving the objective focus or the stage. The advantage of this method is that less nanosensors need to be used, since only a surface is covered instead of filling a 3D space. The downside is that the substrate could affect the diffusion kinetics.

5.5 High throughput

In the introduction of this dissertation, a gap between screening and verification methods of protein-protein interactions has been identified and used to motivate the work presented here. Additionally, the lack of methods tailored towards unveiling kinetic information of protein-protein interactions was one of the driving factors. Initial measurements of kinetic events are presented in Chapter 4.2.6 and the potential for protein-protein interactions is shown. However, the method in its current state is unable to compete with high-throughput methods. Therefore, this section discusses the observed bottlenecks from my view and elucidates them, even trying to present solutions for improvement.

5.5.1 Nanosensor Synthesis Scale-up and Quality Control

The nanosensors are an important part of the method, whose complexity might be underestimated. Even though synthetic protocols exist in the literature, it took 2 PostDocs (Dr. Fangyuan Song and Dr. Jieying Zhou) and me almost 2 years to obtain reasonably stable protocols and synthetic procedures. Additionally, these syntheses include many steps, which all are dependent on each other. As seen in this dissertation, PEGylated Gold coated Silver decahedron nanoparticles are made of Gold coated Silver decahedron nanoparticles, which in turn are made of Silver decahedron nanoparticles. Whenever something is wrong at the beginning of the pipeline, it causes dramatic changes to the output at the end. Even though, efforts have been made into quality control and stability of these protocols, some batches simply **do not** work, without good understanding of why this particular batch failed. Therefore, more work has to go into understanding the synthetic parameters of the syntheses presented throughout this thesis and/or (re)defining quality control measures.

Another important point about the syntheses, is that we have learned that different proteins behave better in different buffers or some proteins do not go well with the nanosensor's surface. Unfortunately, this means that surface chemistry and buffer optimization have to be performed for (almost) every protein pair at study. This is due to the fact that the particles should be colloidally stable in that specific buffer, and that adsorption of the initial protein to the nanosensor's surface changes its stability. Additionally, my colleague, Dr. Jieying Zhou, has only explored NTA His-tag to attach proteins to the nanosensor's surface. Whereas, many different tags exist, each with their pros and cons and each optimized for different types of proteins.

Lastly, a bottleneck is identified in the volume cost of nanosensors needed for a single experiment. With the current method, $1.5\,\mathrm{mL}$ of PEGylated nanosensors is used to concentrate it down to $\sim 30\,\mu\mathrm{L}$ to obtain the correct number concentration for Photon-Correlation Fourier Spectroscopy experiments. Therefore, the nanosensor syntheses would have to be up-scaled. Namely, running one single 384-wellplate with $30\,\mu\mathrm{L}$ of nanosensors per well would need 96 vials of stock Gold coated Silver decahedra. Unfortunately, trials of 2-fold upscaled syntheses already resulted in outcomes falling outside the range of our current quality control measures (LSPR peak outside $485\,\mathrm{nm}$ to $495\,\mathrm{nm}$), such that more work is needed into proper up-scaling of the nanosensor syntheses. Alternatively, more work can be done on PCFS measurements of more dilute samples by for instance enlarging the laser focal volume.

5.5.2 Speed-up of Method

In Section 4.2.4 sensing experiments of oil micelles detections is shown. Here, two durations for the experiment are compared, and it is shown that measurements of $2\,\mathrm{h}$ can be performed in $20\,\mathrm{min}$. Even though this improvement of a factor of 6 is already promising, in order to run a 96-well plate it would take longer than $1\,\mathrm{d}$. Thus, to be used as a high throughput method the experimental time needs to be reduced even further, preferable to below 1 minute. From the intensity obtained from the nanosensors and the signal-to-noise ratios observed, the limiting factor are not the nanosensors. The data acquisition is the main reason for this "long" measurement time. For PCFS analysis, every path-length difference, needs a measurement time longer than the diffusion time of the particles. Currently, 12 data points are measured with a measurement time of $100\,\mathrm{s}$ to stay out of any dither effects in the cross-correlation. To resolve an interferogram, at least 3 data points are needed, and the measurement time could be reduced to $20\,\mathrm{s}$. Any shorter measurement time would make dither effects show up in the measurement range of the cross-correlations. Therefore, the hypothetically the measurement time could be reduced to $3 \cdot 20\,\mathrm{s} = 60\,\mathrm{s}$.

5.5.3 2 Laser Dichroic Measurement

In the sensing experiments in Section 4.2.4 only 2 CW laser diodes are used for biomolecular sensing. To obtain spectral information an interferometer is currently used, however with 2 distinct laser lines other options are available as well. Here, I propose to use dichroic mirrors, spectrally filtering optics, to direct one laser onto one detector and the second laser onto the second detector. Doing this is similar to collapsing all interferometer measurement points onto one, which is also known as multiplexing. To improve the statistics of this method, 3 or even 4 detectors could be used with different laser lines to obtain intensity cross-correlations from all detector pairs. This method is cheaper and less-sensitive to environmental vibrations, because there is no interferometer needed anymore. Additionally, it would also reduce the measurement time, since the need for multiple path-length differences is removed.

5.6 Conclusion

In this thesis, a novel optical method has been presented which consists of two parts: metallic nanosensors and an optical setup. The dielectric sensitivity of plasmonic

nanoparticles causes optical shifts that can be measured with sensitive optical equipment. When these nanosensors are placed in the proximity of biomolecules, the optical shifts should reflect their interaction kinetics, such that the obtained data are indicative of biomolecular interaction rates.

We have shown in Chapter 2 the computational and experimental search for a promising nanosensor, where sensitivity and figure of merit (FOM) were key characteristics. We found that penta-twinned decahedra nanoparticles are promising candidates because of their theoretical, but also experimentally observed high sensitivity and FOM of $187\,\mathrm{nm\,RIU^{-1}}$ ($1078\,\mathrm{nm\,RIU^{-1}}$) and 6.9, respectively. Not only that, but we then have shown that capping with a thin layer of Gold made these nanosensors more resistant to degradation in biological buffers and that surface modification with PEG aids colloidal stability.

Next, we discussed an optical setup with high temporal and spectral resolution, based on a combination of Fluorescence Correlation Spectroscopy and an interferometer. Experimentally, we measured sub-second dynamics of $129 \pm 5\mathrm{ms}$ (full-period) for a periodic moving spectrum set to switch every $65\,\mathrm{ms}$ (half-period). Additionally, an optical switching system mimicking a rate-process with exponential probabilistics was measured to have $k_{\mathrm{obs}} = k_{\mathrm{on}} + k_{\mathrm{off}} = 18 \pm 1\mathrm{s}^{-1}$ with $k_{\mathrm{on}} = k_{\mathrm{off}} = 10\,\mathrm{s}^{-1}$ as input. In these experiments we were mainly limited by speed of the optical systems that we used and the signal-to-noise (S/N) was found to be good down to $1\,\mu\mathrm{s}$ to $10\,\mu\mathrm{s}$. The periodic switching data has been compared with simulations and seemed to match nicely. Then we simulated sub-ms exponential switching with $k_{\mathrm{on}} = k_{\mathrm{off}} = 1 \cdot 10^{3}\mathrm{s}^{-1}$ and retrieved $k_{\mathrm{obs}} = k_{\mathrm{on}} + k_{\mathrm{off}} = 1.5 \pm 0.2 \cdot 10^{3}\mathrm{s}^{-1}$, giving us confidence that fast and transient interactions are measurable with our in-solution method.

In the last chapter (Chapter 4) both parts are combined to perform in-solution sensing measurements of biomolecules. Here, we first have shown computationally that observations in the μs-regime are possible with our method. We set $k_{\mathrm{on}} = k_{\mathrm{off}} = 1 \cdot 10^{5}\mathrm{s}^{-1}$ as input of an updated computational model that included nanosensor diffusion and obtained $k_{\mathrm{obs}} = k_{\mathrm{on}} + k_{\mathrm{off}} = 1.7 \pm 0.2 \cdot 10^{5}\mathrm{s}^{-1}$. We then experimentally analyzed the intrinsic dynamics of our nanosensor that could come from rotational diffusion or surface ligand mobility.

From these experiments, we learned that continuous wave lasers are needed and updated the excitation/driving light scheme by installing 2 laser diodes into the setup. With which we measured freely diffusing analyte passing by our freely diffusing nanosensor. We measured diffusion times of $0.18 \pm 0.01\mu\mathrm{s}$, $0.23 \pm 0.01\mu\mathrm{s}$, and $0.20 \pm 0.02\mu\mathrm{s}$ for oil micelles, SiO_2 nanoparticles and DNA origami, respectively. Lastly, we measured protein binding pairs, where in the transiently binding protein

pair case, we only observed the diffusion of the His-tagged protein, hypothesizing that the chosen concentrations skewed the equilibrium, such that no binding events were observed. With the permanent binding pair, however, we did observe spectral shifting and were able to track that as a function of time, and confirmed those findings against UV/VIS measurements.

We have thus presented a novel method for biomolecular interaction sensing with both nanosensors and biomolecules freely floating in solution. Kinetic studies of biomolecular interactions could be valuable for both basic and applied research and my hope is that the optical method, described in this dissertation, has the potential to contribute to those studies.

Bibliography

[1] World Health Organization. *Novel Coronavirus(2019-nCoV)SITUATION REPORT-1*. Jan. 2020 (cit. on p. 1).

[2] Varnakavi Naresh and Nohyun Lee. "A review on biosensors and recent development of nanostructured materials-enabled biosensors". In: *Sensors* 21.4 (2021), p. 1109 (cit. on p. 1).

[3] AA Terentiev and NT Moldogazieva. "Alpha-fetoprotein: a renaissance". In: *Tumor Biology* 34 (2013), pp. 2075–2091 (cit. on p. 2).

[4] Alexiou Athanasios, Vairaktarakis Charalampos, Tsiamis Vasileios, et al. "Protein-protein interaction (PPI) network: recent advances in drug discovery". In: *Current drug metabolism* 18.1 (2017), pp. 5–10 (cit. on p. 2).

[5] Seth I Berger and Ravi Iyengar. "Role of systems pharmacology in understanding drug adverse events". In: *Wiley interdisciplinary reviews: systems biology and medicine* 3.2 (2011), pp. 129–135 (cit. on p. 2).

[6] W David Wilson. "Analyzing biomolecular interactions". In: *Science* 295.5562 (2002), pp. 2103–2105 (cit. on p. 2).

[7] James R Perkins, Ilhem Diboun, Benoit H Dessailly, Jon G Lees, and Christine Orengo. "Transient protein-protein interactions: structural, functional, and network properties". In: *Structure* 18.10 (2010), pp. 1233–1243 (cit. on pp. 2, 3).

[8] Tord Berggård, Sara Linse, and Peter James. "Methods for the detection and analysis of protein–protein interactions". In: *Proteomics* 7.16 (2007), pp. 2833–2842 (cit. on pp. 3, 4).

[9] Sahar Mahmoodi, Mohammad Pourhassan-Moghaddam, David W Wood, Hasan Majdi, and Nosratollah Zarghami. "Current affinity approaches for purification of recombinant proteins". In: *Cogent Biology* 5.1 (2019), p. 1665406 (cit. on p. 4).

[10] Christian Von Mering, Roland Krause, Berend Snel, et al. "Comparative assessment of large-scale data sets of protein–protein interactions". In: *Nature* 417.6887 (2002), pp. 399–403 (cit. on pp. 4, 6).

[11] KH Young. "Yeast two-hybrid: so many interactions,(in) so little time..." In: *Biology of reproduction* 58.2 (1998), pp. 302–311 (cit. on p. 4).

[12] Anna Brückner, Cécile Polge, Nicolas Lentze, Daniel Auerbach, and Uwe Schlattner. "Yeast two-hybrid, a powerful tool for systems biology". In: *International journal of molecular sciences* 10.6 (2009), pp. 2763–2788 (cit. on p. 4).

[13]Joana Vieira Silva, Maria João Freitas, Juliana Felgueiras, and Margarida Fardilha. "The power of the yeast two-hybrid system in the identification of novel drug targets: building and modulating PPP1 interactomes". In: *Expert review of proteomics* 12.2 (2015), pp. 147–158 (cit. on p. 4).

[14]Devendra Shivhare, Magdalena Musialak-Lange, Irene Julca, Pawel Gluza, and Marek Mutwil. "Removing auto-activators from yeast-two-hybrid assays by conditional negative selection". In: *Scientific Reports* 11.1 (2021), pp. 1–9 (cit. on p. 4).

[15]Julian Vasilescu and Daniel Figeys. "Mapping protein–protein interactions by mass spectrometry". In: *Current opinion in biotechnology* 17.4 (2006), pp. 394–399 (cit. on p. 5).

[16]Katrina Meyer and Matthias Selbach. "Quantitative affinity purification mass spectrometry: a versatile technology to study protein–protein interactions". In: *Frontiers in genetics* 6 (2015), p. 237 (cit. on p. 5).

[17]Janet Piñero, Laura I Furlong, and Ferran Sanz. "In silico models in drug development: where we are". In: *Current Opinion in Pharmacology* 42 (2018), pp. 111–121 (cit. on p. 5).

[18]Ya Chen and Johannes Kirchmair. "Cheminformatics in natural product-based drug discovery". In: *Molecular informatics* 39.12 (2020), p. 2000171 (cit. on p. 5).

[19]Carla Tameling, Stefan Stoldt, Till Stephan, et al. "Colocalization for super-resolution microscopy via optimal transport". In: *Nature computational science* 1.3 (2021), pp. 199–211 (cit. on p. 6).

[20]Anna Smallcombe. "Multicolor imaging: the important question of co-localization". In: *Biotechniques* 30.6 (2001), pp. 1240–1246 (cit. on p. 6).

[21]Catherine G Galbraith and James A Galbraith. "Super-resolution microscopy at a glance". In: *Journal of cell science* 124.10 (2011), pp. 1607–1611 (cit. on p. 6).

[22]Daniel McBride, Chin Su, Jun Kameoka, and Stanislav Vitha. "A low cost and versatile STED superresolution fluorescent microscope". In: (2013) (cit. on p. 6).

[23]Yingying Jing, Chenshuang Zhang, Bin Yu, Danying Lin, and Junle Qu. "Super-resolution microscopy: shedding new light on in vivo imaging". In: *Frontiers in Chemistry* 9 (2021), p. 746900 (cit. on p. 6).

[24]Ola Söderberg, Karl-Johan Leuchowius, Mats Gullberg, et al. "Characterizing proteins and their interactions in cells and tissues using the in situ proximity ligation assay". In: *Methods* 45.3 (2008), pp. 227–232 (cit. on p. 6).

[25]Ola Söderberg, Mats Gullberg, Malin Jarvius, et al. "Direct observation of individual endogenous protein complexes in situ by proximity ligation". In: *Nature methods* 3.12 (2006), pp. 995–1000 (cit. on p. 7).

[26]Matthias Selbach and Matthias Mann. "Protein interaction screening by quantitative immunoprecipitation combined with knockdown (QUICK)". In: *Nature methods* 3.12 (2006), pp. 981–983 (cit. on p. 7).

[27] Steven Wang, Runxin Wu, Jiaqi Lu, et al. “Protein-protein interaction networks as miners of biological discovery”. In: *Proteomics* 22.15-16 (2022), p. 2100190 (cit. on p. 7).

[28] Pranveer Singh. “SPR biosensors: historical perspectives and current challenges”. In: *Sensors and actuators B: Chemical* 229 (2016), pp. 110–130 (cit. on p. 7).

[29] Michael J Skaug, Joshua N Mabry, and Daniel K Schwartz. “Single-molecule tracking of polymer surface diffusion”. In: *Journal of the American Chemical Society* 136.4 (2014), pp. 1327–1332 (cit. on p. 7).

[30] Phineus RL Markwick, Thérèse Malliavin, and Michael Nilges. “Structural biology by NMR: structure, dynamics, and interactions”. In: *PLoS computational biology* 4.9 (2008), e1000168 (cit. on p. 8).

[31] Marco Y Hein, Nina C Hubner, Ina Poser, et al. “A human interactome in three quantitative dimensions organized by stoichiometries and abundances”. In: *Cell* 163.3 (2015), pp. 712–723 (cit. on p. 9).

[32] Katja Luck, Dae-Kyum Kim, Luke Lambourne, et al. “A reference map of the human binary protein interactome”. In: *Nature* 580.7803 (2020), pp. 402–408 (cit. on p. 9).

[33] Mohamed Ali Ghadie and Yu Xia. “Are transient protein-protein interactions more dispensable?” In: *PLoS Computational Biology* 18.4 (2022), e1010013 (cit. on p. 9).

[34] Evelyn Ploetz, Eitan Lerner, Florence Husada, et al. “Förster resonance energy transfer and protein-induced fluorescence enhancement as synergetic multi-scale molecular rulers”. In: *Scientific reports* 6.1 (2016), p. 33257 (cit. on p. 9).

[35] Stefan A Maier et al. *Plasmonics: fundamentals and applications*. Vol. 1. Springer, 2007 (cit. on p. 18).

[36] Arpan Dutta, Ville Tiainen, and J Jussi Toppari. “Numerical study on the limit of quasi-static approximation for plasmonic nanosphere”. In: *AIP Conference Proceedings*. Vol. 2220. 1. AIP Publishing LLC. 2020, p. 050012 (cit. on p. 18).

[37] John David Jackson. *Classical electrodynamics*. 1999 (cit. on pp. 19, 20).

[38] Craig F Bohren and Donald R Huffman. *Absorption and scattering of light by small particles*. John Wiley & Sons, 1983 (cit. on pp. 21–23, 34).

[39] Peter B Johnson and R. W. Christy. “Optical constants of the noble metals”. In: *Physical review B* 6.12 (1972), p. 4370 (cit. on pp. 21, 27, 156, 217, 218).

[40] Gustav Mie. “Grundlagen einer theorie der materie”. In: *Annalen der Physik* 344.11 (1912), pp. 1–40 (cit. on p. 22).

[41] Julius Adams Stratton. *Electromagnetic theory*. Vol. 33. John Wiley & Sons, 2007 (cit. on p. 22).

[42] Hitoshi Kuwata, Hiroharu Tamaru, Kunio Esumi, and Kenjiro Miyano. “Resonant light scattering from metal nanoparticles: Practical analysis beyond Rayleigh approximation”. In: *Applied physics letters* 83.22 (2003), pp. 4625–4627 (cit. on p. 25).

[43]Arthur L Aden and Milton Kerker. “Scattering of electromagnetic waves from two concentric spheres”. In: *Journal of Applied Physics* 22.10 (1951), pp. 1242–1246 (cit. on pp. 26, 31).

[44]Harold P Erickson. “Size and shape of protein molecules at the nanometer level determined by sedimentation, gel filtration, and electron microscopy”. In: *Biological procedures online* 11 (2009), pp. 32–51 (cit. on p. 32).

[45]Yujin E Kim, Mark S Hipp, Andreas Bracher, Manajit Hayer-Hartl, and F Ulrich Hartl. “Molecular chaperone functions in protein folding and proteostasis”. In: *Annual review of biochemistry* 82 (2013), pp. 323–355 (cit. on p. 32).

[46]Álvaro Barroso Peña, Steffi Ketelhut, Peter Heiduschka, et al. “Refractive index properties of the retina accessed by multi-wavelength digital holographic microscopy”. In: *Three-Dimensional and Multidimensional Microscopy: Image Acquisition and Processing XXVI*. Vol. 10883. SPIE. 2019, pp. 44–49 (cit. on p. 32).

[47]Richard Gans. “Über die form ultramikroskopischer goldteilchen”. In: *Annalen der Physik* 342.5 (1912), pp. 881–900 (cit. on p. 34).

[48]Paul Latimer. “Light scattering by ellipsoids”. In: *Journal of Colloid and Interface Science* 53.1 (1975), pp. 102–109 (cit. on p. 34).

[49]Hendrik Antoon Lorentz. *The theory of electrons and its applications to the phenomena of light and radiant heat*. Vol. 29. GE Stechert & Company, 1916 (cit. on p. 34).

[50]Maxim A Yurkin and Alfons G Hoekstra. “The discrete-dipole-approximation code ADDA: capabilities and known limitations”. In: *Journal of Quantitative Spectroscopy and Radiative Transfer* 112.13 (2011), pp. 2234–2247 (cit. on p. 35).

[51]V Varyshchuk, T Bulavinets, I Yaremchuk, and Ya Bobitski. “The shape effect on the optical properties of metallic nanoparticles”. In: *2018 14th International Conference on Advanced Trends in Radioelecrtronics, Telecommunications and Computer Engineering (TCSET)*. IEEE. 2018, pp. 458–461 (cit. on p. 39).

[52]Brendan Pietrobon and Vladimir Kitaev. “Photochemical synthesis of monodisperse size-controlled silver decahedral nanoparticles and their remarkable optical properties”. In: *Chemistry of Materials* 20.16 (2008), pp. 5186–5190 (cit. on pp. 39, 44, 49).

[53]Peter Zijlstra, Pedro MR Paulo, and Michel Orrit. “Optical detection of single non-absorbing molecules using the surface plasmon resonance of a gold nanorod”. In: *Nature nanotechnology* 7.6 (2012), pp. 379–382 (cit. on pp. 40, 217).

[54]Li Lin, Xinyuan Bi, Yuqing Gu, Fu Wang, and Jian Ye. “Surface-enhanced Raman scattering nanotags for bioimaging”. In: *Journal of Applied Physics* 129.19 (2021), p. 191101 (cit. on pp. 40, 176).

[55]Peipei Yang, Jianzhong Zheng, Yong Xu, Qiao Zhang, and Lin Jiang. “Colloidal synthesis and applications of plasmonic metal nanoparticles”. In: *Advanced materials* 28.47 (2016), pp. 10508–10517 (cit. on p. 41).

[56]John Turkevich, Peter Cooper Stevenson, and James Hillier. “A study of the nucleation and growth processes in the synthesis of colloidal gold”. In: *Discussions of the Faraday Society* 11 (1951), pp. 55–75 (cit. on p. 42).

[57]Roya Herizchi, Elham Abbasi, Morteza Milani, and Abolfazl Akbarzadeh. “Current methods for synthesis of gold nanoparticles”. In: *Artificial cells, nanomedicine, and biotechnology* 44.2 (2016), pp. 596–602 (cit. on p. 42).

[58]PC Lee and D Meisel. “Adsorption and surface-enhanced Raman of dyes on silver and gold sols”. In: *The Journal of Physical Chemistry* 86.17 (1982), pp. 3391–3395 (cit. on p. 42).

[59]Asta Šileikaitė, Igoris Prosyčevas, Judita Puišo, Algimantas Juraitis, and Asta Guobienė. “Analysis of silver nanoparticles produced by chemical reduction of silver salt solution”. In: *Mater. Sci* 12.4 (2006), pp. 1392–1320 (cit. on p. 42).

[60]Yunhu Gao and Laura Torrente-Murciano. “Mechanistic insights of the reduction of gold salts in the Turkevich protocol”. In: *Nanoscale* 12.4 (2020), pp. 2740–2751 (cit. on p. 42).

[61]Dennis Steinigeweg and Sebastian Schluecker. “Monodispersity and size control in the synthesis of 20–100 nm quasi-spherical silver nanoparticles by citrate and ascorbic acid reduction in glycerol–water mixtures”. In: *Chemical Communications* 48.69 (2012), pp. 8682–8684 (cit. on p. 42).

[62]Nimer Murshid and Vladimir Kitaev. “Role of poly (vinylpyrrolidone)(PVP) and other sterically protecting polymers in selective stabilization of {111} and {100} facets in pentagonally twinned silver nanoparticles”. In: *Chemical communications* 50.10 (2014), pp. 1247–1249 (cit. on pp. 43, 44, 47, 54).

[63]Yugang Sun and Younan Xia. “Shape-controlled synthesis of gold and silver nanoparticles”. In: *science* 298.5601 (2002), pp. 2176–2179 (cit. on p. 43).

[64]Younan Xia, Yujie Xiong, Byungkwon Lim, and Sara E Skrabalak. “Shape-controlled synthesis of metal nanocrystals: simple chemistry meets complex physics?” In: *Angewandte Chemie International Edition* 48.1 (2009), pp. 60–103 (cit. on p. 43).

[65]Rongchao Jin, YunWei Cao, Chad A Mirkin, et al. “Photoinduced conversion of silver nanospheres to nanoprisms”. In: *science* 294.5548 (2001), pp. 1901–1903 (cit. on p. 43).

[66]Kevin G Stamplecoskie and Juan C Scaiano. “Light emitting diode irradiation can control the morphology and optical properties of silver nanoparticles”. In: *Journal of the American Chemical Society* 132.6 (2010), pp. 1825–1827 (cit. on p. 43).

[67]Kazuo Watanabe, Dietrich Menzel, Niklas Nilius, and Hans-Joachim Freund. “Photochemistry on metal nanoparticles”. In: *Chemical reviews* 106.10 (2006), pp. 4301–4320 (cit. on p. 44).

[68]Israel Pala Rosas, José Luis Contreras, José Salmones, et al. “Catalytic dehydration of glycerol to acrolein over a catalyst of Pd/LaY zeolite and comparison with the chemical equilibrium”. In: *Catalysts* 7.3 (2017), p. 73 (cit. on p. 47).

[69]Yih Hong Lee, Huanjun Chen, Qing-Hua Xu, and Jianfang Wang. “Refractive index sensitivities of noble metal nanocrystals: the effects of multipolar plasmon resonances and the metal type”. In: *The Journal of Physical Chemistry C* 115.16 (2011), pp. 7997–8004 (cit. on pp. 48, 60).

[70]Kosuke Sugawa, Hironobu Tahara, Ayane Yamashita, et al. “Refractive index susceptibility of the plasmonic palladium nanoparticle: Potential as the third plasmonic sensing material”. In: *Acs Nano* 9.2 (2015), pp. 1895–1904 (cit. on p. 48).

[71]Hemant Ramakant Hegde, Santhosh Chidangil, and Rajeev K Sinha. “Refractive index sensitivity of triangular Ag nanoplates in solution and on glass substrate”. In: *Sensors and Actuators A: Physical* 305 (2020), p. 111948 (cit. on p. 48).

[72]LD Marks and L Peng. “Nanoparticle shape, thermodynamics and kinetics”. In: *Journal of Physics: Condensed Matter* 28.5 (2016), p. 053001 (cit. on p. 55).

[73]Saran Poovarodom, John D Bass, Son-Jong Hwang, and Alexander Katz. “Investigation of the Core- Shell Interface in Gold@ Silica Nanoparticles: A Silica Imprinting Approach”. In: *Langmuir* 21.26 (2005), pp. 12348–12356 (cit. on p. 56).

[74]Nimer Murshid, Ilya Gourevich, Neil Coombs, and Vladimir Kitaev. “Gold plating of silver nanoparticles for superior stability and preserved plasmonic and sensing properties”. In: *Chemical Communications* 49.97 (2013), pp. 11355–11357 (cit. on p. 56).

[75]Hung-Jen Wu, Joel Henzie, Wan-Chen Lin, et al. “Membrane-protein binding measured with solution-phase plasmonic nanocube sensors”. In: *nature methods* 9.12 (2012), pp. 1189–1191 (cit. on p. 60).

[76]Jung Soo Suk, Qingguo Xu, Namho Kim, Justin Hanes, and Laura M Ensign. “PEGylation as a strategy for improving nanoparticle-based drug and gene delivery”. In: *Advanced drug delivery reviews* 99 (2016), pp. 28–51 (cit. on p. 61).

[77]Anna Tycova, Karel Kleparnik, and Frantisek Foret. “Bi-Ligand Modification of Nanoparticles: An Effective Tool for Surface-Enhanced Raman Spectrometry in Salinated Environments”. In: *Nanomaterials* 9.9 (2019), p. 1259 (cit. on p. 62).

[78]Peter Zijlstra, Pedro MR Paulo, Kuai Yu, Qing-Hua Xu, and Michel Orrit. “Chemical Interface Damping in Single Gold Nanorods and Its Near Elimination by Tip-Specific Functionalization”. In: *Angewandte Chemie International Edition* 33.51 (2012), pp. 8352–8355 (cit. on p. 64).

[79]Eric P Goodwin and James C Wyant. “Field guide to interferometric optical testing”. In: SPIE Bellingham, WA. 2006 (cit. on p. 68).

[80]David J Griffiths. *INTRODUCTION TO ELECTRODYNAMICS Fourth Edition*. 2015 (cit. on p. 68).

[81]Richard J Williams, Andrew J Gatesman, Thomas M Goyette, and Robert H Giles. “Radar cross section measurements of frequency selective terahertz retroreflectors”. In: *Terahertz physics, devices, and systems VIII: advanced applications in industry and defense*. Vol. 9102. SPIE. 2014, pp. 171–183 (cit. on p. 73).

[82]Photonics Handbook. “https://www.photonics.com/EDU/Handbook.aspx”. In: (2023) (cit. on p. 74).

[83]Optical Coatings Thorlabs GmbH. “https://www.thorlabs.com/newgrouppage9.cfm?objectgroup_id=5840”. In: (2023) (cit. on p. 74).

[84]Sander Konijnenberg, J. L. Aurele, and Paul H. Urbach. *Optics*. LibreTexts, 2022 (cit. on p. 83).

[85]JB Bates. “Fourier transform spectroscopy”. In: *Computers & Mathematics with Applications* 4.2 (1978), pp. 73–84 (cit. on pp. 86, 88).

[86]Robert John Bell. “Introductory fourier transform spectroscopy”. In: *American Journal of Physics* 41.1 (1973), pp. 149–151 (cit. on pp. 86, 88).

[87]Julius Cohen. *Introduction to Fourier transform spectroscopy*. US Department of Commerce, National Bureau of Standards, 1986 (cit. on p. 88).

[88]AS Filler. “Photon-noise-limited Fourier spectroscopy”. In: *JOSA* 63.5 (1973), pp. 589–591 (cit. on p. 88).

[89]Douglas Magde, Elliot L Elson, and Watt W Webb. “Fluorescence correlation spectroscopy. II. An experimental realization”. In: *Biopolymers: Original Research on Biomolecules* 13.1 (1974), pp. 29–61 (cit. on pp. 91, 93).

[90]Elliot L Elson and Douglas Magde. “Fluorescence correlation spectroscopy. I. Conceptual basis and theory”. In: *Biopolymers: Original Research on Biomolecules* 13.1 (1974), pp. 1–27 (cit. on pp. 91, 93).

[91]Watt W Webb. “Applications of fluorescence correlation spectroscopy”. In: *Quarterly Reviews of Biophysics* 9.1 (1976), pp. 49–68 (cit. on p. 91).

[92]Jerker Widengren, Uelo Mets, and Rudolf Rigler. “Fluorescence correlation spectroscopy of triplet states in solution: a theoretical and experimental study”. In: *The Journal of Physical Chemistry* 99.36 (1995), pp. 13368–13379 (cit. on p. 91).

[93]R Rigler, Ülo Mets, J Widengren, and P Kask. “Fluorescence correlation spectroscopy with high count rate and low background: analysis of translational diffusion”. In: *European Biophysics Journal* 22 (1993), pp. 169–175 (cit. on p. 91).

[94]Ted A Laurence, Samantha Fore, and Thomas Huser. “Fast, flexible algorithm for calculating photon correlations”. In: *Optics letters* 31.6 (2006), pp. 829–831 (cit. on pp. 94, 105, 228).

[95]Lisa Faye Marshall. “Spectral dynamics of single quantum dots: A study using photon-correlation Fourier spectroscopy for submillisecond time resolution at low temperature and in solution”. PhD thesis. Massachusetts Institute of Technology, 2011 (cit. on pp. 95, 192).

[96]Jian Cui et al. “Deconstructing the room-temperature emission spectra of nanocrystals using Photon-Correlation Fourier Spectroscopy”. PhD thesis. Massachusetts Institute of Technology, 2014 (cit. on pp. 95, 192).

[97]Andrew Paul Beyler. “Single-nanocrystal photon correlation: A versatile tool for elucidating basic physics and characterizing applications-relevant properties”. PhD thesis. Massachusetts Institute of Technology, 2015 (cit. on pp. 95, 97, 98, 225, 233).

[98]Lisa F Marshall, Jian Cui, Xavier Brokmann, and Moungi G Bawendi. “Extracting spectral dynamics from single chromophores in solution”. In: *Physical review letters* 105.5 (2010), p. 053005 (cit. on pp. 99, 238).

[99]Dirk P Kroese, Thomas Taimre, and Zdravko I Botev. *Handbook of monte carlo methods*. John Wiley & Sons, 2013 (cit. on p. 101).

[100]Jian Cui and Korneel Ridderbeek. “Method, Apparatus and System for Characterizing Transient Interactions Betwen Biomolecules”. 2022 (cit. on pp. 103, 134).

[101]Joseph W Goodman. *Statistical optics*. John Wiley & Sons, 2015 (cit. on p. 106).

[102]Xavier Brokmann, Moungi Bawendi, Laurent Coolen, and Jean-Pierre Hermier. “Photon-correlation Fourier spectroscopy”. In: *Optics express* 14.13 (2006), pp. 6333–6341 (cit. on p. 111).

[103]Jian Cui, Andrew P Beyler, Lisa F Marshall, et al. “Direct probe of spectral inhomogeneity reveals synthetic tunability of single-nanocrystal spectral linewidths”. In: *Nature chemistry* 5.7 (2013), pp. 602–606 (cit. on pp. 131, 140, 238).

[104]Jian Cui, Andrew P Beyler, Igor Coropceanu, et al. “Evolution of the single-nanocrystal photoluminescence linewidth with size and shell: implications for exciton–phonon coupling and the optimization of spectral linewidths”. In: *Nano letters* 16.1 (2016), pp. 289–296 (cit. on p. 131).

[105]Youju Huang and Dong-Hwan Kim. “Dark-field microscopy studies of polarization-dependent plasmonic resonance of single gold nanorods: rainbow nanoparticles”. In: *Nanoscale* 3.8 (2011), pp. 3228–3232 (cit. on p. 139).

[106]Mengmeng Liu, Jie Chao, Suhui Deng, et al. “Dark-field microscopy in imaging of plasmon resonant nanoparticles”. In: *Colloids and Surfaces B: Biointerfaces* 124 (2014), pp. 111–117 (cit. on p. 139).

[107]Gert Frens. “Controlled nucleation for the regulation of the particle size in monodisperse gold suspensions”. In: *Nature physical science* 241.105 (1973), pp. 20–22 (cit. on p. 145).

[108]Carola Schopf, Ethel Noonan, Aidan J Quinn, and Daniela Iacopino. “Self-assembly of gold nanocrystals into discrete coupled plasmonic structures”. In: *Crystals* 6.9 (2016), p. 117 (cit. on p. 153).

[109]Jun Hee Yoon, Florian Selbach, Ludmilla Schumacher, Jesil Jose, and Sebastian Schlücker. “Surface plasmon coupling in dimers of gold nanoparticles: Experiment and theory for ideal (spherical) and nonideal (faceted) building blocks”. In: *Acs Photonics* 6.3 (2019), pp. 642–648 (cit. on p. 153).

[110]Erik Martinsson, Marinus A Otte, Mohammad Mehdi Shahjamali, Borja Sepulveda, and Daniel Aili. “Substrate effect on the refractive index sensitivity of silver nanoparticles”. In: *The Journal of Physical Chemistry C* 118.42 (2014), pp. 24680–24687 (cit. on p. 155).

[111]JP Wilcoxon, JE Martin, F Parsapour, B Wiedenman, and DF Kelley. “Photoluminescence from nanosize gold clusters”. In: *The Journal of chemical physics* 108.21 (1998), pp. 9137–9143 (cit. on p. 157).

[112]Mona B Mohamed, Victor Volkov, Stephan Link, and Mostafa A El-Sayed. “Thelightning’gold nanorods: fluorescence enhancement of over a million compared to the gold metal”. In: *Chemical Physics Letters* 317.6 (2000), pp. 517–523 (cit. on p. 157).

[113]Alexei Tcherniak, Sergio Dominguez-Medina, Wei-Shun Chang, et al. “One-photon plasmon luminescence and its application to correlation spectroscopy as a probe for rotational and translational dynamics of gold nanorods”. In: *The Journal of Physical Chemistry C* 115.32 (2011), pp. 15938–15949 (cit. on p. 157).

[114]Sergey Burikov, Tatiana Dolenko, Svetlana Patsaeva, Yuriy Starokurov, and Viktor Yuzhakov. “Raman and IR spectroscopy research on hydrogen bonding in water–ethanol systems”. In: *Molecular physics* 108.18 (2010), pp. 2427–2436 (cit. on pp. 157, 158).

[115]JH Yan, CG Wang, H Zhang, and C Cheng. “Evaluation of emission cross section of CdSe quantum dots for laser applications”. In: *Laser Physics Letters* 9.7 (2012), p. 529 (cit. on p. 159).

[116]MV Smoluchowski. “Mathematical theory of the kinetics of the coagulation of colloidal solutions”. In: *Z. Phys. Chem.* 92 (1917), pp. 129–168 (cit. on pp. 163, 189).

[117]Maximilian Schlosshauer and David Baker. “Realistic protein–protein association rates from a simple diffusional model neglecting long-range interactions, free energy barriers, and landscape ruggedness”. In: *Protein science* 13.6 (2004), pp. 1660–1669 (cit. on p. 163).

[118]Martin Dieter Baaske, Peter Sebastian Neu, and Michel Orrit. “Label-free plasmonic detection of untethered nanometer-sized Brownian particles”. In: *ACS nano* 14.10 (2020), pp. 14212–14218 (cit. on pp. 166, 175, 176, 184).

[119]Roberto Ortiz, Stefan Olsen, and Esben Thormann. “Salt-induced control of the grafting density in poly (ethylene glycol) brush layers by a grafting-to approach”. In: *Langmuir* 34.15 (2018), pp. 4455–4464 (cit. on p. 172).

[120]Maartje MC Bastings, Frances M Anastassacos, Nandhini Ponnuswamy, et al. “Modulation of the cellular uptake of DNA origami through control over mass and shape”. In: *Nano letters* 18.6 (2018), pp. 3557–3564 (cit. on p. 177).

[121]Martin D Baaske, Nasrin Asgari, Deep Punj, and Michel Orrit. “Nanosecond time scale transient optoplasmonic detection of single proteins”. In: *Science Advances* 8.2 (2022), eabl5576 (cit. on pp. 177, 184).

[122]Jae-Yeol Kim, Fanjie Meng, Janghyun Yoo, and Hoi Sung Chung. “Diffusion-limited association of disordered protein by non-native electrostatic interactions”. In: *Nature communications* 9.1 (2018), p. 4707 (cit. on p. 179).

[123]Bingbo Zhang, Xiaohui Wang, Fengjun Liu, Yingsheng Cheng, and Donglu Shi. “Effective reduction of nonspecific binding by surface engineering of quantum dots with bovine serum albumin for cell-targeted imaging”. In: *Langmuir* 28.48 (2012), pp. 16605–16613 (cit. on p. 181).

[124]Guillaume Baffou. *Thermoplasmonics: Heating Metal Nanoparticles Using Light*. Cambridge University Press, 2017 (cit. on p. 190).

[125]Mark J Richards, Chih-Yun Hsia, Rohit R Singh, et al. “Membrane protein mobility and orientation preserved in supported bilayers created directly from cell plasma membrane blebs”. In: *Langmuir* 32.12 (2016), pp. 2963–2974 (cit. on p. 191).

List of Figures

List of Tables

List of Listings

Appendix

A

This is the appendix of the dissertation of Korneel Ridderbeek.

A.1 Data Availability

All data and analysis code is available on `https://ascgitlab.helmholtz-muenchen.de/korneel.ridderbeek`. Some raw data files are not uploaded to the Gitlab folder due to size constraints, however these are available upon request.

A.2 DDA Convergence

To test the convergence of our Discrete Dipole Approximation (DDA) simulations, we compared Silver spherical nanoparticles (AgSNP) of $40\mathrm{nm}$ with the analytical expression from Mie theory, see Figure A.1. The dielectric constants for Silver are obtained from Johnson & Christy.[39] Here, the spectra of AgSNP with various dipole densities are plotted (Figure A.1a). Of which the convergence in peak height, by computing the residuals of the curve, (Figure A.1b) and the peak position (Figure A.1c), by Lorentzian fitting, are computed. Note that in the simulation with 300 dipoles several wavelengths are missing, since these simulations hit the maximum run time of $5\mathrm{days}$ on the computational cluster. Additionally, we observe little difference between 200 and 250 dipoles in their peak position, telling us that we converged well enough for our purposes, since we only are interested in peak positions and relative shifts therein. Therefore, we chosen to perform simulations with $\frac{250}{40} = 6.25\mathrm{dipoles/nm}$. This number compares well to literature, were other choose $6.25\mathrm{dipoles/nm}$.[53] Interestingly, we do still observe a mismatch of $0.5\mathrm{nm}$ in the peak position and also in the sum of the height residuals. We attribute this difference to a loss in volume from converting an analytical $40\mathrm{nm}$ into cubical dipoles.

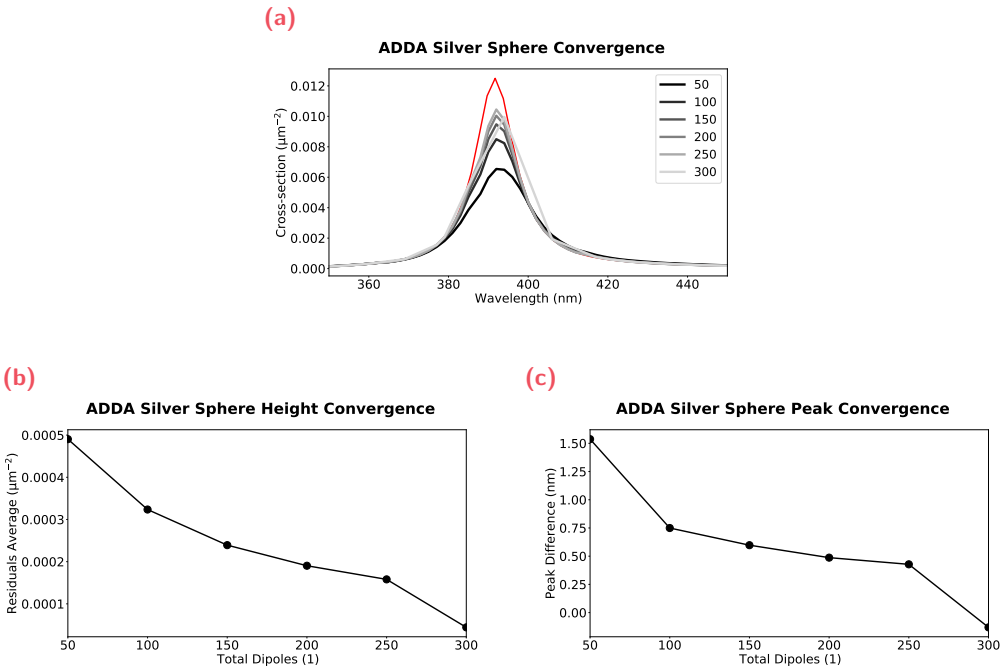

Fig. A.1.: DDA simulations of spherical Silver nanoparticles (AgSNP) with *(a)* their spectrum containing various dipole densities, *(b)* the residuals of their height compared with Mie theory, and *(b)* The difference in their resonance peak.

A.3 DDA Absorption AgDNP

In Figure A.2 an absorption cross-section of a Silver decahedra nanoparticle is shown. The dielectric constants for Silver are obtained from Johnson & Christry.[39] From this computation we obtain a absorption maximum of $0.012\,\mu\mathrm{m}^{-2}$.

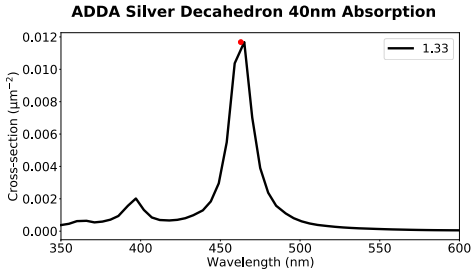

Fig. A.2.: Absorption cross-section of a Silver decahedra nanoparticle computed with DDA

A.4 DDA Sensitivities

Figure A.3 shows the scattering cross-section of various nanoparticles simulated in water ($n = 1.33$). To obtain their sensitivities the refractive index is stepwise increased with $\delta n = 0.02\mathrm{RIU}$ for 5 different refractive indices. First, scattering spectra of a spherical Silver nanoparticle and its sensitivity curve by tracking the dipolar resonance are shown in Figure A.3a and Figure A.3b. For the sphere we extract a sensitivity of $110\,\mathrm{nm\,RIU^{-1}}$ ($880\,\mathrm{meV\,RIU^{-1}}$) and a FOM of 8.2. For a Silver cubical nanoparticles the scattering cross-sections are shown in Figure A.3c and from its sensitivity curve (Figure A.3d) a sensitivity of $196.9\,\mathrm{nm\,RIU^{-1}}$ ($1177.3\,\mathrm{meV\,RIU^{-1}}$) and a FOM of 12.4 are found.

For rods and decahedra, different scattering cross-sections are obtained for the x and y polarization of the incident light. This is due to the asymmetry of those shapes along those axes. Therefore, we show the average cross-section of both polarizations. In Figure A.3e the cross-sections are shown, of which the dipolar resonance along the longitudinal axis of the rod is chosen for the sensitivity curves, see Figure A.3f. A sensitivity of $300\,\mathrm{nm\,RIU^{-1}}$ ($1025\,\mathrm{meV\,RIU^{-1}}$) and a FOM of 8.6 are found for the rod. Additionally, we computed the scattering cross-sections and sensitivity curves for a Gold-coated Silver decahedra nanoparticle, shown in Figure A.3g and Figure A.3h. From these data a sensitivity of $349\,\mathrm{nm\,RIU^{-1}}$ ($2315.8\,\mathrm{meV\,RIU^{-1}}$) and a FOM of 3.4 are extracted. We hypothesize that the interfaces between the Silver and the Gold were too sharply defined such that the spectra became multi-peaked and very broad.

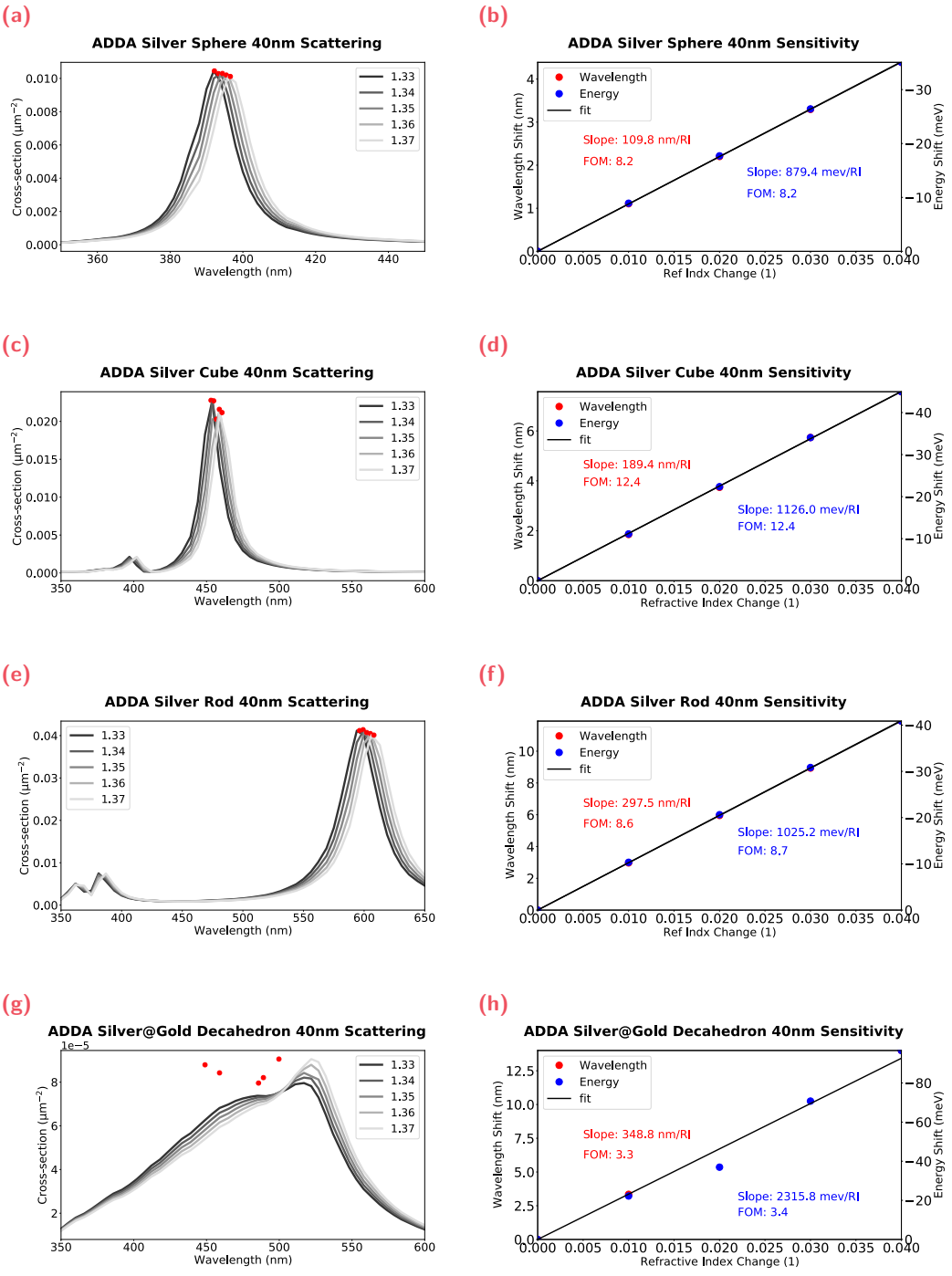

Fig. A.3.: Discrete Dipole Approximation simulations of Silver spherical, cubical, and rod-shaped, and Silver@Gold decahedral nanoparticles.

A.5 Fickian Focal Volume Diffusion

Throughout this thesis light coming from particles diffusing through a focal volume has been simulated by computing the typical diffusion time needed to cross a spherical focal volume. During this time photons have been randomly generated through a Monte-Carlo method. In this section a more adequate model is proposed, which still utilizes the time-efficiency from Monte-Carlo style simulations, but has diffusion dynamics much closer to Molecular Dynamics (MD) simulations. First, the realization is made that with Fickian diffusion the expected displacement, x, goes as:

$$x = \sqrt{2nDt} \tag{A.1}$$

with n the dimension parameter, D the diffusion coefficient, and t the time. From this equation it is evident that as time progresses the expected displacement would increase less. Assuming a spherical focal volume that has a Gaussian distribution for expected photon return rate, it would not be correct to simply simulate photon arrival times with a Gaussian distribution. Rather, the Gaussian distribution distance term should be a square root function as just has been introduced.

$$I \propto e^{-\left(x-\frac{w}{2}w\right)^2} I \qquad \propto e^{-\left(\sqrt{2nDt}-\frac{w}{2}w\right)^2} \tag{A.2}$$

with w, the $1/e^2$ bream radius of a focussed laser beam. In Figure A.4a, we plotted the theoretical intensity distribution of a particle moving from one side of a Gaussian focal volume to the other side. This curve is compared with a full MD simulation of 2000 particles in a simulation box that are showing Brownian diffusion through time computation of Langevin equations. In the center of the simulation box a Gaussian 3 dimensional sphere is defined as a focal volume with typical width w. Particles inside this sphere contribute to the output intensity and are more intense closer to the center. Particles intensities summed over 10 runs of each $0.05\mathrm{s}$ simulation time resulted in the second curve. That matches our theoretical particle very well. We do note that for a single particle the intensity traces and thus auto- and cross-correlations might be very different. However, in the high particle number limit these approximations yield. Next, we simulated photon streams with our initial implementation and with Fickian diffusion intensity distributions. In the latter case, Monte-Carlo sampling has been performed on the theoretical intensity distribution described above to yield photon arrival times. In Figure A.4b, we find the auto-

correlations from those Monte-Carlo simulations. Additionally they have been fitted with a 3D Fluorescence Correlation Spectroscopy (FCS) curve.

$$g^2(\tau) = \frac{1}{\langle N \rangle} \frac{1}{1+\tau/\tau_D} \frac{1}{(1+\tau/(\kappa^2\tau_D))^{1/2}} \tag{A.3}$$

with, $\tau_D = \frac{w^2}{4D}$ and κ a geometrical factor for the focal volume. In our special case of a spherical focal volume $\kappa = 1$. Firstly, we observe that the fits match the Fickian diffusion distribution much better than our initial implementation. We also find this from the fitted values, where the simulation was initialized with a diffusion coefficient of $D_{sim} = 8.6 \cdot 10^{-12}\mathrm{m}^2/\mathrm{s}$. We retrieved $D_{current} = 18.5 \cdot 10^{-12}\mathrm{m}^2/\mathrm{s}$ and $D_{Fickian} = 6.6 \cdot 10^{-12}\mathrm{m}^2/\mathrm{s}$. Note that this section only discusses a more adequate model for when the characteristic particle diffusion through the focal volume is desired. Since throughout this thesis, we correct for the focal volume diffusion (solution Photon-Correlation Fourier Spectroscopy), the results are not affected by this better diffusion implementation.

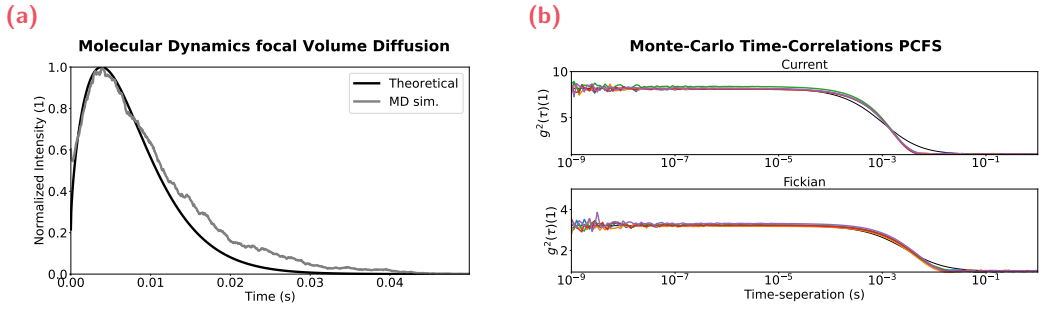

Fig. A.4.: *(a)* Molecular Dynamics (MD) simulations intensity in a spherical focal volume compared with theoretical intensity distribution from Fick's theory. *(b)* Full Sparse Monte Carlo Simulations with auto-correlations of particles diffusion through a focal volume as presented in this thesis compared with Fick's theoretical intensity distribution.

A.6 Components Lists of Optical Setup

This section summarizes all the components used to build the optical setup. For completeness, a schematic of the setup is shown again in Figure A.5.

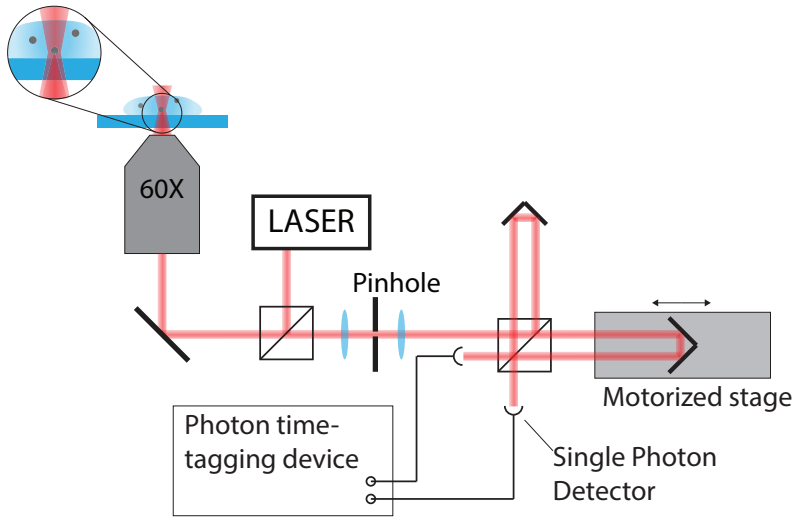

Fig. A.5.: A schematic of the optical setup built in this dissertation.

Amount	Description	Manufacturer	Product Number
Lasers			
1	Super Continuum White Light Laser	NKT	Fianium 15
1	Green HeNe Laser	NewPort	30972
1	Laser diode 450 nm	Thorlabs	PL450B
1	Laser diode 530 nm	Thorlabs	CPS520
1	Laser diode 488 nm	Sharp	GH048850B2G
Filterbox			
1	Variable filterbox	NKT	NKT VARIA
1	tunable filterbox	Photon Etc.	LLTF
Detectors			
2	single photon detector	MPD	PC-100-CTE
1	Time tagging device	PicoQuant	HydraHarp 400
Stages			
1	linear stage	Newport	XMS100-S
1	linear stage	Newport	XPS-D
1	custom sample stage	own	
Optics			
10	metal mirrors	Thorlabs	PF10-03-P01
2	Hollow retroreflectors	Newport	UBBR2.5-1
10	kinematic mounts	Thorlabs	Polaris
1	water immersion objective	Olympus	60xWI UPLANAPO
1	Beamsplitter cube	Newport	CG15KH1
1	Beamsplitter cube	Thorlabs	BS028
2	30 μm pinhole	Thorlabs	AC254-030-A-ML
3	100 mm lens	Thorlabs	AC254-100-A-ML
1	40 mm lens	Thorlabs	AC254-040-A-ML
1	free-space coupler	Thorlabs	TC06FC-543
2	3D axis manual stage	Thorlabs	PT3
many	Optical Post Assembly	Thorlabs	
various	Neutral Density filters	Thorlabs	

Tab. A.1.: Table of optical components used for the optical device introduced in this dissertation.

A.7 Hints for Performing PCFS Experiments

This section discusses some tips and tricks to perform PCFS experiments. The hope of this section is to accumulate the knowledge that is usually passed along members in the lab, but never written down.

First, the built of the interferometer is discussed. The choice of optical components is obviously free to anyone who wants to build a PCFS setup, however we tested several beamsplitters and found that a non-polarizing cube beamsplitter is the least sensitive to vibrations. The transmission efficiencies might not be as high as other beamsplitters, the equal amount of glass does ensure that both optical paths behave similar, such that compensation plates are not needed. The footprint of the interferometer is not discussed in this dissertation, but during some exchange with Dr. Hendrick Utzat he mentioned that a reduction of the footprint of the interferometer helps with thermal fluctuation in the room. In this case an additional mirror is needed to translate both optical path parallel to each other.

Second, the alignment of interferometer is discussed. This is a task that a PCFS user will experience regularly. For this, I advice to use of long coherence length laser. In that case the stage can be moved to its extremes and a piece of paper can be used to align circular fringes at the detector positions. First the stage is moved to close to the beamsplitter, then the steering mirror to guide the light into the interferometer can be used. Whereafter the stage is moved to far from the beamsplitter, to align the retroreflector of the other arm. These steps can be performed iteratively, much like walking the beam. More information is found on page 132 from Dr. Andrew Beyler's Dissertation.[97]

Third, sample selection. Ideally before every real measurement, some known sample is used as a control to find that the setup is working correctly. Then, I advice that when doing fluorescence, sample inhomogeneity might not be causing too many issues such that only the concentration has to be chosen correctly. Here, I would aim to keep the auto-correlation height between 1.3 to 2.0 and ideally at 1.5. This leaves enough photon pairs for sPCFS analysis, without causing sampling issues. However, when a user would like to perform scattering PCFS, I would advice to try to minimize sample inhomogeneity through centrifugation. First a slow centrifugation can be used to sediment the big clusters, whereafter a fast centrifugation can be used to separate small seeds out of solution. These latter particles would have less effect on the outcomes.

Fourth, the choice of dither frequency and measurement time. These settings depend on your sample. The dither frequency should be chosen slower than the diffusion time of the particles through the laser focal volume. Additionally, crosscorrelations close to the white fringe should be checked to make sure that the dither is slow enough such that a flat section in the cross-correlation at long time-seperations is available to select the ensemble at. This is important, since artefacts can be introduced in the outcomes by choosing the ensemble from a non-flat cross-correlation. Generally, the slower the dither, the better, with the downside that this results in longer measurement times.

A.8 Filtering of Time Trace

In Section 4.1.4, the difference in intensity between luminescence and scattering is discussed. Intensity fluctuations would be introduced by nanoparticles diffusing through the focal volume. Unfortunately, clusters or very big nanoparticles cause very large spikes in the intensity traces. The unwanted effect is that the auto- and cross-correlations are completely dominated by these spikes. Therefore, we explored the possibility to filter the intensity traces from large spikes. First, we explored the most simple idea to just cut the large spikes from the intensity traces. Figure A.6, shows the time-trace of a 2 laser scattering experiment on Gold spherical nanoparticles (AuSNP). The filtering introduces a kink in the auto-correlation function by removing the spikes, but introducing troughs of zero intensity. When calculating auto-correlations, these troughs act as the inverse of a spike.

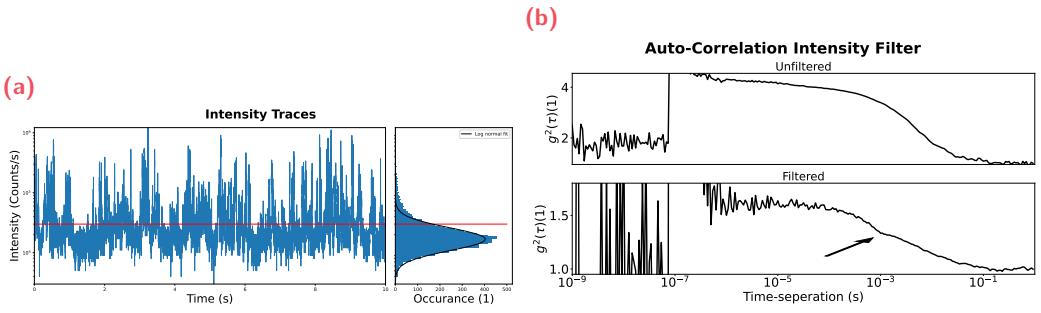

Fig. A.6.: Filtering on a *(a)* intensity trace, whereafter *(b)* the auto-correlation is computed on the cut intensity trace with zero intensity in the throughs.

To circumvent the problem of trough formation, we explored a second version of intensity trace filtering. Namely, we would filter the intensity traces and stitch them back together. Figure A.7 uses the same intensity trace as in Figure A.6, however this

time the auto-correlations are computed on stitched traces. These results look much better but are still flawed. The main problem with this approach is that, dynamics from large time-separations is introduced on smaller time-separations. Assume a diffusion event that causes a large intensity spike. This will come into the focal volume and emit light, before it hits our cut-off. Then we cut our the main part, but when it drops below the cut-off we do allow those photons to be part of our analysis. Then by stitching, the typical dynamics is sped-up by the amount that we cut out. For a few spikes in a time-trace these effects do not matter so much, since they will be washed by average effects. Unfortunately, the traces shown in this example almost consist half of intensity spikes. Therefore, this method would affect the outcome too much to be valid.

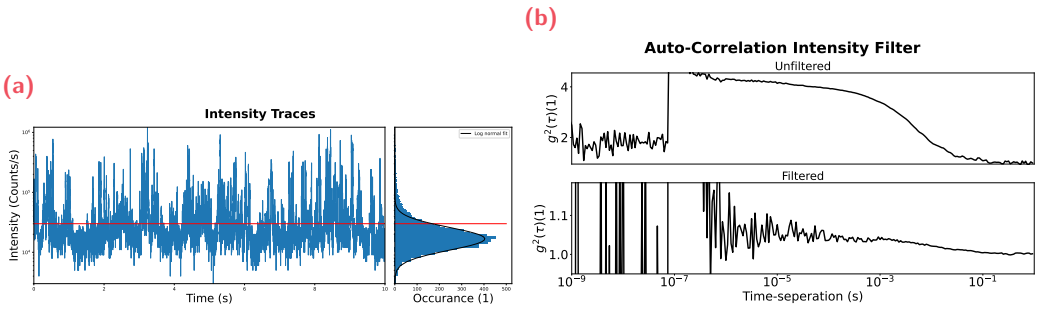

Fig. A.7.: Filtering on a *(a)* intensity trace, whereafter *(b)* the auto-correlation is computed on the cut **and** stitched intensity trace.

A.8.1 Intensity Filtering Algorithm

During a discussion with my Mentor Dr. Thomas Bischof, he mentioned a mathematical way to filter the intensity traces without introducing throughs or shifting timing information. This approach modifies the computation of the auto- or cross-correlation from Equation 3.75. Typically, the denominator is simplified by saying $\langle I(t)\rangle = \langle I(t+\tau)\rangle$, since the intensity spikes are Poissonian and the average intensity is assumed to remain equal. When filtering is applied this assumption no longer holds, and the terms have to be computed individually. Let us consider the computation of the auto-correlation to illustrate the new computation framework.

$$g^{(2)}(\tau) = \frac{\langle I(t)\, I(t+\tau)\rangle}{\langle I(t)\rangle \langle I(t+\tau)\rangle} \tag{A.4}$$

For the counting of the photon pairs, an algorithm such as Laurence's can still be used.[94] However, the normalization factor will become different. Here, we conceptually discuss the effects of the new framework and write it down in psuedo-code for later implementation. Let us define the filtering of the intensity trace through masks that indicate which region of the intensity trace we are interested in. In this case photons that arrived between T_1 and T_2 are photons that we are interested in. This is graphically shown in Figure A.8.

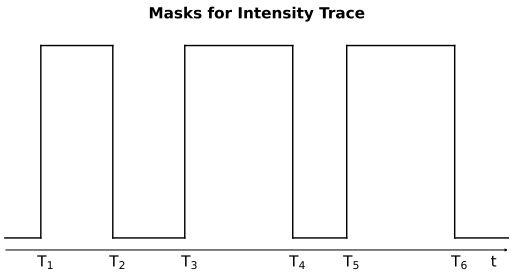

Fig. A.8.: Graphical representation of a masking function

In psuedo-code we define a function $masks_tau(masks, \tau, T)$, which takes an mask array ($masks$), a time-separation value (τ), and total time (T) as input. The output of this function is an array of new masks that are shifted by the time-separation value (τ) and it confines all the masks within the total time. From this function, we can already observe that $\langle I(t)\rangle \neq \langle I(t+\tau)\rangle$, since τ will shift certain masks out of the total time window. Next, we define a function $masked_array(photons, masks)$, that takes photon arrival times ($photons$) and masks ($masks$) as input. This function returns the photon arrival times that are within the masked regions. Note that it assumes that both $photons$ and $masks$ are monotonically increasing. Lastly, we need a function $normalize(g2, photons, masks, tau)$, which normalizes the photon pair count at a specific tau. To achieve this, the photons in the non-shifted and shifted masked arrays are simply counted. These functions can be used at one specific time-separation value. Therefore, to compute entire correlation curves, the computation has to be repeated to different tau values, as done so with a for loop.

```
def masks_tau(masks, tau, T):
  for left, right in masks:
  if left + tau > T:
    break
  elif right + tau > T:
    yield(left + tau, T)
  else:
    yield(left + tau, right + tau)

```

```
def masked_array(photons, masks):
  photon = next photons
  mask = next masks
  while True:
    if photon == None:
      break
    if masks == None:
      break
    if photon < mask
      next photon
    elif photon in mask
      yield
      next photon
    elif photon > mask
      next mask

def normalize(g2, photons, masks, tau):
  I_t = sum(masked_array(photons, masks))
  I_tau = sum(photons + tau, masks_tau(masks, tau, T)))
  return g2/(I_t * I_tau)

masks = [(T-1,T_2), ((T_3,T_4), ((T_5,T_6), ...]
tau_bin_array = [(tau_1,tau_2), ((tau_3,tau_4), ((tau_5,tau_6),
    ↪ ...]
G2_tau = []

for tau_left, tau_right in tau_bin_array:
  tau = (tau_left + tau_right)/2
  g2 = photon_pair_counter(masked_array(photons, masks),
            masked_array(photons + tau, masks_tau(masks, tau, T)),
          (tau_left, tau_right))

  G2 = normalize(g2, photons, masks, tau)
  G2_tau.append(G2)
```

Listing A.1: Psuedo-code of an auto-correlation algorith with intensity trace filtering.

A.9 Aid for Deciphering PCFS Intensity Correlations

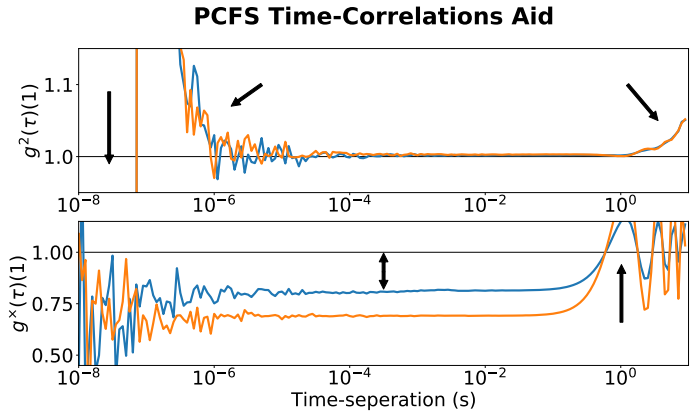

Fig. A.9.: Example of PCFS intensity correlations with arrows indicating features that a reader might observe.

This section is meant to aid the reader who is less familiar with Photon-Correlation Fourier Spectroscopy (PCFS) and the data shown. PCFS is an interferometric measurement technique that obtains interferogram envelopes oppose to the full interferogram from Fourier Transform Spectroscopy. The envelopes are obtained by introducing a small oscillation motion over path-length differences (dither) during measurements of the interference of the spectrum. The data obtained from any PCFS measurement are intensity correlations, such as auto- and cross-correlations. These are then later used to construct corrected cross-correlations, then interferograms, and then spectral correlations. However, this section only focusses on the features could be observed in the intensity correlations themselves, since I think it is useful for the reader to get a handle on this, before discussing processing steps further down the line. In Figure A.9, an example of PCFS intensity correlations are given. Arrows are draw to indicate features that might be observed.

1. Arrow at $\sim 10^{0}$s: an oscillation might be observed in the **auto-correlations** around these time scales due to the dither.

2. Arrow at $\sim 10^{1}$s: a rise might be observed in both the **auto- and cross-correlations** due to the dither normalization issues from the correlation computing algorithm (less photon pairs available for computation).

3. Arrow not shown at $\sim 10^{-3}$s: a decay might be observed in both the **auto- and cross-correlations** due to particle diffusing through the focal volume.

4. Arrow at $\sim 10^{-4}$s: an offset from 1 might be observed in the **cross-correlations** due to spectral anti-correlation.

5. Arrow at $\sim 10^{-7}$s: a rise might be observed in the **auto-correlations** due to afterpulsing of the single photon detectors.

6. Arrow at $\sim 10^{-8}$s: zero intensity might be observed in the **auto-correlations** due to the detector dead time.

A.10 PCFS and FTS Comparison Broad Spectra

In this paragraph data obtained with PCFS, FTS and handheld spectrometer (Thorlabs CCS100/M) as shown in Figure A.10. In this experiment the super continuum white light laser was used together with the NKT VARIA to create a spectrum at $500\,\mathrm{nm}$ with a bandwidth of $100\,\mathrm{nm}$. The raw obtained data are shown in Figure A.10a. Spectral correlations are computed from the raw data, which are shown in Figure A.10b. Here, we observe a mismatch between the PCFS spectral correlation and the other two methods. We hypothesize that the interferometric asymmetry caused by chromatic aberrations causes a "wrong" observation of the PCFS spectral correlations. Appendix A.11.4 goes deeper into a method that can be used to correct the PCFS interferogram by measuring a FTS interferogram.

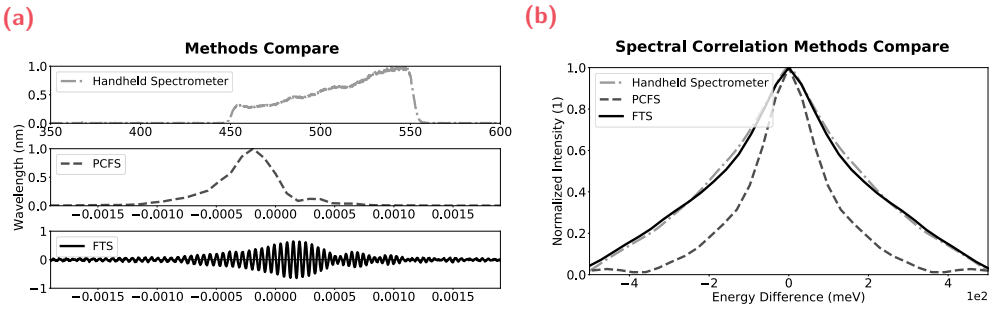

Fig. A.10.: A comparison spectral correlations obtained through PCFS, FTS and a handheld spectrometer *(a)* with their raw data and *(b)* the spectral correlations computed from the raw data in *(a)*.

A.11 Corrections in Scattering Photon-Correlation Fourier Spectroscopy

This section discusses three different types of corrections of scattering PCFS: driving light correction, interferogram asymmetry correction, and dither correction. For the latter, we find that the effect is rather minimum. The driving light does have an effect, however we explored under which conditions the effects would be minimum. These conditions can then be applied experimentally to not have to worry about the driving light. Unfortunately, the interferogram asymmetry has been found to have the largest effect of the extracted linewidths and experimental efforts to reduce or remove it have been unsuccessful. In this section, we describe mathematical and experimental corrections that can be performed to obtain the correct linewidths in scattering PCFS. Lastly, all three corrections are combined into one single correction method. The downside to this global correction is that it assumes that the single and ensemble linewidths are not too far off.

A.11.1 Driving Light Correction

In Section 2.1, it is mentioned that for scattering the resonance does not have its own unique spectrum. Rather it is resonating with a driving light spectrum. Also, in that section it is explored mathematically to derive a correction measurement. Unfortunately, this results in a unsolvable convolution in either path-length difference space of interferometer space. Therefore, the best approximation we have come up with is to simply divide the spectral correlations, such that $p_{LSPR}(\zeta,\tau) = p_{NP}(\zeta,\tau)/p_{DL}(\zeta,\tau)$. To test, whether this assumption is correct and to explored what conditions the driving light should apply to in order obtain the true LSPR linewidth from PCFS experiments, we simulated various resonances driven by various lights with our Monte-Carlo simulation model. Driving light spectrum shapes, such as Gaussian, Rectangular, Triangular, and Sawtooth, have been simulated with various widths, in combination with resonances of various widths. Prior to the simulation, we hypothesized that:

- the driving light spectrum should be flat
- the driving light bandwidth should be broader than the LSPR linewidth

From over 25 simulations, we found that the shape of the driving light does not matter greatly. The width of the driving light compared to the LSPR linewidth however is very important and can result in in errors of up to 50%. The results are

summarized in Table A.2 with the average percentual mismatch of all four shapes. Adding all the parameters into this table would only distract for the main point. However, the data and code are available upon request or can be found on Gitlab. From this table, we establish a rule-of-thumb that the driving light linewidth must be $2 - 2.5$ times larger than the expected resonance linewidth, in order to obtain correct results.

Driving Light Linewidth	**Resonance Linewidth**	**Percentual Mismatch**
20	10	$8\,\%$
500	100	$2\,\%$
500	400	$44\,\%$
50	10	$1\,\%$
200	100	$8\,\%$
125	100	$21\,\%$

Tab. A.2.: Table with different ratios of linewidths for the driving light and the resonance with their percentual errors indicating the findings made with Photon-Correlation Fourier Spectroscopy.

A.11.2 Afterpulsing Correction

Afterpulsing is a source of error in auto-correlations. Single photon detectors are designed to generate a large number of electrons from only a single photon detection event. Some of these electrons might get trapped in the active area of the detector, causing a second detection event much later after the initial photon absorption. The trapping and retriggering of a detection event are detector and intensity dependent. Dr. Andrew Beyler write in his dissertation about the characterization and subsequent subtraction from auto-correlation curves.[97] In Figure A.11, we characterized the shape of the afterpulsing pedestal on our setup and we find that when normalized with the maximum intensity, the shape is well conserved (Figure A.11a). A linear relationship is found between the inverse of the counts and the maximum intensity of the afterpulsing pedestal, see Figure A.11b. Lastly, we demonstrate that the subtraction of the afterpulsing pedestal from auto-correlation curves does indeed remove it. However, it should be noted that the noise increases. Additionally, due to the error on the linear fit, some curves are over- and others are under-corrected.

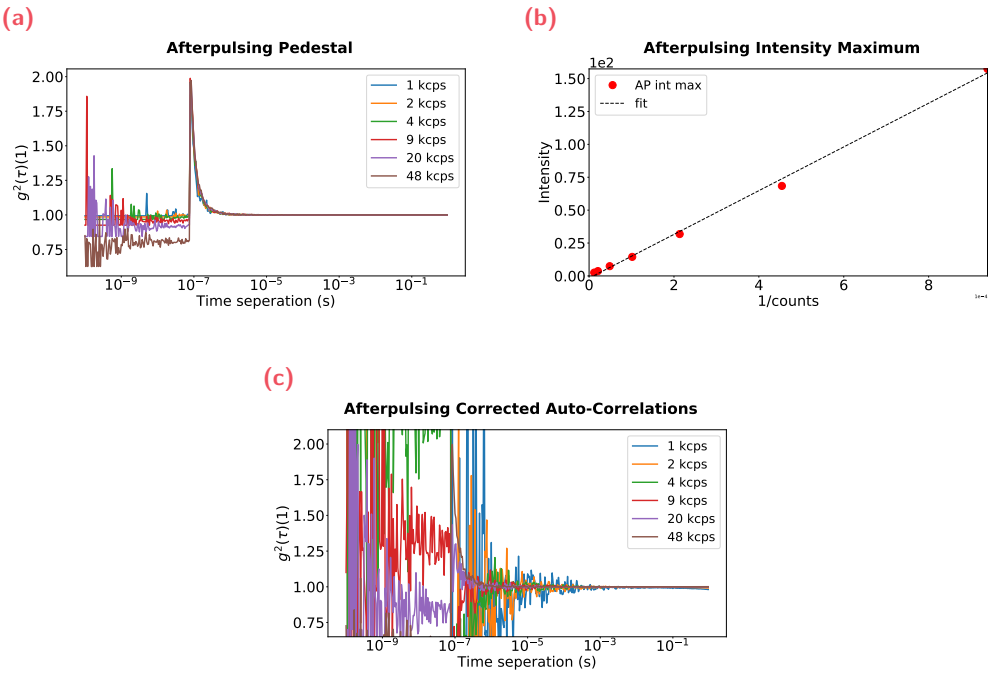

Fig. A.11.: Afterpulsing correction characterization through changing laser intensity. *(a)* Normalized auto-correlations give the same afterpulsing shape. *(b)* The maximum of the afterpulsing pedestal scales inversely with counts. *(c)* Auto-correlations corrected with the afterpulsing pedestal.

A.11.3 Dither Correction

In this section a method to correct dither artefacts in PCFS interferograms is discussed. The dither, a small periodic oscillation, samples the FTS interferogram to obtain the envelope squared. This sampling is dependent on the amplitude of the dither and the steepness of the interferogram. For sharp spectra ($< 300\,\mathrm{meV}$) the interferograms are broad enough, such that when the dither goes over a few fringes no real artefacts are observed. However for broad spectra ($> 300\,\mathrm{meV}$) the interferogram only consist of a handful of fringes, that vary in amplitude quite drastically. Because of this reason dither artefacts are obtained. The dither then samples over fringes multiple fringes and outputs the averaged cross-correlation. For linear symmetric dithers, such as the scanning and triangular dither, the sampling can be seen as a rectangular function. The obtained PCFS interferogram then becomes convolved with a rectangular function. We thus propose a correction of the dither, by simply deconvolving the obtained PCFS interferogram with a rectangular function with a width equal to the dither amplitude. In Figure A.14 a MC simulation is shown of a Gaussian Spectrum with a linewidth of $500\,\mathrm{meV}$. In Figure A.12a, the PCFS

interferogram and the convoluted spectrum with a rectangular function are shown. When both are Fourier transformed the spectral correlations are obtained as seen in Figure A.12b. Here, we observe that the PCFS simulation has a broader FWHM than theoretically expected, but when the convoluted PCFS interferogram is used to obtain the spectral correlations a better match is found with theory.

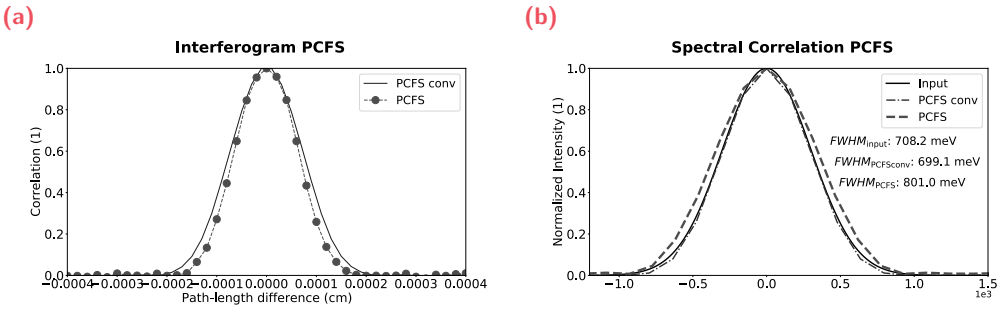

Fig. A.12.: Dither correction of PCFS interferograms. *(a)* Raw obtained PCFS interferogram and corrected interferogram through convolution with a rectangular pulse. *(b)* Spectral correlations of corrected and uncorrected PCFS interferograms compared to the input spectral correlation of the computation.

A.11.4 Asymmetry Correction Method

In this paragraph, a correction method to remove the asymmetry of PCFS interferograms is discussed. In Section 3.2 we have seen that FTS spectra are not affected by interferogram asymmetry. Additionally, a double Fourier transform trick was introduced, that removes the phase dependent part of the interferogram resulting in a perfect symmetric FTS interferogram.

A double Fourier transform would not work for PCFS interferograms, because of the loss of the absolute information. Therefore, we introduce a method which uses FTS interferograms to correct the asymmetry in a PCFS interferogram. With the double Fourier transform trick two FTS interferograms are obtained which can be mapped onto each other. Since we actually are interested in the envelope squared of those interferograms, we use the absolute Hilbert transform to obtain the envelopes. The square of the envelopes can then be mapped, and this correction function can be used on PCFS interferograms.

The asymmetry correction process is shown in Figure A.13, where first the envelopes of asymmetric and corrected FTS interferograms are obtained (Figure A.13a). FTS and PCFS data are obtained on AgDNPs driven with the superK white light laser and

the superK VARIA set to $470\,\mathrm{nm}$ with a bandwidth of $100\,\mathrm{nm}$. The mapping function of the two envelopes squared is used to correct PCFS interferograms, which can be turned into spectral correlations. Figure A.13b shows the uncorrected spectral correlations and Figure A.13c. We observe that the average single linewidth and ensemble linewidth have broadened due to the asymmetry correction. Unfortunately, this correction is rather sensitive to the exact shape of the mapping function. In the presented method no filtering of the FTS interferograms has been performed, which leads to greater noise in the mapping function. The mismatch between the FTS spectral correlation and ensemble PCFS spectral correlation in Figure A.13b and Figure A.13c could be explained by this.

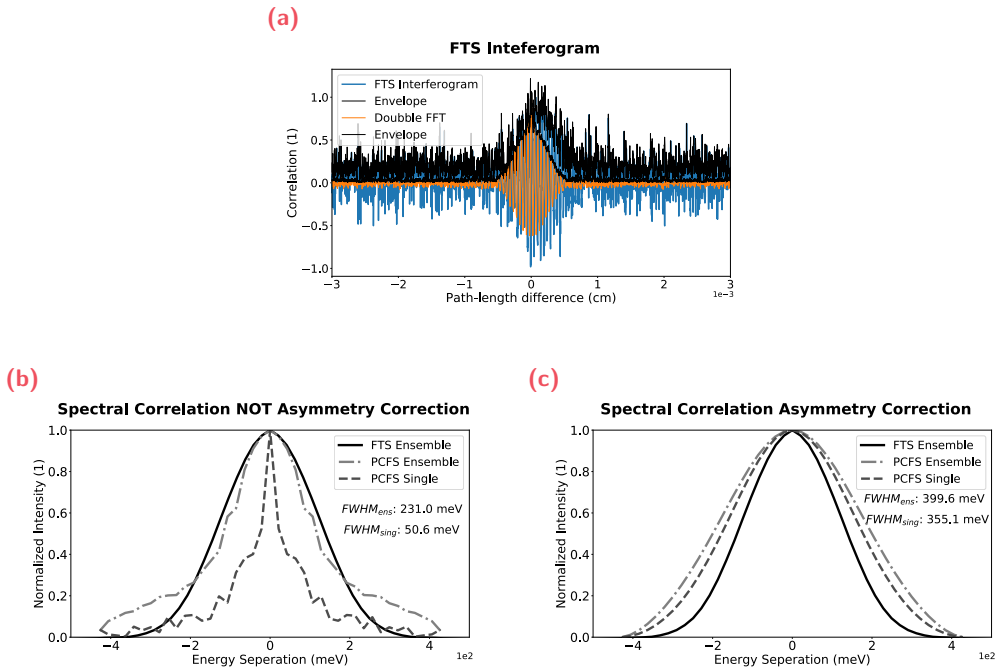

Fig. A.13.: Dither correction of PCFS interferograms. *(a)* Raw obtained PCFS interferogram and corrected interferogram through convolution with a rectangular pulse. *(b)* Spectral correlations of corrected and uncorrected PCFS interferograms compared to the input spectral correlation of the computation.

A.11.5 Global Correction Method

In this paragraph, a global correction method for PCFS experiments is discussed. This method captures all of the above corrections into one. Unfortunately, this method also seems the most arbitrary. For the global correction, a FTS measurement and a PCFS measurement are needed. Thanks to the math from Section 3.2, we know

that the spectra that are obtained through FTS are not affected by the asymmetry. Additionally, they are not affected by the dither, since it is not present. Thirdly, they are not affected by intensity fluctuations, since they are filtered out when doing dual-detector FTS. Lastly, driving light correction can be applied to obtain the pure LSPR spectrum, from which the LSPR ensemble spectral correlation can be computed.

As a correction, we would simply match the PCFS ensemble spectral correlation to the FTS ensemble spectral correlation, and use the same correction curve on the single PCFS spectral correlation. We do this, since we know that the PCFS and FTS spectral correlations in principle should be identical. We only assume that the correction can be taken over to the average single spectral correlation, which is valid as long as both the average single and the ensemble spectral correlation are comparable to each other.

In Figure A.14a, the spectral correlations obtained with FTS and PCFS are shown of Silver decahedra nanoparticles (AgDNP). The particles are driving with the superK white light laser and the spectrum is filtered with the VARIA set to $470\,\mathrm{nm}$ with a bandwidth of $100\,\mathrm{nm}$. We observe a slight mismatch between the FTS spectral correlation and the PCFS ensemble spectral correlation. In Figure A.14b the ensemble PCFS spectral correlation is mapped onto the FTS spectral correlation, since we know that they should be identical. The same mapping is then used to correct the average single nanoparticle PCFS spectral correlation.

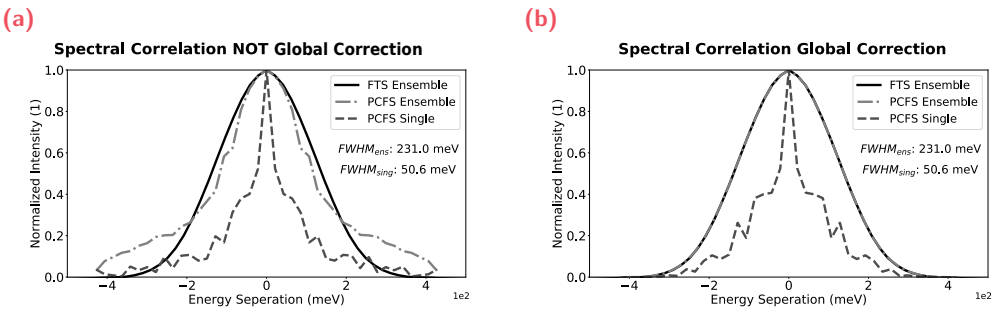

Fig. A.14.: A global correction method to correct scattering PCFS spectral correlations that takes into account interferogram asymmetry, dither effects, and the driving light. *(a)* Uncorrected spectral correlations of Silver decahedra nanoparticles (AgDNP). *(b)* Corrected spectral correlations, where the ensemble PCFS spectral correlation is mapped onto the FTS spectral correlation. The same mapping is used for the average single PCFS spectral correlation.

A.12 PCFS Interferogram Fitting Functions

This section explains how fitting functions in PCFS can be used to extract spectral information. The spectral correlations in PCFS tell something about the spectrum shape and linewidth. However, the raw data, the PCFS interferograms, also contains this information. Previously, in PCFS literature [98, 103] fits of the PCFS interferograms have been used to report spectral linewidth values. One major not to this method is that the experimenter needs to assume a spectral shape, whereas reporting the Full Width at Half Maximum of the spectral correlations does not rely on any assumptions.

Let us define a spectrum, $s(\widetilde{\nu})$, of which we measured the spectral correlation through PCFS:

$$p(\zeta) = \int_{-\infty}^{\infty} s(\widetilde{\nu}+\zeta)\,\overline{s(\widetilde{\nu})}d\widetilde{\nu} = \int_{-\infty}^{\infty} s(\widetilde{\nu})\,\overline{s(\widetilde{\nu}-\zeta)}d\widetilde{\nu} \tag{A.5}$$

For our sake, we can assume that the spectra are purely real ($s(\widetilde{\nu}) \in \mathbb{R}$) such that:

$$p(\zeta) = \int_{-\infty}^{\infty} s(\widetilde{\nu}+\zeta)\,s(\widetilde{\nu})\,d\widetilde{\nu} = \int_{-\infty}^{\infty} s(\widetilde{\nu})\,s(\widetilde{\nu}-\zeta)\,d\widetilde{\nu} \tag{A.6}$$

$$= (s \star s)(\widetilde{\nu}) \qquad = (s * s)(\widetilde{\nu}) \tag{A.7}$$

In that case the spectral auto-correlations become spectral (auto-)convolutions. From this finding we can find fitting functions for the interferogram, $\widetilde{g}(\delta)$, from the PCFS equation (Equation 3.91):

$$\widetilde{g}(\delta) = \mathfrak{Re}\{\mathcal{F}[p(\zeta)]\} \tag{A.8}$$

$$= \mathfrak{Re}\{\mathcal{F}[(s * s)(\widetilde{\nu})]\} \tag{A.9}$$

$$= \mathfrak{Re}\{\mathcal{F}[s(\widetilde{\nu})] \cdot \mathfrak{F}[s(\widetilde{\nu})]\} \tag{A.10}$$

$$= \mathfrak{Re}\left\{\mathcal{F}[s(\widetilde{\nu})]^2\right\} \tag{A.11}$$

So the approach of deriving fitting functions for PCFS interferograms will be:

1. Define spectrum mathematically
2. Compute Fourier transform
3. Square findings
4. Take the real part of it

For the correct fitting function the definition of the Fourier transform is important, since there exists a few different conventions. Important is for the user to work with units that can be transformed from spectral space (cm^{-1}) into interferometer space (cm) cm. Therefore, the Fourier transform convention should be used where $[\widetilde{\nu}] \rightarrow [\delta]^{-1}$. Thus, the following definition for the Fourier Transform is used:

$$S(\delta) = \mathcal{F}[s(\widetilde{\nu})] = \int_{-\infty}^{\infty} s(\widetilde{\nu})\, e^{-2\pi i \delta \widetilde{\nu}} d\widetilde{\nu} \tag{A.12}$$

In the following paragraphs various spectra are shown as examples, in case the reader finds him/herself ever needing them:

A.12.1 Derivation for a single Gaussian Spectrum

These paragraphs start off with the derivation of a fitting function for a Gaussian lineshape. This function is predominantly used in PCFS fitting, because of lot ergodic systems behaving like Gaussian distributions. A Gaussian spectrum, $s_{\mathrm{sg}}\left(\widetilde{\nu}\right)$, as function of the wavenumber, $\widetilde{\nu}$, is given as:

$$s_{\mathrm{sg}}\left(\widetilde{\nu}\right) = Ae^{-\frac{\left(\widetilde{\nu}-\widetilde{\nu}_0\right)^2}{2c^2}} \tag{A.13}$$

with A being the amplitude, $\widetilde{\nu}_0$ is the center peak position, and c is the standard deviation. Now, the Fourier transform of this single Gaussian is calculated as:

$$\begin{aligned}
\mathcal{F}\left[s\left(\widetilde{\nu}\right)\right]\left(\delta\right) &= \int_{-\infty}^{\infty} Ae^{-\frac{\left(\widetilde{\nu}-\widetilde{\nu}_0\right)^2}{2c^2}} \cdot e^{-2\pi i\delta\widetilde{\nu}} d\widetilde{\nu} \\
&= A\int_{-\infty}^{\infty} e^{-\frac{\left(\widetilde{\nu}-\widetilde{\nu}_0\right)^2}{2c^2}} \cdot e^{-2\pi i\delta\widetilde{\nu}} d\widetilde{\nu} \\
&= A\int_{-\infty}^{\infty} e^{-\frac{u^2}{2c^2}} \cdot e^{-2\pi i\delta\left(u+\widetilde{\nu}\right)} du \\
&= A\cdot e^{-2\pi i\delta\widetilde{\nu}_0}\int_{-\infty}^{\infty} e^{-\frac{u^2}{2c^2}} \cdot e^{-2\pi i\delta u} du \\
&= \sqrt{2}cA\cdot e^{-2\pi i\delta\widetilde{\nu}_0}\int_{-\infty}^{\infty} e^{-\widetilde{u}^2} \cdot e^{-2\pi i\delta\sqrt{2}c\widetilde{u}} d\widetilde{u} \\
&= \sqrt{2}cA\cdot e^{-2\pi i\delta\widetilde{\nu}_0}\int_{-\infty}^{\infty} e^{-\widetilde{u}^2} \cdot e^{-2\pi i\widetilde{\delta}\widetilde{u}} d\widetilde{u}
\end{aligned} \tag{A.14}$$

where $\widetilde{\delta} = \sqrt{2}c\delta$. The latter integral has a well-known solution, such that the Fourier transform of a single Gaussian spectrum is given by:

$$\mathcal{F}\left[s_{\mathrm{sg}}\left(\widetilde{\nu}\right)\right]\left(\delta\right) = \sqrt{2\pi}A\cdot c\cdot e^{-2\pi^2c^2\delta^2}e^{-2\pi i\delta\widetilde{\nu}_0} \tag{A.15}$$

To derive the fitting function for a PCFS interferogram we take into account that the oscillation produced by $e^{-2\pi i\delta\widetilde{\nu}_0}$ is removed by the dither, such that $e^{-2\pi i\delta\widetilde{\nu}_0} \approx 1$.

$$\widetilde{g}_{\mathrm{sg}}\left(\delta\right) = \mathfrak{Re}\left\{\mathcal{F}\left[s_{\mathrm{sg}}\left(\widetilde{\nu}\right)\right]^2\right\} = 2\pi A^2c^2e^{-4\pi^2c^2\delta^2} \tag{A.16}$$

A.12.2 Derivation for a double Gaussian Spectrum

Many spectra can be fitted with a single Gaussian lineshape, however sometimes there are two main contributors to a spectrum. Therefore, I will now discuss the double Gaussian spectrum, $s_{\mathrm{dg}}\left(\widetilde{\nu}\right)$, as function of the wavenumber, $\widetilde{\nu}$, is given as:

$$s_{\mathrm{dg}}\left(\widetilde{\nu}\right) = Ae^{-\frac{\left(\widetilde{\nu}-\widetilde{\nu}_0\right)^2}{2c^2}} + Be^{-\frac{\left(\widetilde{\nu}-\widetilde{\nu}_0\right)^2}{2d^2}} \tag{A.17}$$

with A and B being the amplitudes for the respective Gaussians, $\widetilde{\nu}_0$ is the center peak position, and c and d are the standard deviations for the respective Gaussians. Since Fourier transforms are additive we can simple add the individual Fourier transforms of this double Gaussian as:

$$\begin{aligned}\mathcal{F}\left[s_{\mathrm{dg}}\left(\widetilde{\nu}\right)\right]\left(\delta\right) &= \mathcal{F}\left[s_{\mathrm{sg},1}\left(\widetilde{\nu}\right) + s_{\mathrm{sg},2}\left(\widetilde{\nu}\right)\right] \\ &= \mathcal{F}\left[s_{\mathrm{sg},1}\left(\widetilde{\nu}\right)\right] + \mathcal{F}\left[s_{\mathrm{sg},2}\left(\widetilde{\nu}\right)\right] \\ &= \sqrt{2\pi}A\cdot c\cdot e^{-2\pi^2c^2\delta^2}e^{-2\pi i\delta\widetilde{\nu}_0} + \sqrt{2\pi}B\cdot d\cdot e^{-2\pi^2c^2\delta^2}e^{-2\pi i\delta\widetilde{\nu}_0}\end{aligned} \tag{A.18}$$

Now, to compute the fitting function for a double Gaussian spectrum we again identify that the oscillation due to $e^{-2\pi i\delta\widetilde{\nu}_0}$ is removed in PCFS experiments, such that:

$$\begin{aligned}\widetilde{g}_{\mathrm{dg}}\left(\delta\right) = \mathfrak{Re}\left\{\mathcal{F}\left[s_{\mathrm{dg}}\left(\widetilde{\nu}\right)\right]^2\right\} &= \left(\sqrt{2\pi}A\cdot c\cdot e^{-2\pi^2c^2\delta^2} + \sqrt{2\pi}B\cdot d\cdot e^{-2\pi^2c^2\delta^2}\right)^2 \\ &= 2\pi\left(A^2c^2e^{-4\pi^2c^2\delta^2} + B^2d^2e^{-4\pi^2c^2\delta^2} + 2ABcde^{-2\pi^2\delta^2\left(c^2+d^2\right)}\right)\end{aligned} \tag{A.19}$$

A.12.3 Derivation for a single Lorentzian Spectrum

Another spectral lineshape that is sometimes found in nature is a Lorentzian spectrum ($s_{\mathrm{L}}\left(\widetilde{\nu}\right)$) given as:

$$s_{\mathrm{L}}\left(\widetilde{\nu}\right) = \frac{A}{\pi}\frac{\frac{1}{2}\Gamma}{\left(\widetilde{\nu}-\widetilde{\nu}_0\right)^2+\left(\frac{1}{2}\Gamma\right)^2} \tag{A.20}$$

where A is the amplitude, Γ is the FWHM, and $\widetilde{\nu}_0$ is the center peak position. The Fourier transform takes on the following shape:

$$\begin{aligned}
\mathcal{F}\left[s_{\mathrm{L}}\left(\widetilde{\nu}\right)\right]\left(\delta\right) &= \int_{-\infty}^{\infty}\frac{A}{\pi}\frac{\frac{1}{2}\Gamma}{\left(\widetilde{\nu}-\widetilde{\nu}_0\right)^2+\left(\frac{1}{2}\Gamma\right)^2}\cdot e^{-2\pi i\delta\widetilde{\nu}}d\widetilde{\nu} \\
&= \frac{A}{\pi}\int_{-\infty}^{\infty}\frac{\frac{1}{2}\Gamma}{u^2+\left(\frac{1}{2}\Gamma\right)^2}\cdot e^{-2\pi i\delta\left(u+\widetilde{\nu}_0\right)}du \\
&= \frac{A}{\pi}e^{-2\pi i\delta\widetilde{\nu}_0}\int_{-\infty}^{\infty}\frac{\frac{1}{2}\Gamma}{u^2+\left(\frac{1}{2}\Gamma\right)^2}e^{-2\pi i\delta u}du \\
&= Ae^{-2\pi i\delta\widetilde{\nu}_0}e^{-\Gamma|\delta|/2}
\end{aligned} \tag{A.21}$$

Again we drop the oscillation $e^{-2\pi i\delta\widetilde{\nu}_0}$, such that:

$$\begin{aligned}
\widetilde{g}_{\mathrm{L}}\left(\delta\right) = \mathfrak{Re}\left\{\mathcal{F}\left[s_{\mathrm{L}}\left(\widetilde{\nu}\right)\right]^2\right\} &= \left(Ae^{-\Gamma|\delta|/2}\right)^2 \\
&= A^2e^{-\Gamma|\delta|}
\end{aligned} \tag{A.22}$$

A.12.4 Derivation for a Voigt profile

The third theoretical basic lineshape is given by the Voigt profile, $s_{\mathrm{V}}\left(\widetilde{\nu}\right)$. The Voigt profile is defined as the convolution of a Gaussian and a Lorentzian:

$$s_{\mathrm{V}}\left(\widetilde{\nu}\right) = \left(s_{\mathrm{sg}} * s_{\mathrm{L}}\right)\left(\widetilde{\nu}\right) = \int_{-\infty}^{\infty} s_{\mathrm{sg}}\left(\widetilde{\nu}'\right) s_{\mathrm{L}}\left(\widetilde{\nu} - \widetilde{\nu}'\right) d\widetilde{\nu}' \tag{A.23}$$

with s_{sg} being a single Gaussian lineshape and s_{L} a Lorentzian lineshape as define earlier. The Fourier transform becomes:

$$\begin{aligned}
\mathcal{F}\left[s_{\mathrm{V}}\left(\widetilde{\nu}\right)\right]\left(\delta\right) &= \mathcal{F}\left[\left(s_{\mathrm{sg}} * s_{\mathrm{L}}\right)\left(\widetilde{\nu}\right)\right] \\
&= \mathcal{F}\left[s_{\mathrm{sg}}\left(\widetilde{\nu}\right)\right] \cdot \mathcal{F}\left[s_{\mathrm{L}}\left(\widetilde{\nu}\right)\right] \\
&= \sqrt{2\pi} A_{\mathrm{sg}} c e^{-2\pi^2 c^2 \delta^2} e^{-2\pi i \delta \widetilde{\nu}_0} \cdot A_{\mathrm{L}} e^{-2\pi i \delta \widetilde{\nu}_0} e^{-\Gamma|\delta|/2} \\
&= \sqrt{2\pi} A_{\mathrm{sg}} c A_{\mathrm{L}} e^{-2\pi^2 c^2 \delta^2 - \Gamma|\delta|/2} \cdot e^{-2 \cdot 2\pi i \delta \widetilde{\nu}_0}
\end{aligned} \tag{A.24}$$

Now, the oscillation $e^{-2\pi i \delta \widetilde{\nu}_0}$ is removed because of the PCFS dither. Notably, the frequency of this oscillation has doubled for the Voigt profile, but that will still be filtered out in PCFS experiments. The fitting function then becomes:

$$\begin{aligned}
\widetilde{g}_{\mathrm{V}}\left(\delta\right) = \mathfrak{Re}\left\{\mathcal{F}\left[s_{\mathrm{V}}\left(\widetilde{\nu}\right)\right]^2\right\} &= \left(\sqrt{2\pi} A_{\mathrm{sg}} c A_{\mathrm{L}} e^{-2\pi^2 c^2 \delta^2 - \Gamma|\delta|/2}\right)^2 \\
&= 2\pi A_{\mathrm{sg}}^2 c^2 A_{\mathrm{L}}^2 e^{-4\pi^2 c^2 \delta^2 - \Gamma|\delta|}
\end{aligned} \tag{A.25}$$

A.12.5 Derivation for a Rectangular profile

Next a rectangular lineshape is considered, $s_{\mathrm{R}}\left(\widetilde{\nu}\right)$. This lineshape is taken into account, because the spectral shapes of the driving light used in this dissertation.

$$s_{\mathrm{R}}\left(\widetilde{\nu}\right)=\begin{cases}0 & \text{if } |\widetilde{\nu}-\widetilde{\nu}_0|>w/2\\ A & \text{if } |\widetilde{\nu}-\widetilde{\nu}_0|<w/2\\ A/2 & \text{if } |\widetilde{\nu}-\widetilde{\nu}_0|=w/2\end{cases} \tag{A.26}$$

with A being the amplitude and w the linewidth of the rectangular function. Then, the Fourier transform takes on the following shape:

$$\begin{aligned}\mathcal{F}\left[s_{\mathrm{R}}\left(\widetilde{\nu}\right)\right]\left(\delta\right)&=\int_{-\infty}^{\infty}s_{\mathrm{R}}\left(\widetilde{\nu}\right)\cdot e^{-2\pi i\delta\widetilde{\nu}}d\widetilde{\nu}\\&=\int_{\widetilde{\nu}_0-w/2}^{\widetilde{\nu}_0+w/2}A\cdot e^{-2\pi i\delta\widetilde{\nu}}d\widetilde{\nu}\\&=\frac{A}{2\pi i\delta}\left(e^{-2\pi i\delta\left(\widetilde{\nu}_0+w/2\right)}-e^{-2\pi i\delta\left(\widetilde{\nu}_0-w/2\right)}\right)\\&=\frac{A}{2\pi i\delta}\left(e^{-2\pi i\delta w/2}-e^{+2\pi i\delta w/2}\right)\cdot e^{-2\pi i\delta\left(\widetilde{\nu}_0\right)}\\&=\frac{A}{\pi\delta}\sin\left(2\pi\delta w/2\right)\cdot e^{-2\pi i\delta\left(\widetilde{\nu}_0\right)}\\&=Aw\frac{\sin\left(\pi\delta w\right)}{\pi\delta w}\cdot e^{-2\pi i\delta\left(\widetilde{\nu}_0\right)}\\&=Aw\,\mathrm{sinc}\left(\pi\delta w\right)\cdot e^{-2\pi i\delta\left(\widetilde{\nu}_0\right)}\end{aligned} \tag{A.27}$$

To obtain the fitting function $e^{-2\pi i\delta\widetilde{\nu}_0}$ is dropped from the equation, because of the PCFS dither, such that the fitting function becomes:

$$\begin{aligned}\widetilde{g}_{\mathrm{R}}\left(\delta\right)&=\left(Aw\,\mathrm{sinc}\left(\pi\delta w\right)\right)^2\\&=A^2w^2\,\mathrm{sinc}^2\left(\pi\delta w\right)\end{aligned} \tag{A.28}$$

A.12.6 Derivation for a Triangular profile

Lastly the triangular lineshape is considered, $s_{\mathrm{R}}\left(\widetilde{\nu}\right)$. This lineshape is taken into account, because it is a non-symmetric lineshape.

$$s_{\mathrm{R}}\left(\widetilde{\nu}\right)=\begin{cases}0 & \text{if } |\widetilde{\nu}-\widetilde{\nu}_0|>w/2\\ \pm A\cdot\dfrac{\widetilde{\nu}-\widetilde{\nu}_0}{w}+\dfrac{1}{2} & \text{if } |\widetilde{\nu}-\widetilde{\nu}_0|<w/2\\ \dfrac{A}{2} & \text{if } \pm(\widetilde{\nu}-\widetilde{\nu}_0)=w/2\end{cases} \tag{A.29}$$

with A being the amplitude and w being FWHM of the triangular lineshape. The Fourier transform takes on the following shape:

$$\begin{aligned}\mathcal{F}\left[s_{\mathrm{R}}\left(\widetilde{\nu}\right)\right]\left(\delta\right)&=\int_{-\infty}^{\infty}s_{\mathrm{R}}\left(\widetilde{\nu}\right)\cdot e^{-2\pi i\delta\widetilde{\nu}}d\widetilde{\nu}\\&=\int_{\widetilde{\nu}_0-w/2}^{\widetilde{\nu}_0+w/2}A\cdot(\frac{\widetilde{\nu}-\widetilde{\nu}_0}{w}+\frac{1}{2})\cdot e^{-2\pi i\delta\widetilde{\nu}}d\widetilde{\nu}\\&=\frac{A}{w}\int_{\widetilde{\nu}_0-w/2}^{\widetilde{\nu}_0+w/2}\widetilde{\nu}\cdot e^{-2\pi i\delta\widetilde{\nu}}d\widetilde{\nu}+\int_{\widetilde{\nu}_0-w/2}^{\widetilde{\nu}_0+w/2}(\frac{A}{2}-\frac{A\widetilde{\nu}_0}{w})\cdot e^{-2\pi i\delta\widetilde{\nu}}d\widetilde{\nu}\\&=\frac{A}{4w\pi^2\delta^2}\left(\left(1+2i\delta\pi\left(\widetilde{v}_0+w/2\right)\right)e^{-2\pi i\delta\left(\widetilde{\nu}_0+w/2\right)}-\left(1+2i\delta\pi\left(\widetilde{v}_0-w/2\right)\right)e^{-2\pi i\delta\left(\widetilde{\nu}_0-w/2\right)}\right)\\&+(\frac{Aw}{2}-\frac{Aw\widetilde{\nu}_0}{w})\operatorname{sinc}\left(\pi\delta w\right)\cdot e^{-2\pi i\delta\widetilde{\nu}_0}\\&=[\frac{A}{4w\pi^2\delta^2}\left(\left(2i-4\delta\pi\widetilde{v}_0\right)\cdot\sin\left(2\pi\delta w/2\right)+w\cdot\cos\left(2\pi\delta w/2\right)\right)\\&+A(\frac{w}{2}-\widetilde{\nu}_0)\operatorname{sinc}\left(\pi\delta w\right)]\cdot e^{-2\pi i\delta\widetilde{\nu}_0}\\&=[\frac{Aw}{4}\left(\left(2i-4\delta\pi\widetilde{v}_0\right)\cdot\frac{\sin\left(\pi\delta w\right)}{\left(\pi\delta w\right)^2}+w\cdot\frac{\cos\left(\pi\delta w\right)}{\left(\pi\delta w\right)^2}\right)\\&+A(\frac{w}{2}-\widetilde{\nu}_0)\operatorname{sinc}\left(\pi\delta w\right)]\cdot e^{-2\pi i\delta\widetilde{\nu}_0}\end{aligned} \tag{A.30}$$

Lastly, we remove the oscillation $e^{-2\pi i\delta\widetilde{\nu}_0}$ to obtain the fitting function as:

$$\begin{aligned}\widetilde{g}_{\mathrm{R}}\left(\delta\right)&=\left(Aw\operatorname{sinc}\left(\pi\delta w\right)\right)^2\\&=A^2w^2\operatorname{sinc}^2\left(\pi\delta w\right)\end{aligned} \tag{A.31}$$

A.13 Dynamic Light Scattering Measurements of Oil Micelles

In Figure A.15 a Dynamic Light Scattering (DLS) measurement is shown of oil micelles synthesized according to Section 4.2.4. From DLS we find that the majority of micelles has a size of $8.28 \pm 0.09\text{nm}$ in diameter. A second peak is observed at $40 \pm 7\text{nm}$, which could indicate bigger micelles or clusters of small micelles. The solution however does not appear to be cloudy or milky, thus we hypothesize that these bigger particles are present in much lesser extend than the 8nm micelles. These DLS graphs are averaged values over three measurements and show the size distribution by intensity.

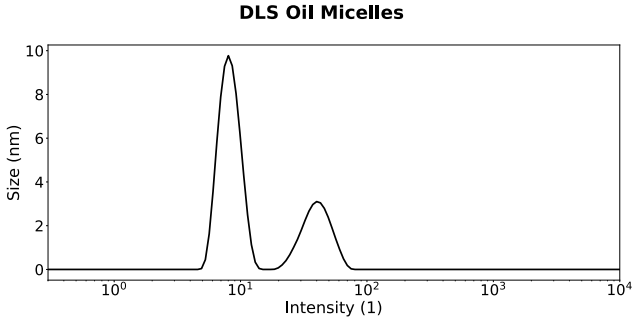

Fig. A.15.: Dynamic Light Scattering measurement of Oil Micelles.

A.14 2 Laser Scattering Laser Stability

In Figure A.16 the amplitude of the Zero peak of a 2 laser scattering experiment is shown. Here, the laser light is reflected off of a mirror into the optical setup to measure the stability of the laser. At sub-μs we find the afterpulsing pedestal that is present in all of the 2 laser measurements because of the detectors that we use. At $10\,\mu$s to $100\,\mu$s, we do not observe the typical intrinsic dynamics that we see when nanosensors are measured. The curves we obtain are very flat indicating that the laser are stable for the durations of our experiments.

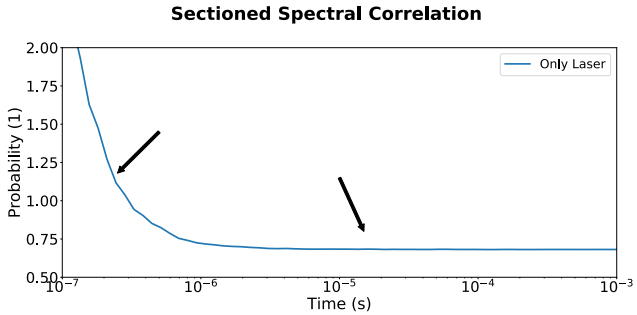

Fig. A.16.: Zero peak of a 2 laser scattering experiment of only the two lasers.

Colophon

This thesis was typeset with LaTeX 2_ε. It uses the *Clean Thesis* style developed by Ricardo Langner. The design of the *Clean Thesis* style is inspired by user guide documents from Apple Inc.

Download the *Clean Thesis* style at `http://cleanthesis.der-ric.de/`.